Droplet evaporation on smooth patterns

Thesis

Droplet evaporation on smooth patterns

Michael Ewetola

The Open University
Milton Keynes, UK

This dissertation is submitted for the degree of
Doctor of Philosophy in Mathematics

September 2021

Abstract

Controlling the shape and location of evaporating droplets on a solid surface is critical in a variety of industrial applications where droplet dynamics is important. Ink-jet printing, display technologies, DNA analysis, lab-on-a-chip device design, coating, micro-patterning, and heat transfer are examples. This thesis investigates how to control droplet evaporation on smooth surfaces with well-defined patterns.

The evaporation of a two-dimensional droplet on a solid surface is initially investigated. The solid is flat, but there are smooth chemical variations that cause a space-dependent local contact angle. We conduct a detailed bifurcation analysis of the droplet's equilibrium properties as its size changes, observing the emergence of a hierarchy of bifurcations that is strongly dependent on the underlying chemical pattern. Symmetric and periodic patterns give rise to a series of pitchfork and saddle-node bifurcations, causing stable solutions to become saddle nodes. This change in stability under dynamic conditions implies that any perturbation in the system can cause the droplet to shift laterally while relaxing to the nearest stable point in a snap event, as confirmed by numerical computations of the Cahn-Hilliard and Navier-Stokes systems of equations. Also, with asymmetric patterns we are able to effectively control droplet evaporation.

This enables the investigation of the effect of wetting strength and droplet properties such as size, viscosity, and surface tension on the snap speed of evaporating droplets on a smooth pattern. We investigate the interaction of chemical and topographical patterns on non-planar surfaces. We discover that combining periodic chemical and topographical patterns can either amplify or annihilate snap effects. A well-defined wetting pattern can also be used to control the direction of evaporating droplets on a non-planar surface.

Gravity's effect on evaporating droplets on a flat surface with periodic wetting patterns is also investigated. Gravity changes the shape of a droplet by increasing its radius and decreasing its height while keeping its size constant. As it evaporates on an incline plane with a symmetric chemical pattern, a droplet will prefer to move in the direction of gravity. However, it is discovered that when the effect of gravity is weaker than the strength of the wetting pattern, a droplet can be made to move in the opposite direction dictated by gravity on an asymmetric pattern with amplitude gradient.

Acknowledgements

First and foremost, I will like to give thanks to God for helping me to achieve this feat of completing a PhD.

I will also like to express my gratitude to my supervisor, Dr. Marc Pradas, for his unwavering support and guidance during my doctoral journey. I am grateful beyond words. Thank you very much.

My acknowledgements go to the School of Mathematics and Statistics as well as the Faculty of Science, Technology, Engineering and Mathematics at The Open University for funding my PhD and providing support in various forms throughout the past three and half years.

Special thanks go to Dr. Matthew Haynes for useful contributions and collaborations and for always asking important questions that helped to solidify my knowledge. I will also like to thank Dr. Rodrigo Ledesma-Aguilar of the University of Edinburgh for important collaborations. Additionally, my thanks goes to Alex Round for interesting conversations.

My warm thanks go to my darling wife, Deborah for being very helpful and understanding. Thank you for all your encouragements.

Declaration

I hereby declare that except where specific reference is made to the work of others, the contents of this dissertation are original and have not been submitted in whole or in part for consideration for any other degree or qualification in this, or any other university. The research described in this thesis was performed at the School of Mathematics and Statistics at the Open University between December 2017 and May 2021 and was supervised by Dr Marc Pradas.

This dissertation is my own work and collaborations were made as follows. At the time of submission, one paper based on the work presented in this thesis has been published, co-authored with Dr Rodrigo Ledesma-Aguilar and Dr Marc Pradas. The paper is based on the results of Chapter 3 and has been published in Physical Review Fluids. In this publication, I developed the mathematical modelling, performed the theoretical analysis and all computational work, including the development of appropriate numerical algorithms, while R. Ledesma-Aguilar and M. Pradas supervised the research.

The theoretical analysis based on energy balance of Chapter 4 and the bifurcation analysis presented in Chapter 6 have been done in collaboration with Dr Matthew Haynes.

Michael Ewetola
September 2021

Table of contents

Chapter 1

Introduction

Droplets are everywhere and we encounter them on a daily basis. For example, when rain falls, droplets of water roll off leaves while some remain stationary and eventually dry up, see Fig. 1.1(a). On vehicles such as cars and aeroplanes, water droplets can stick to or roll off windscreens and windows on a rainy day. Figure 1.1(b) shows a scenario where water droplets either roll off or stick to an aeroplane window. The emergence of droplets in our day-to-day life is however not limited to rain alone. When coffee is spilled on a paper for example, see Fig. 1.1(c), it evaporates after some time, leaving a ring-like stain, see Fig. 1.1(d). This is due to the flow triggered by evaporation where depleted liquid from the droplet edge is being replenished by liquid from the droplet interior. The dispersed

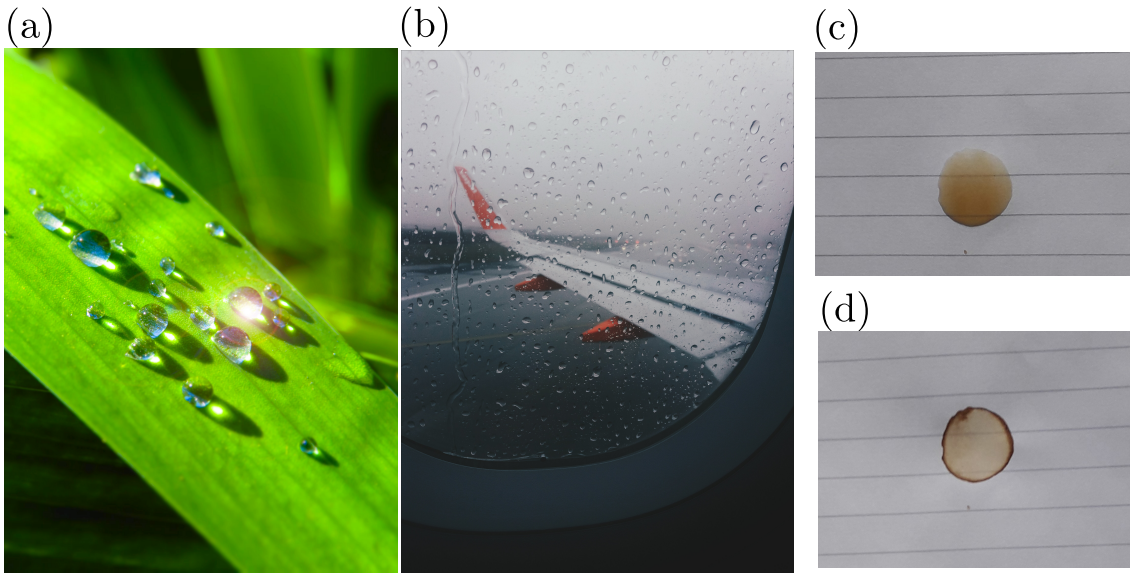

Fig. 1.1 Examples of droplets in real life. (a) Droplets on leaves [1]. (b) Droplets on aeroplane window [2]. (c) Coffee droplet on a paper. (d) Coffee stain on a paper.

material in the liquid is then brought to the droplet edge forming a ring-like pattern when the droplet dries. This effect can be undesirable but has significant industrial applications in printing which relies heavily on evaporating droplets containing dispersed particles leaving patterns on solid surfaces [3].

Controlling the shape and location of evaporating droplets on a solid surface is therefore critical not just for printing applications in ink-jet printing [4], but also in several other industrial and technological processes in which droplet dynamics plays a fundamental role. These include display technologies [5], DNA analysis [6], design of lab-on-a-chip devices which do not require external forces for droplet merging and transport [7], coating, micro-patterning, and heat transfer. This thesis explores how the wetting properties of solids can be used to regulate the shape, size and motion of evaporating droplets on solid surfaces. In this first chapter, we introduce a number of basic concepts that are required to understand the physics and mathematical modelling of droplets.

1.1 Wetting phenomena

Wetting is the study of the spread of a liquid placed on a solid surface. When a droplet of water is placed on a very clean glass it completely spreads, but when placed on a plastic sheet it forms a solitary droplet. This contrasting property of a droplet on various substrates suggests the existence of two wetting regimes. The parameter which characterises these regimes is the so-called spreading parameter S, which measures the difference between the energy E of the surface in the dry and wet area of the substrate:

$$S = E|_{dry} - E|_{wet}. \tag{1.1}$$

When S is positive, the fluid fully spreads or wets completely [8]. If S is negative instead, a droplet rests on the substrate with an angle of intersection of the liquid-gas interface with respect to the substrate, called the equilibrium contact angle, which is denoted as θ_e, see Fig. 1.2. The wetted area of the droplet is limited by the point where the liquid, gas and solid phases meet, called the contact line and characterized by its contact angle and contact radius i.e. the distance between the droplet's mid-point and its contact line.

Liquid droplets adopt spherical shapes at equilibrium, the reason for this phenomenon is surface tension. To understand surface tension, it is useful to think of a liquid surface as a stretched membrane characterized by a force per unit length that opposes its distortion. In the bulk of a liquid, a molecule is surrounded by more liquid molecules than one located at the liquid surface. Hence a molecule in the midst of a liquid has an advantage

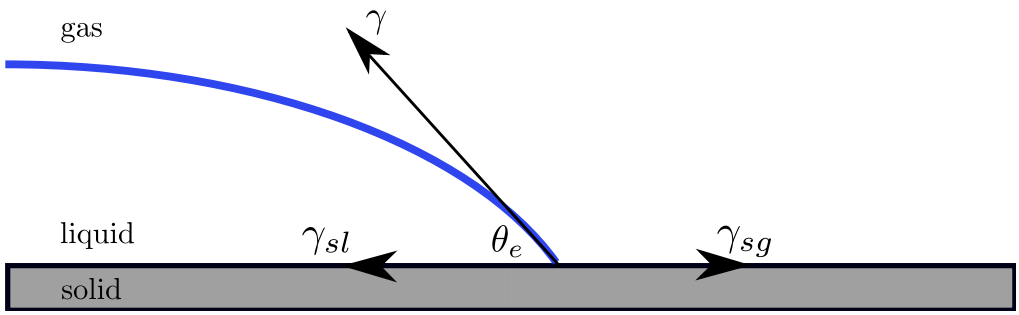

Fig. 1.2 Surface tensions acting on the contact line of a sessile droplet, where θ_e is the equilibrium contact angle.

of interacting with all its neighbours. However, a molecule close to the surface loses half its cohesive interactions. This means that the cohesion energy per molecule at the interface is less than inside the liquid. Therefore, molecules at the interface are energetically unfavourable and so liquids adopt spherical cap shapes to minimise the exposed interfacial area [8]. The units of surface tension is usually given in force per unit length, and equivalently, energy per unit area. Typical values are: water-air, 72.86 mN / m, ethanol-air, 22.39 mN / m, and mercury-air, 486.5 mN / m, at room temperature.

The capillary length of a liquid of density ρ, defined as $\ell_c = \sqrt{\frac{\gamma}{\rho g}}$, determines how the capillary forces due to surface tension γ compete with graviational forces ρg to influence droplet shape [9], where g is the acceleration due to gravity. For a droplet with a base radius R that is smaller than the capillary length ℓ_c, gravity is negligible and the shape of the droplet is determined solely by surface tension. The droplet shape is spherical in this regime, but when the droplet base radius exceeds the capillary length, it resembles the shape of a pancake with constant thickness, bent only at the surface, (see Fig. 1.3) as gravity becomes a dominant force in the system.

Under equilibrium conditions the contact angle of a droplet is given by the Young-Dupré relation [10]:

$$\cos\theta_e = \frac{\gamma_{sg} - \gamma_{sl}}{\gamma}, \tag{1.2}$$

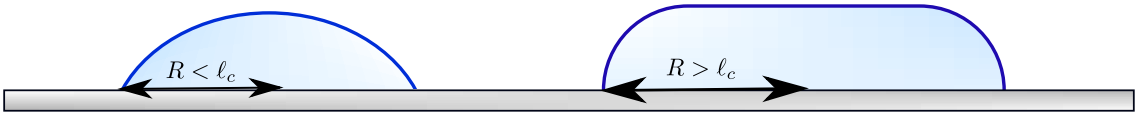

Fig. 1.3 Droplets on a flat surface. The left panel represents the regime in which the droplet base radius is less than the capillary length $R < \ell_c$, and the right panel represents the regime in which the droplet base radius is greater than the capillary length $R > \ell_c$.

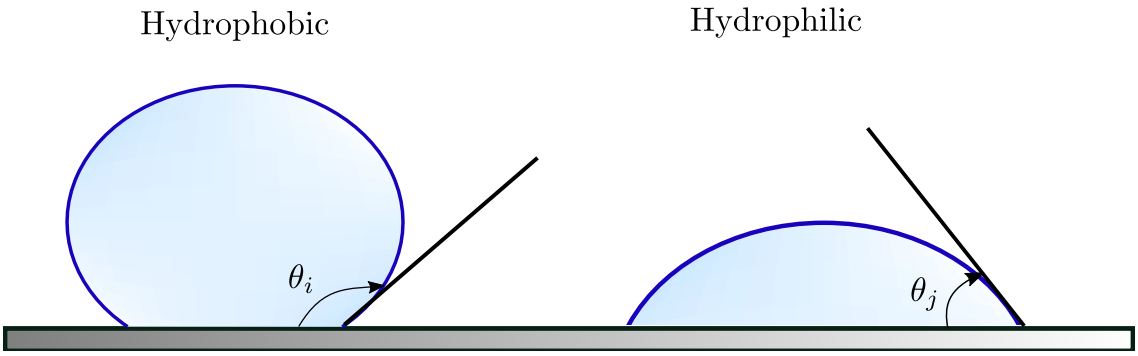

Fig. 1.4 Droplets on a flat surface. The left panel corresponds to an hydrophobic droplet where the equilibrium contact angle $\theta_e = \theta_i > 90°$, the right panel shows an hydrophilic droplet whose equilibrium contact angle $\theta_e = \theta_j < 90°$.

where γ_{sg}, γ_{sl}, and γ are the interfacial tensions for the solid-gas, solid-liquid, and liquid-gas interfaces respectively, see Fig. 1.2. When the equilibrium contact angle is less than 90°, the droplet is termed hydrophilic and hydrophobic if greater than 90°, (see Fig. 1.4). Young-Dupré equation can be interpreted as a mechanical force balance on the three-phase contact line, as a consequence of all surface tensions acting at the contact line, see Fig. 1.2.

The Young-Dupré relation (1.2) can be rewritten in terms of the wetting parameter S defined in Eq. (1.1) by describing S through the interfacial surface tensions as:

$$S = \gamma_{sg} - (\gamma_{sl} + \gamma),$$

which upon substitution into Eq. (1.2) yields:

$$\cos\theta_e = 1 + \frac{S}{\gamma},$$

which shows that a well-defined equilibrium contact angle θ_e exits whenever the wetting parameter S is negative.

1.1.1 Contact line dynamics

Let's consider a liquid droplet that is initially on a solid surface with a contact angle θ that is far from the equilibrium configuration, θ_e. Under these conditions a flow is set in motion until the equilibrium contact angle is reached. As the droplet aims to reach equilibrium, it spreads with its contact line moving. In the limit of small equilibrium contact angles $\theta_e \ll 1$, its profile $h(x)$ can be approximated as a thin liquid film of thickness $h(x,t)$,

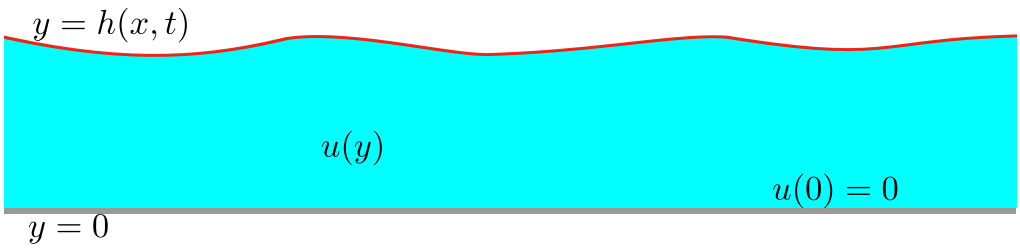

Fig. 1.5 One-dimensional liquid/gas interface with velocity profile $u(y)$, where a no-slip boundary condition is imposed on the solid $y = 0$.

one-dimensional liquid/gas interface, see Fig. 1.5, and viscosity μ flowing along a solid substrate at $y = 0$. The velocity profile u of such flow can be obtained by considering the steady Navier-Stokes equation in the horizontal direction:

$$\frac{d^2u}{dy^2} = \frac{1}{\mu}\frac{dp}{dx},$$

where p is the pressure and the velocity is uni-directional $\mathbf{u} = u(y)\,\mathbf{i}$, where $\mathbf{i}$ is the unit vector along the x direction. Solving the above equation subject to the no-slip boundary condition, $u = 0$ at the solid surface $y = 0$ and the tangential stress balance, $\frac{du}{dy} = 0$, at the free surface $h(x)$, the velocity profile is obtained as:

$$u(y) = -\frac{q}{2\mu}(y^2 - 2h(x)y), \tag{1.3}$$

where $q = -\frac{dp}{dx}$. One consequence of fluid flowing on a solid is viscous dissipation which is quantified by the dissipation function $\Phi(x, y)$, which for this problem can be written as:

$$\Phi(x,y) = \frac{9U^2\mu}{h(x)^2}\left[1 - \frac{y}{h(x)}\right],$$

where $U = \frac{1}{h(x)}\int_0^{h(x)} u(y)\,dy$ is the contact line speed. Near the contact point, $\frac{\partial h}{\partial x} = \tan\theta$, this gives $h(x) = x\tan\theta$, where the boundary condition at the contact point $h(0) = 0$ has been used. In the limit of small contact angle $\theta \ll 1$, we can assume that $h(x) \sim x\theta$. Hence, the total viscous dissipation from the contact point $x = 0$ to a length L inside the droplet is then obtained as:

$$D_{\text{visc}} = \int_0^L dx \int_0^{h(x)} \Phi(x,y)\,dy = \frac{3\mu U^2}{\theta}\int_0^L \frac{dx}{x}. \tag{1.4}$$

Evaluating Eq. (1.4) will lead to divergence to infinity, meaning that there is a singularity at the contact point. This contact line singularity first discovered by Huh and Scriven [11] implies that viscous friction at the contact point diverges and as a result it would be impossible for a contact line to move along the substrate. Since contact line do move in real life, we are faced with a paradox which can be resolved by introducing a cut-off length ℓ_s called the slip length that eliminates the singularity as follows [12]:

$$D_{\text{visc}} = \frac{3\mu U^2}{\theta} \int_{\ell_s}^{L} \frac{dx}{x} = \frac{3\mu U^2}{\theta} \ell_D, \tag{1.5}$$

where $\ell_D = \ln(L/\ell_s)$. The contact line singularity can also be resolved by using other methods like the precursor film [13] or diffuse interface formulation [14] which we will describe in Chapter 2.

Using the slip length formulation to regularise the contact line singularity allows us to find some explicit results for the time evolution of the contact line as the droplet spreads on a solid surface. An important result is Tanner's law [15, 16], which describes the evolution of the droplet's contact radius $R(t)$ as a function of time t in the limit of small contact angles:

$$R(t) \sim t^n, \tag{1.6}$$

where $n = 1/7$ for a two-dimensional droplet, and $n = 1/10$ for a three-dimensional droplet. The idea behind Tanner's law is that the main physical mechanisms that govern the spreading of a droplet are capillary forces and viscous dissipation, with inertia being ignored because the motion of the droplet is very slow. We also consider the regime where the droplet size is smaller than the capillary length, so gravity is also ignored.

To derive Tanner's law, we start by considering the total capillary force F_c at the contact line:

$$F_c = \gamma_{sg} - \gamma_{sl} - \gamma\cos\theta = \gamma(\cos\theta_e - \cos\theta),$$

where θ_e is the equilibrium contact angle and the Young-Dupré relation (1.2) has been used. Under perfect wetting conditions where $\theta_e = 0$, the capillary force can be approximated as:

$$F_c = \gamma\theta^2/2. \tag{1.7}$$

The work done by this capillary force is $F_c U$ and has to be balanced by the viscous dissipation at the contact line described in Eq. 1.5, which yields $\frac{3\mu U^2}{\theta}\ell_D = \gamma\theta^2 U/2$. By noting that the cross-sectional area A of a two-dimensional droplet in the limit of $\theta \ll 1$

is $A = 2R^2\theta/3$, (see Section 1.2), the contact line speed can be obtained as:

$$U = \frac{dR}{dt} = \frac{\gamma}{6\mu\ell_D}\left(\frac{3A}{2}\right)^3 \frac{1}{R(t)^6},$$

which can then be integrated to obtain the relation between the contact radius and spreading time as:

$$R(t) \sim t^{1/7}.$$

A similar approach can be followed to derive the exponent 1/10 in three dimensions, see e.g. [16].

1.1.2 Contact line pinning

The evolution of the contact line on a perfectly flat and smooth surface can be approximated by Tanner's law in the limit of small contact angles. However, real surfaces are affected by microscopic roughness and/or chemical defects that affect the motion of the contact line. This brings up the concept of contact line pinning, which refers to the process by which the contact line motion is inhibited as a result of the properties of the solid surface.

Let's consider the simple case of a planar solid on which the chemical properties change discontinuously from one region to another, leading to a sharp discontinuous change of the equilibrium contact angle. Let's denote region 1 with a contact angle θ_1 and region 2 with a contact angle θ_2, see Fig. 1.6(a). Let's further assume that $\theta_1 < \theta_2$, and that a moving contact line is slowly moving from region 1 to region 2.

As the contact line is advancing along region 1, the contact angle is $\theta = \theta_1$, which is imposed by the chemical properties of region 1. The contact line continues to move until it reaches the point where θ_1 discontinuously changes to θ_2. At this point the contact angle of the contact line is $\theta < \theta_2$ and so it has to adjust to the new equilibrium contact angle while the contact line remains stationary. This process is known as contact line pinning [17] and it is also referred to as Gibbs pinning [18]. Once the contact line has reached the value of region 2, $\theta = \theta_2$, the contact line depins and its translational motion resumes along region 2. This process is illustrated in 1.6(a). A similar phenomenon is observed when the solid surface has a homogeneous constant contact angle but there is a sharp discontinuous topographical change. Consider the simplest case for which the height of the solid surface discontinuously changes from ϵ_1 to ϵ_2 with $\epsilon_1 > \epsilon_2$, see Fig. 1.6(b). Here the contact angle is the same throughout the solid but as the contact line approaches the sharp discontinuity, the contact line will remain stationary at the

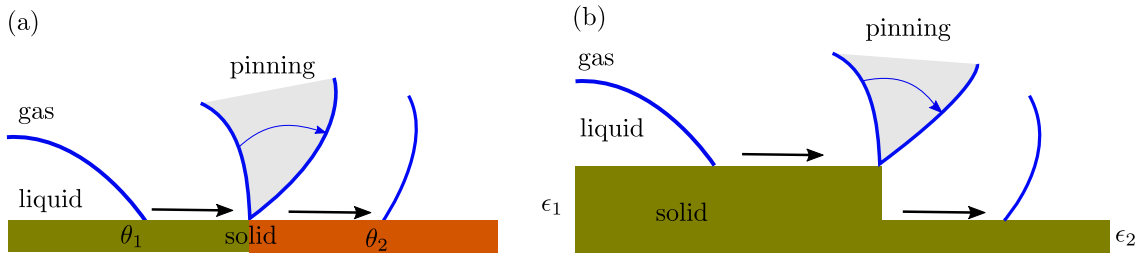

Fig. 1.6 Contact line pinning due to a sharp discontinuity in either the equilibrium contact angle on a solid (Panel a), or the surface height of a solid (Panel b).

edge until the angle between the liquid/gas interface and the side of the solid is equal to the equilibrium contact angle, as it is illustrated in Fig. 1.6(b).

These simple settings can be extended to more complex solid surfaces, and in particular in the cases of microscopic roughness or randomly distributed chemical defects with sharp discontinuities, the contact line moves along the surface with a pinning-depinning motion, which is commonly known as stick-slip motion [19]. An important point to note here is that because pinning may arise as a consequence of microscopic roughness the emergence of stick-slip motion is in general very difficult to model and control.

As we will describe below, in this thesis we will consider solid surfaces that are pinning-free, i.e., they are sufficiently smooth with no sharp (discontinuous) changes on any of their properties. From an experimental viewpoint, this can be achieved by making use of slippery surfaces [20–22], which have become very popular over the last decade.

1.2 Equilibrium properties of sessile droplets

We consider here the mathematical modelling of droplets at rest. As two fluids (for example, liquid and gas) come into contact, the pressure difference Δp across the interface, known as the Laplace pressure, is equal to the product of the surface tension γ, and the curvature of the surface κ defined as divergence of the outward normal $\mathbf{n}$ to the liquid-gas interface $\kappa = -\boldsymbol{\nabla} \cdot \mathbf{n}$ [23], (see Fig. 1.7):

$$\Delta p = \gamma \kappa. \tag{1.8}$$

Since the pressure inside a droplet is always higher than the pressure outside, it means that the curvature κ is positive. Equation (1.8) which is generally referred to as the Young-Laplace equation, can be derived by minimizing the work done by the forces of pressure and the capillary forces during an infinitesimally small displacement of the liquid-gas interface, see e.g. [8].

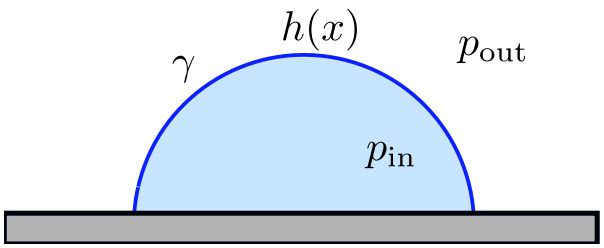

Fig. 1.7 The pressure inside a droplet is always higher than outside because of surface tension. The droplet interface, $h(x)$ satisfies the Young-Laplace equation.

1.2.1 Droplet's shape

To find the profile of a two-dimensional (2D) droplet with interface $y = h(x)$ that satisfies the Young-Laplace equation, we start by computing its curvature. This can be done by defining the functional $F(x, y) = y - h(x)$ which vanishes at the interface. The normal to the interface is then defined as:

$$\mathbf{n} = \frac{\boldsymbol{\nabla} F}{|\boldsymbol{\nabla} F|} = \frac{(-h_x, 1)}{\sqrt{1 + h_x^2}},$$

where h subscript x denotes the derivative of h with respect to x. Taking the divergence of the above expression for $\mathbf{n}$, we obtain the curvature of a 2D droplet as:

$$\kappa = \frac{h_{xx}}{(1 + h_x^2)^{\frac{3}{2}}}. \tag{1.9}$$

Substituting Eq. (1.9) in Eq. (1.8), we obtain that in the absence of gravity, the shape of the free surface of the droplet is given by a circular arc and satisfies the Young-Laplace equation:

$$\frac{\Delta p}{\gamma} = \frac{h_{xx}}{(1 + h_x^2)^{\frac{3}{2}}}. \tag{1.10}$$

To obtain the position of the droplet interface $h(x)$, we solve the above equation (1.10) subject to the conditions: $h_x(\ell \pm R) = \mp \tan\theta$ and $h(\ell \pm R) = 0$, where ℓ, R and θ are the mid point, contact radius and contact angle of the droplet respectively. The solution is given as:

$$h(x) = \pm\sqrt{\left(\frac{R}{\sin\theta}\right)^2 - x^2} - \frac{R}{\tan\theta}. \tag{1.11}$$

The above expression for a droplet shape is valid for all contact angles. For $\theta \leq \pi/2$, Eq. (1.11) is a single valued function of x, however when $\pi/2 < \theta < \pi$, Eq. (1.11) is a double-valued function of x for $R \leq x < R/\sin\theta$. Having obtained the position of the

droplet interface $h(x)$, we can proceed to obtain its cross-sectional area as:

$$A = \int_{\ell-R}^{\ell+R} h(x)\ dx, \tag{1.12}$$

this becomes:

$$A = \frac{R^2}{2}\frac{2\theta - \sin(2\theta)}{\sin^2\theta}. \tag{1.13}$$

Given a droplet of size A, and equilibrium contact angle $\theta = \theta_e$, its radius can be obtained from Eq. (1.13).

1.2.2 Interfacial energy and droplet's stability

The interfacial energy E of the droplet can be obtained by evaluating the work per unit area required to bring droplet molecules to its surface [23]. This is the sum of the energy, on the liquid-gas interface E_i, and the net energy on the solid surface E_s. The liquid-gas interfacial energy E_i is obtained as the integral of surface tension γ along the liquid-gas interface $E_i = \int \gamma\ ds$. By using $ds = dx\sqrt{1 + h_x^2}$, we find

$$\frac{E_i}{\gamma} = \frac{2\theta R}{\sin\theta}. \tag{1.14}$$

To obtain the net surface energy E_s, on the solid-gas and solid-liquid interfaces, we consider a horizontal force balance on a droplet on a smooth plane surface, which leads to the well-known Young's relation (1.2) for the contact angle. At equilibrium, the surface energy E_s of a droplet can be written as

$$\frac{E_s}{\gamma} = \int_{\ell-R}^{\ell+R} \frac{(\gamma_{sl} - \gamma_{sg})}{\gamma} dx = -\int_{\ell-R}^{\ell+R} \cos\theta_e\, dx. \tag{1.15}$$

Combining equations (1.14) and (1.15), we obtain the interfacial energy rescaled with surface tension as:

$$E = \frac{2\theta R}{\sin\theta} - 2R\cos\theta_e, \tag{1.16}$$

where R and θ are related through Eq. (1.13), this ensures that the interfacial energy (1.16) satisfies the Young-Laplace equation. Hence, for a fixed droplet size A, and equilibrium contact angle θ_e its radius (termed equilibrium solution) corresponds to the extrema of the interfacial energy of the droplet. Equations (1.13) and (1.16) show that for a droplet on an homogeneous solid where the contact angle is constant, its equilibrium shape is independent of the location of the droplet on the solid. Panel (a) of Fig. 1.8 shows the interfacial energy of droplet of size $A = 1.5$. Given an equilibrium contact

angle $\theta_e = 60°$, the radius of the droplet obtained from Eq. (1.13) corresponds to the extrema of the interfacial energy (red circle). Panel (d) shows the equilibrium shape of the droplet given by Eq. (1.11).

The contact angle on a surface can be made to vary spatially by imposing a wetting pattern $\Theta(x)$ on it so that the equilibrium contact angle becomes $\theta_e = \Theta(\ell \pm R)$, where ℓ is the midpoint of the droplet with respect to a reference point. Here the contact angle vary smoothly and not discontinuously thereby ruling out pinning when the contact line moves. In this scenario, the interfacial energy (1.16) is modified as:

$$E = \frac{2\theta R}{\sin\theta} - \int_{\ell-R}^{\ell+R} \cos\Theta(x)\, dx. \tag{1.17}$$

On such surfaces, the equilibrium shape of the droplet depends on the location since the contact angle is now a spatially varying function. To illustrate how such functions affect the stability of the equilibrium solutions we consider the simple example of a quadratic wetting pattern of the form:

$$\Theta(x) = \theta_0 + \epsilon x^2, \tag{1.18}$$

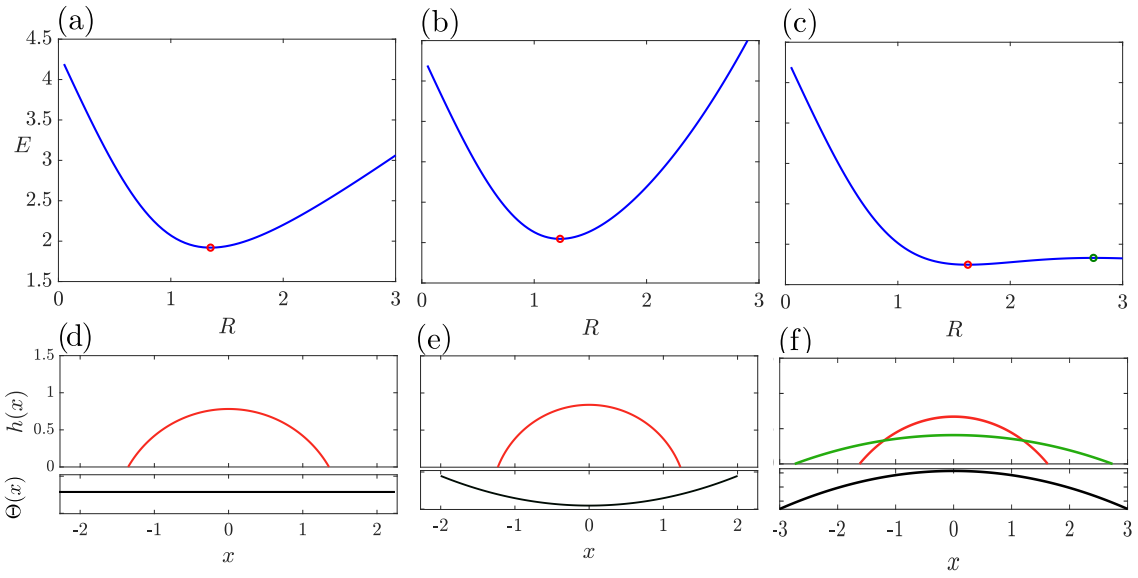

Fig. 1.8 Interfacial energies and droplet shapes given by Eq. (1.11) of size $A = 1.5$ on a solid with a constant contact angle, panels (a and d), and spatially varying contact angle, where the droplet is aligned with the minimum contact angle, panels (b and e), maximum contact angle panels (c and f). The equilibrium contact angle θ_e of the droplet corresponds to the minimum and maximum of the interfacial energy, denoted by the red and green circles respectively.

where θ_0 is the homogeneous contact angle and ϵ is the strength of the pattern. To obtain equilibrium solutions on this surface, the left and right contact angles must be equal, i.e $\Theta(\ell - R) = \Theta(\ell + R)$. This gives $(\ell - R)^2 = (\ell + R)^2$ which is satisfied if $\ell = 0$ for $R \neq 0$.

The energy profile and shape of a droplet of size $A = 1.5$ located at $\ell = 0$ on a flat surface with a quadratic wetting pattern (1.18) are shown in panels (b) and (e) of Fig. 1.8 respectively. The droplet is aligned with the minimum of the wetting pattern with wetting strength $\epsilon = 0.1$ and homogeneous contact angle $\theta_0 = 60°$. It is seen that the droplet's equilibrium radius R_e corresponds to the minimum of the interfacial energy, denoted by the red circle, see Fig. 1.8(b). Let's imagine the equilibrium point (red circle) as a droplet in a cup with shape equivalent to the energy profile (blue solid line). If we move the droplet slightly away from its equilibrium position by ΔR so that its new configuration is now $R = R_e + \Delta R$, the droplet will always move back to its original position $R = R_e$. Hence we see that the equilibrium radius R_e is unaffected by radius or axisymmetrical perturbations and as a result, the equilibrium solution R_e is stable to axisymmetrical perturbations.

When the droplet is aligned with the maximum of the wetting pattern, (i.e. when $\epsilon < 0$, see Fig. 1.8(c, f)), two equilibrium solutions appear, one of which correspond to a minimum of the interfacial energy (red circle) and as a result is stable to axisymmetric perturbations. The other equilibrium solution corresponds to a maximum on the interfacial energy profile. Because of this, a slight perturbation ΔR to the equilibrium radius R_e will ensure that the droplet does not return to its original position. Hence the equilibrium radius is unstable to axisymmetric perturbations.

The stability of droplet equilibrium solutions can in general be obtained by checking if the corresponding extrema point on the interfacial energy landscape is a minimum or a maximum. This can be found by computing the second derivative of E with respect to the droplet radius R at the equilibrium point $E_{RR}(R_e)$, where R_e is the equilibrium solution. If $E_{RR}(R_e) > 0$, then R_e is a minimum and hence stable, otherwise it is unstable. When the location ℓ of a droplet is allowed to vary instead of being fixed so that it is obtained as part of the droplet's equilibrium solution (ℓ_e, R_e), the interfacial energy $E(\ell, R)$ becomes a two-variable function of ℓ and R. In this scenario the stability of the equilibrium solutions can be obtained by examining the eigenvalues of the following Hessian matrix H_E given by:

$$H_E(\ell, R) = \begin{pmatrix} E_{\ell\ell} & E_{\ell R} \\ E_{\ell R} & E_{RR} \end{pmatrix}. \tag{1.19}$$

Let λ_1 and λ_2 be the eigenvalues of the Hessian matrix $H_E(\ell_e, R_e)$ at the equilibrium point (ℓ_e, R_e). If $\lambda_1 > 0$ and $\lambda_2 > 0$, then (ℓ_e, R_e) is a minimum and hence stable. If $\lambda_1 < 0$ and $\lambda_2 < 0$, then (ℓ_e, R_e) is a maximum and hence unstable. If $\lambda_1\lambda_2 < 0$, then (ℓ_e, R_e) is a saddle point or saddle node. This approach will be used throughout this thesis to determine the stability of droplets, as we will see later.

1.3 Droplet evaporation

Liquid droplet evaporation is a natural phenomenon that is essential in a variety of applications, including ink-jet printing, pesticide deposition, spray cooling, and thin film coating. Evaporation of sessile droplets is particularly important due to the complexities involved in modelling the evaporative mass flux, droplet lifetimes, and various modes of evaporation, which contributes to a number of interesting effects. These effects are essential in a variety of problems, including the so-called coffee-stain phenomenon [3, 24] which involves deposition of solid particles close to a contact line, and its numerous applications, including the manufacturing and operation of nano- and micro-devices.

Droplet evaporation is driven by a combination of temperature gradient between substrate and the droplet, and vapour concentration gradient between droplet molecules at the interface and in the atmosphere far away. Consequently, to completely model droplet evaporation, a two-sided model is needed in which the two impacts are accounted for [25]. This is a rather complex model and can be simplified by focusing on vapour concentration field that results in diffusion-limited models where evaporation flux can be controlled by the stationary diffusion of the liquid molecules in the gas phase, so that the liquid interface is in equilibrium with the gas phase just above it [26–28, 22, 29]. Alternatively, one can focus on the liquid phase, which yields a thermal control one-sided model where a temperature difference ΔT between the substrate and the atmosphere far away causes droplet evaporation [30, 31]. In this case evaporation rate would depend on the substrate's and droplet's thermal conductivities. However, the two models only differ slightly from the primary highlights of the evaporative flow, and in most cases what one realises is appropriate for another [29, 31].

In the diffusion-limited framework, droplets evaporate when the atmosphere in their immediate vicinity is not saturated with the vapour of the liquid. The vapour concentration c is distributed non uniformly above the droplet, and at the liquid-vapour interface, the vapour concentration is assumed to be equal the saturation value $c_{sat}(T)$, which depends on temperature. In isothermal conditions, where temperature difference is negligible, the dependence on temperature can be ignored. Far above the droplet, the

vapour concentration approaches an ambient value c_∞. It is the difference in vapour concentration $c_{sat} - c_\infty$ that creates a diffusive flux $\mathbf{J} = -D\,\boldsymbol{\nabla}\,c$ (where D is the vapour diffusivity), which drives the evaporation of liquid according to the diffusion equation [26]:

$$\frac{\partial c}{\partial t} = \boldsymbol{\nabla}\cdot\mathbf{J}\,. \tag{1.20}$$

At the surface of the droplet the vapour quickly establishes a steady-state concentration profile which obeys the steady-state diffusion equation $\boldsymbol{\nabla}^2\,c = 0$. The rate of change of the droplet size $A(t)$ with respect to time is proportional to the droplet radius $R(t)$, so that the droplet radius scales with time according to [32, 33]:

$$R(t) \sim (t_e - t)^{1/2}, \tag{1.21}$$

where t_e is the evaporation time.

In this thesis, we assume isothermal conditions where temperature difference is not important and consider quasi-static evaporation where a droplet evaporates at a rate slower than its relaxation rate. This means that the time $t_{\Delta e}$ it takes for a droplet of size A to decrease by ΔA via evaporation is much less that the time t_r required for the droplet of size A with contact angle θ, to assume its equilibrium configuration θ_e. Due to this large time scale separation where $t_{\Delta e} \ll t_r$, a droplet attains its equilibrium shape faster than it evaporates and as a result, its shape while it is evaporating can be approximated by the equilibrium properties. As we will see in Chapter 3, this assumption will allow us to build a mathematical model based on Young-Laplace formulation

1.3.1 Evaporation modes

The behaviour of an evaporating droplet is usually dictated by the nature of the solid on which it is evaporating. One of the key issues is to understand how the properties of the solid affect the contact line of the droplet. In the ideal limit of a perfectly smooth and flat solid surface, a droplet keeps a constant shape characterised by the intersection angle of the liquid-gas interface with the solid. Such constant-contact-angle (CA) mode of evaporation implies the smooth retraction of the contact line as the droplet evaporates [35], (see Fig. 1.9(a)). A droplet evaporating in a CA mode with initial size A_0, initial contact radius R_0 and initial contact angle θ_0 at time $t = 0$, on an ideal smooth and chemically homogeneous substrate does so with a constant contact angle $\theta(t) = \theta_0$ while it's contact radius $R = R(t)$ and size $A = A(t)$ decrease with time.

In contrast, surfaces with microscopic defects, either chemical or topographical, are able to induce the phenomenon known as contact-line pinning, whereby the translational motion of the contact line is suppressed [35], see also Section 1.1.2. Therefore, in the limiting situation of complete pinning, an evaporating droplet would exhibit a constant-contact-radius (CR) mode of evaporation, (see Fig. 1.9(b)). In this mode of droplet evaporation, the contact angle $\theta = \theta(t)$ and size $A = A(t)$ decrease while the contact radius $R(t) = R_0$ remains constant.

The pinning of a droplet contact line as it evaporates is the major mechanism behind the so called coffee-ring effect [3] where a spilled drop of coffee leaves a ring-like deposit along this edges as it dries on a solid surface. When coffee evaporates on a rough surface, the microscopic roughness of the solid pins the droplet's contact line, allowing only the droplet's height to steadily decrease while its radius remains constant. The fluid is squeezed outwards to compensate for evaporative losses due to the geometrical restriction of the droplet's free surface by a pinned contact line. The liquid that evaporates at the droplet edge is replenished by a capillary flow from the droplet's interior, which carries coffee particles with it to the edge, forming a ring-like pattern.

In practice, a widely accepted view is that droplet evaporation proceeds as a combination of these two limiting modes, often called a stick-slip (SS) mode of evaporation [27], where a droplet initially evaporates in a CR phase in which $R = R_0$ and $\theta(t)$ and $A(t)$ decrease until $\theta(t)$ reaches the receding contact angle θ^* at which the contact line depins and subsequently the droplet evaporates in a CA phase in which $\theta(t) = \theta^*$ and $R(t)$ and

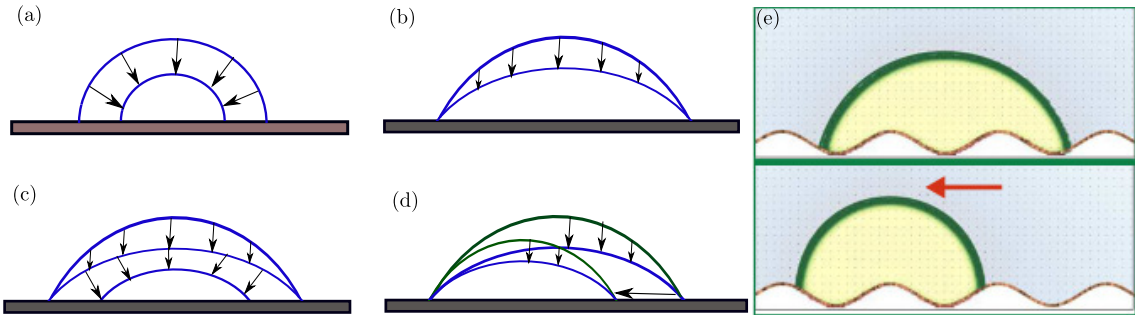

Fig. 1.9 Droplet evaporation modes. (a) Constant angle mode on a smooth surface where the contact line gradually retracts. (b) Constant radius mode on a rough surface where the contact line is pinned. (c) Stick-slip mode of evaporation where the droplet contact line is pinned until the contact angle reaches a value where it depins and the droplet evaporates with constant contact angle. (d) Stick-jump mode of evaporation where the contact line of a droplet pins and return to its initial shape when it depins. (e) Snap evaporation on smooth surface with well defined topography [34]. There is an abrupt change in the droplet location and radius at some point as the droplet evaporates.

$A(t)$ decrease until the droplet vanishes, (see Fig. 1.9(c)), or could be followed by one or more subsequent stick-slip cycles .

Another mode of evaporation observed on solid substrates that involves a combination of pinning and depinning of the contact line, is the stick-jump mode [28] where a droplet with contact angle θ_0 initially evaporates with constant radius due to contact line pinning and the contact angle decreases until the angle θ^* is reached. After this stage, unlike the stick-slip mode where the contact line smoothly retracts with θ^*, the droplet 'jumps' to (or assume) a new geometry where the contact angle returns to its initial value θ_0. This cycle continues until the droplet disappears, (see Fig. 1.9(d)).

Li et al. [36] numerically investigated the contact line pinning and depinning process during droplet evaporation on chemically patterned surfaces with hydrophilic and hydrophobic patches using a thermal multiphase lattice Boltzmann model with liquid-vapour phase transition. At the hydrophilic-hydrophobic boundary where the contact angle on the surface sharply changes from hydrophilic to hydrophobic, the contact line is pinned until the droplet's contact angle adjusts to the hydrophobic patch. As a result, evaporating droplets on such chemically patterned surfaces exhibit a stick-slip-jump behaviour in which the droplet contact line is initially pinned (stick) and then evaporates in the CR mode. This is followed by a slow inward motion (slip) when the contact line depins, where the droplet evaporates with constant angle, after which it jumps to a new configuration (jump). This cycle is repeated until the droplet disappears and the number of cycles observed is determined by the number of the stripes covered by the droplet.

An important question relevant for industrial application is how long it takes a droplet to evaporate. The lifetime of an evaporating droplet is the time it takes for its size A to reach zero and it depends on the manner in which it evaporates. A two-dimensional droplet with small contact angles $\theta \ll 1$ evaporating in the CR mode always has a larger surface area and hence a larger total flux and thus a shorter lifetime, than the same droplet evaporating in the CA mode, $t_{CR} < t_{CA}$ and the lifetime of a droplet evaporating in the SS mode, t_{SS} lies between the life time of the CR and CA modes, $t_{CR} \leq t_{SS} \leq t_{CA}$ [37]. For a three-dimensional droplet, the relationships between the evaporation lifetimes for different contact angles is summarised in the work of Stauber et al. [27].

The pinning effect of the contact line limits droplet mobility on solid surfaces and hence makes it difficult to control droplet evaporation. However, recently, ultra-smooth pinning-free surfaces which allow large-scale wettability patterns (comparable to the droplet size) have been developed. Such surfaces can be achieved by introducing an intermediary smooth layer that shields the droplet from the underlying solid surface,

and include Slippery Liquid Infused Porous Surfaces (SLIPS) [20–22] and Slippery Covalently Attached Liquid Surfaces (SOCALS) [38]. On flat SLIPS and SOCALS, a constant-contact-angle mode of evaporation has been reported, supporting the absence of contact-line pinning on these surfaces [39, 40].

The top panel of Fig. 1.9(e) shows a droplet on a smooth well defined topography. The location of the mid-point of the droplet is initially aligned with the minimum of the topographic pattern. As the droplet evaporates quasi-statically, its location remain the same but its base radius reduces gradually until it reaches a point where it changes abruptly while the droplet moves to a new location, (see the bottom panel of Fig. 1.9(e)). This sudden change in the droplet radius and location during evaporation is termed "snap" evaporation [34], and is attributed to the introduction of the large-scale topographical patterning. This phenomenon can be described mathematically using bifurcation theory which is based on studying the equilibrium properties of the droplet as it size varies. In particular, a droplet with fixed size A on a smooth well defined topography has multiple equilibrium solutions and as the droplet size is varied quasi-statically via evaporation, the equilibrium solutions for different droplet sizes yields different branches of solutions. This means that changing the droplet size A, can lead to a change in the droplet behaviour. This has opened up the possibility to use solid surfaces with smooth wettability variations to control both the evaporation process and the motion of the droplet, which is indeed one of the key goals of this thesis.

1.4 Thesis aim and structure

The aim of this thesis is to study evaporating droplets theoretically and computationally and to quantify how droplet evaporates on smooth patterns. Understanding the different factors that affect the motion of a droplet during evaporation will allow for efficient and accurate control of droplet evaporation. For example, the direction of motion of a droplet as it evaporates, and the speed of a droplet as its location changes suddenly in a snap event. To this end, we will initially consider a flat (or planar) surface that has a smoothly-varying wetting pattern described in the terms of the local equilibrium contact angle, which controls the angle of the droplet interface at the solid contact point. We will also examine smooth non-planar surfaces in order to study how imposing a wetting pattern on a topography can influence the snap events.

To investigate this problem, we consider two-dimensional droplets and assume quasi-static evaporation so that we can mathematically study the equilibrium properties of a droplet as it evaporates using the Young-Laplace equation and bifurcation analysis. To

confirm our theoretical results, we will perform dynamic simulations of the Cahn-Hilliard and Navier-Stokes equations under isothermal conditions so that temperature difference is negligible. We will first consider the regime where the droplet size is smaller than the capillary length scale so that gravity is negligible. Later on, gravity will be introduced to study the effect it has on droplet shape and the evaporation process.

The structure of this thesis is as follows. The next chapter discusses the Cahn-Hilliard and Navier-Stokes equations which is used to simulate droplets on smooth surfaces through out this thesis. The validity of the model is tested by simulating droplet spreading on smooth surfaces as well as droplet evaporation. In Chapter 3, we present analytical and computational results on quasi-static evaporation of a 2D droplet on a flat, chemically patterned surface where we consider patterns that are pinning free but have a smooth and periodic variation of the local equilibrium contact angle. Different bifurcations that arises on such surfaces will be quantified and a way to effectively control the direction of motion of evaporating droplets will be examined by exploring asymmetric wetting patterns.

Chapter 4 studies the snap dynamics of evaporating droplets on a smooth pattern. This will be done by performing a series of simulations with different wetting strengths, which gives possibility of controlling the critical droplet size by tuning the wetting strength. The droplet speed during the snap event will also be shown to be related to the wetting strength, droplet size and droplet properties such as viscosity and surface tension. Chapter 5 investigates the interplay between chemical and topographical patterns where it is observed that the combination of periodic chemical and topographical patterns can either amplify or annihilate snap effects. Also the direction of evaporating droplets can be controlled on a non-planar surface by imposing a well defined wetting pattern.

In Chapter 6, we will consider droplets evaporating under the influence of gravity on a flat surface with periodic wetting patterns. On an inclined plane with a symmetric chemical pattern, a droplet will prefer to move in the direction of gravity as it evaporates. However we will see that on an asymmetric pattern with amplitude gradient a droplet can be made to move in the opposite direction dictated by gravity when the effect of gravity is weaker that the strength of the wetting pattern. Chapter 7 compares the theoretical results derived in Chapter 6 with simulations of the Cahn-Hilliard and Navier-Stokes system of equations that models droplets under the influence of gravity. It will be observed that on a surface with asymmetric pattern, the direction of motion of an evaporating droplet can be effectively controlled. In the scenario where gravity is weak the asymmetric pattern can move an evaporating droplet against gravity.

The conclusion of the thesis is given in Chapter 8 where summary of main results are highlighted along side future research directions of droplet evaporation.

Chapter 2

Diffuse interface model

In this chapter, we introduce the Cahn-Hilliard and Navier-Stokes (CH-NS) system of equations. The finite element method (FEM) used in solving this system of equations is also discussed. To test the validity of our model, we consider the case where the length scale of the system is less than the capillary length scale so that gravity is negligible. In this regime, droplet spreading on smooth surfaces is simulated as well as droplet evaporation.

When liquid droplets make contact with a solid substrate, they begin to spread; the dynamics of this spreading are governed by viscous effects near the contact line and are defined by an apparent contact angle. Traditionally problems involving moving contact lines are usually accompanied by the implementation of the no-slip boundary condition where the velocity at the solid is set to zero. This however leads to a singularity as discussed in Chapter 1 which implies that moving a contact line would require an infinite force [11].

Several methods have been proposed to overcome this difficulty. These include the introduction of a slip length λ_s which relaxes the no-slip condition on the surface [41, 12]. The precursor film method can also be used to regularize the contact line singularity. In this case a thin film of thickness λ_t made by one of the phases shields the surface so that the interface is not directly in contact with the surface [13]. The apparent contact line can then be studied using classical continuum mechanics.

Alternatively, a transition area of limited but finite width may be used to replace the conventional infinitely thin boundary of separation between two immiscible fluids, across which the fluid composition varies continuously. Diffuse-interface models are those that implement this. The interface is modelled as a diffuse layer in which fluid properties differ steeply but continuously, causing the contact line to move naturally as diffusion through the interface, guided by gradients in the chemical potential, which is the rate of

change of the system's free energy. It is this diffusion that regularizes the singularity at the contact line [42, 43, 14]. A common diffuse interface model is the Cahn-Hilliard equation.

Regardless of the model adopted, the physics of the phenomenon being modelled will be the same. Sibley et al. [44] compared different models including slip and diffuse interface models for the quasi-static spreading of a thin two-dimensional droplet. In certain parameter regimes it is shown that all of the models predict the same quasi-static droplet spreading behaviour.

Real-world interfaces with thickness on the order of nanometres are computationally costly and well beyond the capabilities of current computers and algorithms. However, when the interfacial thickness is reduced below a threshold while the other parameters remain constant, the Cahn–Hilliard model approaches a sharp-interface limit. In sharp-interface models, the diffusion length of the contact line is related to the slip length [45, 14, 46, 47]. In this thesis, the Cahn-Hilliard equation is implemented to model droplets on solid surfaces.

2.1 Diffuse interface formulation

The basic idea is to introduce a conserved order parameter ϕ, that varies continuously over thin interfacial layers and constant in the liquid and gaseous phases. In the phase-field model, sharp fluid interfaces are replaced by thin but non-zero thickness χ, transition regions where the interfacial forces are smoothly distributed. The conserved field ϕ takes two equilibrium limiting values, $\phi = +\phi_e$ and $\phi = -\phi_e$, which represent the liquid and gaseous phases, respectively, so that the interface is located where $\phi = 0$, (see Fig. 2.1(a)).

The equilibrium property of the system is given through the free energy of the system,

$$\mathcal{F}[\phi] = \int_\Omega \frac{\sigma}{\chi}\left[F_m(\phi) + \frac{\chi^2}{2}|\boldsymbol{\nabla}\phi|^2\right] d\Omega + \int_{\Gamma_B} F_w(\phi)\, ds, \tag{2.1}$$

where Ω is the domain of integration, $F_m(\phi) = \frac{1}{4}(\phi_e - \phi^2)^2$ is a double-well potential that ensures the existence of both liquid and gaseous phases. This is because its minima corresponds to the values of the phase field ϕ in the liquid and gaseous phase respectively, (see Fig. 2.1(b)). The gradient term in the free energy ensures the existence of a well defined interface of width χ, σ is related to the surface tension of the droplet as we will see later and $F_w(\phi)$ is the wall component of the free energy that models fluid/solid (wetting) interactions on the solid boundary Γ_B. The chemical potential η which is the

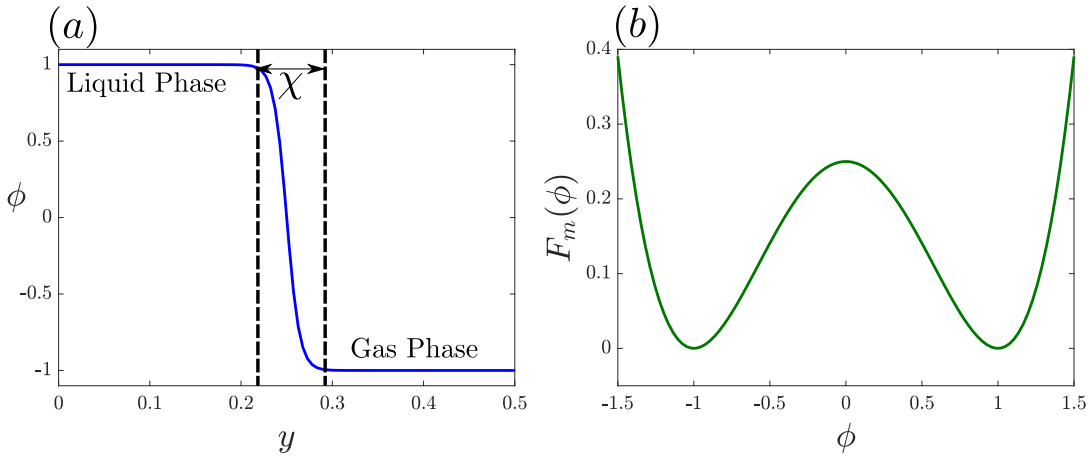

Fig. 2.1 (a) Phase-field profile, $\phi(y)$, in one dimension. The two limiting values ± 1 represent the liquid and gas phases respectively, the width of the interface is denoted by χ. (b) Double well potential that ensures the existence of the liquid and gaseous phases.

rate of change of the free energy (2.1), is defined as $\eta = \delta\mathcal{F}[\phi]/\delta\phi$:

$$\frac{\chi}{\sigma}\eta = F'_m(\phi) - \chi^2\nabla^2\phi. \tag{2.2}$$

Minimizing the free energy also leads to the natural boundary condition [50]:

$$\sigma\chi\,\mathbf{n}\cdot\boldsymbol{\nabla}\,\phi = -F'_w, \tag{2.3}$$

which is applied on the bottom boundary Γ_B. By considering a flat interface located at $y = y_0$ in a one-dimensional system where the solid is located at $y = 0$, we obtain the exact solution for the phase-field ϕ from Eq. (2.2) by noting that the chemical potential vanishes at equilibrium

$$\phi = \phi_e \tanh\left(\frac{y - y_0}{\sqrt{2}\chi}\right). \tag{2.4}$$

We have discussed the equilibrium properties of the system, next we consider the dynamics of the system by coupling the Cahn-Hilliard equation with the Navier-Stokes equation.

2.2 Cahn-Hilliard and Navier-Stokes equations

The Cahn-Hilliard equation that describe the evolution of the order parameter is coupled with the Navier-Stokes equation which models the hydrodynamic flow of two immiscible

and incompressible fluids with comparable densities and viscosities as follows [48]:

$$\frac{\partial \phi}{\partial t} + \mathbf{u} \cdot \boldsymbol{\nabla} \phi = M \nabla^2 \eta(\phi), \tag{2.5a}$$

$$\boldsymbol{\nabla} \cdot \mathbf{u} = 0, \tag{2.5b}$$

$$\rho \left(\frac{\partial \mathbf{u}}{\partial t} + (\mathbf{u} \cdot \boldsymbol{\nabla}) \mathbf{u} \right) = - \boldsymbol{\nabla} p + \mu \nabla^2 \mathbf{u} - \phi \boldsymbol{\nabla} \eta, \tag{2.5c}$$

where $\mathbf{u}$ is the velocity field, p the pressure, ρ the density, μ the dynamic viscosity, and M a mobility parameter.

Although the system (2.5) models two fluids with identical densities and viscosities, it can still be used to understand the quasi-static (or slow) dynamics of fluids with different densities and viscosities. This is because the equilibrium properties, which is comparable to quasi-static dynamics, of a droplet is insensitive to the effects of density and viscosity difference between the fluids when the influence of gravity is not important. As a result, we refer to the phase where the phase-field $\phi = -1$ as the gas phase and where $\phi = 1$ as the liquid phase.

The Cahn-Hilliard equation (2.5a) is coupled with the velocity field via the convection term $\mathbf{u} \cdot \boldsymbol{\nabla} \phi$ and the Navier-Stokes equation (2.5c) is coupled with the phase-field through the surface tension term $-\phi \boldsymbol{\nabla} \eta$. The surface tension term can take several forms, for example it can be given by the stress term $-\sigma\chi \boldsymbol{\nabla} \cdot (\boldsymbol{\nabla} \phi \otimes \boldsymbol{\nabla} \phi)$ known as Korteweg force [49] which is balanced by a pressure gradient $- \boldsymbol{\nabla} \bar{p}$ at equilibrium in the Navier-Stokes equation. This surface tension term is equivalent to different terms including $-\phi \boldsymbol{\nabla} \eta$. This is shown as follows, using the differential identity:

$$\boldsymbol{\nabla} \cdot (\boldsymbol{\nabla} \phi \otimes \boldsymbol{\nabla} \phi) = \boldsymbol{\nabla} \phi \nabla^2 \phi + \frac{1}{2} \boldsymbol{\nabla} |\boldsymbol{\nabla} \phi|^2,$$

the surface tension term $-\sigma\chi \boldsymbol{\nabla} \cdot (\boldsymbol{\nabla} \phi \otimes \boldsymbol{\nabla} \phi)$ is then equivalent to $-\sigma\chi \boldsymbol{\nabla} \phi \nabla^2 \phi$ with a modified pressure: $\hat{p} = \bar{p} + \sigma\chi \frac{1}{2} \boldsymbol{\nabla} |\boldsymbol{\nabla} \phi|^2$. By making use of the definition of the chemical potential in Eq. (2.2), this term can be simplified further to $\eta \boldsymbol{\nabla} \phi$ with a modified pressure: $\tilde{p} = \hat{p} + \frac{\sigma}{\chi} F_m(\phi)$. Using the differential identity $\boldsymbol{\nabla}(\eta\phi) = \eta \boldsymbol{\nabla} \phi + \phi \boldsymbol{\nabla} \eta$, the surface tension term can also be written as $-\phi \boldsymbol{\nabla} \eta$ with a modified pressure: $p = \tilde{p} - \eta\phi$. Hence we see that the surface tension term can take difference forms, however we have chosen $-\phi \boldsymbol{\nabla} \eta$ for computational ease.

It is convenient to non-dimensionalise Eqs. (2.5a), (2.5b), (2.5c), and (2.2) by choosing the following dimensionless variables:

$$\mathbf{r}^* = \frac{\mathbf{r}}{L}, \quad \mathbf{u}^* = \frac{\mathbf{u}}{U}, \quad t^* = \frac{Ut}{L}, \quad p^* = \frac{p}{\rho U^2}, \quad \eta^* = \frac{\eta}{\eta_0}, \quad \phi^* = \frac{\phi}{\phi_\mathrm{e}}, \tag{2.6}$$

where L and U are the characteristic length and velocity scales of the system respectively and $\eta_0 = \sigma/L$. With these new variables the system of governing equations become:

$$\frac{\partial \phi}{\partial t} + \mathbf{u} \cdot \boldsymbol{\nabla} \phi = \frac{1}{Pe} \nabla^2 \eta, \tag{2.7a}$$

$$\eta = \frac{1}{Cn} \left(-\phi + \phi^3 - Cn^2 \nabla^2 \phi \right), \tag{2.7b}$$

$$\boldsymbol{\nabla} \cdot \mathbf{u} = 0, \tag{2.7c}$$

$$\frac{\partial \mathbf{u}}{\partial t} + (\mathbf{u} \cdot \boldsymbol{\nabla}) \mathbf{u} = -\boldsymbol{\nabla} p + \frac{1}{Re} \nabla^2 \mathbf{u} - \frac{1}{We} \phi \boldsymbol{\nabla} \eta, \tag{2.7d}$$

where we have defined the dimensionless parameters:

$$Re = \frac{\rho U L}{\mu}, \qquad Pe = \frac{UL^2}{\sigma M}, \qquad We = \frac{\rho L U^2}{\sigma}, \qquad Cn = \frac{\chi}{L},$$

corresponding to the Reynolds, Peclet, Weber, and Cahn numbers respectively. The Reynolds, Peclet, Weber, and Cahn numbers define the ratios between inertia and viscous forces, advective and diffusive transport, inertia and surface tension, and diffuse interface width and the characteristic length scale respectively.

The values of the dimensionless parameters used are as follows. Yue et al. [46] showed that the Cahn–Hilliard model reaches a sharp-interface limit when the Cahn number approaches zero while the other parameters remain constant, using scaling arguments and numerical computations. This limit can be achieved for $Cn = \mathcal{O}(10^{-2})$. Following this, the Cahn number in this thesis is taken to be $Cn = 0.01$. Magaletti et al. [48] showed from asymptotic expansion and numerical simulation of the CH-NS equations that the mobility is an effective parameter to be chosen proportional to the square of the interface thickness in order to ensure that the diffuse interface model approaches the sharp-interface limit. This implies that the Peclet number must be inversely proportional to the square of the Cahn number. Hence, throughout this study the Peclet number is set to $Pe = 1/(3Cn^2)$. The values of the Reynolds and Weber numbers used in this thesis ranges from 0.1 to 1.

2.2.1 Initial and boundary conditions

To solve the CH-NS system of equations completely in a rectangular domain, initial conditions are required for the phase-field ϕ, chemical potential η, velocity $\mathbf{u}$ and pressure p. Also boundary conditions for the variables ϕ, η, $\mathbf{u}$ and p are needed on the four walls of the domain. Initially, the droplet shape is defined as a circular arc S. Mathematically, this is given as:

$$S = \{(x, y) \quad | \quad \sqrt{(x - x_0)^2 + (y + y_0)^2} \leq R_0\}, \tag{2.8}$$

where x_0 is the location of the droplet mid-point and $R_0 = R/\sin\theta$, $y_0 = R/\tan\theta$, here R and θ are the droplet contact radius and angle respectively. The profile of the phase-field, $\phi(x, y, t)$ at time $t = 0$ is then chosen such that liquid is enclosed in the arc S:

$$\phi(x, y, 0) = \begin{cases} +1 & (x, y) \in S, \\ -1 & \text{otherwise.} \end{cases} \tag{2.9}$$

The chemical potential, pressure and velocity are set to zero at time $t = 0$. For the boundary conditions, on the bottom boundary, the wetting property of the solid wall is imposed using the natural boundary condition given by Eq. (2.3) obtained by minimizing the free energy of the system [50]:

$$\sigma\chi\, \mathbf{n} \cdot \boldsymbol{\nabla}\, \phi = -F_w', \tag{2.10}$$

where F_w is a wetting function that enables us to introduce wetting effects into the model. The wetting function can be cubic in ϕ, $F_{w3} = a(\phi^3/3 - \phi)$ [51, 43] or a linear function of ϕ, $F_w = a\phi$ [52, 53], where a describe the preference of the surface for either the liquid phase ($a > 0$, hydrophilic conditions) or the gas phase ($a < 0$, hydrophobic conditions). When a cubic function F_{w3} is used $F_{w3}'(\pm 1) = 0$. This confines the wetting condition to the contact line since the phase-field is $+1$ and -1 in the liquid and gaseous phase respectively so that Eq. 2.10 becomes $\mathbf{n} \cdot \boldsymbol{\nabla}\, \phi = 0$. As a result the cubic function is suitable for superhydrophilic droplets where the contact angle is close to zero and superhydrophobic droplets with contact angles close to 180° where it remove the emergence of interfacial fluxes close to the solid fluid interface which occur when a linear function is used where $F_w'(\pm 1) = a$. However, in the case of partial wetting, $30° < \theta_e < 150°$, both formulations are equivalent. In this thesis, for simplicity, we consider the linear function

$$F_w = -a\phi_s. \tag{2.11}$$

Here ϕ_s represents the value of the phase field at the wall. For a constant value of a, the corresponding static equilibrium contact angle θ_e, can be obtained via the Young-Dupre relation discussed in Chapter 1. This is the horizontal force balance on a droplet on a smooth plane surface [54, 55]:

$$\cos\theta_e = \frac{\gamma_{sg} - \gamma_{sl}}{\gamma}. \tag{2.12}$$

By computing all different surface tensions, it is possible to obtain the following relation between the parameter a and the equilibrium contact angle θ_e:

$$\cos\theta_e = \frac{1}{2}\left[(1+\omega)^{3/2} - (1-\omega)^{3/2}\right], \tag{2.13}$$

where the wetting potential is $\omega = \frac{\sqrt{2}}{\sigma}a$, see Appendix A on the derivation of the above equation. Equation (2.13) can be inverted to obtain the wetting potential as:

$$\omega = 2sgn(\pi/2 - \theta_e)\sqrt{\beta(1-\beta)}, \tag{2.14}$$

where $\beta(\theta_e) = \cos[\arccos(\sin^2\theta_e)/3]$. In the limit of small values of ω, that is $\omega \ll 1$, an excellent approximation for ω from Eq. (2.13) is [55]:

$$\omega \approx \omega' = \frac{2}{3}\cos\theta_e, \tag{2.15}$$

Equation (2.10) in dimensionless form then becomes:

$$\sigma\frac{\chi}{L}\,\mathbf{n}\cdot\boldsymbol{\nabla}^*\,\phi^* = \omega\frac{\sigma}{\sqrt{2}}.$$

Non dimensionalizing gives:

$$\mathbf{n}\cdot\boldsymbol{\nabla}\,\phi = \frac{\omega}{\sqrt{2}Cn}, \tag{2.16}$$

which on substituting Eq. (2.15) becomes:

$$\mathbf{n}\cdot\boldsymbol{\nabla}\,\phi \approx \frac{\sqrt{2}}{3Cn}\cos\theta_e. \tag{2.17}$$

Equation (2.17) only caters for the boundary condition imposed on the bottom wall for the phase-field, on the top boundary, a no flux condition is applied. For the chemical potential and pressure, a no flux condition is also applied on the top and bottom boundaries, while a no slip boundary condition is applied for the velocity field at the top and bottom boundaries. For the left and right boundaries, a periodic condition is

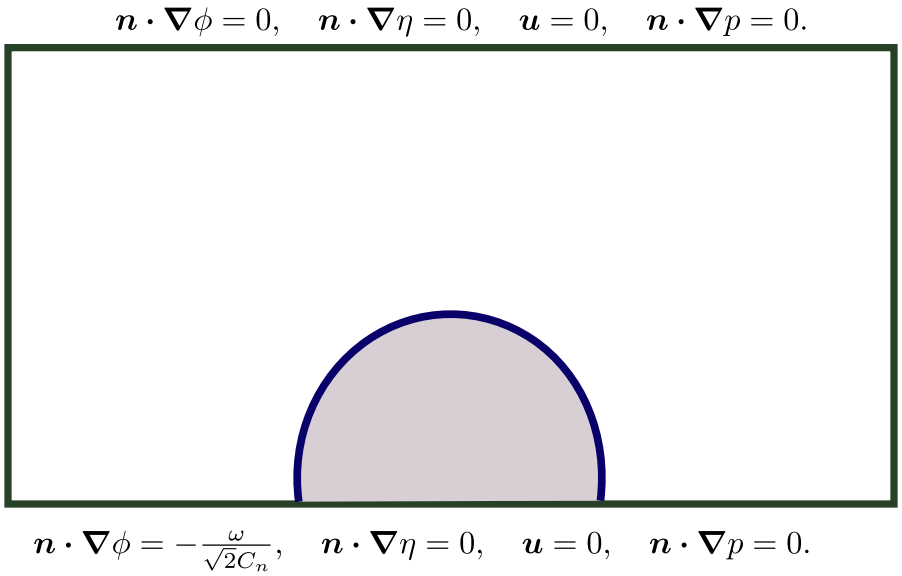

Fig. 2.2 Boundary conditions imposed on the domain. No flux is imposed for the chemical potential and pressure on the top and bottom boundaries. A no-slip boundary condition is imposed for the velocity on the top and bottom boundaries. The wetting function is imposed on the bottom boundary for the phase-field while no flux is imposed on the top boundary. A periodic boundary is imposed on the left and right walls.

applied for the phase-field, chemical potential, pressure and velocity. A summary of all boundary conditions is shown in Fig. 2.2.

With these boundary conditions, the CH-NS system of equation conserves mass. To see this, we integrate the Cahn-Hilliard equation (2.5a) over the domain Ω and make use of the continuity equation (2.5b) together with divergence theorem to obtain:

$$\frac{d}{dt}\int_\Omega \phi(x,t)\, d\Omega = -\int_{\partial\Omega} \phi\, \mathbf{u}\cdot\mathbf{n}\; ds - M\int_{\partial\Omega} \boldsymbol{\nabla}\,\eta\cdot\mathbf{n}\; ds. \tag{2.18}$$

By using the no-slip $\mathbf{u} = 0$ and no flux $\boldsymbol{\nabla}\,\eta\cdot\mathbf{n}$ conditions on the boundary $\partial\Omega$, we obtain the mass conserving property of the CH-NS system of equations:

$$\frac{d}{dt}\int_\Omega \phi(x,t)\, d\Omega = 0 \tag{2.19}$$

Also, the CH-NS system of equations (2.5) satisfy the following dissipation law:

$$\frac{dE_T}{dt} + \frac{\mu}{2}\int_\Omega (\boldsymbol{\nabla}\,\mathbf{u}){:}(\boldsymbol{\nabla}\,\mathbf{u})\, d\Omega + \int_\Omega M\,|\boldsymbol{\nabla}\,\eta|^2\; d\Omega = 0, \tag{2.20}$$

where

$$E_T = \int_\Omega \frac{\rho \left|\mathbf{u}\right|^2}{2} d\Omega + \mathcal{F}[\phi], \tag{2.21}$$

here $\mathcal{F}[\phi]$ is the system free energy (2.1). This law is obtained by multiplying the chemical potential (2.2), Cahn-Hilliard equation (2.5a), continuity equation (2.5b), and the Navier-Stokes equation (2.5c) by $-\partial\phi/\partial t$, η, $\mathbf{u}$, and p respectively, integrating over the domain Ω, and adding the resulting equations while applying the no-slip and no-flux boundary conditions. This dissipation law will prove useful in Chapter 4 when we examine the energy balance of an evaporating droplet.

2.3 Numerical scheme

We now proceed to develop a scheme for solving our model of droplet on a solid surface. We consider the system (2.7a) - (2.7d) along side its boundary conditions, for clarity we write here again the full system of equations and boundary conditions as follows. Our aim is to solve for the phase-field ϕ, chemical potential η, pressure p and velocity u, hence we find $\phi(x,y,t), \eta(x,y,t), p(x,y,t), u(x,y,t)$ such that:

$$\frac{\partial \phi}{\partial t} + \mathbf{u}\cdot\boldsymbol{\nabla}\,\phi = \frac{1}{Pe}\nabla^2\eta, \qquad \text{in } \Omega_T := \Omega \times (0,T), \tag{2.22a}$$

$$\eta = \frac{1}{Cn}\left(-\phi + \phi^3 - Cn^2\nabla^2\phi\right), \qquad \text{in } \Omega_T, \tag{2.22b}$$

$$\boldsymbol{\nabla}\cdot\mathbf{u} = 0, \qquad \text{in } \Omega_T, \tag{2.22c}$$

$$\frac{\partial\,\mathbf{u}}{\partial t} + (\mathbf{u}\cdot\boldsymbol{\nabla})\,\mathbf{u} = -\boldsymbol{\nabla}\,p + \frac{1}{Re}\nabla^2\,\mathbf{u} - \frac{1}{We}\phi\,\boldsymbol{\nabla}\,\eta, \qquad \text{in } \Omega_T, \tag{2.22d}$$

$$\phi(x,0) = \phi_0(x), \quad \mathbf{u}(x,0) = \mathbf{u}_0(x), \qquad \forall \quad x \in \Omega, \tag{2.22e}$$

$$\mathbf{n}\cdot\boldsymbol{\nabla}\,\eta = \mathbf{n}\cdot\boldsymbol{\nabla}\,p = 0, \qquad \text{on } \Gamma_{T,B}, \tag{2.22f}$$

$$\mathbf{n}\cdot\boldsymbol{\nabla}\,\phi = 0, \qquad \text{on } \Gamma_T, \tag{2.22g}$$

$$\mathbf{n}\cdot\boldsymbol{\nabla}\,\phi = w, \qquad \text{on } \Gamma_B, \tag{2.22h}$$

$$\mathbf{u} = 0, \qquad \text{on } \Gamma_{T,B}, \tag{2.22i}$$

$$\Gamma_L = \Gamma_R, \qquad \forall \quad \phi, \eta, p, \text{and } \mathbf{u}\,. \tag{2.22j}$$

The domain of integration is Ω and the T is the total time. The left right, top and bottom boundaries are denoted by Γ_L, Γ_R, Γ_T and Γ_B respectively and w is the wetting term given by Eq. (2.17). The functions ϕ_0 and $\mathbf{u}_0$ are the initial phase-field and velocity respectively. A periodic condition is imposed so that the values of all variables are the same on the left and right boundaries. We will refer to Eqs. (2.22) as the strong form

which will be discretized to obtain a weak form. To solve the CH-NS system of equations (2.22a) - (2.22j), the equations needs to be discritized in time and in space. For the temporal discretization, finite difference method is used. To discretize in space there are several options available in literature including the spectral element [56], Lattice Boltzmann [57], finite difference [48], and finite volume [58]. Here the finite element method (FEM) [49] is used for the spatial discretization.

We first consider the Cahn-Hilliard equation (2.22a) and discritize it in time using the Crank Nicolson scheme. The Navier-Stokes equations, (2.22d), is then discretized using the implicit Euler scheme:

$$\frac{\phi^n - \phi^{n-1}}{\Delta t} + \mathbf{u}^{n-1} \cdot \boldsymbol{\nabla}\, \phi^m = \frac{1}{Pe} \nabla^2 \eta^m, \tag{2.23a}$$

$$\eta^n = \frac{1}{Cn} \left(-\phi^n + (\phi^n)^3 - Cn^2 \nabla^2 \phi^n \right), \tag{2.23b}$$

$$\boldsymbol{\nabla} \cdot \mathbf{u}^n = 0, \tag{2.23c}$$

$$\frac{\mathbf{u}^n - \mathbf{u}^{n-1}}{\Delta t} + (\mathbf{u}^{n-1} \cdot \boldsymbol{\nabla})\, \mathbf{u}^{n-1} = -\boldsymbol{\nabla}\, p^n + \frac{1}{Re} \nabla^2\, \mathbf{u}^n - \frac{1}{We} \phi^n\, \boldsymbol{\nabla}\, \eta^n, \tag{2.23d}$$

where Δt is the time step and ϕ^n, ϕ^{n-1} are the values of ϕ at time $t = t^n$ and $t = t^{n-1}$ respectively. The value of ϕ at the mid-point of t^n and t^{n-1} is defined as $\phi^m = (\phi^n + \phi^{n-1})/2$.

2.3.1 Finite element methods

For the spatial discretization, we make use of the FEM which is a numerical method for solving partial differential equations (PDE). The fundamental idea behind FEM is to divide the computational domain into small segments, typically triangles, known as sub-domains or components, and find polynomial approximations to the unknown function on each element. A global solution can be obtained by combining these piecewise approximations on these sub-domains [59].

Let the unknown function in an element, called a trial function, be $f(x)$. An approximation $f'(x)$ of $f(x)$ can be obtained by a sum as:

$$f'(x) = \sum_{i=0}^{N} c_i \psi_i(x), \tag{2.24}$$

where N is the number of the prescribed finite element basis functions $\psi_i(x)$ called test functions. The unknown coefficients to be determined are $c_0, c_1, ...c_N$. The test functions can either be linear, quadratic, cubic or a higher order polynomial. Alternative names,

frequently used are $\mathcal{P}_1$ elements for linear elements, $\mathcal{P}_2$ for quadratic elements, and so forth: $\mathcal{P}_d$ signifies degree d of the polynomial basis functions. To determine the best approximation, the distance between f and f' is minimized resulting in a linear system of equations of the form;

$$\sum_{j=0}^{N} A_{i,j} c_j = b_j \tag{2.25}$$

where

$$A_{i,j} = \langle \psi_i, \psi_j \rangle, \tag{2.26}$$

$$b_j = \langle f, \psi_j \rangle, \tag{2.27}$$

here the L^2 inner product is denoted by $\langle ., . \rangle$. This linear system can then be solved using a Newton method.

To discretize the Cahn-Hilliard and Navier-Stokes equations, we begin by introducing a triangulation τ of Ω into cells τ_i, such that $\tau = \cup_{i=1}^{N} \tau_i$. On τ, we then introduce finite element spaces:

$$Q_h := \{v \in H^1(\Omega) | \quad v|_{\tau_i} \in \mathcal{P}_1\}, \tag{2.28a}$$

$$P_h := \{v \in L^2(\Omega) | \quad v|_{\tau_i} \in \mathcal{P}_1\}, \tag{2.28b}$$

$$V_h := \{v \in H^1(\Omega) \times H^1(\Omega) | \quad v|_{\tau_i} \in (\mathcal{P}_2)^2, \quad v = 0 \quad \text{on} \quad \Gamma\}, \tag{2.28c}$$

where $H^1(\Omega)$, $L^2(\Omega)$ are the Sobolev and L^2 spaces respectively. The linear and quadratic elements are denoted by $\mathcal{P}_1$ and $\mathcal{P}_2$ respectively. We use Q_h to define discrete approximations ϕ_h, and η_h, of the corresponding continuous variables, ϕ and η respectively. The discrete approximations p_h and $\mathbf{u}_h$ of p and $\mathbf{u}$ are defined using P_h and V_h respectively so that the standard Taylor-Hood elements is used for the Navier-Stokes equation which satisfies the inf-sup condition [49].

A fully implicit scheme to solve Eqs.(2.22a)- (2.22j) is given as follows. Given $\phi^{n-1} \in Q_h$, $\eta^{n-1} \in Q_h$, and $\mathbf{u}^{n-1} \in V_h$, find $\phi_h^n \in Q_h$, $\eta_h^n \in Q_h$, $p_h^n \in P_h$ and $\mathbf{u}_h^n \in V_h$,

such that for all $\Phi \in Q_h$, $\Psi \in Q_h$, $\Pi \in P_h$, and $\Xi \in V_h$, the following equations hold:

$$\langle \frac{\phi^n - \phi^{n-1}}{\Delta t}, \Phi \rangle + \left\langle \mathbf{u}^{n-1} \cdot \boldsymbol{\nabla} \phi^m, \Phi \right\rangle + \frac{1}{Pe} \langle \boldsymbol{\nabla} \eta^m, \boldsymbol{\nabla} \Phi \rangle = 0, \tag{2.29a}$$

$$\langle \eta^n, \Psi \rangle + \left\langle \left(\frac{\phi^n - (\phi^n)^3}{Cn} \right), \Psi \right\rangle - Cn \langle \boldsymbol{\nabla} \phi^n, \boldsymbol{\nabla} \Psi \rangle + Cn \langle \mathbf{n} \cdot \boldsymbol{\nabla} \phi^n, \Psi \rangle_{\Gamma_B} = 0, \tag{2.29b}$$

$$\langle \frac{\mathbf{u}^n - \mathbf{u}^{n-1}}{\Delta t}, \Xi \rangle + \langle \mathbf{u}^{n-1} \cdot \boldsymbol{\nabla} \mathbf{u}^{n-1}, \Xi \rangle + \frac{1}{Re} \langle \boldsymbol{\nabla} \mathbf{u}^{n-1}, \boldsymbol{\nabla} \Xi \rangle + \langle \boldsymbol{\nabla} p^n, \Xi \rangle + \frac{1}{We} \langle \phi^n \boldsymbol{\nabla} \eta^n, \Xi \rangle = 0, \tag{2.29c}$$

$$\langle \boldsymbol{\nabla} \cdot \mathbf{u}, \Pi \rangle = 0. \tag{2.29d}$$

Here the unknown functions (Φ, Ψ, Ξ, Π) to be approximated are the test functions corresponding to the trial functions $(\phi, \eta, \mathbf{u}, p)$ respectively. The fully coupled system of equations (2.29a)- (2.29d) can be solved using a Newton method giving rise to a large system matrix which must be assembled and solved iteratively. Splitting the processes of phase-field transport and hydrodynamic flow so that the equations governing each of these processes are solved separately is a faster and simpler approach. This means that we solve Eqs. (2.29a) and (2.29b) first for the phase-field and chemical potential, then Eqs. (2.29c) and (2.29d) for the velocity and pressure. The fluid flow phase necessitates a coupled solution for velocity and pressure. This has the benefit of accurate pressure computation, but the disadvantage of being computationally difficult to solve. Alternatively, using Chorin's method, we further divide the fluid flow phase into the following sub-steps [60]. We first ignore the pressure in Eq. (2.29c) to compute the tentative velocity $\mathbf{u}_T$:

$$\langle \left(\frac{\mathbf{u}_T - \mathbf{u}^{n-1}}{\Delta t} \right), \Xi \rangle + \langle \mathbf{u}^{n-1} \cdot \boldsymbol{\nabla} \mathbf{u}^{n-1}, \Xi \rangle + \frac{1}{Re} \langle \boldsymbol{\nabla} \mathbf{u}^{n-1}, \boldsymbol{\nabla} \Xi \rangle + \frac{1}{We} \langle \phi \boldsymbol{\nabla} \eta^{n-1}, \Xi \rangle = 0. \tag{2.30}$$

The pressure is then computed as follows:

$$\langle \boldsymbol{\nabla} p^n, \boldsymbol{\nabla} \Pi \rangle = -\frac{1}{\Delta t} \langle \boldsymbol{\nabla} \cdot \mathbf{u}_T, \Pi \rangle. \tag{2.31}$$

After which the tentative velocity is corrected to obtain the final velocity $\mathbf{u}^n$ as:

$$\langle \mathbf{u}^n, \Xi \rangle = \langle \mathbf{u}_T, \Xi \rangle - \Delta t \langle \boldsymbol{\nabla} p^n, \Xi \rangle. \tag{2.32}$$

The scheme is implemented using the finite element package, called FEniCS [61], which is an open-source computing platform for solving PDEs. FEniCS enables easy translation of scientific models into efficient finite element code using the Unified Form

Language – UFL [62]. This code can be used with the C++/Python library DOLFIN, to efficiently assemble linear systems and compute solutions to PDEs, (see the Appendix B for the Python code used in this thesis).

2.4 Model validation

In this section we consider a series of simple problems that we use to validate the diffuse interface model and the numerical algorithm introduced in the previous sections.

2.4.1 Equilibrium sessile droplets

We start by studying the equilibrium states of droplets resting on homogeneous surfaces and in particular we compare the analytically imposed contact angle with the numerically obtained contact angle that arise from the diffuse interface model. Figure 2.3(a) shows the

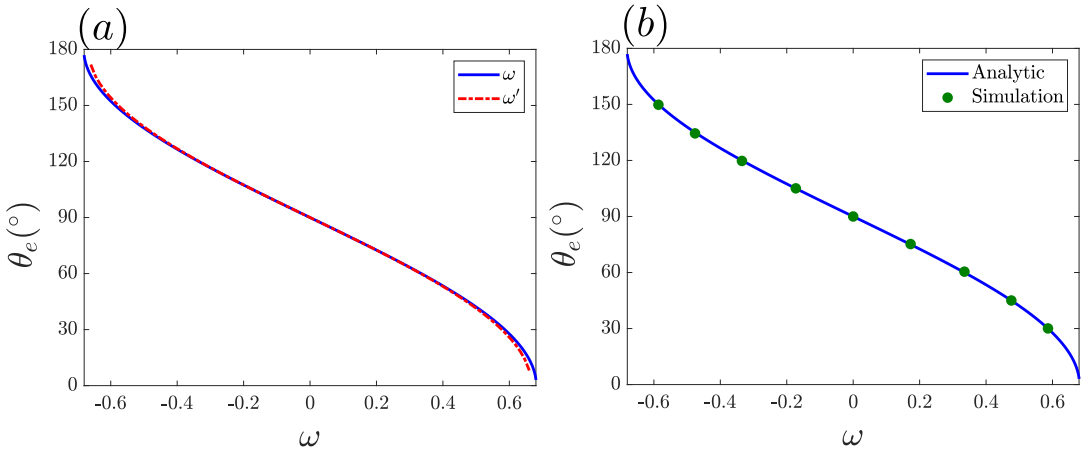

Fig. 2.3 Wetting potentials and their corresponding equilibrium contact angles (a) Exact and approximate, and (b) Analytic and simulation.

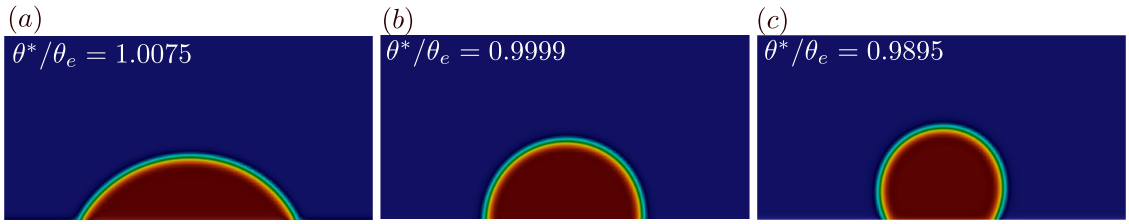

Fig. 2.4 Equilibrium droplet shapes on homogeneous substrates with different wetting properties (a) $\theta_e = 60^\circ$, (b) $\theta_e = 90^\circ$, and (c) $\theta_e = 120^\circ$. The contact angle imposed by condition (2.17) is denoted as θ_e and the angle calculated numerically as θ^*. Blue represent the gas region while red denotes the liquid region.

wetting potential ω (2.14), and its approximation ω' (2.15) along side their corresponding equilibrium contact angles. It is seen that ω' is an excellent approximation for ω, as a result it can be used in place of ω in our simulation. The advantage of using ω' instead of ω is that it easy to implement computationally. Next we ensure that imposing the appropriate wetting potentials yield desired equilibrium contact angles.

A plot of wetting potentials imposed using the condition (2.17) together with their corresponding contact angles is shown in Fig. 2.3(b). It is observed that there is an excellent agreement between the analytic and simulation wetting potentials. The equilibrium shapes of hydrophilic ($\theta_e = 60°$), neutral ($\theta_e = 90°$), and hydrophobic ($\theta_e = 120°$) droplets are also shown in Fig. 2.4. The contact angle imposed by condition (2.17) is denoted as θ_e and the angle calculated numerically as θ^*. It is seen that there is an excellent agreement between the numerically imposed and theoretical contact angles. Next, to study the dynamics of a droplet we consider droplet spreading on homogeneous surfaces.

2.4.2 Droplet spreading on homogeneous surfaces

We consider a partial wetting regime with a finite contact angle and examine how a droplet spreads on a flat homogeneous substrate to study the wettability of the solid surface by varying the equilibrium contact angle over a wide range. In this section, we

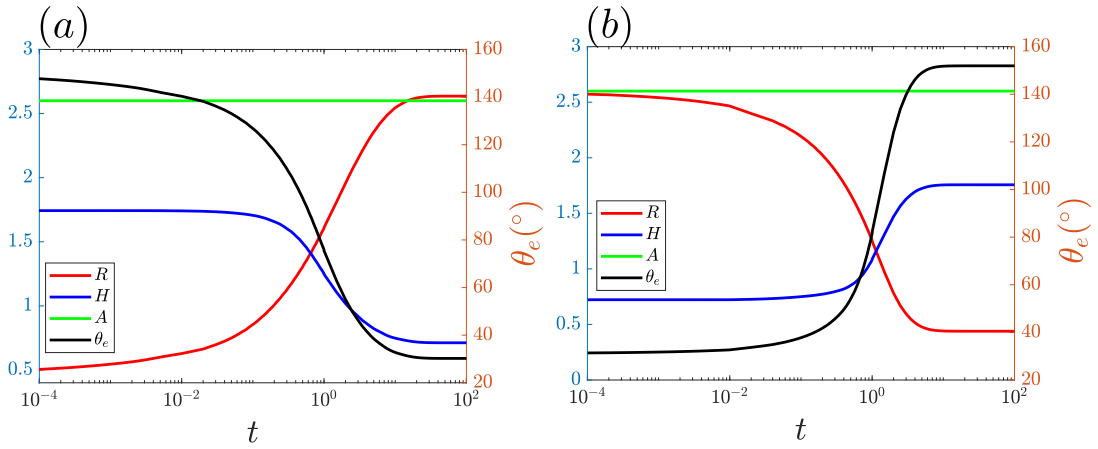

Fig. 2.5 The evolution of droplet contact angle (black line), radius (red line) and height (blue line) during spreading (*a*) from $\theta_e = 150°$ to $\theta_e = 30°$ (*b*) from $\theta_e = 30°$ to $\theta_e = 150°$, where the droplet cross-sectional area A (green line) is constant throughout the spreading duration in both cases. The Weber and Reynolds numbers used are 0.2 and 1 respectively in both cases.

perform numerical experiments to investigate the validity of our model and study how contact angles and non dimensional parameters affect the spreading dynamics.

For Weber number 0.2, and Reynolds number 1, we start by placing a droplet with contact angle $\theta_e = 150°$ on a solid surface imposed with an equilibrium contact angle $\theta_e = 30°$. Figure 2.5(a) shows that the droplet radius R, increases as the droplet spreads, while its height H, decreases. By starting with a 30° droplet and imposing $\theta_e = 150°$, see Fig. 2.5(b), the droplet radius decreases while its height increases as the droplet approaches its equilibrium shape. Notice that in both cases, the size of the droplet remains the same, this means that our model conserves mass and that the size of the droplet does not change as it spreads. At about $t = 0.1$, the droplet angle, radius and height changes rapidly until about $t = 50$ when droplet attains its equilibrium shape. This rapid spreading rate can be explained by noting that the contact-line region is out of equilibrium at the start of the process, resulting in a local gradient of capillary pressure and rapid initial spreading.

The rate at which liquid droplets spread depends on the droplets' viscosity and surface tension. This can be studied by examining the Weber number which describes the ratio of inertia and surface tension forces and Reynolds number which is the ratio of inertia and viscous forces. By varying the Weber number while keeping the Reynolds number constant at 1, it is seen that as the Weber number decreases (equivalent to surface tension forces becoming more important), the droplet spreads faster with the droplet reaching its equilibrium shape quicker, (see Fig. 2.6). If the Reynolds number is varied instead, with the Weber number being kept constant at 0.2, it is seen that a droplet spreads slower as the Reynolds number decreases, (see Fig. 2.7). Since the Reynolds number is the ratio of inertia and viscous forces, it means that viscous liquids spread slower. Figure (2.8)

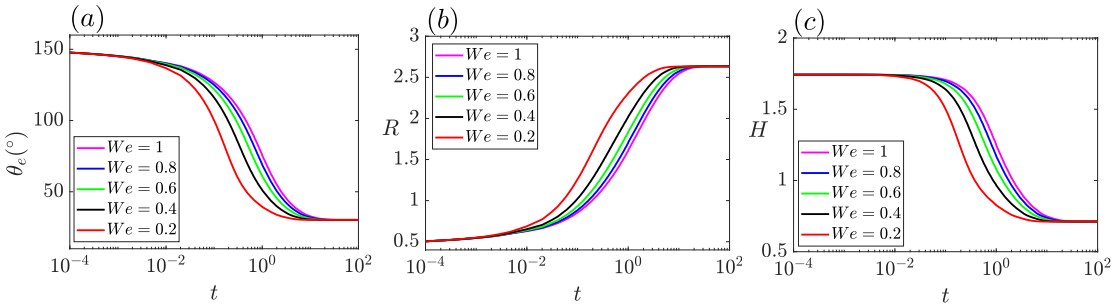

Fig. 2.6 Time evolution of the contact angle from 150° to 30° (a), base radius (b), and height (c) of a droplet relaxing to equilibrium. The Reynolds number is set to 1, different lines correspond to different values of the Weber number and the plot is given in a semi-log scale.

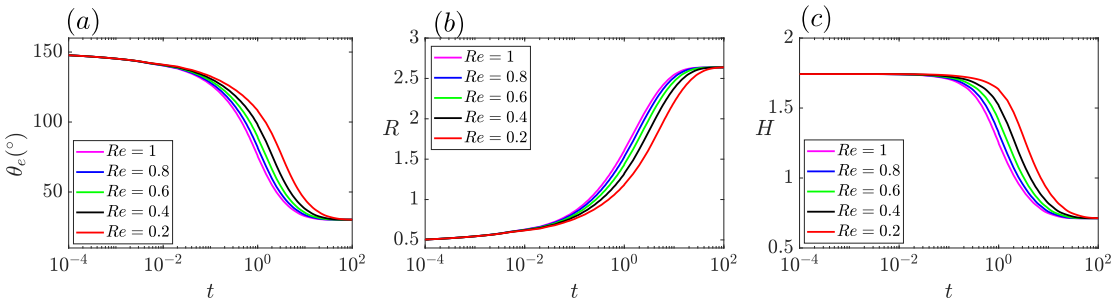

Fig. 2.7 Time evolution of the contact angle from 150° to 30° (a), base radius (b), and height (c) of a droplet relaxing to equilibrium. The Weber number is set to 0.2, different lines correspond to different values of the Reynolds number and the plot is given in a semi-log scale.

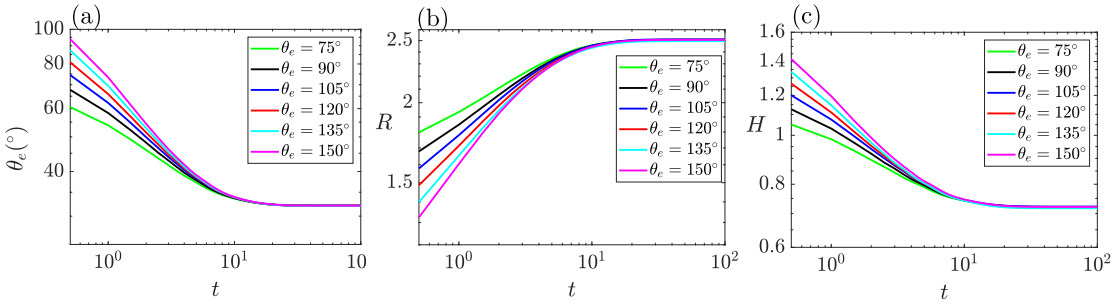

Fig. 2.8 Time evolution of the contact angle from different initial contact angles to 30° (a), base radius (b), and height (c) of a droplet relaxing to equilibrium. The Reynolds and Weber numbers are set to 1 and 0.2 respectively. Different lines correspond to different initial contact angles and the plot is given in a semi-log scale.

shows that droplet spreading to its equilibrium shape is independent of the initial droplet shape, with the only difference being the time the spreading takes, the closer the initial contact angle is to the final equilibrium contact angle, the lesser time the spreading takes, where the Weber and Reynolds numbers have been set to 0.2 and 1 respectively.

2.4.3 Droplet evaporation on homogeneous surfaces

We have shown that our model accurately captures the equilibrium properties of a droplet. The spreading dynamics of a droplet on a flat surface has also been validated. We will now simulate droplet evaporation by assuming a quasi-static evaporation where the size A of a droplet with contact angle θ slowly decreases at a constant rate α:

$$\frac{dA}{dt} = -\alpha.$$

As we will see, this leads to the law: $R(t) \sim (t_e - t)^{1/2}$, where t_e is the evaporation time. We will find an expression for the proportionality coefficient of this relation from Equation (1.12) with $\theta = \theta_0$. Since the droplet evaporates very slowly, the contact radius is

$$R^2 = Ag(\theta_0),$$

where $g(\theta_0) = 2\sin^2\theta_0/(2\theta_0 - \sin 2\theta_0)$. As the droplet's size decreases linearly in time, $A(t) = A_0 - \alpha t$, where α is the evaporation rate and A_0 the initial size, we have

$$R^2(t) = R_0^2 - \alpha g(\theta_0)t, \tag{2.33}$$

where $R_0 = A_0 g(\theta_0)$. Hence, we can see that the proportionality coefficient depends on the contact angle and the evaporation rate. The life time of the droplet can be obtained from Eq. (2.33) by noting that the droplet evaporates at time t_e when $R = 0$. This gives the evaporation time as:

$$t_e = \frac{R_0^2}{\alpha g(\theta_0)}.$$

To obtain the evaporation rate α, we note that evaporation can be imposed by creating a gradient in the chemical potential that drives mass diffusion of the droplet. This can be achieved by prescribing a Dirichlet condition $\phi = \phi_H$ on the top boundary Γ_T, where $\phi < -\phi_e$ [57]. Alternatively, a gradient in the chemical potential can be created by imposing a Neumann condition $\boldsymbol{\nabla}\eta \cdot \mathbf{n} = -\eta_w$ at the top boundary Γ_T, where $\eta_w > 0$ controls the evaporation rate. These two methods of imposing droplet evaporation will be explained in turn.

For the case where imposing a Dirichlet condition $\phi = \phi_H$ on the top boundary Γ_T drives droplet evaporation, a phase-field imbalance $\Delta\phi_H = -\phi_e - \phi_H$ causes a gradient in the chemical potential. To understand how evaporation can be imposed by inducing a gradient in the chemical potential, we consider the Cahn-Hilliard equation (2.5a):

$$\frac{\partial\phi}{\partial t} + \mathbf{u}\cdot\boldsymbol{\nabla}\phi = M\nabla^2\eta(\phi), \tag{2.34}$$

For quasi-static dynamics, the chemical potential in gas phase satisfies Laplace's equation $\nabla^2\eta(\phi) = 0$. Here we are interested in the profile of the chemical potential η in the gas phase. To make this more tractable analytically, we assume that the domain is circular and consider the polar coordinate system:

$$\frac{1}{r}\frac{\partial}{\partial r}\left[r\frac{\partial\eta}{\partial r}\right] = 0. \tag{2.35}$$

Here, r is the radial component. To obtain the profile of the chemical potential in the gas phase, we solve Eq. (2.35) subject to the boundary conditions: $\eta(R_0) = \eta_R$, $\eta(R_H) = \eta_H$, where R_0, R_H, η_R, and η_H, is the position of the droplet interface, the top boundary of the domain, chemical potential at the droplet interface and chemical potential at the top boundary respectively. Integrating Eq. (2.35):

$$\eta = K_1 \ln r + K_2,$$

where K_1 and K_2 are constants, which are obtained from the boundary conditions as:

$$\begin{aligned} K_1 =& \frac{\eta_H - \eta_R}{\ln[\frac{R_H}{R_0}]} \\ K_2 =& \eta_H - K_1 \ln R_H. \end{aligned}$$

The chemical potential in the gas phase then becomes:

$$\eta = \eta_H + \frac{\eta_H - \eta_R}{\ln[\frac{R_H}{R_0}]} \ln\left[\frac{r}{R_H}\right]. \tag{2.36}$$

To model evaporation, an important component needed is the diffusive flux at the interface j, which obeys the constitutive equation [57]:

$$j = -M \frac{d\eta}{dr}\Big|_{R_0}.$$

Using Eq. (2.36), the flux over the droplet interface is obtained by multiplying j by $\theta_0 R_0$:

$$J = -\theta_0 M \frac{\eta_H - \eta_R}{\ln[\frac{R_H}{R_0}]}, \tag{2.37}$$

The droplet's cross-sectional area A, is related to the flux through the relation:

$$\frac{dA}{dt} = \frac{J}{\Delta\phi},$$

here, $\Delta\phi$ is defined as $+\phi_e - (-\phi_e) = 2$. This yields:

$$\frac{dA}{dt} = -\frac{\theta_0 M \Delta\eta}{\ln[\frac{R_H}{R_0}]},$$

where $\Delta\eta = \eta_H - \eta_R$. By non-dimensionalizing this, we have:

$$\frac{dA}{dt} = -\frac{1}{Pe}\frac{\theta_0 \Delta\eta}{\ln[\frac{R_H}{R_0}]}. \tag{2.38}$$

Hence, when evaporation is driven by imposing a Dirichlet boundary condition at the top boundary, the evaporation rate α is $\frac{1}{Pe}\frac{\theta_0\Delta\eta}{\ln[\frac{R_H}{R_0}]}$. This means that the evaporation rate depends on the contact angle, the difference between the chemical potential at the domain's boundary and droplet interface, and the ratio of the droplet's radius and domain radius. Figure 2.9(a) shows the chemical potential profile at $x = 0.5$ and $t = 50$

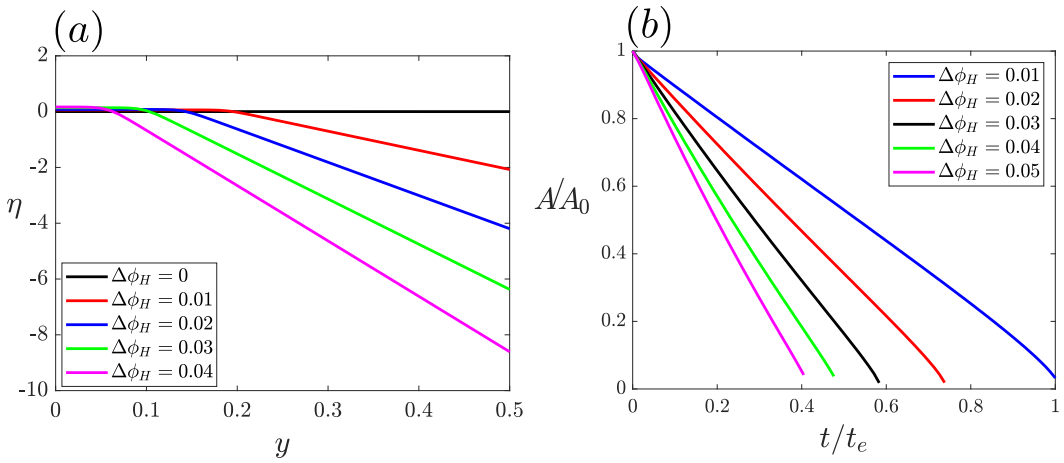

Fig. 2.9 Imposing evaporation with a Dirichlet condition on the phase-field. (a) Different values of the phase-field at the top boundary ϕ_H induces a gradient in the chemical potential η that drives evaporation. (b) Evolution of droplet area A with time t for different values of ϕ_H. The initial droplet size is denoted by A_0, the droplet evaporation time by t_e, and $\Delta\phi_H = -\phi_H - \phi_e$.

for Weber number 0.2 and Reynolds number 1. It is observed that a gradient in chemical potential is created by imposing $\phi = -\phi_e - \Delta\phi_H$ at the domain top wall. Also, the chemical potential gradient increases as $\Delta\phi_H > 0$ increases. Panel (b) of Fig. 2.9 shows that the chemical potential gradient in turn drives droplet evaporation following the $R \sim (t_e - t)^{1/2}$ law since A, varies linearly as time t, and $A \sim R^2$.

The droplet's size can also be changed dynamically by imposing a Neumann condition at the top boundary: $\boldsymbol{\nabla}\eta \cdot \mathbf{n} = -\eta_w$. In this scenario, Eq. (2.38) becomes:

$$\frac{dA}{dt} = -\frac{1}{Pe}\theta R_H \eta_w. \tag{2.39}$$

Here the evaporation rate, $\alpha = \frac{1}{Pe}\theta_0 R_H \eta_w$, depends on the contact angle, the domain radius and the value of the chemical potential at the domain boundary.

Figure 2.10(a) shows the chemical potential profile at $x = 0.5$ and $t = 50$ for Weber number 0.2 and Reynolds number 1. It is observed that when $\eta_w = 0$, there is no gradient in the chemical potential and hence no evaporation, however for $\eta_w \neq 0$, a gradient is induced on the chemical potential, which increases as η_w increases. Hence, the rate of evaporation can be effectively controlled by varying η_w. Figure 2.10(b) shows that the droplet radius obeys the law $R \sim (t_e - t)^{1/2}$ since A varies linearly as time t, and $A \sim R^2$.

In this thesis, dynamic simulations of the CH-NS system of equations for evaporating droplets will be compared with droplet equilibrium properties that satisfies the Young-Laplace equation discussed in Chapter 1. This comparison is valid because we have assumed quasi-static evaporation which is implemented in the simulation of the CH-NS system of equations by making use of small evaporation rate to ensure slow droplet evaporation. As a result, a droplet assumes its equilibrium configuration faster than it evaporates. This allows us to approximate the properties of an evaporating droplet using its equilibrium properties.

Essentially, for different scenarios of droplet evaporation that will be considered in this thesis, an analytical model based on the Young-Laplace equation will be used along side a numerical simulation of fully dynamic CH-NS system of equations that includes inertial with imposed quasi-static evaporation. It is important to note that the term "quasi-static

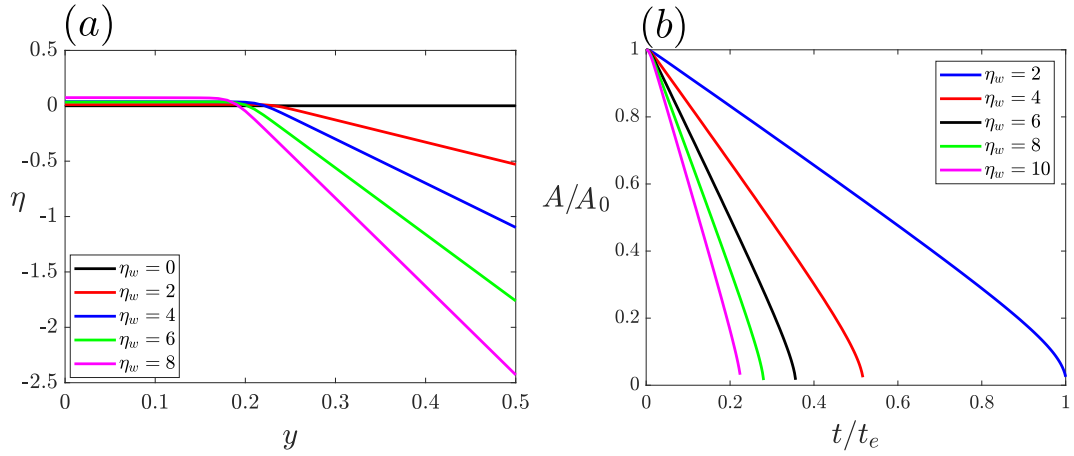

Fig. 2.10 Imposing evaporation with a Neumann condition on the chemical potential. (a) Different values of the chemical potential at the top boundary η_w induces a gradient in the chemical potential that drives evaporation. (b) Evolution of droplet area A with time t for different values of η_w. The initial droplet size is denoted by A_0 and the droplet evaporation time by t_e.

evaporation" simply refers to slow decrease in the droplet size via evaporation, and not to any approximation or asymptotic expansion assuming that velocities are slow.

2.5 Summary

In this chapter we have introduced the Cahn-Hilliard and Navier-Stokes (CH-NS) system of equations, which will be used throughout the rest of the thesis to study droplet dynamics on solid surfaces. We have described the numerical algorithm to solve the CH-NS system that is based on finite element methods. The validity of the method has been tested with a series of numerical experiments, including equilibrium shapes of droplets as well as the dynamics of a droplet spreading and relaxing to equilibrium. We have observed that droplet spreads faster as it becomes less viscous and its surface tension becomes higher. Droplet evaporation on solid surfaces is also simulated by creating a gradient in the chemical potential. It is observed that footprint of a droplet evaporating on an homogeneous surface follows the $R(t) \sim (t_e - t)^{1/2}$ law.

Chapter 3

Droplet evaporation on smooth surfaces with chemical patterns

In this chapter we investigate the evaporation of a two-dimensional (2D) droplet on a solid surface that is flat but with smooth chemical patterns. The analytical treatment is based on a quasi-static approximation where the shape of the droplet is assumed to be dictated by its equilibrium properties. We then examine how multiplicity of solutions for a 2D sessile droplet on a perfectly and smooth but chemically patterned surface give rise to bifurcations such as pitchfork, saddle node and cusp that emerge when the wetting strength is varied and the cross-sectional area of the droplet changes due to evaporation.

Most of the results of this chapter have been published in [63]. Here we build on the ideas presented in [34] for non-planar surface to study the evaporation of 2D droplets on a perfectly flat and smooth, but chemically patterned surface. We consider chemical patterns that lead to a smooth variation of the local equilibrium contact angle, thus eliminating pinning effects that may arise as a consequence of sharp discontinuities. Such smooth variation of the chemical pattern occurs over a typical length scale λ which we assume to be comparable to the droplet footprint. This limit is particularly relevant for applications as this type of surfaces are easier to implement experimentally [22].

The equilibrium properties of the system depend on both the droplet's size and the specific chemical pattern of the substrate. By constructing the interfacial energy landscape of the system, we identify all possible equilibrium solutions of the droplet shape. On perfectly symmetric patterns, equilibrium solutions correspond to branches parametrised by the droplet's cross-sectional area, position and contact radius. Such branches form a network in the three-dimensional parameter space, where nodes correspond to pitchfork bifurcation points.

Increasing the amplitude of the wettability pattern gives rise to folded nodes that signal the onset of saddle-node bifurcations. Introducing a weak bias in the pattern leads to a disconnection of the equilibrium branches and to the symmetry breaking of the pitchfork bifurcation nodes. Increasing the strength of the bias creates a set of continuous branches of stable equilibrium solutions where the droplet's position varies smoothly upon changes in the cross-sectional area, suggesting that directed motion is possible on this type of surfaces.

To understand the droplet dynamics upon evaporation on chemically patterned surfaces, we present numerical simulations of the Cahn-Hilliard and Navier-Stokes system of equations introduced in Chapter 2. We focus on the quasi-static regime, where droplet evaporation is dominated by diffusion into the gas phase. For periodic and symmetric patterns, the droplet exhibits lateral movements when its cross-sectional area reaches the pitchfork bifurcations predicted by the theory, equivalent to the snap evaporation mode reported by Wells et al. [34]. On asymmetric patterns, the pitchfork branches are disconnected, and the droplet follows a smooth motion in a preferred direction as its size decreases in time, also in good agreement with the theory. Our results show that the interplay between a phase change and surface wettability can be exploited to control the motion of droplets on patterned solid surfaces in the absence of the anchoring effect of pinning. We will start with a complete analysis of the equilibrium properties of the system by making use of bifurcation theory. Appendix C provides a brief revision of bifurcation analysis on dynamical systems in general.

3.1 Equilibrium properties: Bifurcation analysis

Figure 3.1(a) shows a schematic representation of the system considered in this chapter. A 2D droplet rests on a solid flat surface of non-uniform wettability. Here, we consider a periodic variation of the surface chemical properties along the lateral coordinate x, which we model using a spatially-dependent function $\Theta(x)$, given by:

$$\cos\Theta(x) = \cos\theta_0 - \epsilon\mathcal{F}(x), \tag{3.1}$$

where θ_0 is the reference homogeneous contact angle, which we take to be $\theta_0 = 70°$, ϵ controls the strength of the chemical pattern and $\mathcal{F}(x)$ is a generic periodic function. (We note that the reason to write $\cos\Theta(x)$ in the above equation is to simplify the analytical treatment presented below, see Eq. (3.3)).

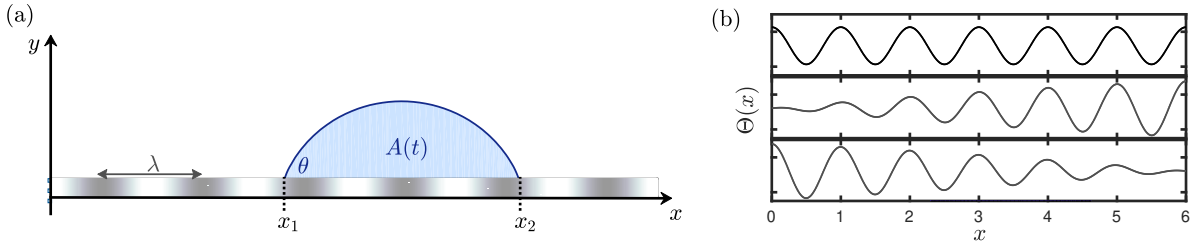

Fig. 3.1 (a) Two-dimensional droplet on a flat substrate with a smoothly varying chemical pattern. The location of the droplet's contact points is x_1 and x_2, and the contact angle is θ. The droplet size $A(t)$ decreases in time and λ is the wavelength of the periodic pattern. (b) Examples of chemical patterns, which are described by the local contact angle $\Theta(x)$.

We assume that the function $\mathcal{F}(x)$ varies smoothly over a length scale λ without sharp discontinuities, hence ruling out the presence of pinning effects. Consequently, at equilibrium, and in the absence of gravity, the contact angle θ on both contact points of the droplet, x_1 and x_2, is the same and equal to the contact angle imposed by the chemical pattern, i.e. $\theta = \Theta(\ell \pm R)$. Here, $\ell = (x_1 + x_2)/2$ is the droplet shift and corresponds to the location of the droplet's midpoint relative to the origin $x = 0$, and $R = (x_2 - x_1)/2$ is the droplet footprint, see Fig. 3.1. Therefore, the shape of the free surface of the droplet, which we denote as $h(x)$, is given by a circular arc whose cross-sectional area A satisfies the relation:

$$A = \frac{R^2}{2}\frac{2\theta - \sin(2\theta)}{\sin^2\theta}, \tag{3.2a}$$

$$\cos\theta = \cos\theta_0 - \epsilon\mathcal{F}(\ell \pm R). \tag{3.2b}$$

Equation (3.2a) was derived in Section 1.2.1 of Chapter 1, and for a given droplet's area A, it can be thought of as a nonlinear function for the droplet's radius $F(R; A) = A - \frac{R^2}{2}\frac{2\theta - \sin(2\theta)}{\sin^2\theta} = 0$. For a fixed droplet area, the stability of the equilibrium solutions for (ℓ, R) that satisfy Eqs. (3.2a) can be determined from the interfacial energy (per unit length of the contact line)

$$E(\ell, R) = \frac{2\gamma\theta R}{\sin\theta} - \gamma\int_{\ell-R}^{\ell+R}\cos\Theta(x)dx, \tag{3.3}$$

where γ is the liquid/gas surface tension. Inserting Eq. (3.1) into Eq. (3.3) gives:

$$E(\ell, R) = 2\gamma R \left(\frac{\theta}{\sin\theta} - \cos\theta_0 \right) + \gamma \int_{\ell-R}^{\ell+R} \epsilon \mathcal{F}(x)\, dx, \tag{3.4}$$

where R and θ are related through Eqs. (3.2a). For a given droplet's area A, we can compute the interfacial energy and find its extrema, which correspond to the equilibrium states of the droplet. In the following, we will analyse how the stability of the equilibrium states changes with the droplet area, leading to a hierarchy of bifurcation diagrams that are dictated by the underlying chemical pattern. These bifurcation diagrams will, in turn, inform about the possible (stable) trajectories in the (A, ℓ, R) space, which can be observed as the droplet's size is dynamically changed. This analysis will lead to a series of bifurcations and a brief summary of classic bifurcation theory is provided in Appendix C.

3.1.1 Periodic and symmetric chemical patterns

We start by considering periodic and symmetric patterns. For simplicity, we consider the the function $\mathcal{F}(x) = \cos(kx)$, where $k = 2\pi/\lambda$ and λ is the wavelength of the chemical variation. We non-dimensionalise the system of equations (3.2a) and (3.4) by taking λ as the typical length scale, such that the new dimensionless variables are $x' = x/\lambda$, $R' = R/\lambda$, $A' = A/\lambda^2$, and $E' = E/(\gamma\lambda)$. For convenience, we will drop the primes. Under these conditions, Eq. (3.4) becomes:

$$E(\ell, R) = 2R \left(\frac{\theta}{\sin\theta} - \cos\theta_0 \right) + \frac{\epsilon}{\pi} \sin(2\pi R)\cos(2\pi\ell), \tag{3.5}$$

where θ and R are related through Eqs. (3.2a).

We will now show that depending on the strength of variation of the chemical pattern, given by the amplitude ϵ, different bifurcation points emerge as the droplet's size is changed.

3.1.2 Pitchfork bifurcation

We first consider relatively small values of ϵ. We note that the work done in Ref. [64] analysed this case with a chemical pattern given by $\Theta(x) = \theta_0 + \epsilon\cos(kx)$, reporting the emergence of subcritical pitchfork bifurcations on the (ℓ, A) diagram. In this section, we revisit this case with the chemical pattern given by Eq. (3.2b), which has the advantage that it leads to the explicit expression of the energy, Eq. (3.5).

Figure 3.2(a) shows a contour plot of the energy for a fixed droplet size, $A = 1.5$, and for $\epsilon = 0.1$. We first focus on equilibrium solutions for the droplet shape aligned with minima and maxima of the chemical pattern, marked with blue circles and red crosses in the figure. Solutions that are aligned with a minimum of the chemical pattern (i.e., $\ell = \pm(2n+1)/2$ for $n = 0, 1, 2, \dots$) are stable, whereas solutions that are aligned with a maximum ($\ell = \pm n$ for $n = 0, 1, 2, \dots$) are saddle nodes, which are stable to axisymmetric perturbations but unstable against lateral displacements along the solid surface, (see the Appendix C).

Therefore, if the droplet is on a saddle node, any perturbation on the system will destabilise the droplet's location and make the droplet shift laterally to either of the two stable solutions that are located to the left or right [64].

By fixing the location of the droplet to be aligned with either a maximum or minimum of the chemical pattern, and by changing the droplet size A, we construct two branches of solutions that are parametrised by the droplet's lateral radius R, as shown in Fig. 3.2(b),

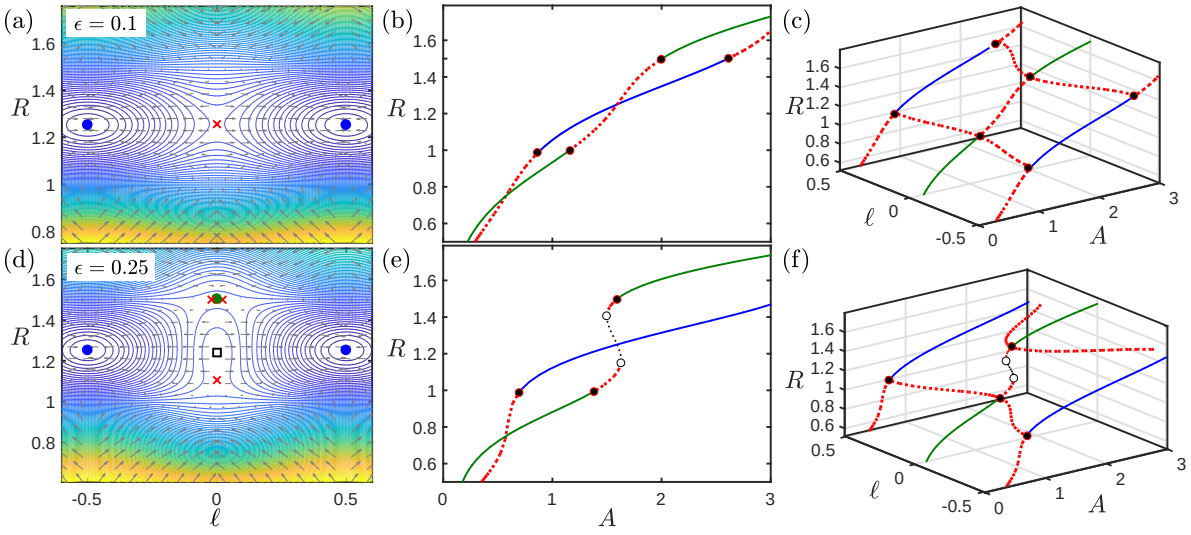

Fig. 3.2 Top panels (a,b,c) correspond to $\epsilon = 0.1$ and lower panels (d,e,f) to $\epsilon = 0.25$. (a,d) Interfacial energy contour plots for $A = 1.5$, where energy levels increase from blue to yellow. Blue and green circles correspond to stable equilibrium solutions, crosses to saddle nodes that are stable to axisymmetric perturbations but unstable against lateral displacements, and empty squares correspond to unstable solutions. (b,e) Droplet lateral radius R as function of the area A, where green and blue branches correspond to droplet stable solutions that are aligned with a maximum and a minimum of the chemical pattern, respectively. The red dashed branches are saddle nodes and the black dotted branch corresponds to unstable solutions. (c,f) Bifurcation diagrams showing all possible solutions. Solid points represent subcritical pitchfork bifurcations and empty circles mark the onset of saddle-node bifurcations. In all cases $\theta_0 = 70°$.

where dashed lines correspond to saddle nodes and solid lines correspond to stable solutions. The stability of these solutions changes from stable to saddle node (or viceversa) at specific values of A. Extending this analysis to include droplet solutions that are located between minima and maxima of the chemical pattern, yields the three-dimensional bifurcation diagram shown in Fig. 3.2(c).

Stability transitions correspond to pitchfork bifurcations: a stable point (green solid line) collides with two saddle nodes to become a saddle node (subcritical pitchfork bifurcation), and a saddle node collides with two saddle nodes to become a stable solution (inverted subcritical pitchfork bifurcation), see the Appendix C.

Figure 3.3 gives a clearer picture of the stability transitions of the equilibrium solutions for $\epsilon = 0.25$, and $\theta_0 = 70°$ for different droplet sizes around the critical droplet size, A_p. At $A < A_p$, there are three equilibrium solutions aligned with the maximum of the chemical pattern, one stable and two saddle nodes. These solutions collide and become a saddle node at the pitchfork point, $A = A_p$. At this point the droplet could move to the left or right towards stable points at the minimum of the chemical pattern. Therefore, in a dynamic situation, where the droplet's area is slowly decreasing in time, it is expected that around these bifurcation points, any perturbation that can break the plane symmetry will make the droplet shift and change location: if it is aligned with a maximum of the chemical pattern it will move to a minimum and vice versa.

The critical droplet footprint R_p at which the pitchfork bifurcations occur can be determined explicitly by noting that at these points the stability of the solution changes from a stable to a saddle node. Hence, these points satisfy $\partial^2_\ell E(\ell, R_\mathrm{p}) = 0$. Imposing

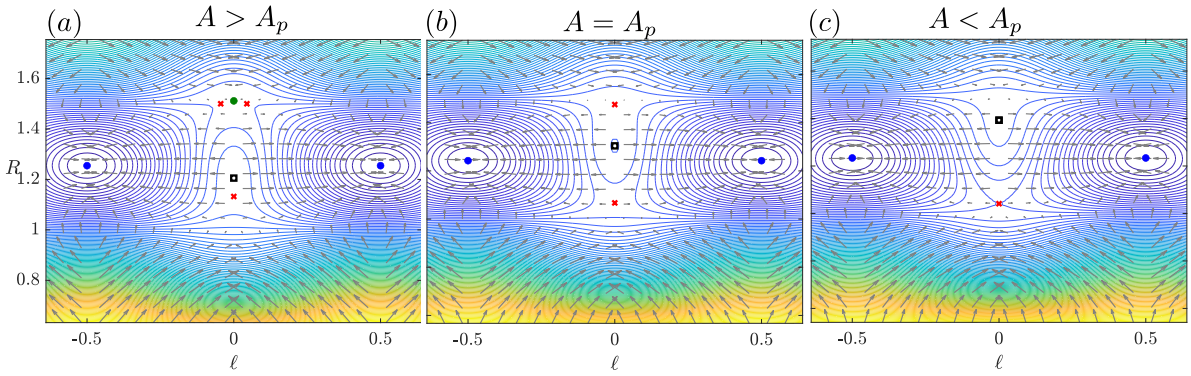

Fig. 3.3 Interfacial energy contour plots for different droplet sizes, where energy levels increase from blue to yellow. Blue and green circles correspond to stable equilibrium solutions, crosses to saddle nodes that are stable to axisymmetric perturbations but unstable against lateral displacements, and empty squares correspond to unstable solutions for $\epsilon = 0.25$, and $\theta_0 = 70°$. Panel (a) $A > A_p$. Panel (b) $A = A_p$ Panel (c) $A < A_p$.

this condition to Eq. (3.5) gives the relation

$$\sin(2\pi R_{\mathrm{p}}) = 0, \tag{3.6}$$

and hence the pitchfork critical radii are

$$R_{\mathrm{p}} = \frac{n}{2}, \tag{3.7}$$

for $n = 1, 2, \ldots$. Therefore, pitchfork bifurcations occur at precise locations of the droplet's edges: either at minima or maxima of the chemical pattern. Remarkably, this geometrical property holds regardless of the chemical pattern, i.e., R_p is independent of the homogeneous contact angle θ_0, and the amplitude of the substrate's chemical variation ϵ. Instead, the effect of these parameters is to determine the critical contact angle θ_{p} and area A_{p} at the bifurcation points, which follow from Eq. (3.2a).

3.1.3 Cusp and saddle-node bifurcations

For large values of ϵ, we observe multiple solutions for the same droplet area and midpoint location [see green circle, empty box and red cross at $\ell = 0$ in Fig. 3.2(d)]. Such solutions lie within S-shaped branches of the $R(A)$ curve characterised by two turning points [see Fig. 3.2(e)]. These turning points mark the onset of saddle-node bifurcations whereby a saddle node solution collides with an unstable solution, (see the Appendix C). Such transitions are identified as empty circles in the three-dimensional bifurcation diagram shown in Fig. 3.2(f).

The emergence of unstable solutions is a consequence of a cusp bifurcation that occurs as ϵ is continuously increased, as is shown in Fig. 3.4(a). At the critical cusp point ϵ_c, two new branches of solutions emerge, which correspond to the two turning points, (see the Appendix C). Figs. 3.4(b,c) show the evolution of these turning points on the (ϵ, A) and (ϵ, R) planes, in agreement with the standard form of the cusp bifurcation [65], (see the Appendix C). It is important to note that the saddle-node bifurcations (i.e. the turning points on the $R(A)$ curve) are not only observed as ϵ increases, but also as the droplet size A increases for a fixed value of ϵ, as is shown in Fig. 3.4(d). We can understand this set of folds as a result of a series of cusp bifurcations that occur at different critical points in the (ϵ, A, R) space, i.e. each cusp bifurcation is described in terms of a critical strength ϵ_c, a critical size A_c and critical radius R_c.

Fig. 3.4(e) shows the set of critical amplitudes ϵ_c as a function of the critical droplet size A_c. To understand the scaling relation between ϵ_c and A_c, we consider the regime

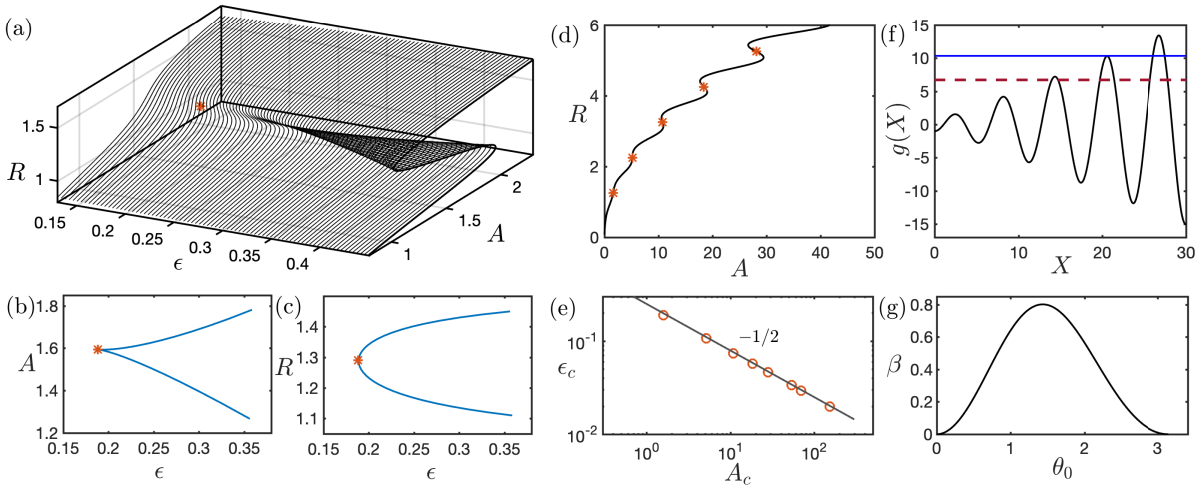

Fig. 3.4 (a,b,c) Emergence of a cusp bifurcation as the strength of the chemical pattern, ϵ, is increased for the case with $\theta_0 = 70°$. Panel (a) shows the three-dimensional plot (ϵ, A, R), where the red asterisk marks the critical cusp point. Panels (b) and (c) show the corresponding projections onto the (ϵ, A) and (ϵ, R) planes, respectively. (d) Droplet footprint as function of its size for $\epsilon = 0.1$ and $\ell = 0$. Red asterisk mark the critical radii at which a cusp bifurcation occurs. (e) Critical values of the strength of the chemical pattern to induce a cusp bifurcation as function of the droplet size. Solid line corresponds to a power law with exponent $-1/2$. (f) Plot of the function $g(X)$ where solid and dashed lines correspond to β/ϵ with $\theta_0 = 70°$ and $\epsilon = 0.046$ and $\epsilon = 0.058$, respectively. (g) Plot of the function $\beta(\theta_0)$.

where ϵ is small. In this limit, $\epsilon \ll 1$, the contact angle Eq. (3.1) can be written using the Taylor's expansion as:

$$\theta = \theta_0 + \epsilon\theta_1(R, \theta_0) + \mathcal{O}(\epsilon^2), \tag{3.8}$$

where $\theta_1(R, \theta_0) = \cos 2\pi R / \sin\theta_0$. With this expansion of the contact angle, we can now also find an expansion for the droplet area. We begin by noting that the droplet area A, (3.2a) can be rewritten as:

$$A = R^2 G(\theta), \tag{3.9}$$

where

$$G(\theta) = \frac{1}{2}\frac{2\theta - \sin 2\theta}{\sin^2\theta}. \tag{3.10}$$

Equation (3.10) can be expanded using Taylor's series as:

$$G = \frac{1}{2}\frac{2(\theta_0 + \epsilon\theta_1) - \sin 2\theta_0 - 2\theta_1\epsilon\cos 2\theta_0}{\sin^2\theta_0 + 2\epsilon\theta_1 \sin\theta_0\cos\theta_0} + \mathcal{O}(\epsilon^2),$$

which can be rewritten as:

$$G = G(\theta_0) + 2\theta_1\epsilon(1 - \cot\theta_0 G(\theta_0)) + \mathcal{O}(\epsilon^2),$$

where $G(\theta_0)$ is as defined in equations (3.10). Inserting G into equation (3.9) then yields:

$$A = R^2\left[G(\theta_0) + 2\theta_1\epsilon(1 - \cot\theta_0 G(\theta_0)) + \mathcal{O}(\epsilon^2)\right].$$

Hence, in the limit of $\epsilon \to 0$, Eq. (3.2a) becomes:

$$A = A_0(R)\left[1 + \frac{\epsilon}{\beta}\cos(2\pi R)\right] + \text{h.o.t}, \tag{3.11}$$

where $A_0 = R^2(2\theta_0 - \sin(2\theta_0)/2\sin^2\theta_0$ is the droplet size when $\epsilon = 0$, and we have defined the parameter

$$\beta = \frac{(\theta_0 - \sin\theta_0\cos\theta_0)\sin\theta_0}{2(1 - \theta_0\cot\theta_0)}. \tag{3.12}$$

Figure 3.5 shows a comparison between the exact droplet size, A, and it's approximation, A' in the limit of small ϵ for $\theta_0 = 90°$. The approximation is excellent for values of $\epsilon < 0.1$ and $A < 5$.

To find the radii R_s at which the saddle-node bifurcations occur, we find the stationary points for A, these are the points where: $dA/dR = 0$. We have that

$$\frac{X}{2}\sin X - \cos X = \frac{\beta(\theta_0)}{\epsilon}, \tag{3.13}$$

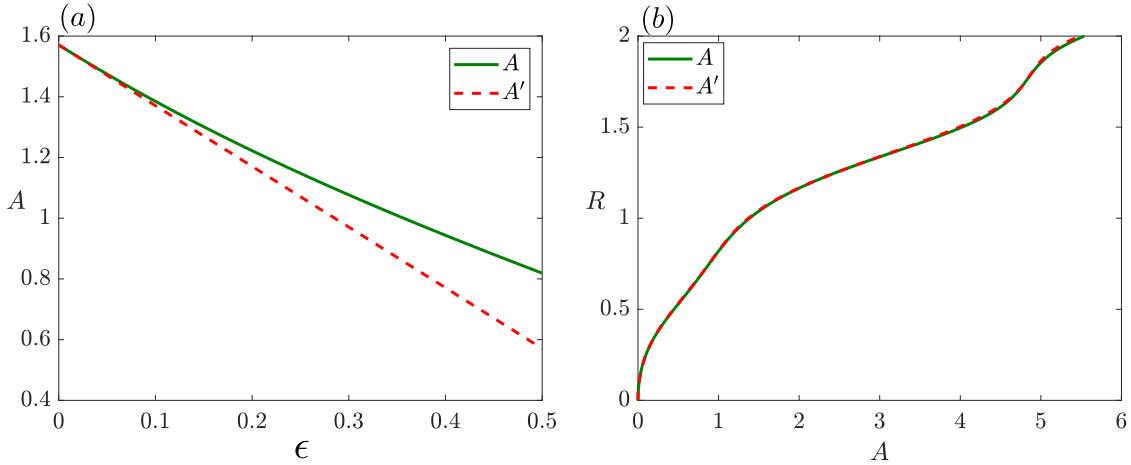

Fig. 3.5 Comparison between exact droplet size A, and it's approximation A' in the limit of small ϵ for $\theta_0 = 90°$ on (a) (A, ϵ), and (b) (R, A) planes.

where $X = 2\pi R$. Let

$$g(X) = \frac{X}{2}\sin X - \cos X, \tag{3.14}$$

this corresponds to the onset of cusp bifurcation. We are interested in the stationary points X_s of g. These are points where $dg/dX = 0$:

$$3\sin X_s + X_s \cos X_s = 0. \tag{3.15}$$

Expanding the function $g(X)$ around the cusp point X_c gives:

$$g(X) = g(X_c) + g'(X_c)(X - X_c) + \frac{1}{2}g''(X_c)(X - X_c)^2 + \mathcal{O}(X^3).$$

Since $g'(X_c) = 0$, we have that:

$$X = X_c \pm \sqrt{\frac{2}{g''(X_c)}(g(X) - g(X_c))}, \tag{3.16}$$

we then find that the solutions near the cusp bifurcation are given by:

$$X \simeq X_c \pm \delta\left(\frac{1}{\epsilon} - \frac{1}{\epsilon_c}\right)^{1/2}, \tag{3.17}$$

where $\delta = \sqrt{2\beta(\theta_0)/g''(X_c)}$ is a constant that depends on θ_0 only. The critical value where the cusp bifurcation emerges, where $X = X_c$ occurs when $g(X) = g(X_c)$, and is given by:

$$\epsilon_c = \frac{\beta(\theta_0)}{g(X_c)} \sim \beta(\theta_0) A_c^{-1/2}, \tag{3.18}$$

where we have approximated $g(X_c) \sim X_c/2$, transformed back to the radius variable R, and made use of the fact that at the onset of the cusp bifurcation $A \sim R^2$. The above relation is in agreement with the scaling behaviour shown in Fig. 3.4(e). Because β is always finite [cf. 3.4(g)], an important conclusion is that cusp, and, consequently saddle node bifurcations are observed for any wetting condition, as long as $\epsilon \neq 0$. Figure 3.4(f) shows a plot of the function $g(X) = (X/2)\sin X - \cos X$, and the constant β/ϵ for $\theta_0 = 70°$ and two arbitrary values of ϵ. For $\epsilon = 0.046$ the plot shows a cusp bifurcation that corresponds to the first intersection between the constant β/ϵ (blue solid line) and the function $g(X)$ at the maximum $X_c \approx 20$. Increasing the amplitude of the chemical pattern to $\epsilon = 0.058$ around $X = 20$, the constant β/ϵ (red dashed line) intersects $g(X)$ at two points that correspond to the saddle node bifurcations. In addition, because the

critical cusp area A_c is normalised by the squared wavelength λ^2, we conclude that, for a fixed droplet area, cusp bifurcations are favoured in the microscopic limit of $\lambda \to 0$.

3.1.4 Patterns with an amplitude gradient

The results shown in Fig. 3.2 indicate that, on symmetric chemical patterns, a droplet will adopt equilibrium configurations which are aligned with either a maximum or a minimum of the pattern. As the droplet's size changes, the stability of such configurations alternates between stable and saddle nodes through a sequence of pitchfork bifurcations that can promote droplet lateral motion: any perturbation that breaks the plane symmetry will make the droplet change from a saddle node to a stable location where the interfacial energy is at a minimum. However, and because of symmetry, there is no bias for the change in position of the droplet, hence ruling out the possibility to induce droplet motion towards a *preferred* direction. To this end, here we explore a non-symmetrical chemical pattern with the aim to determine whether it is possible to achieve directed displacement in the droplet's location as the droplet size is changed.

We consider a pattern with an amplitude gradient described by the function:

$$\mathcal{F}(x) = \frac{2}{\pi} \arctan\left(\frac{x}{L}\right) \cos(2\pi x), \tag{3.19}$$

where L is the length over which the gradient varies. An example of the above pattern with $\epsilon = 0.2$ and $L = 6$ is shown in Fig. 3.1(b). (We note that the change of sign of the gradient can be imposed by replacing x by $L - x$ in the argument of the arctan). In principle, any chemical pattern with amplitude gradient can be considered. The reason why we choose $\mathcal{F}(x) = (2/\pi)\arctan(x/L)\cos(2\pi x)$ is because it allows us to study a regime with strong bias but also the transition to the limit of symmetric patterns by changing the parameter L. By doing so we can relate the emergence of disconnected branches with imperfect pitchfork bifurcations as shown in Fig. 3.6, see the Appendix C.

We solve Eqs. (3.2a) alongside Eq. (3.19) to find the equilibrium solutions for a given droplet size. Following the same procedure as in the previous section, we construct the bifurcation diagrams as the droplet size is changed. Figure 3.6 shows the branches of solutions on the (A, ℓ) plane and in the (A, ℓ, R) space. We observe that the lack of symmetry of the chemical pattern leads to a topological change in the bifurcation diagrams, characterised by a series of disconnected branches, which are either stable or saddle node. In particular, we can see that as the droplet size is changed, there always exists a set of stable branches that can be continuously parametrised by the droplet's

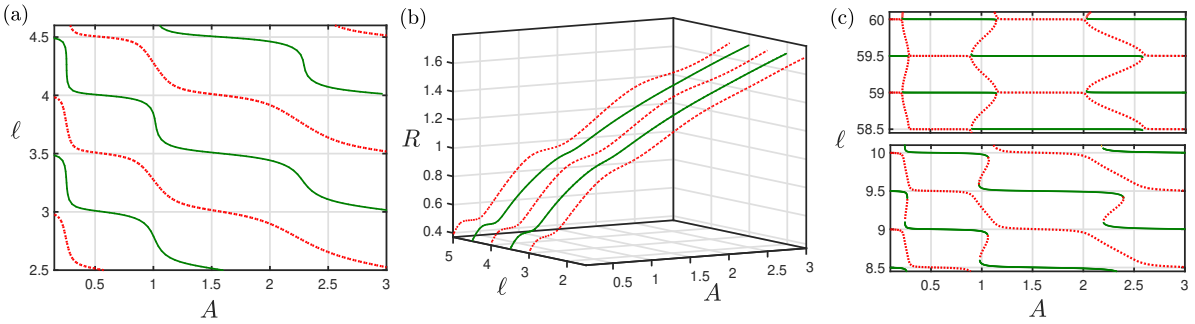

Fig. 3.6 Bifurcation diagrams for the case of a chemical pattern with an amplitude gradient, given by Eq. (3.19) with $\epsilon = 0.1$ and $L = 6$. Panel (a) shows the equilibrium solutions of the droplet's midpoint location, ℓ, as function of its size A and panel (b) the bifurcation diagram in the three-dimensional space (A, ℓ, R). Solid green lines correspond to stable solutions and dashed red lines correspond to saddle nodes. Panel (c) shows the bifurcation diagram on the (A, ℓ) plane when $\ell > L$ (bottom) and $\ell \gg L$ (top). In all cases $\theta_0 = 70°$.

midpoint, i.e. $\ell(A)$. This implies that changing the droplet size can lead to a continuous lateral displacement along a preferred direction.

To understand the onset of symmetry breaking and the consequent topological change in the bifurcation diagram, let us focus on the case of $\ell > L$, noting that in the limit of $\ell \gg L$, the chemical pattern given by Eq. (3.19) becomes symmetric and equivalent to the case considered in the previous section. The bottom panel of Fig. 3.6(c) shows the emergence of turning points along the stable branches for $\ell > L$, which in the limit of $\ell \gg L$ (top panel), become pitchfork bifurcation points, thereby connecting the two previously disconnected stable and saddle node branches. This shows how the topological change in the bifurcation diagrams is purely controlled by the degree of asymmetry of the chemical pattern.

3.2 Droplet evaporation

In this section we study the evaporation of a 2D droplet on a solid surface. We assume that evaporation is quasi-static and driven by mass diffusion in the gas phase; hence, we neglect the effect of a temperature difference between the solid, liquid and gas phases. To model such a system, we adopt a diffuse-interface formulation that includes a wetting boundary condition at the solid substrate as well as an open boundary to drive the evaporation of the droplet, (see Chapter 2). In all cases $\theta_0 = 70°$.

3.2.1 Symmetric patterns

We first consider a droplet evaporating on a symmetric chemical pattern given by Eq. (3.1) with $\mathcal{F}(x) = \cos(2\pi x)$ and $\epsilon = 0.1$. The droplet is initially aligned with a maximum of the chemical pattern. We set the evaporation rate to $\eta_w = 2$. Figure 3.7(a), left panel, shows that, as the droplet size decreases quasi-statically, the evolution of the lateral radius $R(A)$ is in excellent agreement with the trajectory predicted by the theoretical bifurcation diagram (shown in gray lines).

For droplet sizes larger than the critical value A_p, which marks the onset of a pitchfork bifurcation, the droplet is fully stable and aligns with the maximum of the chemical pattern. When $A < A_\mathrm{p}$, the droplet solution becomes unstable against asymmetric perturbations and any small perturbation (in the present case, numerical noise) is able to break the plane symmetry forcing the droplet to shift laterally to a stable branch of solutions, which are aligned with a minimum of the chemical pattern and are located either to the left or right of the droplet's original location ($\ell = 3$) [see Fig. 3.7(b)]. The droplet then continues following the bifurcation diagram in this new location until another pitchfork bifurcation occurs, forcing the droplet to shift and to be aligned with a maximum again.

The inlet panels of Fig. 3.7(a) show the time evolution of $R^2(t)$, where we can see that it smoothly and continuously decreases over time, except at the pitchfork bifurcation

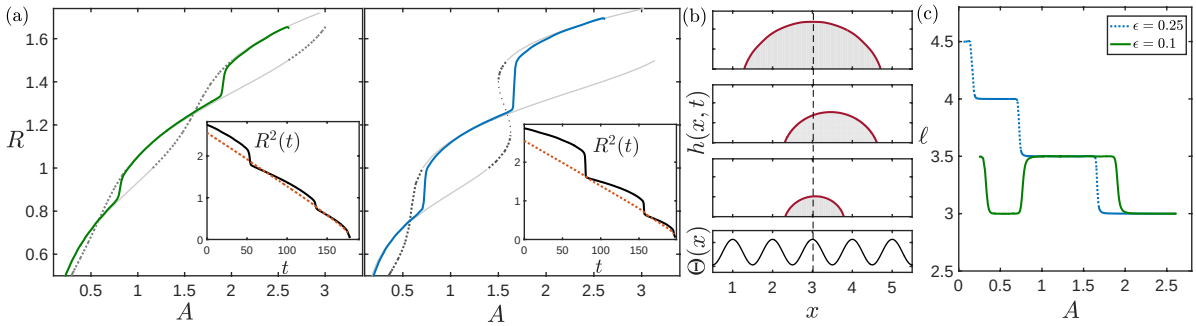

Fig. 3.7 Numerical simulations of slow evaporation by solving the CH-NS system of equations, Eqs. (2.5), with a symmetric chemical pattern, and with an evaporation rate of $\eta_w = 2$. (a) Solid lines show the time evolution of the droplet footprint as function of the droplet size for $\epsilon = 0.1$ (left) and $\epsilon = 0.25$ (right). The underlying gray lines correspond to the theoretical bifurcation diagrams shown in Fig. 3.2. The solid lines of the inlet panels show the time evolution of $R^2(t)$ and the red dotted lines show the evolution of $[2\sin^2\theta_0/(2\theta_0 - \sin 2\theta_0)]A(t)$. Panel (b) shows droplet snapshots at different times and panel (c) shows the evolution of the droplet's midpoint as function of the droplet size. In all cases $\theta_0 = 70°$.

points, when an abrupt step change is observed. The red dotted line corresponds to the linear behaviour that would be expected on a homogeneous surface with contact angle θ_0, which is given by $R^2(t) = [2\sin^2\theta_0/(2\theta_0 - \sin 2\theta_0)]A(t)$. We can see that only for long times (i.e. small droplet sizes), both curves converge to the same point. These results show that the contact line motion is not affected by pinning and de-pinning mechanisms but by the underlying bifurcation sequence that is induced by the wetting pattern.

The trajectory of droplet's midpoint as a function of its size is shown in Fig. 3.7(c), where we can see that lateral movements occur over a much faster time-scale than the timescale of evaporation, [see also the inlet panels of Fig. 3.7(a)]. We note that a similar behaviour is observed for larger values of the strength of the chemical pattern [see Figs. 3.7(a,c) for $\epsilon = 0.25$]. Such fast lateral movements correspond to the snap events that have been reported on topographical smooth surfaces [34], where the same behaviour was observed. This indicates that both smooth wetting patterns and smooth topographies lead to the same type of dynamics. It is important to remark that, because of the symmetry of the chemical pattern, the direction taken by the droplet at each pitchfork bifurcation is not predictable and hence cannot be controlled, i.e. the droplet can shift either to the right or to the left.

3.2.2 Asymmetric patterns

In this section we study the evaporation of a droplet on an asymmetric pattern. We impose a chemical pattern with an amplitude gradient, described by Eq. (3.19) where the amplitude of the chemical pattern gradually increases or decreases with x. Figure 3.8(a) shows the trajectories of the droplet's midpoint as the droplet size decreases for the case with a positive gradient (blue solid line) and negative gradient (red solid line). We observe that in both cases, the asymmetry of the chemical pattern induces a continuous change in the droplet's midpoint location, forcing the droplet to move either to the left or right as its size decreases in time. This phenomenon is independent of the specific form of $\mathcal{F}(x)$. In fact, considering

$$\mathcal{F}(x) = \frac{x}{L}\cos(kx), \tag{3.20}$$

leads to the same behaviour, (see Fig. 3.9).

We note that, as predicted by the theoretical analysis shown in Fig. 3.6, the bifurcation diagrams for this type of chemical patterns consists of a series of disconnected branches, which are either stable or saddle node. If the droplet is initially located at a stable location, it will remain on this branch during the entire process and continuously move

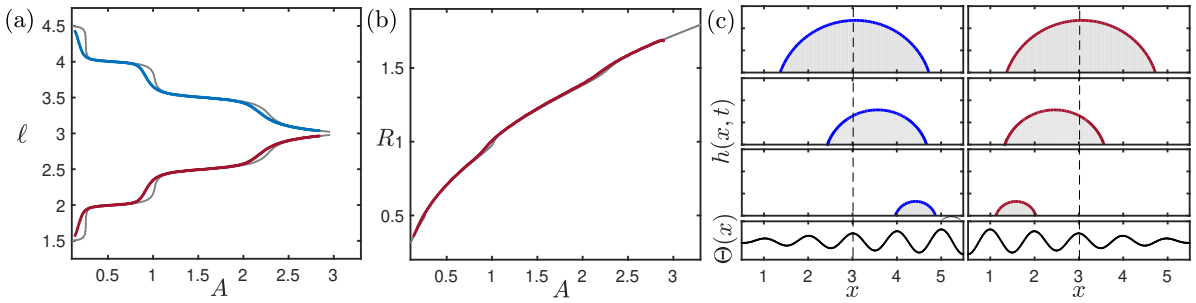

Fig. 3.8 Numerical simulations of the CH-NS system of equations, Eqs. (2.5), with a chemical pattern given by Eq. (3.19) with $\epsilon = 0.1$ and $L = 6$. Panel (a) shows the evolution of the droplet's midpoint as function of its size for a positive gradient (blue solid line) and negative gradient (red solid line). The underlying gray lines correspond to the stable solutions predicted by the theory. Panel (b) shows the droplet's footprint versus its size (red solid line) compared to the theoretical prediction (gray line). Panels in (c) show the corresponding droplet profiles at different times.

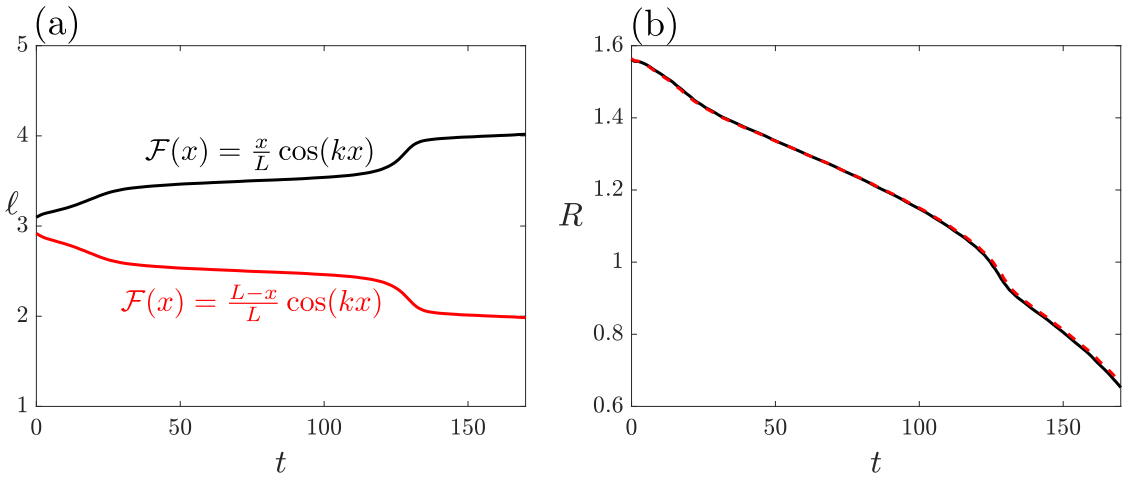

Fig. 3.9 Numerical simulations of the CH-NS system of equations, Eqs. (2.5), with a chemical pattern given by Eq. (3.20) with $\epsilon = 0.1$ and $L = 6$. Panel (a) shows the evolution of the droplet's midpoint as function of its size for a positive gradient (black solid line) and negative gradient (red solid line). Panel (b) shows the droplet's footprint versus its size for a positive gradient (black solid line) and negative gradient (red dashed line).

following the stable branch of solutions, as it is observed in Fig. 3.8(a). It is worth noting that in both cases of the gradient sign the droplet's footprint decreases continuously in time following the same trajectory on the (A, R) plane, as predicted by the theory [see Fig. 3.8(b)]. Counter-intuitively, it is seen that the droplet moves towards higher amplitude of the chemical pattern, moving to the right with positive gradient and to the left with negative gradient, see Fig. 3.8(c). Such behaviour can be understood by tracking

the dynamics of the droplet's contact points, $x_1(t)$ and $x_2(t)$. Figure 3.10 shows the time evolution of the droplet's profile and contact points, where we distinguish between two dynamic stages.

In a first stage both contact points move in opposite directions towards a minimum of the wetting pattern [see top panel of Fig. 3.10(a) and squared blue points in Fig. 3.10(b)]. As the droplet evaporates quasi-statically both contact angles remain the same while the contact points $x_1(t)$ and $x_2(t)$ slowly recede in time. Hence, over a time interval Δt, the contact points will have moved a distance Δx_1 and Δx_2 while the change in contact angle $\Delta\theta$ is the same at both points. On symmetric patterns the local gradient of the wetting pattern, $m = \Delta\Theta/\Delta x$, has the same magnitude on both contact points and so $|\Delta x_1| = |\Delta x_2|$, and hence the droplet remains aligned with either a minimum or maximum of the chemical pattern until a snap occurs [cf. 3.7(c)]. However, on asymmetric patterns, the local gradient is different at each contact point, say m_1 and m_2, leading to different lateral displacements: $\Delta x_1 = (m_2/m_1)\Delta x_2$. A chemical pattern with a positive gradient has $|m_1| < |m_2|$, so $|\Delta x_1| > |\Delta x_2|$ and the droplet overall moves to the right, as observed numerically. If the gradient is negative the opposite behaviour is observed.

When the left contact point $x_1(t)$ reaches the minimum of the chemical pattern located around $x = 2.5$ [see Fig. 3.10(a)] a different dynamic behaviour is observed, in which the right contact point x_2 starts to move to the right in the same direction as x_1 (see t_5 – t_8 in Fig. 3.10). This is a consequence of the amplitude gradient of the wetting

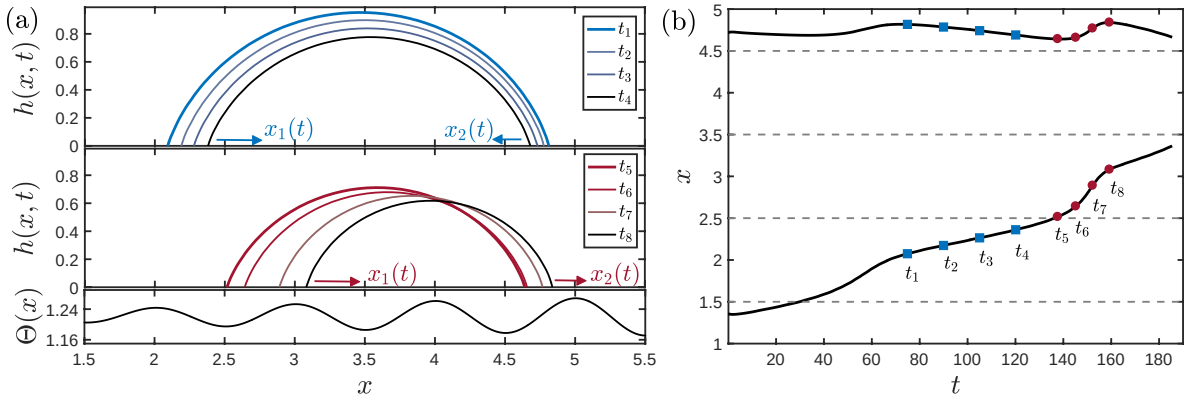

Fig. 3.10 (a) Droplet profiles at different times of the numerical simulations shown in the left panel of Fig. 3.8(c). Numerical times are $t_1 = 75$, $t_2 = 90$, $t_3 = 105$, $t_4 = 115$, $t_5 = 138$, $t_6 = 145$, $t_7 = 152$, and $t_8 = 159$. The bottom graph shows the asymmetric chemical pattern. Panel (b) shows the evolution of the droplet's contact points, $x_1(t)$ (bottom curve) and $x_2(t)$ (top curve). The times shown in panel (a) are marked with solid squares and circles for reference. Dashed lines denote the location of the minima of the wetting pattern.

pattern, and in particular of the difference between its minimum values. Let Θ_1 and Θ_2 be the minima located at around $x = 2.5$ and $x = 4.5$, respectively. As $x_1(t)$ passes through Θ_1 and $x_2(t)$ approaches Θ_2, because $\Theta_1 > \Theta_2$ there is an energy barrier that prevents x_2 to move further to the left. Therefore, both contact points can only move to the right as the droplet evaporates. (And the opposite behaviour is observed with a negative amplitude gradient.) By setting $L = 0.6$ and keeping the same numerical domain size we approach the limit described in Fig. 3.6(c) of Section 3.1.4, in which the chemical pattern is nearly symmetric. Figures 3.11(a,b) show the trajectories of the droplet's midpoint and footprint as function of the droplet size, respectively. We can recognise the presence of turning points on the $\ell(A)$ trajectory (see gray lines in Fig. 3.11(a)) leading to a rapid change in both the droplet's midpoint and footprint, similar to the snap events observed under symmetric patterns. However, because there is now a symmetry breaking the change in droplet's location is induced by imperfect pitchfork bifurcations. Hence, all movements are directed towards the same direction allowing for a better control of droplet's position.

The presence of snap events is clearly demonstrated in Fig 3.11(c), where we plot the speed of the droplet's midpoint, $v(t) = \dot{\ell}(t)$. We can see that droplet's lateral movements become faster as the droplet size decreases. Decreasing the wavelength of the chemical pattern (but keeping the same initial droplet size, i.e., effectively increasing the dimensionless variable A) leads to a dynamics with a higher rate of lateral shifts, as expected (see Fig. 3.11(d)).

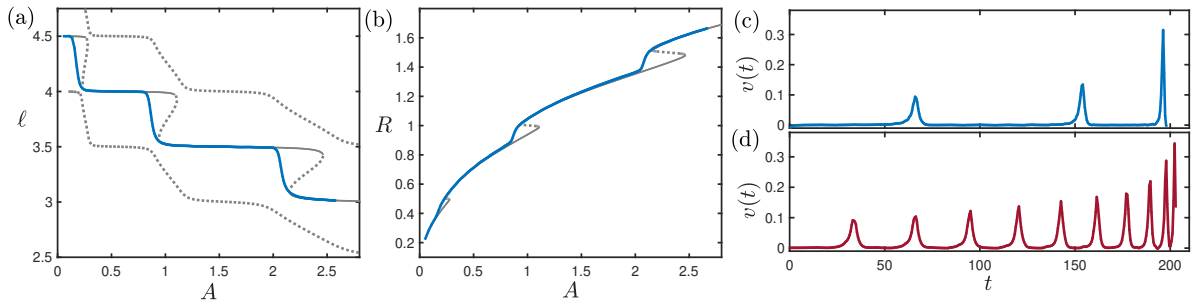

Fig. 3.11 Numerical simulations of the CH-NS system of equations, Eqs. (2.5), chemical pattern given by Eq. (3.19) with $\epsilon = 0.1$ and $L = 0.6$. Panel (a) shows the evolution of the droplet's midpoint as function of its size and the underlying gray lines correspond to the stable solutions predicted by the theory. Panel (b) shows the droplet's footprint versus its size (blue solid line) compared to the theoretical prediction (gray line). Panel (c) shows the speed $v(t)$ of the droplet's midpoint versus time (dashed blue line). Panel (d) shows the same speed but for a chemical pattern with smaller wavelength λ.

Bifurcation	Analytical prediction		Physical consequence
pitchfork	$R_\mathrm{p} = n/2$	$(\epsilon \neq 0)$	symmetry-breaking snap
cusp	$\epsilon_c \sim \beta(\theta_0) A_c^{-1/2}$	$(\epsilon = \epsilon_c)$	multiplicity of solutions
saddle-node	$g(2\pi R_\mathrm{s}) = \beta(\theta_0)/\epsilon$	$(\epsilon > \epsilon_c)$	no symmetry-breaking snap

Table 3.1 Summary of all bifurcations analysed in this work with their associated mathematical prediction, given in terms of the contact radius R_p for the pitchfork bifurcation, the critical amplitude ϵ_c for the cusp bifurcation, and the contact radius R_s for the saddle-node bifurcation. The functions $\beta(\theta_0)$ and $g(x)$ are defined in Eqs. (3.12) and (3.14), respectively. The right column describes the physical consequence of each bifurcation.

3.3 Summary

We have presented analytical and computational results on quasi-static evaporation of a 2D droplet on a flat, chemically patterned surface. We considered patterns that are pinning free but have a smooth and periodic variation of the local equilibrium contact angle. We have shown that symmetric patterns lead to a hierarchy of bifurcations in the three-dimensional parameter space represented by the droplet's cross sectional area, midpoint, and footprint. For an amplitude ϵ of the chemical pattern smaller than a critical value ϵ_c the nodes of the network correspond to pitchfork bifurcations that mark transitions between stable and saddle points. For $\epsilon > \epsilon_c$ a cusp bifurcation occurs leading to multiplicity of solutions and the emergence of turning points that mark the onset of saddle-node bifurcations. A summary of all bifurcations is presented in Table 3.1.

A detailed bifurcation analysis has revealed that pitchfork bifurcations occur at well defined locations of the chemical pattern, which are independent of the homogeneous contact angle and amplitude of the chemical variation. We have also shown that the amplitude critical value scales with the droplet's size as $\epsilon_c \sim A_c^{-1/2}$, hence suggesting that cusp bifurcations are favoured in the microscopic limit. Introducing a bias in the chemical pattern leads to a topological change in the bifurcation diagrams, whereby equilibrium solutions are characterised by disconnected branches in the parameter space. Such branches, which can be either stable or saddle points, are continuously parametrised by the droplet's midpoint, i.e. $\ell(A)$, implying that changing the droplet's size may lead to a continuous lateral displacement.

We have studied droplet dynamics upon evaporation by making use of the Cahn-Hilliard and Navier-Stokes system of equations. Periodic and symmetric patterns lead to a sequence of events where the droplet exhibits rapid lateral movements when its

cross-sectional area reaches the pitchfork bifurcations predicted by the theory, which mark a transition from a stable state to a saddle node. As a consequence of numerical noise the droplet's plane symmetry can be broken, hence triggering lateral motion via a symmetry-breaking snap. It is important to note that if the plane symmetry was not broken the pitchfork bifurcation could be bypassed hence leading to a snap with no symmetry breaking, whereby the droplet would remain on the same location while its radius undergoes a rapid change. Our results show that the *snap evaporation* reported on non-planar symmetric substrates [34] is also observed on planar surfaces with symmetric chemical patterns, and in both cases, this is a consequence of a hierarchy of pitchfork and saddle-node bifurcations.

In asymmetrical chemical patterns, the presence of disconnected branches leads to a smooth droplet's motion where its location continuously changes towards one direction, hence showing that droplet's motion can be controlled upon evaporation. We have established that this is a consequence of the local gradient of the wetting pattern, which is different on each contact point, and the difference between minima of the chemical pattern. Such bias leads to an effective droplet's lateral motion towards regions of higher amplitude. In the limit of weak bias, the droplet dynamics is characterised by snap events but because of the slight symmetry breaking of the chemical pattern, they always occur towards the same direction. We have also shown that the maximum droplet's speed during a snap event increases as the droplet's size decreases. In the next chapter we focus on quantifying the dynamics of such snap events.

Chapter 4

Snap dynamics

In the previous chapter, we have shown that a droplet evaporating on smooth periodic patterns may exhibit rapid changes in its position as its footprint approaches the minima of the wetting pattern. We have referred to these events as snaps, which were dictated by the underlying bifurcation arising due to the wetting pattern. Here we perform a series of simulations to examine how the wetting strength ϵ, and the droplet properties such as its size A, inertia effects, viscosity and surface tension affect the speed and duration of the snaps. This is done by solving the Cahn-Hilliard and Navier-Stokes (CH-NS) system of equation considering the wetting pattern:

$$\mathcal{F}(x) = \frac{2}{\pi} \arctan\left(\frac{x}{L}\right) \cos(2\pi x), \tag{4.1}$$

with amplitude gradient so that the droplet always move to the right. The value of L is taken to be 0.6, which ensures a small bias in the wetting pattern that makes the droplet always to move to the right (positive x). The homogeneous contact angle is taken to be 70°. To simplify our analysis, we consider the Ohnesorge number defined as $Oh = \frac{\mu}{\sqrt{\sigma \rho L}}$ which is a dimensionless number that relates the viscous forces to inertia and surface tension forces. It is related to the Reynolds and Weber numbers as follows:

$$Oh = \frac{\sqrt{We}}{Re}.$$

4.1 Effect of wetting strength

We first study the effect of the strength of the wetting pattern on the speed and duration of the snaps. A droplet evaporating on a flat surface with periodic wetting pattern (4.1) snaps as the droplet reaches the point where its stability changes from stable to a saddle

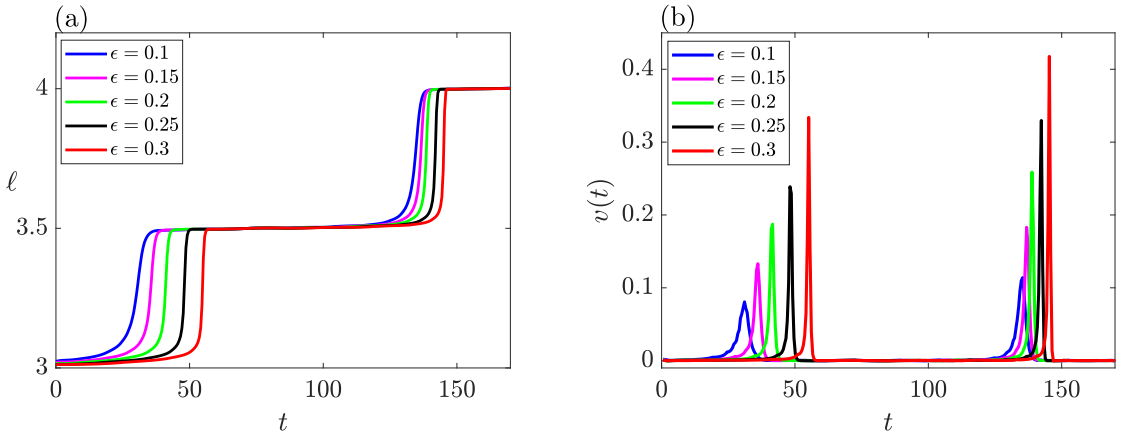

Fig. 4.1 Numerical simulations of the CH-NS system of equations, with chemical pattern given by Eq. (4.1) with $L = 0.6$. Panel (a) shows the evolution of the droplet's midpoint as function of time for different wetting strength. Panel (b) shows the speed $v(t)$ of the droplet's midpoint versus time for different values of the wetting strength ϵ.

node. By performing a series of simulation for different wetting strengths solving the CH-NS system of equation, where the Ohnesorge number is taken to be $\sqrt{0.1}$, we obtain the profile of the droplet location and speed as the droplet evaporates. Figure 4.1(a) shows the location of the mid-point of an evaporating droplet as a function of time for different wetting strengths. It is seen that the droplet rapidly changes its location in snap events at distinct times for different wetting strengths, with the droplet snapping earlier when the strength of the wetting pattern is weaker. As the wetting strength becomes stronger the snap is delayed. The speed $v(t)$ of the droplet for the different wetting strengths is shown in Fig. 4.1(b). We see two snap events where the droplet speed rapidly increases from zero until it reaches a peak value and then decreases to zero during a short time compared to the evaporation time. It is seen that the snap speed increases as the wetting strength increases and that the width of the snap speed curves becomes smaller as the wetting strength increases. This gives an indication that the time it takes a droplet to change its location during a snap event decreases as the wetting strength increases.

The point where a droplet snaps can be determined by examining the equilibrium solution of the droplet and its stability. The pitchfork point where the droplet's stability changes from stable to saddle is the point where the droplet snaps. On a symmetric pattern, this has been determined analytically to be $R = n/2$, where $n \in \mathbb{Z}$. However, since we are dealing with an asymmetric pattern in this chapter, the pitchfork points will have to be obtained numerically. Figure 4.2(a) shows the droplet bifurcation diagram and the droplet simulation result in the (A, ℓ) plane for wetting strength $\epsilon = 0.1$. The green

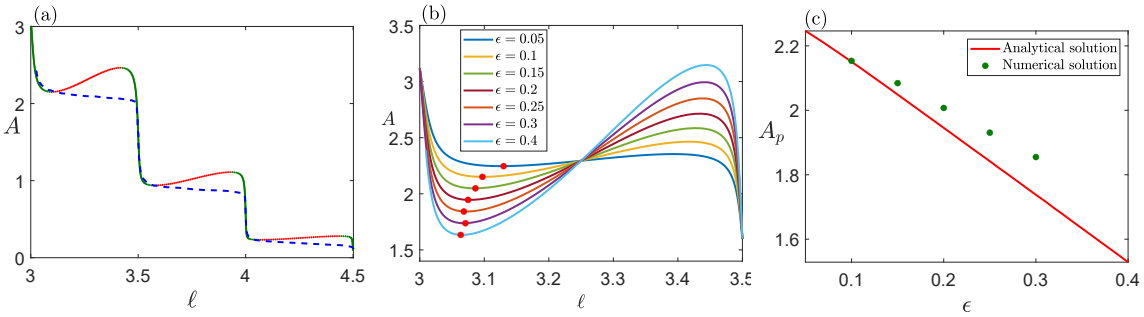

Fig. 4.2 Panel (a) shows the droplet bifurcation diagram and the droplet simulation result in the (A, ℓ) plane for wetting strength $\epsilon = 0.1$. The green lines denote stable solutions while the red lines represent saddle node, the simulation result is represented by the blue dashed lines. Panel (b) shows droplet equilibrium solutions for different wetting strengths ϵ in the (A, ℓ) plane where $\ell \in (3, 3.5)$. The red circles represent the minima of the curves. Panel (c) shows the critical droplet size A_p where the droplet snaps as a function of the wetting strength. Red line and green circles denote theoretical and simulation results respectively.

lines denote stable solutions while the red lines represent saddle node where the droplet is stable to axisymmetric perturbations but unstable against lateral displacements. Hence as the stability of an evaporating droplet changes from stable to saddle node at the pitchfork point, it snaps. This is confirmed by simulation result represented by the blue dashed lines. As the droplet size decreases via evaporation it experiences a first snap event where its location changes from $\ell = 3$ to $\ell = 3.5$. The pitchfork point in this region can be obtained by numerically extracting the minimum of the bifurcation curve. Figure 4.2(b) shows droplet equilibrium solutions for different wetting strengths ϵ in the (A, ℓ) plane where $\ell \in (3, 3.5)$. The minima of these curves corresponding to the pitchfork points where the droplet snaps are represented by red circles. This critical droplet size where the stability of a droplet changes from stable to saddle nodes can be plotted as a function of wetting strength to see how they are related.

Figure 4.2(c) shows the plot of the critical droplet size A_p, corresponding to the minima of the bifurcation curves, where the droplet snaps, as a function of the wetting strength. Red line and green circles denote theoretical and simulation results respectively. It is seen that the critical droplet size A_p decreases as the wetting strength increases and that there is a qualitative agreement between theoretical and simulation results. The slight quantitative disparity between the results, which increases as the wetting strength increases, is only due to numerical noise that makes droplets snap near the pitchfork point but not exactly at the pitchfork point. A droplet evaporating on a flat surface with wetting pattern snaps at lower droplet sizes as the wetting strength increases. Also since

the droplet size decreases with time, it follows that the time interval between when a droplet starts evaporating and when it snaps increases with the wetting strength. This implies that we can control the droplet size and the time when a snap occurs by varying the wetting strength.

The time during which the droplet changes its location, which we call snap time τ defined as the difference between the time t_1 when a droplet starts moving at the minimum or maximum of the wetting pattern, and the time t_2, when it stops moving at the maximum or minimum of the wetting pattern. To extract these times, we define a cut off speed $v_c = 0.01$ and define t_1 and t_2 as the points when the line v_c intersects the speed profiles in Fig. 4.1(b). Figures 4.3(a, d) show the logarithmic plot of the snap time as a function of the wetting strength. The red circles denotes simulation results while the blue lines represent linear curves fitted to the simulation data. It is seen that the snap time decreases as the wetting strength increases. The implication of this is that we can determine the duration it takes a droplet to change its location in a snap event by varying the wetting strength.

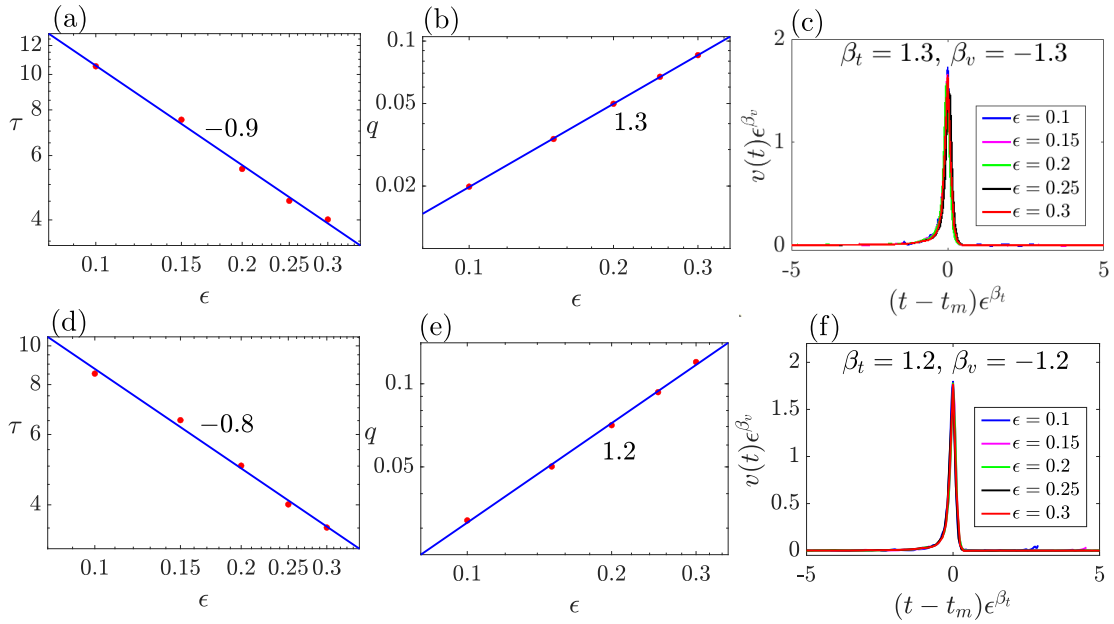

Fig. 4.3 Numerical simulations of the CH-NS system of equations, with chemical pattern given by Eq. (4.1) with $L = 0.6$. Panels (a, d) show snap time τ as a function of wetting strength ϵ. Panels (b, e) show the quantity q defined as $q = \int_0^\tau v(t)^2\, dt$, versus wetting strength. Red circles denotes simulation results while the blue lines represent the linear curves fitted to the simulation data. Panels (c, f) show speed profiles $(v(t), t)$ rescaled as $(v(t)\epsilon^{\beta_v}, (t - t_m)\epsilon^{\beta_t})$. The time where the droplet attains its maximum speed is denoted as t_m and $\beta_t = -\beta_v = 1.3$, and 1.2 for the first and second snap events respectively.

By defining the quantity $q = \int_0^\tau v(t)^2\, dt$, that quantifies the snap speed, so that the average speed is $v_{avg} = \sqrt{q/\tau}$, the effect of the wetting strength on the snap speed can be studied. Figures 4.3(b, e) show the plot of q as a function of the wetting strength. The red circles denotes simulation results while the blue lines represent linear curves fitted to the simulation data. This reveals that q increases as the wetting strength ϵ becomes stronger according to $q \sim \epsilon^{m_1}$, where $m_1 = 1.3$ and 1.2 for the first and second snap events respectively. This means that the snap speed can be controlled by tuning the wetting strength.

The shapes of the speed profiles $v(t)$ during snap events for different wetting strengths look similar and as a result can be rescaled by defining the following variables in terms of the wetting strength ϵ:

$$t^* = (t - t_m)\epsilon^{\beta_t},$$
$$v(t)^* = v(t)\epsilon^{\beta_v},$$

where t_m is the time when the droplet speed reaches its peak value. By choosing $\beta_t = m_1$, and $\beta_v = -m_1$, the speed profiles collapse into a single universal curve, (see Fig. 4.3(c, f)). This data collapse reveals that the snap speed is a function of the wetting strength and time (and by extension, the droplet size).

4.2 Effect of droplet properties

We now examine how droplet properties such as its size, surface tension, viscosity and inertia effects affect snap dynamics. This is done computationally by starting evaporation at a large droplet size for wetting strengths $\epsilon = 0.1$, 0.2, and 0.3, and Ohnesorge number $Oh = \sqrt{0.1}$, with small wavelength of wetting pattern $\lambda = 1/24$. Figure 4.4(a) shows the droplet speed as a function of time for $\epsilon = 0.1$. It is observed that, unlike the previous section, there are more snap events where the speed of the droplet rapidly increases. This is because the size of the droplet is larger. Hence the number of snap events a droplet experiences depends on its size. Figure 4.4(b) shows the droplet maximum snap speed as a function of the droplet size for different wetting strengths $\epsilon = 0.1$, 0.2, and 0.3. The circles denotes simulation results while the solid lines represent the linear curve fitted to the simulation data. It is seen that the maximum snap speed increases as the droplet size decreases in all cases but the rate of change differs for different wetting strengths. It is observed that the rate at which the maximum speed changes with respect to the droplet

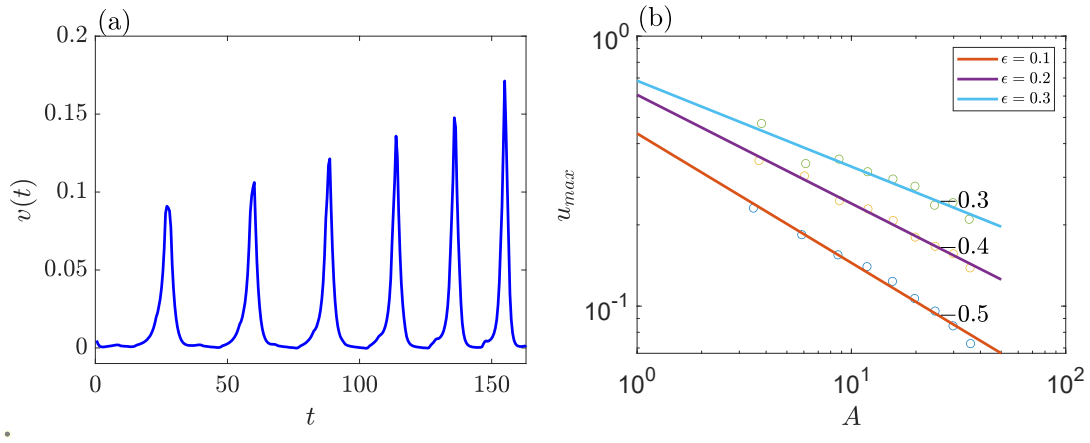

Fig. 4.4 Numerical simulations of the CH-NS system of equations, with chemical pattern given by Eq. (4.1) with $L = 0.6$. Panel (a) shows droplet speed profile for $\epsilon = 0.1$. Panel (b) shows droplet maximum speeds for different droplet sizes and different wetting strengths. The circles denotes simulation results while the solid lines represent the linear curve fitted to the simulation data.

size, becomes smaller as the wetting strength increases. This means that by changing the size of a droplet, its snap speed can be effectively controlled.

In Chapter 2, we saw that the rate at which liquids spread increases with surface tension when its viscosity and inertia effects are fixed. This means that as the surface tension forces becomes stronger, the droplet spreads faster and attains its equilibrium shape quicker. We also saw that when surface tension and inertia effects are held constant, a viscous liquid spreads slower and takes more time to reach its equilibrium configuration. Here we investigate how a droplet's surface tension, its inertia effects and viscosity influence its snap speed and time. To this end, we study the effects of the Ohnesorge number on snap speed while keeping the wetting strength fixed at $\epsilon = 0.1$.

Figure 4.5(a) shows the droplet location for different values of the Ohnesorge numbers. The droplets starts at the same location, which is what we expect since the wetting strength is the same in all cases but reaches the maximum of the chemical pattern at distinct times, with droplets with lower values of the Ohnesorge number reaching a new location earlier than those with higher values. This means that when surface tension and inertia effects are fixed, a more viscous droplet moves slower than a less viscous droplet. The speed of the droplet for different Ohnesorge numbers is shown in Fig. 4.5(b). It is observed that maximum speed decreases as the Ohnesorge number increases. This means that droplets with higher surface tension move faster than droplets with lower values when viscosity and inertia effects are held constant. For fixed inertia effects and surface tension, a viscous droplet moves slower than a less viscous droplet. Also, it is observed

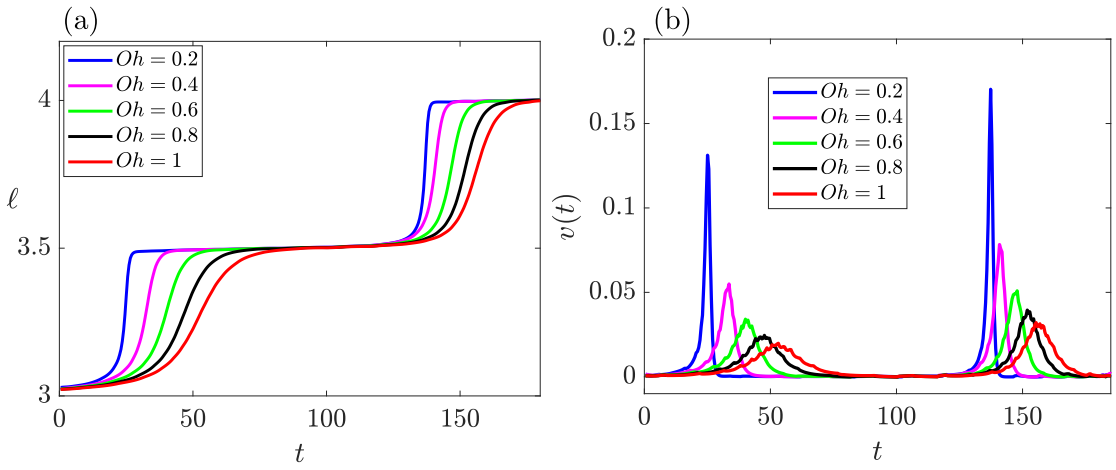

Fig. 4.5 Numerical simulations of the CH-NS system of equations, with chemical pattern given by Eq. (4.1) with $\epsilon = 0.1$ and $L = 0.6$. Panel (a) shows droplet position ℓ as a function of time and panel (b) shows the droplet speeds $v(t)$ for different values Ohnesorge number Oh as a function of time.

that the width of the snap speed curves increases as the Ohnesorge number increases. This suggests that the snap time increases with the Ohnesorge number.

Figures 4.6(a, d) show the logarithmic plot of the snap time τ, as a function of the Ohnesorge number. The red circles denote simulation results that has been fitted with linear curves represented by the blue lines. It is seen that the snap time increases as the Ohnesorge number increases, this implies that for a fixed surface tension and inertia effects, a viscous droplet will take more time to change its location during a snap event, while a droplet with high surface tension with fixed viscosity and inertia effects will take less time. Figures 4.6(b, e) show the logarithmic plot of the quantity q during the snap events. It is also observed that q varies inversely as the Ohnesorge number, $q \sim Oh^{-m_2}$ where $m_2 = 1.2$ and 1 for the first and second snap events respectively. This implies that the speed of a droplet increases as it becomes less viscous when its surface tension and inertia effects are fixed. The speed of a droplet also increases as its surface tension becomes stronger when its viscosity and inertia effects are held constant. The speed profiles $v(t)$ can also be rescaled by using the variables defined in terms of the Ohnesorge number Oh:

$$t^* = (t - t_m)Oh^{\beta_t},$$
$$v(t)^* = v(t)Oh^{\beta_v},$$

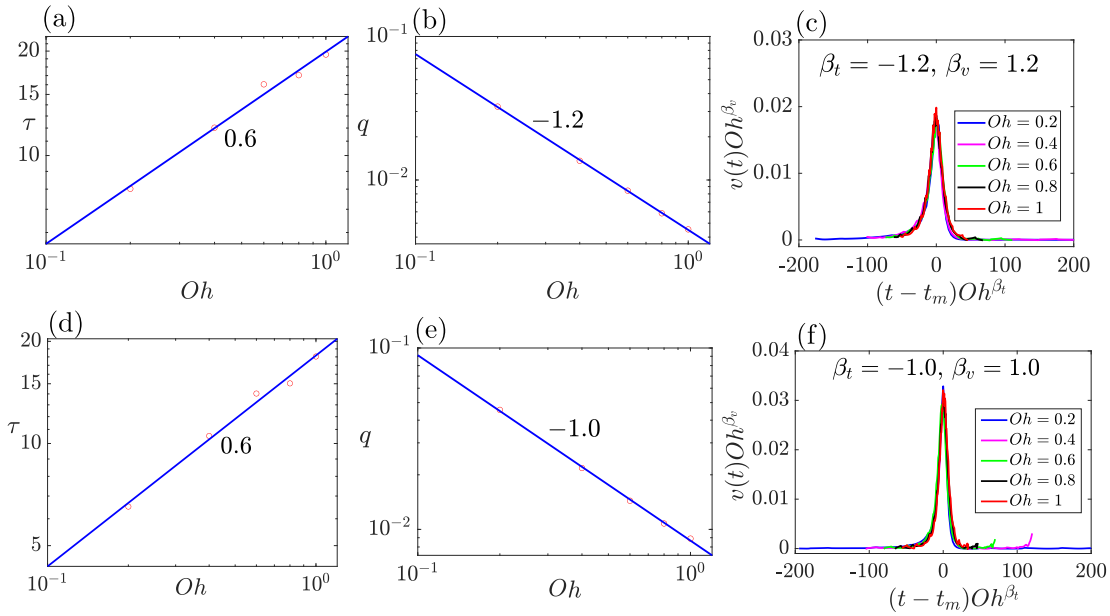

Fig. 4.6 Panels (a, d) show snap time τ as a function of the Ohnesorge number Oh. Panels (b, e) show the quantity q defined as $q = \int_0^\tau v(t)^2\ dt$, versus Ohnesorge number. Red circles denotes simulation results while the blue lines represent linear curves fitted to the simulation data. Panels (c, f) show speed profiles $(v(t), t)$ rescaled as $(v(t)Oh^{\beta_v}, (t - t_m)Oh^{\beta_t})$. The time where the droplet attains its maximum speed is denoted as t_m and $\beta_t = -\beta_v = 1.2$, and 1.0 for the first and second snap events respectively.

and choosing $\beta_t = -m_2$, and $\beta_v = m_2$, so that the speed profiles $v(t)$ collapse into a single universal curve, (see Fig. 4.6(c,f)). This reveals that the snap speed is a function of the Ohnesorge number (i.e. surface tension, inertia effects and viscosity) and time (and by extension, droplet size).

Having understood how the snap speed $v(t)$ is related to the wetting strength ϵ and the Ohnesorge number Oh independently, we can now proceed to find a general scaling law that dictates how both ϵ and Oh are related to $v(t)$. By defining the following variables in terms of the wetting strength ϵ and Ohnesorge number Oh:

$$t^* = (t - t_m)\epsilon^{\beta_3} Oh^{\beta_4},$$
$$v(t)^* = v(t)\epsilon^{\beta_1} Oh^{\beta_2},$$

and choosing $\beta_1 = -m_1$, $\beta_2 = m_2$, $\beta_3 = m_1$, and $\beta_4 = -m_2$, the speed $v(t)$ can be rescaled to obtain a single universal curve for all wetting strengths and Ohnesorge numbers. Figure 4.7 shows the numerical simulations of the CH-NS system of equations, with chemical pattern given by Eq. (4.1) with $L = 0.6$ for an evaporating droplet. The

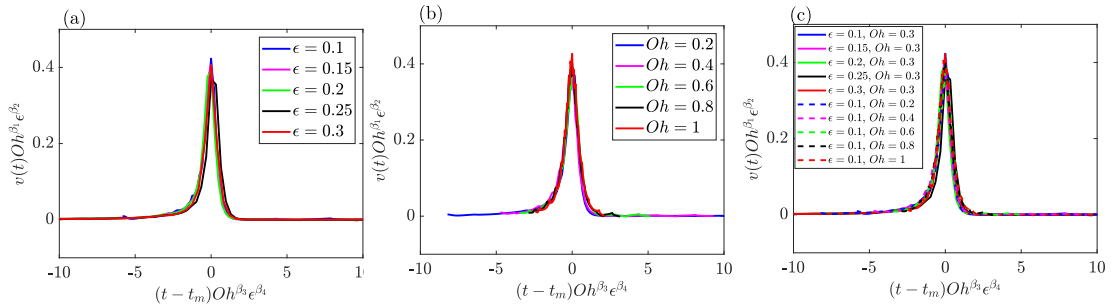

Fig. 4.7 Numerical simulations of the CH-NS system of equations, with chemical pattern given by Eq. (4.1) with $L = 0.6$. Speed profiles $(v(t), t)$ for the first snap event rescaled with the wetting strength ϵ and Ohnesorge number Oh as: $(v(t)\epsilon^{\beta_1}Oh^{\beta_2}, (t-t_m)\epsilon^{\beta_3}Oh^{\beta_4})$. The time where the droplet attains its maximum speed is denoted as t_m and $\beta_1 = -\beta_3 = 1.3$, $\beta_2 = -\beta_4 = 1.2$. Panel (a) shows results for $Oh = 0.3$ for different wetting ϵ. Panel (b) shows results for $\epsilon = 0.1$ for different Oh. Panel (c) shows results for different Oh and ϵ.

speed profiles $(v(t), t)$ for the first snap event is rescaled with the wetting strength ϵ and Ohnesorge number Oh as: $(v(t)\epsilon^{\beta_1}Oh^{\beta_2}, (t-t_m)\epsilon^{\beta_3}Oh^{\beta_4})$. By choosing $\beta_1 = -\beta_3 = 1.3$, $\beta_2 = -\beta_4 = 1.2$ a universal curve is obtained when the Ohnesorge number is fixed and the wetting strength changes, see panel (a), when the wetting strength is fixed and the Ohnesorge number is varied, see panel (b). It is observed that the shape of the speed profile is similar in both cases where the maximum speed is around 0.4. When both the wetting strength and the Ohnesorge number are allowed to vary, all the data collapse into the universal curve, see panel (c).

4.3 Energy balance

The snap dynamics can also be understood by examining the energy balance of the system during the snap process. We note that as shown in Section 2.2.1 of Chapter 2, the Cahn-Hilliard and Navier-Stokes system of equations (2.5) satisfy the following energy law:

$$\frac{dE_T}{dt} + \frac{\mu}{2}\int_\Omega (\boldsymbol{\nabla}\,\mathbf{u}) : (\boldsymbol{\nabla}\,\mathbf{u})\, d\Omega + \int_\Omega M\,|\boldsymbol{\nabla}\,\eta|^2\, d\Omega = 0, \tag{4.2}$$

where

$$E_T = \int_\Omega \frac{\rho\,|\mathbf{u}|^2}{2}\, d\Omega + \mathcal{F}[\phi], \tag{4.3}$$

is the total energy of the system which is the sum of kinetic energy and the free energy. The second and third terms of Eq. (4.2) correspond to the total energy dissipation in the bulk of the fluid due to viscous friction and diffusion respectively. By choosing the

velocity scale to be the capillary velocity, $U = \sqrt{\frac{\sigma}{\rho L}}$, and using :

$$\mathbf{r}^* = \frac{\mathbf{r}}{L}, \quad \mathbf{u}^* = \frac{\mathbf{u}}{U}, \quad t^* = \frac{Ut}{L}, \quad \eta^* = \frac{\eta}{\eta_0}, \quad E_T^* = \frac{E_T}{\sigma}, \tag{4.4}$$

where L is the characteristic length scale and $\eta_0 = \sigma/L$, Eqs. (4.2) and (4.3) are non-dimensionalized as:

$$\frac{dE_T}{dt} + \frac{Oh}{2}\int_\Omega (\boldsymbol{\nabla}\,\mathbf{u}){:}(\boldsymbol{\nabla}\,\mathbf{u})\,d\Omega + \int_\Omega \frac{1}{Pe}\left|\boldsymbol{\nabla}\,\eta\right|^2 d\Omega = 0, \tag{4.5a}$$

$$E_T = \int_\Omega \frac{|\mathbf{u}|^2}{2}\,d\Omega + \mathcal{F}[\phi], \tag{4.5b}$$

where we have used the Ohnesorge number $Oh = \frac{\mu}{\sqrt{\sigma\rho L}}$ which is a dimensionless number that relates the viscous forces to inertia and surface tension forces. Here we are interested in the energy exchanges that occur during the snap process. Since the snap event happens faster than diffusion, we can assume that diffusive contribution to the energy dissipation is negligible, so that Eqs. (4.5) becomes:

$$\frac{d}{dt}\left(\int_\Omega \frac{|\mathbf{u}|^2}{2}\,d\Omega + \mathcal{F}[\phi]\right) = -\frac{Oh}{2}\int_\Omega (\boldsymbol{\nabla}\,\mathbf{u}){:}(\boldsymbol{\nabla}\,\mathbf{u})\,d\Omega. \tag{4.6}$$

Our aim here is to find a relation between the snap speed, the Ohnesorge number and wetting strength. To this end we assume that the velocity profile $\mathbf{u}$ has the same profile throughout the snap process, the magnitude of the velocity $v(t)$ however may vary in time. The velocity can then be written as:

$$\mathbf{u} = v(t)\widetilde{\mathbf{u}(x)}.$$

With this, Eq.(4.6) can be integrated over the snap time τ and noting that the kinetic energy $\int_\Omega \frac{|\mathbf{u}|^2}{2}\,d\Omega$ is zero before and after the snap event, we obtain:

$$\Delta\mathcal{F}[\phi] = -\frac{Oh}{2}\int_0^\tau v(t)^2 dt \int_\Omega (\boldsymbol{\nabla}\,\tilde{\mathbf{u}}){:}(\boldsymbol{\nabla}\,\tilde{\mathbf{u}})\,d\Omega, \tag{4.7}$$

where $\Delta\mathcal{F}[\phi]$ is the difference between the free energy of the initial and final droplet positions. Hence we obtain the following relation:

$$q = -2\frac{\Delta\mathcal{F}[\phi]}{OhD}, \tag{4.8}$$

where $q = \int_0^\tau v(t)^2 dt$ and $D = \int_\Omega (\boldsymbol{\nabla}\,\tilde{\mathbf{u}}) : (\boldsymbol{\nabla}\,\tilde{\mathbf{u}})\, d\Omega$. This implies that q varies inversely as the Ohnesorge number, $q \sim Oh^{-1}$.

A relation between the droplet size and maximum snap speed can be deduced by assuming that all surface energy E available to a droplet of size A is converted to kinetic energy during the snap events: $E = Av_{max}^2/2$, this gives the maximum snap speed as $v_{max} = \sqrt{2E}A^{-1/2}$, so that the velocity increases as the droplet size decreases according to $v_{max} \sim A^{-1/2}$.

It is important to note that the relation derived from the energy balance only agrees qualitatively with the results obtained from numerical simulations. This may be due to the assumptions used on the energy balance. For example, in deriving the relation between the droplet speed and Ohnesorge number $q \sim Oh^{-1}$, we assumed that diffusive contribution to the energy dissipation during the snap event is negligible. A better quantitative agreement between the simulation results and those obtained from the energy balance can however be gotten by relaxing this assumption by including the diffusive contribution. Further analysis is however needed to verify this. Also when obtaining the expression $v_{max} \sim A^{-1/2}$, we assumed that all surface energy E available to a droplet of size A is converted to kinetic energy during the snap events. This is not entirely true as some of the surface energy is dissipated by viscosity. Taking this into account can also facilitate a good quantitative agreement between simulation and energy balance results.

4.4 Summary

In this chapter, the snap dynamics of evaporating droplets on smooth asymmetric pattern has been examined. We have shown that a droplet evaporating on smooth periodic asymmetric patterns may exhibit rapid changes in its position as its footprint approaches the pitchfork points where the stability of the droplet changes from stable to saddle node. We obtain these points numerically and showed that the critical droplet size A_p where snaps occur is related to the wetting strength and that it decreases as the wetting strength increases. This is verified by performing a series of simulations with different wetting strengths, which opens up the possibility of controlling the critical droplet size by tuning the wetting strength. It is also observed that the snap time decreases as the wetting strength increases, $\tau \sim \epsilon^{-k_1}$ while the snap speed increases with the wetting strength, $q \sim \epsilon^{k_2}$, where k_1 and k_2 are constants.

By considering different values of the Ohnesorge number, we see that the snap time increase with the Ohnesorge number, $\tau \sim Oh^{k_3}$ and the snap speed decreases as the

Ohnesorge number increases, $q \sim Oh^{-k_4}$, where k_3 are k_4 are constants. Meaning that the viscosity, inertia effects and surface tension of a droplet affects its snap time and speed.

By considering energy conversion during the snap events under certain assumptions, we conclude that the maximum snap speed is related to the the droplet size according to $v_{max} \sim A^{-1/2}$. We also derived from the dissipation energy law that the quantity q that quantifies the droplet snap speeds obey the following scaling law $q \sim Oh^{-1}$. Hence a general scaling law for the snap time and speed v can be obtained in terms of the wetting strength ϵ, and the Ohnesorge number Oh as:

$$\tau \sim \frac{Oh^{k_3}}{\epsilon^{k_1}},$$
$$v \sim \frac{\epsilon^{k_2}}{Oh^{k_4}}.$$

These results indicates that the snap time and speed can be effectively controlled by varying the wetting strength, droplet size, and by considering different liquids with distinct viscosities, surface tensions and inertia effects.

Chapter 5

Droplet evaporation on non-planar surfaces with chemical patterns

It has been observed that non-planar (or topographic) surfaces promote snap evaporation where evaporating droplets rapidly change their location at pitchfork points [34]. This phenomenon has also been observed on flat surfaces with well defined wetting (or chemical) patterns, (see Chapter 3). Here we investigate the effects of imposing well defined wetting patterns on non-planar surfaces. On such surfaces, the combination of periodic chemical and topographical patterns can either amplify or annihilate snap effects.

5.1 Planar surfaces with chemical patterns

As discussed in Chapter 3, the bifurcation diagram of a droplet evaporating on a planar surface with well defined smooth chemical patterns has branches aligned with the minima and maxima of the chemical patterns and along pitchfork points located at $R = n/2$, where $n \in \mathbb{Z}$. This information can also be extracted by examining the droplet equilibrium condition without constructing the bifurcation diagram. We start by noting that on a flat surface with well defined wetting pattern:

$$\Theta(x) = \theta_0 + \epsilon_C \mathcal{F}(x), \tag{5.1}$$

where θ_0 and ϵ_C are the homogeneous contact angle and amplitude of the periodic function $\mathcal{F}(x)$. The left and right contact angles, denoted by θ_L, and θ_R respectively are

defined as:

$$\theta_L = \Theta(\ell - R), \tag{5.2}$$
$$\theta_R = \Theta(\ell + R). \tag{5.3}$$

At equilibrium, it is required that the left and right contact angles are equal, $\theta_L = \theta_R$, this gives:

$$\mathcal{F}(\ell - R) = \mathcal{F}(\ell + R). \tag{5.4}$$

By choosing $\mathcal{F}(x) = \cos 2\pi x$, (see the top panel Fig. 5.1), Eq. (5.4) is satisfied if:

$$\sin(2\pi\ell)\sin(2\pi R) = 0.$$

This requires either one of $\sin 2\pi\ell$ or $\sin 2\pi R$ to be zero. This gives:

$$\ell = \frac{n}{2}, \quad n = 0, \pm 1, \pm 2, ..., \text{for any } R > 0,$$
$$R = \frac{n}{2}, \quad n = 1, 2, 3, ..., \text{for any } \ell.$$

This confirms that there are equilibrium solutions aligned with the minima and maxima of the chemical pattern and along the pitchfork points, $R_C = n/2$.

The periodic function $\mathcal{F}(x)$ can be chosen as $\sin 2\pi x$, (see the bottom panel of Fig. 5.1), so that the location of its maxima and minima is shifted by $1/4$. In this case, Eq. (5.4) is satisfied if:

$$\cos(2\pi\ell)\sin(2\pi R) = 0,$$

which leads to

$$\ell = \frac{n}{2} + \frac{1}{4}, \quad n = 0, \pm 1, \pm 2, ...\text{for any } R > 0,$$
$$R = \frac{n}{2}, \quad n = 1, 2, 3, ..., \text{for any } \ell.$$

This shows that even though the location of the maxima and minima have been shifted, there are equilibrium solutions aligned with them. Also the pitchfork point is the same regardless of the periodic function imposed on the contact angle. A droplet evaporating on a planar surface with periodic pattern can either be aligned with the minima or maxima of the chemical pattern as its size decreases until it reaches the pitchfork point where it changes its radius and location rapidly in a snap event.

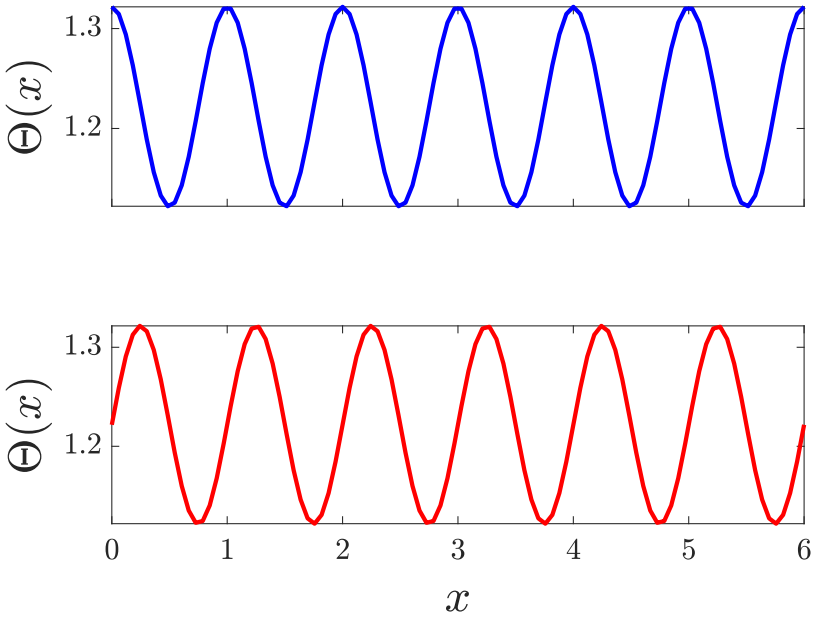

Fig. 5.1 Wetting patterns for $\theta_0 = 70°$, and $\epsilon_C = 0.1$ for periodic functions $\mathcal{F}(x) = \cos 2\pi x$ (Top panel), and $\mathcal{F}(x) = \sin 2\pi x$ (Bottom panel).

5.2 Non-planar surfaces

The same principle can also be applied to a non-planar surface where the equilibrium condition of a droplet on such surface can be explored to gain insight into the evolution of its equilibrium solution. We consider a smooth non-planar surface, (see Fig. 5.2) given as:

$$\zeta(x) = \epsilon_T \cos(kx), \tag{5.5}$$

here $k = \frac{2\pi}{\lambda}$, where ϵ_T and λ are the amplitude and wavelength of the variation, respectively. This topography is smooth in the sense that its wavelength λ is comparable to the droplet radius R. It is important to note that this type of surface is related to rough surfaces which have several engineering applications [66]. Also, by combining several of these sinusoidal patterns, random rough surfaces can be constructed [67].

Equation (5.5) can be non-dimensionalized using the wavelength of the surface variation as a length scale to obtain:

$$\zeta(x) = \epsilon_T \cos(2\pi x). \tag{5.6}$$

The apparent contact angles θ_a at the left and right contact points can be obtained by noting that: $\tan(\theta_e - \theta_a) = \pm\zeta_x|_{\ell \pm R}$, where θ_e, ℓ and R are the equilibrium contact angle,

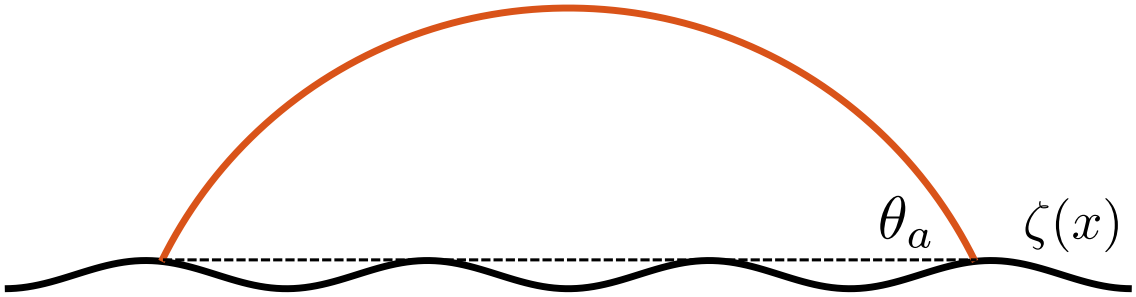

Fig. 5.2 Droplet on a surface $\zeta(x)$. The apparent contact angle θ_a is the angle between the droplet contact line and the horizontal line.

droplet mid-point and contact radius respectively. The equilibrium condition requiring the left and right apparent contact angles to be equal then gives:

$$\sin(2\pi\ell)\cos(2\pi R) = 0.$$

This yields:

$$\ell = \frac{n}{2}, \quad n = 0, \pm1, \pm2, ..., \text{for any } R > 0,$$
$$R = \frac{n}{2} + \frac{1}{4}, \quad n = 0, 1, 2, 3, ..., \text{for any } \ell.$$

This shows that on a non-planar surface $\zeta(x)$, similar to planar surface with chemical patterns, equilibrium solutions are aligned with the minima and maxima of the surface. However the pitchfork points R_T have been shifted by $1/4$, with respect to the pitchfork points R_C on a planar surface with a periodic pattern, that is, $R_T = R_C + 1/4$. As a result, a droplet evaporating on a non-planar surface $\zeta(x)$ can either be aligned with the minima or maxima of the chemical pattern as its size decreases until it reaches the pitchfork point where it changes its radius and location rapidly in a snap event.

The apparent contact angle of a droplet on $\zeta(x)$ can then be obtained by adding the left and right apparent contact angles while noting that they are equal at equilibrium.

$$\theta_a = \theta_e + \tan^{-1}[\epsilon_T 2\pi\cos(2\pi\ell)\sin(2\pi R)]. \tag{5.7}$$

The shape of the droplet $h(x)$ in equilibrium is given by the Young-Laplace equation:

$$\frac{\Delta p}{\gamma} = \kappa = \frac{y_{xx}}{(1 + y_x^2)^{\frac{3}{2}}},$$

where Δp is the change in pressure that occurs upon traversing the boundary between liquid and vapour phases, γ is the surface tension at the liquid-vapour interface and $y(x) = h(x) + \zeta(x)$. With the boundary conditions $y_x(\ell) = y(\ell \pm R) = 0$, the droplet shape $h(x)$ can be obtained as:

$$h(x) = \sqrt{\left(\frac{R}{\sin\theta_a}\right)^2 - (x-\ell)^2} - \frac{R}{\tan\theta_a} + 2\epsilon_T \cos(2\pi\ell))\cos(2\pi R) - \epsilon_T \cos(2\pi x). \quad (5.8)$$

The droplet shape $h(x)$ can be integrated from $\ell - R$ to $\ell + R$ to obtain its cross-sectional area A, as:

$$A = \frac{R^2}{2}\frac{2\theta_a - \sin 2\theta_a}{\sin^2\theta_a} - 2\epsilon_T R\cos(2\pi\ell)\left(\frac{\sin(2\pi R)}{2\pi R} - \cos(2\pi R)\right). \quad (5.9)$$

The equilibrium solutions of a droplet can be obtained by solving for ℓ and R in Eqs. (5.7) and (5.9). The stability of the equilibrium solutions can then be examined by considering the extrema of the interfacial energy given as:

$$E(R,\ell) = \frac{2\theta_a R}{\sin\theta_a} - \int_{\ell-R}^{\ell+R} \cos\theta_e \sqrt{1 + (\epsilon_T 2\pi \sin(2\pi x))^2}\, dx.$$

With the stability of the equilibrium solutions, bifurcation analysis reveals that similar to a flat surface with chemical pattern discussed in Chapter 3, different types of bifurcation emerges as the droplet size is varied via evaporation [34]. These include saddle node and pitchfork bifurcations. Also cusp bifurcation occurs when both the droplet size and the amplitude of the surface are varied and reach a critical value (A_c, ϵ_{Tc}) similar to what is observed on a flat surface with chemical pattern discussed in Section 3.1.3 of Chapter 3, (see the Appendix D for details on this).

5.3 Non-planar surfaces with chemical patterns

We have seen that a droplet evaporating on a planar surface with chemical pattern has equilibrium solutions aligned with the maxima and minima of the chemical pattern and along pitchfork points located at $R = n/2$, where $n \in \mathbb{Z}$. For a non-planar surface $\zeta(x)$, equilibrium solutions are also aligned with minima and maxima of the surface and along pitchfork points which have been shifted by $1/4$. Here we examine how imposing a chemical pattern on a non-planar surface affects the equilibrium solutions and the location of the pitchfork points. Chemical patterns can be imposed on a non-planar

surface $\zeta(x)$ by prescribing a varying contact angle, as follows:

$$\Theta(x) = \theta_0 + \epsilon_C 2\pi \mathcal{F}(x), \tag{5.10}$$

where $\mathcal{F}(x)$ is a generic periodic function, ϵ_C is the chemical variation amplitude, and θ_0 is the homogeneous contact angle. The equilibrium contact angle then becomes $\theta_e = \Theta(\ell \pm R)$, so that the left and right apparent contact angles are modified as: $\tan(\Theta(\ell \pm R) - \theta_a) = \pm\zeta_x|_{\ell \pm R}$. The equilibrium condition that requires the left and right contact angles to be equal gives:

$$2\pi\epsilon_C \mathcal{F}(\ell - R) + \tan^{-1}\left(\zeta_x(\ell - R)\right) = 2\pi\epsilon_C \mathcal{F}(\ell + R) - \tan^{-1}\left(\zeta_x(\ell + R)\right).$$

Let's consider the case of small and equal amplitudes, i.e. $\epsilon_C = \epsilon_T \ll 1$. In this limit the above relation becomes:

$$\mathcal{F}(\ell + R) - \mathcal{F}(\ell - R) = 2 \sin 2\pi\ell \cos 2\pi R. \tag{5.11}$$

If the chemical pattern is chosen as $\mathcal{F}(x) = \cos 2\pi x$ such that it is in phase with the topographical pattern $\zeta(x)$, and out of phase with the apparent contact angle on the topography (see Fig. 5.3(a)), then the equilibrium condition (5.11) becomes:

$$\sin 2\pi\ell \Big(\sin 2\pi R - \cos 2\pi R \Big) = 0.$$

This condition is satisfied if either $\sin 2\pi\ell = 0$ or $\tan 2\pi R = 1$, which gives:

$$\ell = \frac{n}{2}, \quad n = 0, \pm 1, \pm 2, ..., \text{for any } R > 0,$$
$$R = \frac{n}{2} + \frac{1}{8}, \quad n = 0, 1, 2, 3, ..., \text{for any } \ell.$$

This implies that a droplet on a non-planar surface with an in-phase chemical pattern has equilibrium solutions aligned with the minima and maxima of both patterns and along pitchfork points R_{CT} which is located at the mid-point of the pitchfork point of the chemical and topological patterns, $R_{CT} = \frac{R_C + R_T}{2}$. In this scenario the apparent contact angle becomes:

$$\theta_a = \theta_0 + \epsilon_T 2\pi \cos(2\pi\ell) \left[\cos(2\pi R) + \sin(2\pi R)\right], \tag{5.12}$$

this shows that there is an increase in the strength of variation of the apparent contact angle which will lead to more equilibrium solutions for the same droplet size and as a result amplify the snap event.

If the chemical pattern is chosen as $\mathcal{F}(x) = \sin 2\pi x$ such that it is out of phase with the topographical pattern $\zeta(x)$, but is in phase with the apparent contact angle on the topography, (see Fig. 5.3), the equilibrium condition (5.11) becomes:

$$\sin 2\pi(\ell + R) = 0,$$

this gives:

$$\ell + R = \frac{n}{2}, \quad n = 0, \pm 1, \pm 2, ...$$

This means that as the radius of a droplet changes, its location also changes, hence a droplet evaporating on a topography with an out-of-phase wetting pattern, changes its location continuously. In this case, the apparent contact angle becomes the homogeneous contact angle, implying that the topographical and chemical pattern cancels out and annihilate the snap event.

5.3.1 Bifurcation analysis

On a non-planar surface with chemical patterns, equilibrium solutions can either be amplified or annihilated depending on whether the chemical pattern is in phase or out of phase with the surface $\zeta(x)$. Here we perform detailed bifurcation analysis to investigate this. We first note that the interfacial energy is modified as:

$$E(R, \ell) = \frac{2\theta_a R}{\sin\theta_a} - \int_{\ell-R}^{\ell+R} \cos\Theta(x)\sqrt{1 + (\epsilon_T 2\pi \sin(2\pi x))^2}dx.$$

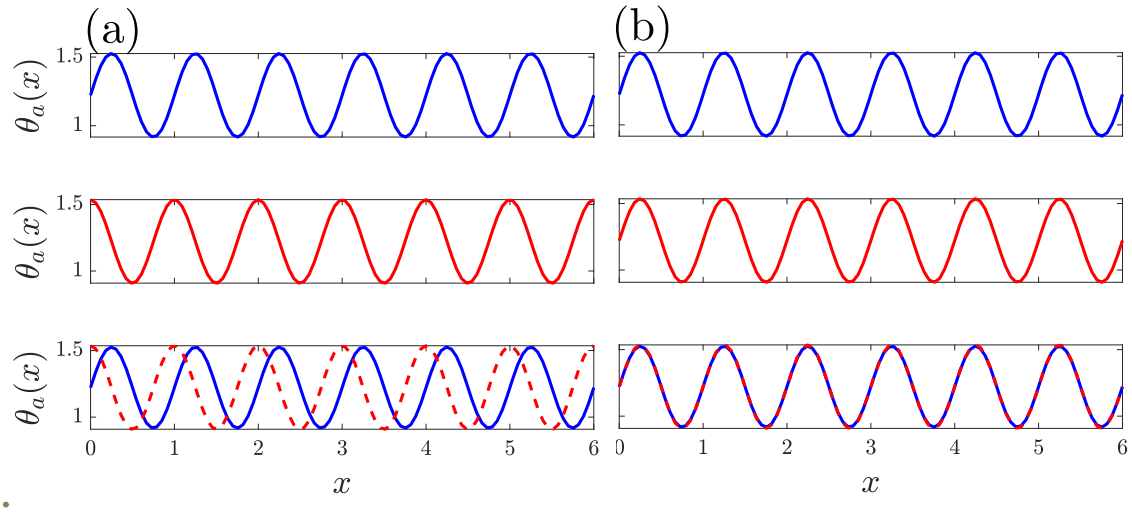

Fig. 5.3 Apparent contact angles for topography (blue lines) and chemical (red lines) patterns (a) out of phase, and (b) in phase.

We then start by considering a case where the wetting pattern is in phase with surface pattern and out of phase with the apparent contact angle on the surface by choosing $\mathcal{F}_1(x) = \cos(2\pi x)$, with this, the contact angle is given by Eq. (5.12):

$$\theta_a = \theta_0 + \epsilon_T 2\pi \cos(2\pi\ell)\left[\cos(2\pi R) + \sin(2\pi R)\right].$$

Hence we see that when the chemical and topographic patterns are in phase, the wetting strength of the surface is increased leading to the emergence of more equilibrium solutions.

Figure 5.4(a) shows energy landscape alongside the equilibrium solutions of a droplet of size $A = 1.6$, on a non-planar surface given by Eq. (5.6) with $\epsilon_T = 0.05$. There are stable solutions aligned with the minimum and maximum of the surface pattern denoted

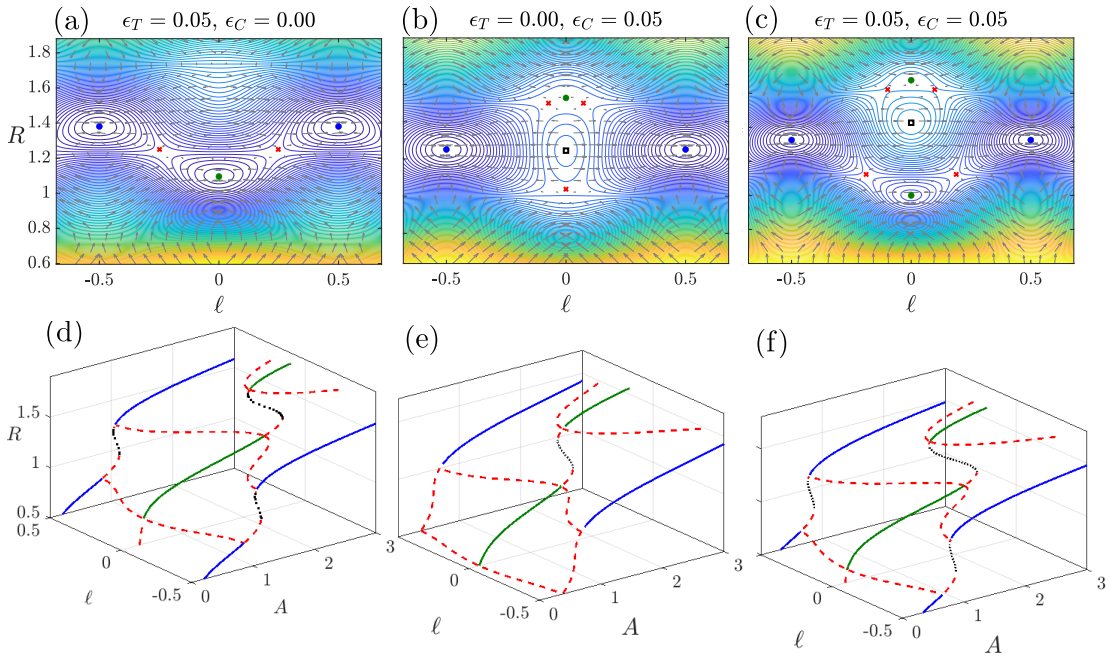

Fig. 5.4 Amplification of equilibrium solutions. Energy landscape and equilibrium solutions of a droplet of size $A = 1.6$, (a) on a non-planar surface given by Eq. (5.6) with $\epsilon_T = 0.05$; (b) on a planar surface with periodic wetting pattern given by Eq. (5.10), where $\mathcal{F}_1(x) = \cos(2\pi x)$ with $\epsilon_C = 0.05$; (c) on a non-planar surface imposed with wetting pattern $\mathcal{F}_1(x) = \cos(2\pi x)$. Blue and green circles correspond to stable equilibrium solutions, crosses to saddle nodes and empty black squares correspond to unstable solutions. Panels (d-f) show the corresponding $3D$ bifurcation diagrams for different droplet sizes. Solid green and blue lines denote stable solutions aligned with the minima and maxima of the patterns respectively. Red dashed lines represent saddle-nodes and black dots denote unstable solutions

by green and blue circles respectively, and saddle nodes in between the minimum and maximum of the surface denoted by red cross. On a planar surface with periodic wetting pattern given by Eq. (5.10), where $\mathcal{F}_1(x) = \cos(2\pi x)$ with $\epsilon_C = 0.05$, (see Fig. 5.4(b)), there are also stable and saddle nodes, additionally, there is an unstable point denoted by a black square. When a wetting pattern is imposed on a non-planar surface, there is a combination of the equilibrium solutions from the non-planar surface and wetting pattern, (see Fig. 5.4(c)). Panels (d-f) show the $3D$ bifurcation diagram for different droplet sizes on a topography $\zeta(x)$, on a flat surface with wetting pattern $\mathcal{F}_1(x)$, and on a topography $\zeta(x)$ with chemical pattern $\mathcal{F}_1(x)$. It is seen that there are more equilibrium solutions when the chemical pattern is combined with topography, hence a droplet evaporating on such surface will experience an amplified snap event as it approaches the pitchfork point.

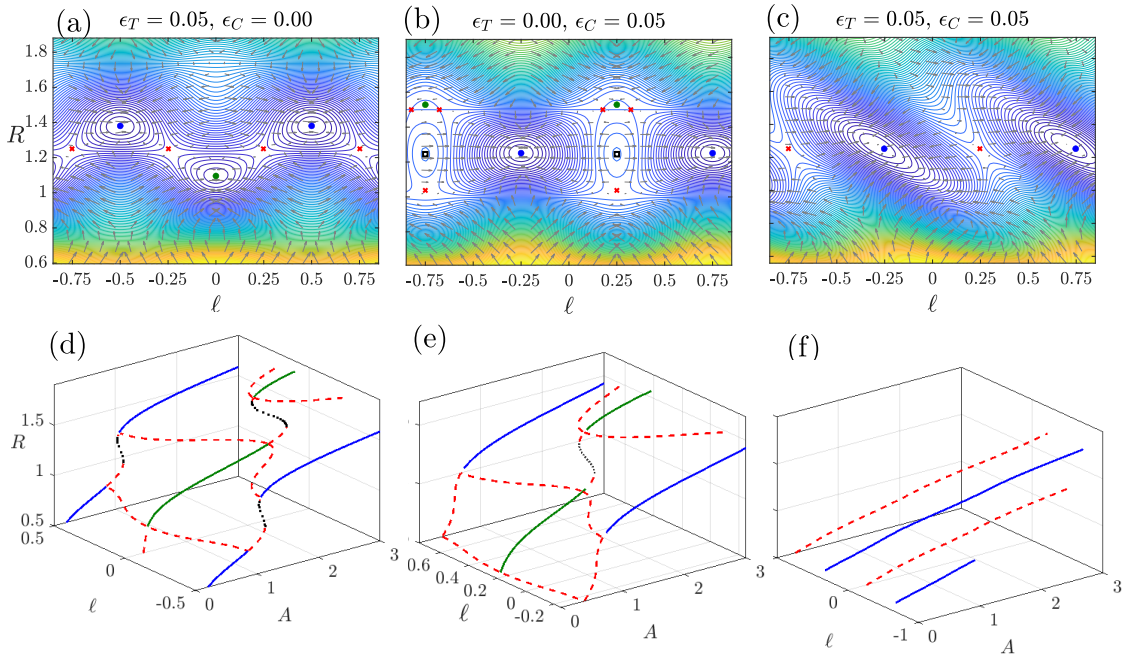

Fig. 5.5 Annihilation of equilibrium solutions. Energy landscape and equilibrium solutions of a droplet of size $A = 1.6$, (a) on a non-planar surface given by Eq. (5.6) with $\epsilon_T = 0.05$; (b) on a planar surface with periodic wetting pattern given by Eq. (5.10), where $\mathcal{F}_2(x) = \sin(2\pi x)$ with $\epsilon_C = 0.05$; (c) a non-planar surface imposed with wetting pattern $\mathcal{F}_2(x) = \sin(2\pi x)$. Blue and green circles correspond to stable equilibrium solutions, crosses to saddle nodes and empty black squares correspond to unstable solutions. Panels (d-f) show the corresponding $3D$ bifurcation diagrams for different droplet sizes. Solid green and blue lines denote stable solutions aligned with the minima and maxima of the patterns respectively. Red dashed lines represent saddle-nodes and black dots denote unstable solutions.

By choosing $\mathcal{F}_2(x) = \sin(2\pi x)$, the topographic and chemical patterns are out of phase, but the apparent contact angle on the surface is in phase with the chemical pattern. In the limit of $\epsilon_C = \epsilon_T \ll 1$, the apparent contact angle becomes: $\theta_a = \theta_0$. We see that when the topographic, (see Fig. 5.5(a, d)) and chemical patterns, (see Fig. 5.5(b, e)) are out of phase, equilibrium solutions are annihilated, (see Fig. 5.5 (c, f)) and the pitchfork branches disappear so that the solutions aligned with the maxima and minima of the patterns are now disconnected leaving only a stable point aligned with the minima and a saddle node aligned with the maxima. As a result, an evaporating droplet is unable to change its location rapidly as it approaches the minima or maxima of the surface or chemical pattern, rather its location and radius gradually changes simultaneously as its size decreases.

5.4 Droplet evaporation

In this section, we present numerical simulations of the CH-NS system of equations for a droplet evaporating on non-planar surfaces with chemical patterns. As we have done in Chapters 3 and 4, we assume a quasi-static evaporation that is driven by mass diffusion in the gas phase, as is discussed in Chapter 2.

We start by considering an evaporating droplet on a topographic surface $\zeta(x)$, with $\epsilon_T = 0.05$, following Gary et al [34]. We also consider a flat surface with well defined wetting pattern $\mathcal{F}_1(x) = \cos(2\pi x)$ with strength $\epsilon_C = 0.05$, in phase with the surface $\zeta(x)$. Figures 5.6(a, b) show the droplet footprint R, and location ℓ as it evaporates on a non-planar surface $\zeta(x)$, (blue solid line) and on a flat surface with wetting pattern $\mathcal{F}_1(x)$, (red solid line). It is seen that the droplet radius and location rapidly changes in a snap event at the pitchfork points in both cases. The topographic and chemical patterns can be combined by imposing the wetting pattern $\mathcal{F}_1(x)$ on the non-planar surface $\zeta(x)$. In this scenario, the droplet snaps at lower sizes than when the wetting pattern $\mathcal{F}_1(x)$ is imposed on the non-planar surface $\zeta(x)$ and the snap speed is amplified (see Fig. 5.6(c)). This means that the snap dynamics can be amplified by adding a chemical pattern to a non-planar surface as dictated by the bifurcation analysis in the previous section.

When a wetting pattern $\mathcal{F}_2(x) = \sin(2\pi x)$ which is out of phase with the non-planar surface $\zeta(x)$ is imposed, the droplet footprint R and location ℓ gradually changes, with the droplet moving to the right when $\epsilon_C > 0$ and to the left when $\epsilon_C < 0$, (see Fig. 5.7(a, b)). This implies that the direction of droplet motion during evaporation on a non-planar surface can be controlled by imposing an out-of-phase chemical pattern. Figure 5.7(c) shows that on a such surfaces, the snap speed is annihilated as dictated by the bifurcation

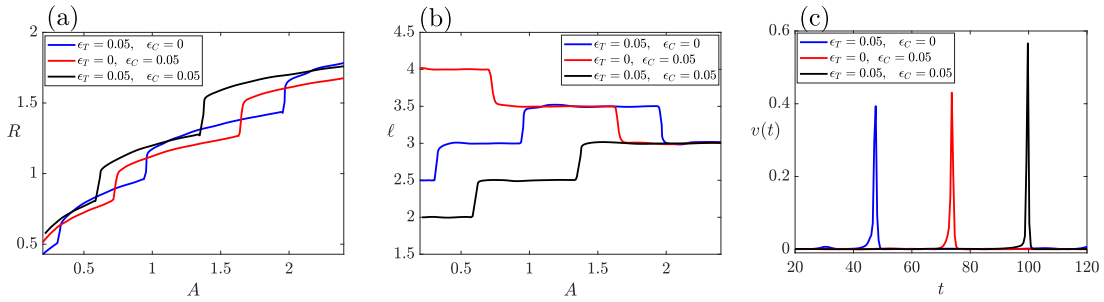

Fig. 5.6 Numerical simulations of the CH-NS system for droplets on non-planar surface (5.2) with symmetric pattern $\mathcal{F}_2(x) = \cos(2\pi x)$, with homogeneous contact angle $\theta_0 = 70°$ for different wetting strengths on (a) (R, A) (b) (ℓ, A), and (c) $(v(t), t)$ diagrams.

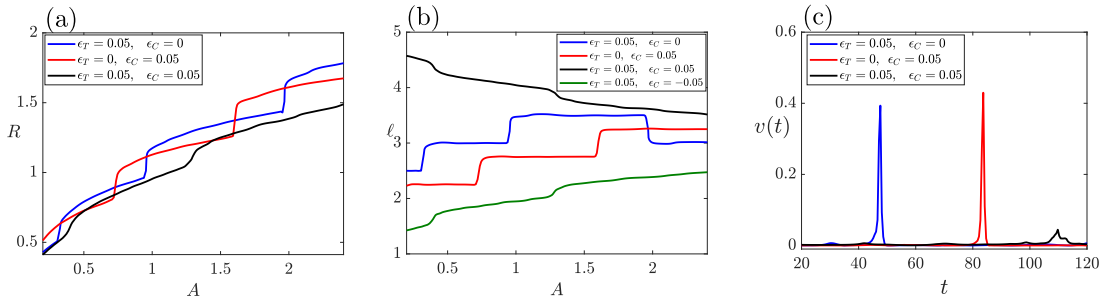

Fig. 5.7 Numerical simulations of the CH-NS system for droplets on non-planar surface (5.2) with symmetric pattern $\mathcal{F}_2(x) = \sin(2\pi x)$, with homogeneous contact angle $\theta_0 = 70°$ for different wetting strengths on (a) (R, A) (b) (ℓ, A), and (c) $(v(t), t)$ diagrams.

analysis in the previous section. This means that the snap effect can be removed, this will be particularly useful in processes where the snapping of evaporating droplet is undesirable.

These results are in agreement with the bifurcation analysis presented in the previous section. For the case where the chemical and topographic patterns are in phase, the resultant wetting strength of both the chemical and topographic patterns is increased leading to the emergence of more equilibrium solutions. From the previous chapter, we know that a droplet snap speed increases as the wetting strength increase. As a result the snap speed of a droplet evaporating on a topography amplifies when an in-phase chemical pattern is imposed on it. For the scenario where the chemical and topographic patterns are out of phase, the resultant wetting strength becomes zero so that the apparent contact angle θ_a is equivalent to the homogeneous value θ_0, in this case the equilibrium solution becomes one. Hence the snap speed of a droplet evaporating on a topography is annihilated when an out-of-phase chemical pattern is imposed on it.

5.5 Summary

We have seen that on topographies with chemical patterns, the combination of periodic chemical and topographical patterns can either increase or decrease the resultant wetting strength of the surface depending on whether the patterns are in phase or out of phase. If the patterns are in phase, the resultant wetting strength is increased and as a result the droplet snap speed is amplified. On the other hand if the patterns are out of phase the resultant wetting strength becomes zero and as a result the droplet snap speed is annihilated. In this scenario the direction of motion of the droplet as it snaps can be effectively controlled through the sign of the wetting strength. These results imply that evaporating droplets can be controlled on a non-planar surface by imposing a well defined wetting pattern.

Chapter 6

Gravitational effects on sessile droplets: Bifurcation analysis

As the size of a droplet becomes comparable or larger than the capillary length, the effect of gravity becomes stronger and no longer negligible. Here we study how gravity affects the shape of a sessile droplet. We first examine the limiting case of small gravity and perform asymptotic analysis to obtain approximate solutions. However at some droplet sizes, these asymptotic solutions become non-physical. To overcome this, we derive exact solutions which lead to elliptic integrals which can only be solved numerically. By examining the stability of the equilibrium solutions, we perform detailed bifurcation analysis.

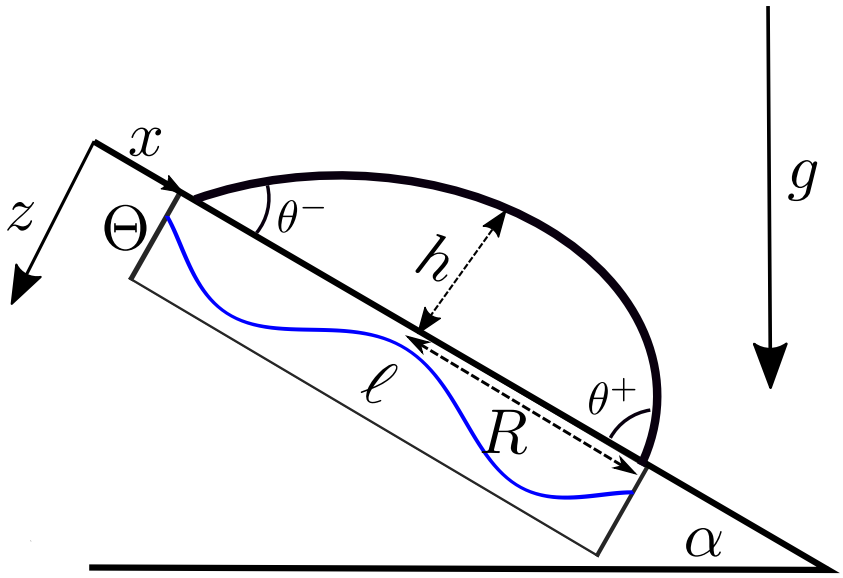

Fig. 6.1 Droplet on a smooth inclined chemically heterogeneous surface.

We start by considering a droplet of size A on a surface with a periodic wetting pattern Θ, inclined with the horizontal at an angle α, (see Fig. 6.1). The upper and lower contact angle are denoted by θ^- and θ^+ respectively. The droplet interface height is h and the mid point and contact radius of the droplet are represented by ℓ and R respectively. The contact angle along the x direction is prescribed by $\Theta(x)$, which we take to be:

$$\Theta(x) = \theta_0 + \epsilon\mathcal{F}(x;\lambda). \tag{6.1}$$

Here, θ_0 is the homogeneous contact angle, ϵ and λ are the amplitude and wavelength of a generic periodic spatially-dependent function $\mathcal{F}(x)$ respectively. This enables us to define our upper and lower contact angles as: $\theta^- = \Theta(\ell - R)$ and $\theta^+ = \Theta(\ell + R)$ respectively. The gravitational force in this coordinate system can be expressed as

$$\boldsymbol{g} = g(\sin\alpha, \cos\alpha), \tag{6.2}$$

where g is the acceleration due to gravity.

6.1 Equilibrium shapes

For a stationary sessile droplet of density ρ, the gradient of the pressure P is balanced by gravitational force:

$$\nabla P = \rho\mathbf{g}, \tag{6.3}$$

which in two dimension $(2D)$ reads:

$$\frac{\partial P}{\partial x} = \rho g \sin\alpha,$$
$$\frac{\partial P}{\partial z} = \rho g \cos\alpha.$$

Integrating this gives the pressure in the droplet as:

$$P = \rho g(x\sin\alpha + h\cos\alpha) + P_0, \tag{6.4}$$

where P_0 is a constant. The Young-Laplace equation is given as:

$$\Delta P = \gamma\kappa, \tag{6.5}$$

here $\Delta P = P - P_{atm}$, where P is defined by Eq. (6.4) and P_{atm} is the atmospheric pressure outside the droplet. The surface tension at the liquid-gas interface is denoted as

γ and κ is the droplet's curvature which is given as:

$$\kappa = -\frac{h_{xx}}{(1+h_x^2)^{\frac{3}{2}}}, \tag{6.6}$$

where h_x denote the derivative of $h(x)$ with respect to x. Equation (6.5) then becomes:

$$p + \rho g(x\sin\alpha + h\cos\alpha) = \gamma\kappa, \tag{6.7}$$

where $p = P_0 - P_{atm}$. We non-dimensionalize Eq. (6.7) by choosing the following dimensionless variables:

$$x^* = \frac{x}{L}, z^* = \frac{z}{L}, \kappa^* = \kappa L, p^* = \frac{p}{P'}, \tag{6.8}$$

where L and P' are the length and pressure scales respectively. The length scale L is taken to be the wave length λ of the pattern. Inserting Eq. (6.8) into Eq. (6.7) and assuming $P'L \sim \gamma$ gives:

$$p + B(x\sin\alpha + h\cos\alpha) = \kappa, \tag{6.9}$$

where the asterisks have been dropped and $B = \frac{\rho g L^2}{\gamma}$ is the Bond number which defines the ratio between the gravitational force and surface tension. Substituting κ in Eq. (6.9) gives:

$$p + B(x\sin\alpha + h\cos\alpha) = -\frac{h_{xx}}{(1+h_x^2)^{\frac{3}{2}}}. \tag{6.10}$$

Our aim is to solve Eq. (6.10) subject to the following boundary conditions:

$$h(\ell - R) = h(\ell + R) = 0, \tag{6.11a}$$

$$h_x(\ell - R) = \tan\theta^-, \tag{6.11b}$$

$$h_x(\ell + R) = -\tan\theta^+. \tag{6.11c}$$

It is possible to obtain the droplet size A, by integrating Eq. (6.9) from $\ell - R$ to $\ell + R$ subject to the boundary conditions, Eqs. (6.11):

$$B(2\ell R\sin\alpha + A\cos\alpha) + 2Rp = \sin\theta^- + \sin\theta^+. \tag{6.12}$$

Equation (6.10) and (6.12) can be solved together with Eqs. (6.11) to obtain the droplet shape $h(x)$. We proceed by introducing the arc-length s and inclination ϕ as follows:

$$\frac{dx}{ds} = \cos\phi, \tag{6.13a}$$

$$\frac{dh}{ds} = \sin\phi. \tag{6.13b}$$

The curvature κ in this definition then becomes:

$$\frac{d\phi}{ds} = p + B(x\sin\alpha + h\cos\alpha). \tag{6.14}$$

To simplify our problem, we can write Eqs. (6.13) in terms of the inclination alone:

$$\frac{dx}{d\phi} = \frac{\cos\phi}{p + B(x\sin\alpha + h\cos\alpha)}, \tag{6.15a}$$

$$\frac{dh}{d\phi} = \frac{\sin\phi}{p + B(x\sin\alpha + h\cos\alpha)}. \tag{6.15b}$$

Given a droplet of size A on a surface with wetting pattern of strength ϵ inclined at an angle α to the horizontal and Bond number B, we aim to solve for x, h, p, ℓ and R, subject to the boundary conditions:

$$x(\phi = -\theta^-) = \ell - R, \qquad h(\phi = -\theta^-) = 0, \tag{6.16a}$$

$$x(\phi = \theta^+) = \ell + R, \qquad h(\phi = \theta^+) = 0. \tag{6.16b}$$

The solutions to this system may not exist physically, we shall be interested in how the droplet's position and radius are related to the cross-sectional area (equivalent to the volume) of the droplet. For an inclined surface it is important to note that there is a maximum droplet size $A_{\max}$ which can be supported on a surface with chemical pattern, below which the droplet is stationary. When this maximum value is exceeded the droplet begins to move since the chemical pattern can no longer balance the droplet size. This maximum droplet size can be obtained by balancing forces acting along a surface. By considering the pattern $\mathcal{F}(x) = \cos(2\pi x)$, we derive the following relation for the maximum size of a droplet,

$$A_{\max} = \frac{2\sin\Theta_0\sin\epsilon}{B\sin\alpha}. \tag{6.17}$$

A droplet of size $A < A_{\max}$ however, may not have equilibrium solution. This is because the derivation of the condition (6.17) is premised on the assumption that the maximum

and minimum contact angles are achieved simultaneously (by the lower and upper contact angle, respectively), which may not be feasible.

6.2 Microgravity

To understand the effect of gravity on a drop on an inclined plane in the limit of small Bond numbers, we pose perturbation expansions as:

$$x = x_0 + Bx_1 + \mathcal{O}(B^2), \tag{6.18a}$$
$$h = h_0 + Bh_1 + \mathcal{O}(B^2), \tag{6.18b}$$
$$p = p_0 + Bp_1 + \mathcal{O}(B^2), \tag{6.18c}$$
$$\ell = \ell_0 + B\ell_1 + \mathcal{O}(B^2), \tag{6.18d}$$
$$R = R_0 + BR_1 + \mathcal{O}(B^2). \tag{6.18e}$$

Consequently, the upper and lower contact angles can also be written as:

$$\theta^- = \theta_0^- + B\theta_1^- + \mathcal{O}(B^2), \tag{6.19a}$$
$$\theta^+ = \theta_0^+ + B\theta_1^+ + \mathcal{O}(B^2), \tag{6.19b}$$

so that the contact angles are related to the contact radius and mid-point as follows:

$$\theta_0^- = \Theta(\ell_0 - R_0), \tag{6.20a}$$
$$\theta_0^+ = \Theta(\ell_0 + R_0), \tag{6.20b}$$
$$\theta_1^- = \Theta'(\ell_0 - R_0)(\ell_1 - R_1), \tag{6.20c}$$
$$\theta_1^+ = \Theta'(\ell_0 + R_0)(\ell_1 + R_1). \tag{6.20d}$$

Now, we have 5 unknowns (x, h, p, ℓ, R) with 4 conditions Eqs. (6.16), hence the system is under-determined. To solve the system completely, we need an extra condition, which is the given volume of the droplet, which in parametric form, is obtained as:

$$A = -\int_{\ell-R}^{\ell+R} h \;\; dx = -\int_{-\theta^-}^{\theta^+} h \frac{dx}{d\phi} d\phi. \tag{6.21}$$

Expanding in Taylor's series and using the Leibniz integral rule yields:

$$A = -\int_{-\theta_0^-}^{\theta_0^+} h_0 \frac{dx_0}{d\phi} d\phi - B\left(\int_{-\theta_0^-}^{\theta_0^+} \left(h_1 \frac{dx_0}{d\phi} + h_0 \frac{dx_1}{d\phi}\right) d\phi + \theta_1^+ \left(h_0 \frac{dx_0}{d\phi}\right)|_{\phi=\theta_0^+} + \theta_1^- \left(h_0 \frac{dx_0}{d\phi}\right)|_{\phi=-\theta_0^-}\right). \tag{6.22}$$

In our formulation, we fix the droplet's size and investigative how the introduction of gravity changes the droplet's contact radius and midpoint, as a result, the droplet size does not depend on the Bond number, hence:

$$A = -\int_{-\theta_0^-}^{\theta_0^+} h_0 \frac{dx_0}{d\phi} d\phi, \tag{6.23a}$$

$$0 = \int_{-\theta_0^-}^{\theta_0^+} \left(h_1 \frac{dx_0}{d\phi} + h_0 \frac{dx_1}{d\phi}\right) d\phi + \theta_1^+ \left(h_0 \frac{dx_0}{d\phi}\right)|_{\phi=\theta_0^+} + \theta_1^- \left(h_0 \frac{dx_0}{d\phi}\right)|_{\phi=-\theta_0^-}. \tag{6.23b}$$

6.2.1 Leading order solution

Inserting the perturbation expansions into Eqs. (6.15) and the boundary conditions (6.16), we obtain the leading systems as follows:

$$\frac{dx_0}{d\phi} p_0 = \cos\phi, \tag{6.24a}$$

$$\frac{dh_0}{d\phi} p_0 = \sin\phi, \tag{6.24b}$$

$$x_0(\phi = -\theta_0^-) = \ell_0 - R_0, \qquad h_0(\phi = -\theta_0^-) = 0, \tag{6.24c}$$

$$x_0(\phi = \theta_0^+) = \ell_0 + R_0, \qquad h_0(\phi = \theta_0^+) = 0, \tag{6.24d}$$

$$A = -\int_{-\theta_0^-}^{\theta_0^+} h_0 \frac{dx_0}{d\phi} d\phi. \tag{6.24e}$$

We first solve for x_0, h_0, θ_0^+, in terms of ℓ_0, and R_0 and θ_0^-as:

$$x_0 = \ell_0 + R_0 \frac{\sin\phi}{\sin\theta_0^-}, \tag{6.25a}$$

$$h_0 = R_0 \frac{\cos\theta_0^- - \cos\phi}{\sin\theta_0^-}, \tag{6.25b}$$

$$p_0 = \frac{\sin\theta_0^-}{R_0}, \tag{6.25c}$$

$$\theta_0^+ = \theta_0^-. \tag{6.25d}$$

Equation (6.25d) gives the equilibrium condition from which ℓ_0 and R_0 can be obtained subject to Eq. (6.23a):

$$A = -\int_{-\theta_0^-}^{\theta_0^+} h_0 \frac{dx_0}{d\phi} d\phi.$$

This can be simplified to obtain:

$$A = \frac{R_0^2}{2\sin^2\theta_0^-}(2\theta_0^- - \sin 2\theta_0^-), \tag{6.26}$$

which is the expression for the droplet size in the absence of gravity derived in Chapter 1. To see how these shapes are affected by gravity, we find the first-order corrections.

6.2.2 First order solution

The first order system is obtained as:

$$\frac{dx_0}{d\phi}(p_1 + x_0\sin\alpha + h_0\cos\alpha) + \frac{dx_1}{d\phi}p_0 = 0, \tag{6.27a}$$

$$\frac{dh_0}{d\phi}(p_1 + x_0\sin\alpha + h_0\cos\alpha) + \frac{dh_1}{d\phi}p_0 = 0, \tag{6.27b}$$

$$x_1(\phi = -\theta_0^-) = x_0'(-\theta_0^-)\theta_1^- + \ell_1 - R_1, \qquad h_1(\phi = -\theta_0^-) = h_0'(\phi = -\theta_0^-)\theta_1^-, \tag{6.27c}$$

$$x_1(\phi = \theta_0^+) = -x_0'(\theta_0^+)\theta_1^+ + \ell_1 + R_1, \qquad h_1(\phi = \theta_0^+) = -h_0'(\phi = \theta_0^+)\theta_1^+, \tag{6.27d}$$

$$0 = \int_{-\theta_0^-}^{\theta_0^+} \left(h_1\frac{dx_0}{d\phi} + h_0\frac{dx_1}{d\phi}\right) d\phi + \theta_1^+\left(h_0\frac{dx_0}{d\phi}\right)|_{\phi=\theta_0^+} + \theta_1^-\left(h_0\frac{dx_0}{d\phi}\right)|_{\phi=-\theta_0^-}. \tag{6.27e}$$

Also, we solve for x_1, h_1, θ_1^+, in terms of ℓ_1, and R_1 and θ_1^- as:

$$x_1 = \ell_1 - R_1 + R_0\theta_1^-\cot\theta_0^- + \frac{R_0^2}{2\sin^3\theta_0^-}\left(X_s\sin\alpha + X_c\cos\alpha + X_p p_1\right), \tag{6.28a}$$

$$h_1 = -R_0\theta_1^- + \frac{R_0^2}{2\sin^3\theta_0^-}(Z_s\sin\alpha + Z_c\cos\alpha + Z_p p_1), \tag{6.28b}$$

$$p_1 = -\frac{\sin\theta_0^-}{R_0^2}R_1 + \frac{\cos\theta_0^-}{R_0}\theta_1^- + \frac{1}{2\sin^2\theta_0^-}(P_s\sin\alpha + P_c\cos\alpha), \tag{6.28c}$$

$$\theta_1^+ = \theta_1^- + \frac{R_0^2}{2\sin^3\theta_0^-}(2\theta_0^- - \sin 2\theta_0^-)\sin\alpha, \tag{6.28d}$$

where

$$X_s = -(\sin\theta_0^- + \sin\phi)(2\ell_0 \sin\theta_0^- - R_0 \sin\theta_0^- + R_0 \sin\phi), \tag{6.29a}$$
$$X_c = R_0(\phi + \theta_0^- - \sin\theta_0^- \cos\theta_0^- + \sin\phi\cos\phi - 2\cos\theta_0^- \sin\phi), \tag{6.29b}$$
$$X_p = -2(\sin^2\theta_0^- + \sin\theta_0^- \sin\phi), \tag{6.29c}$$
$$Z_s = R_0(\sin\theta_0^- \cos\theta_0^- + \sin\phi\cos\phi - \theta_0^- - \phi) + 2\ell_0 \sin\theta_0^-(\cos\phi - \cos\theta_0^-), \tag{6.29d}$$
$$Z_c = -R_0(\cos\theta_0^- - \cos\phi)^2, \tag{6.29e}$$
$$Z_p = -2\sin\theta_0^-(\cos\theta_0^- - \cos\phi), \tag{6.29f}$$
$$P_s = R_0(\theta_0^- \cot\theta_0^- - \cos^2\theta_0^-) - 2\ell_0 \sin^2\theta_0^-, \tag{6.29g}$$
$$P_c = R_0(\theta_0^- - \cos\theta_0^- \sin\theta_0^-). \tag{6.29h}$$

Equation (6.28d) can be re-written in terms of the droplet size as:

$$\theta_1^+ = \theta_1^- + A\frac{\sin\alpha}{\sin\theta_0^-}. \tag{6.30}$$

It is seen that when the inclination is zero, $\alpha = 0$, $\theta_1^+ = \theta_1^-$, the upper and lower contact angle are the same. Meaning that for an horizontal surface, $\alpha = 0$, gravity only affects the droplet shape, it doesn't change its location. Equation (6.27e) can also be re-written as:

$$0 = \frac{2A}{R_0}R_1 + \eta\theta_1^- + Q, \tag{6.31}$$

where

$$\eta = \frac{2R_0^2}{\sin^2\theta_0}(1 - \theta_0^- \cot\theta_0^-), \tag{6.32a}$$
$$Q = \frac{-R_0^4}{\sin^6\theta_0^-}(Q_s \sin\alpha + Q_c \cos\alpha), \tag{6.32b}$$
$$Q_s = \cos\theta_0^- \sin^2\theta_0^- - \theta_0^- \sin\theta_0^-(1 + \cos^2\theta_0^-) + (\theta_0^-)^2 \cos\theta_0^-, \tag{6.32c}$$
$$Q_c = -2\sin^3\theta_0^- + \theta_0^- \cos\theta_0^- \sin^2\theta_0^- + (\theta_0^-)^2 \sin\theta_0^-. \tag{6.32d}$$

Hence ℓ_1 and R_1 are obtained by solving Eqs. (6.30) and (6.31) and noting that $\theta_1^- = \Theta'(\ell_0 - R_0)(\ell_1 - R_1)$, and $\theta_1^+ = \Theta'(\ell_0 + R_0)(\ell_1 + R_1)$:

$$\ell_1 = \frac{R_0}{\Delta}\left([\Theta'(a_0)\eta A - \frac{2A^2}{R_0}]\frac{\sin\alpha}{\sin\theta_0^-} - Q(\Theta'(a_0) + \Theta'(b_0))\right), \tag{6.33a}$$
$$R_1 = \frac{R_0}{\Delta}\left(\Theta'(a_0)\eta A\frac{\sin\alpha}{\sin\theta_0^-} - Q(\Theta'(a_0) - \Theta'(b_0))\right), \tag{6.33b}$$

where $a_0 = \ell_0 - R_0$, $b_0 = \ell_0 + R_0$, and $\Delta = 2\left(A(\Theta'(a_0) - \Theta'(b_0)) + R_0\Theta'(a_0)\Theta'(b_0)\eta\right)$.

By considering a periodic chemical pattern $\mathcal{F}(x) = \cos 2\pi x$ with a wetting strength of $\epsilon = 0.2$ and using Eqs. (6.25), (6.26), (6.28), (6.29), (6.32), and (6.33), droplet shapes for a fixed droplet size A for different Bond numbers and inclinations can be plotted to see how gravity affects droplets' equilibrium shapes. Figure 6.2 shows the plot of the shape of a droplet of size $A = 2$ for Bond number $B = 0.1$ for different inclinations. The blue line denote the leading order solution while the red line represent the solution up to the first order of the Bond number. It is seen that for $\alpha = 0$, gravity decreases droplet height while its radius increases to conserve the droplet size A. For inclination $\alpha \neq 0$, we first note that for a droplet of size $A = 2$, the maximum inclination angle given by Eq. (6.17) required to obtain physical solution is $\alpha = 59°$. Hence for inclinations ranging from 10° to 30°, the droplet tilts to the right as expected.

Apart from the drawback that our asymptotic solution is only valid for small Bond numbers, it also leads to singularities at some droplet sizes. To see this, we note that since $\Theta'(\ell_0 \pm R_0) = -2\pi\epsilon \sin 2\pi(\ell_0 \pm R_0)$, equations (6.33a) and (6.33b) can be simplified for $\ell_0 = 0$ as follows:

$$\Theta'(a_0) = 2\pi\epsilon \sin 2\pi R_0,$$
$$\Theta'(b_0) = -2\pi\epsilon \sin 2\pi R_0,$$

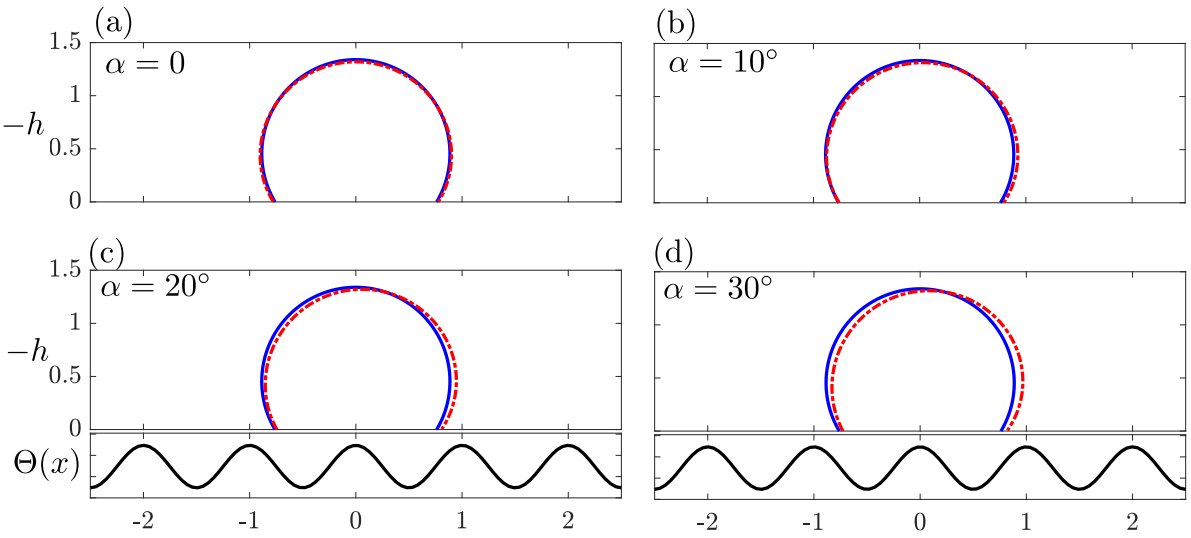

Fig. 6.2 Asymptotic solutions for droplet shapes for different inclinations for $(\epsilon, \theta_0, A, B) = (0.2, 120°, 2, 0.1)$. The solid blue line denote the leading order solution while the dashed red line represent the solution up to the first order.

so that

$$\begin{aligned}
&\Theta'(a_0) + \Theta'(b_0) = 0,\\
&\Theta'(a_0) - \Theta'(b_0) = 4\pi\epsilon \sin 2\pi R_0,\\
&\Delta = 8\pi\epsilon \sin 2\pi R_0 (A - R_0\eta\epsilon\pi \sin 2\pi R_0).
\end{aligned}$$

Inserting this into Eqs. (6.33a) and (6.33b) yields:

$$\begin{aligned}
\ell_1 &= \frac{-A(A - \eta\pi\epsilon R_0 \sin 2\pi R_0)\sin\alpha}{4\pi\epsilon \sin\theta_0^- \sin 2\pi R_0 (A - \eta\epsilon\pi R_0 \sin 2\pi R_0)},\\
R_1 &= \frac{\epsilon\pi \sin 2\pi R_0 (A\eta \sin\alpha - 2Q \sin\theta_0^-)}{4\pi\epsilon \sin\theta_0^- \sin 2\pi R_0 (A - \eta\epsilon\pi R_0 \sin 2\pi R_0)},
\end{aligned}$$

which simplifies into:

$$\ell_1 = \frac{-A \sin\alpha}{4 \sin\theta_0^- \epsilon\pi \sin 2\pi R_0}, \tag{6.34a}$$

$$R_1 = \frac{-R_0(2Q \sin\theta_0^- - A\eta \sin\alpha)}{4 \sin\theta_0^- (A - R_0\epsilon\pi\eta \sin(2\pi R_0))}. \tag{6.34b}$$

From Eq. (6.34a), for $\epsilon \neq 0$ when $\alpha \neq 0$, singularities exist for ℓ_1 when $\sin(2\pi R_0) = 0$, this occurs particularly when $R_0 = \frac{n}{2}$, where $n \in \mathbb{Z}^+$. This implies that varying the volume of a droplet would lead to no solutions at some droplet sizes for $\alpha \neq 0$. However when $\alpha = 0$, as previously noted, solution exists for the droplet mid-point, $\ell_1 = 0$, but there are still some singularities in R_1, (see Eq. 6.34b), when $A = R_0\epsilon\pi\eta \sin(2\pi R_0)$. Hence we see that the asymptotic solution fails at some droplet sizes, as a result we will aim to obtain exact solutions that yields physical results for any droplet size.

6.3 Exact solutions

The singularities that arise from our asymptotic solutions at some droplet sizes can be avoided by seeking exact solutions to the system of equations (6.15):

$$\frac{\mathrm{d}x}{\mathrm{d}\phi} = \frac{\cos\phi}{p + B(x \sin\alpha + h\cos\alpha)}, \tag{6.35a}$$

$$\frac{\mathrm{d}h}{\mathrm{d}\phi} = \frac{\sin\phi}{p + B(x \sin\alpha + h\cos\alpha)}. \tag{6.35b}$$

In this formulation the boundary conditions become

$$h[\phi = \pm\Theta(\ell \pm R)] = 0, \tag{6.36a}$$
$$x[\phi = \pm\Theta(\ell \pm R)] = \ell \pm R, \tag{6.36b}$$

with the volume constraint

$$A = -\int_{-\Theta(\ell-R)}^{\Theta(\ell+R)} h\frac{\mathrm{d}x}{\mathrm{d}\phi}\,\mathrm{d}\phi. \tag{6.37}$$

We proceed by transforming the coordinates (x, h) by rotating it through $-\alpha$ radians to obtain the transformed space coordinates (ξ, η) through

$$\begin{pmatrix}\xi\\ \eta\end{pmatrix} = \begin{pmatrix}\cos\alpha & \sin\alpha\\ -\sin\alpha & \cos\alpha\end{pmatrix}\begin{pmatrix}h\\ x\end{pmatrix}. \tag{6.38}$$

We then find

$$\frac{\mathrm{d}\xi}{\mathrm{d}\phi} = \frac{\sin(\phi+\alpha)}{B\xi + p}, \tag{6.39a}$$
$$\frac{\mathrm{d}\eta}{\mathrm{d}\phi} = \frac{\cos(\phi+\alpha)}{B\xi + p}, \tag{6.39b}$$

with boundary conditions

$$\xi[\phi = \pm\Theta(\ell \pm R)] = (\ell \pm R)\sin\alpha, \tag{6.40a}$$
$$\eta[\phi = \pm\Theta(\ell \pm R)] = (\ell \pm R)\cos\alpha, \tag{6.40b}$$

and the volume constraint can be written as

$$A = -\int_{-\Theta(\ell-R)}^{\Theta(\ell+R)} (\xi\cos\alpha - \eta\sin\alpha)\,\frac{\cos\phi}{B\xi + p}\,\mathrm{d}\phi. \tag{6.41}$$

The main benefit of transforming the system into this form is that we can now integrate directly to obtain

$$\xi = \frac{\sqrt{2}\sqrt{C - B\cos(\phi+\alpha)} - p}{B}, \tag{6.42a}$$
$$\eta = (\ell - R)\cos\alpha + \mathcal{I}(\phi; \alpha, C, B), \tag{6.42b}$$

where

$$\mathcal{I}(\phi;\alpha,C,B)=\int_{\alpha-\Theta(\ell-R)}^{\alpha+\phi}\frac{\cos\varphi}{\sqrt{2}\sqrt{C-B\cos\varphi}}\,\mathrm{d}\varphi, \tag{6.43}$$

which maybe written as the sum of four elliptic integrals. Our goal now is to find the constants C, p, ℓ, R which satisfy the following system:

$$\sqrt{2}\sqrt{C-B\cos[\alpha+\Theta(\ell+R)]}=B(\ell+R)\sin\alpha+p, \tag{6.44a}$$
$$\sqrt{2}\sqrt{C-B\cos[\alpha-\Theta(\ell-R)]}=B(\ell-R)\sin\alpha+p, \tag{6.44b}$$
$$BA\cos\alpha=2pR-[\sin\Theta(\ell+R)+\sin\Theta(\ell-R)]+2B\ell R\sin\alpha. \tag{6.44c}$$
$$2R\cos\alpha=\mathcal{I}\left(\Theta(\ell+R);\alpha,C,B\right), \tag{6.44d}$$

Eliminating p from this system we obtain

$$I=2R\cos\alpha, \tag{6.45a}$$
$$J=2R\sin\alpha, \tag{6.45b}$$
$$KR=BA\cos\alpha+[\sin\Theta(\ell+R)+\sin\Theta(\ell-R)], \tag{6.45c}$$

where

$$I=\mathcal{I}\left(\Theta(\ell+R);\alpha,C,B\right)=\int_{\alpha-\Theta(\ell-R)}^{\alpha+\Theta(\ell+R)}\frac{\cos\varphi}{\sqrt{2}\sqrt{C-B\cos\varphi}}\,\mathrm{d}\varphi, \tag{6.46a}$$
$$J=\frac{\sqrt{2}}{B}\left[\sqrt{C-B\cos(\alpha+\Theta(\ell+R))}-\sqrt{C-B\cos(\alpha-\Theta(\ell-R))}\right], \tag{6.46b}$$
$$K=\sqrt{2}\left[\sqrt{C-B\cos(\alpha+\Theta(\ell+R))}+\sqrt{C-B\cos(\alpha-\Theta(\ell-R))}\right]. \tag{6.46c}$$

Since Eq. (6.46a) is an elliptic integral which can only be treated numerically, Eqs. (6.45) will have to be solved numerically to find all the equilibrium solutions for the droplet's position and radius. Unlike the asymptotic solution, this solution is valid for any Bond number B, inclination α, and droplet size A.

Figure 6.3 shows droplet shapes for hydrophilic and hydrophobic contact angles on an horizontal surface and Bond number $B=1$. Here unlike the microgravity regime, we can consider higher values of the Bond number. For Bond number $B=1$, it is seen that gravity decreases the droplets height in both cases. To balance this height decrease, the droplet increases its radius. This increase in the droplet radius becomes larger as the Bond number B increases, (see Fig. 6.4). To understand this we consider a surface with no wetting pattern $\epsilon=0$ and compute the change in droplet radius as a function of

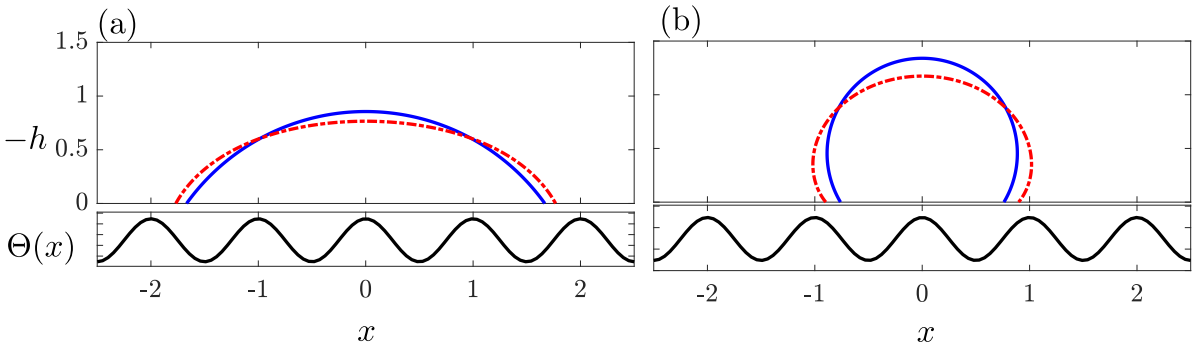

Fig. 6.3 Full solutions for droplet shapes for $(\epsilon, A, B, \alpha) = (0.2, 2, 1, 0)$. (a) $\theta_0 = 60°$, (b) $\theta_0 = 120°$. The solid blue line denote solution for $B = 0$, while the dashed red line represent the solution for $B = 1$.

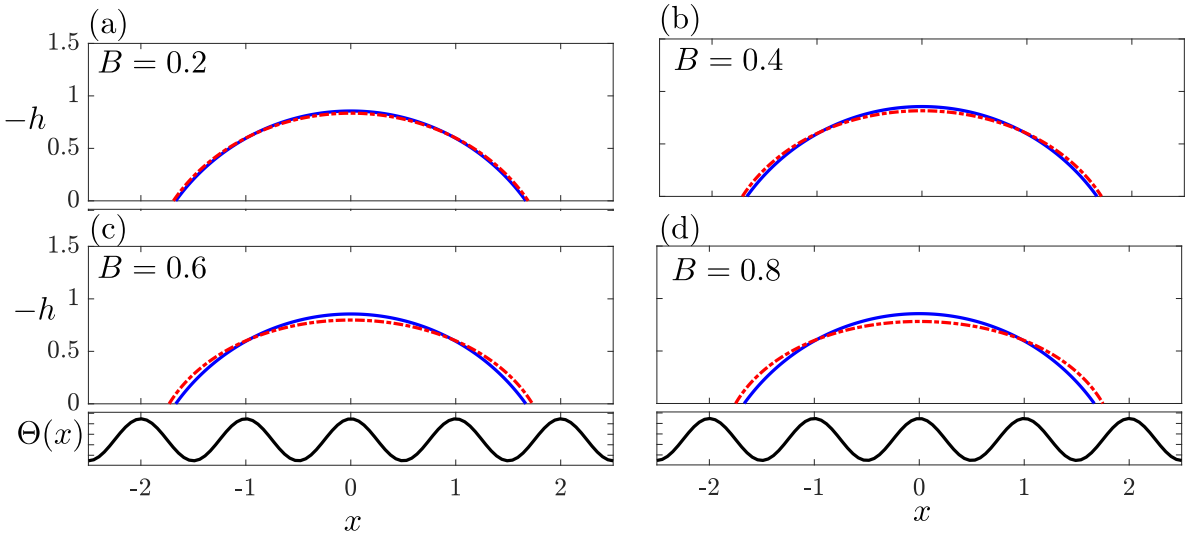

Fig. 6.4 Full solutions for droplet shapes for different Bond numbers for $(\theta_0, \epsilon, A, \alpha) = (60°, 0.2, 2, 0)$. The solid blue line denote solution for $B = 0$, while the dashed red line represent the solution for $B = 1$.

the Bond number as shown in Fig. 6.5(a). Since increasing the Bond number increases the droplet radius, we can find a droplet of size A_0 with no gravity that is equivalent to a droplet size A_B with gravity. To this end we first find the equilibrium solution of a droplet under the influence of gravity, $R_B = f(A_B)$, we then find the droplet size, $A_0(R_B)$ corresponding to this solution in the absence of gravity (see Fig. 6.5(b)). What we see is that on an horizontal surface increasing the influence of gravity is equivalent to increasing the droplet size.

When the surface inclination is non-zero, the location of the droplet is changed. For a Bond number $B = 1$ and droplet size $A = 2$, the maximum inclination possible for physical solutions is, $\alpha = 10°$. Figure (6.6) shows that the droplet position is changed for

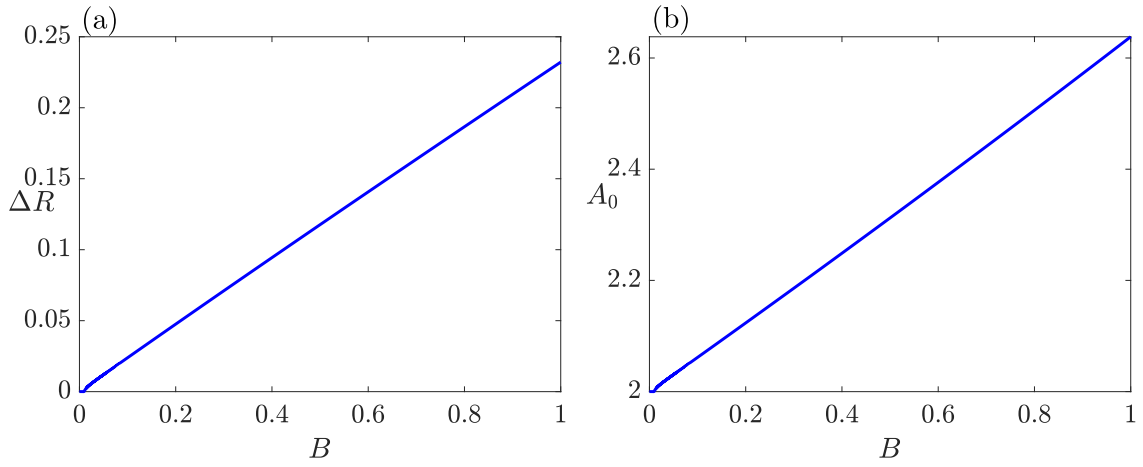

Fig. 6.5 Panel (a) shows that change in radius ΔR caused by gravity versus Bond number B. Panel (b) shows the equivalent droplet size in the absence of gravity A_0.

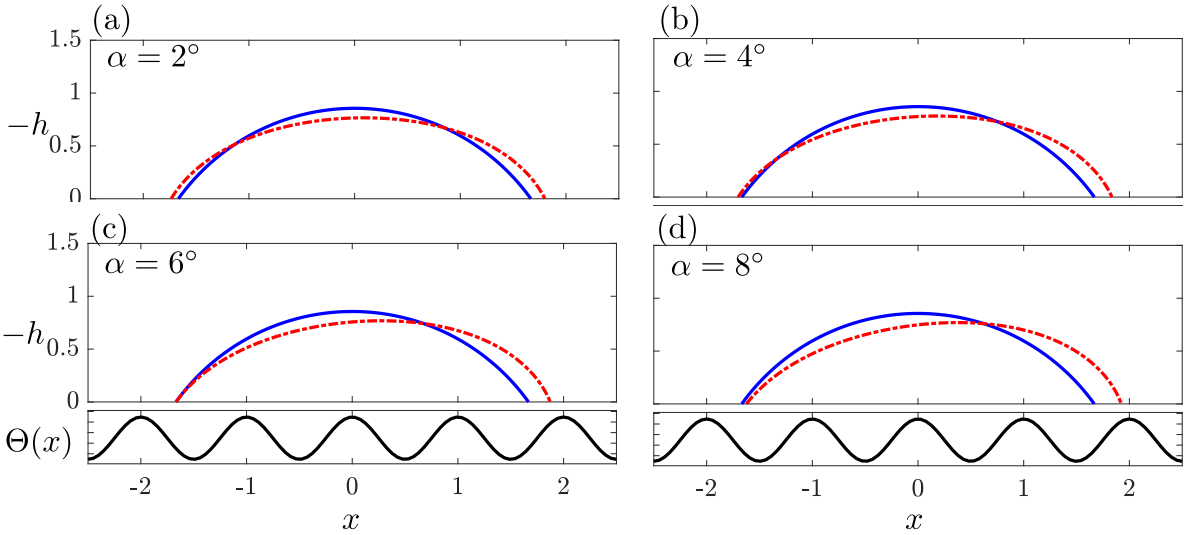

Fig. 6.6 Full solutions for droplet shapes for different inclinations for $(\theta_0, \epsilon, A, B) = (60°, 0.2, 2, 1)$. The solid blue line denote solution for $B = 0$, while the dashed red line represent the solution for $B = 1$.

non zero inclinations. This change in the droplet position increases as the inclination α increases.

6.4 Stability

Droplet equilibrium solutions on a solid with well defined wetting patterns may be stable, saddle node, or unstable when subjected to gravity's effect. Here we examine the energy

E, of the droplet, which is the sum of the gravitational potential energy E_g, solid surface energy E_s, and interfacial energy E_i, that is, $E = E_g + E_s + E_i$. To understand how the stability of a droplet is affected by gravity we will study these energies separately. In all cases, we assume that the droplet's interface is defined by $z = h(x)$ and that this function is single-valued. The left and right contact points are labelled as $x = a$ and $x = b$ respectively.

The gravitational potential energy is given by

$$E_g = \iint_\Omega \rho \boldsymbol{g} \cdot \boldsymbol{x} \, \mathrm{d}\Omega, \tag{6.47}$$

where ρ is the density of the liquid, which we assume to be constant, and Ω is the liquid region, defined as

$$\Omega = (x, z) \in [a, b] \times [0, h(x)], \text{ and } \mathrm{d}\Omega = \mathrm{d}z \, \mathrm{d}x. \tag{6.48}$$

Consequently, we find

$$\begin{aligned} E_g &= \rho g \int_a^b \int_0^{h(x)} (x \sin\alpha + z \cos\alpha) \, \mathrm{d}z \, \mathrm{d}x, \\ &= \rho g \int_a^b \left(xh \sin\alpha + \frac{h^2}{2} \cos\alpha \right) \mathrm{d}x. \end{aligned}$$

The solid surface energy is given by

$$E_s = -\gamma \int_a^b \cos\Theta \, \mathrm{d}x,$$

where γ is the liquid/gas surface tension and Θ, is the spatially dependent contact angle. The interfacial energy is the product of the interfacial surface tension and the surface area:

$$E_i = \gamma \int_a^b \sqrt{1 + h_x^2} \, \mathrm{d}x.$$

The total energy can now be obtained by adding the gravitational, interfacial and surface energies:

$$E = \gamma \int_a^b \left(\sqrt{1 + h'^2} - \cos\Theta \right) \mathrm{d}x + \rho g \int_a^b \left(xh \sin\alpha + \frac{h^2}{2} \cos\alpha \right) \mathrm{d}x. \tag{6.49}$$

This can be non-dimensionalized by choosing the following scalings

$$E = \gamma L E^*, \ (x, h) = L(x^*, h^*), \tag{6.50}$$

where the starred terms are dimensionless. Here the characteristic length scale L, is taken to be the wavelength λ of the function Θ, i.e. $\Theta(x + \lambda) = \Theta(x)$. Applying these (and dropping the stars) we find

$$E = \int_a^b \left(\sqrt{1 + h'^2} - \cos\Theta\right) \mathrm{d}x + B \int_a^b \left(xh \sin\alpha + \frac{h^2}{2}\cos\alpha\right) \mathrm{d}x, \tag{6.51}$$

where $B = \rho g L^2/\gamma$ is the Bond number which relates the body forces (gravity) to the surface forces (interfacial tension). Since the energy (6.51) is a functional of the interfacial surface's shape $z = h(x)$, it can be written in arc-length formulation by applying (6.13a) and (6.13b) to (6.51). This yields:

$$E = s^* - \int_0^{s^*} \cos\Theta(x(s)) \cos\phi(s) \, \mathrm{d}s + B \int_0^{s^*} \left(x(s)h(s)\sin\alpha + \frac{h^2(s)}{2}\cos\alpha\right) \cos\phi(s) \, \mathrm{d}s, \tag{6.52}$$

where s^* is the total arc-length of the interface, i.e., s^* satisfies $x(s^*) = b$ and $h(s^*) = 0$. We calculate the energy (for a given surface patterning, volume, slope and Bond number), as a function of the droplet's centre ℓ, and radius R, using (6.52) where $x(s), h(s), \phi(s), s^*$ are solutions to the system

$$\frac{\mathrm{d}h}{\mathrm{d}s} = \sin\phi, \tag{6.53a}$$

$$\frac{\mathrm{d}x}{\mathrm{d}s} = \cos\phi, \tag{6.53b}$$

$$\frac{\mathrm{d}\phi}{\mathrm{d}s} = B(x\sin\alpha + h\cos\alpha) + p, \tag{6.53c}$$

with boundary conditions

$$h = 0, x = \ell - R, \qquad \text{at } s = 0, \tag{6.54a}$$

$$h = 0, x = \ell + R, \qquad \text{at } s = s^*, \tag{6.54b}$$

and the volume condition

$$-A = \int_0^{s^*} h\cos\phi \, \mathrm{d}s. \tag{6.55}$$

We can use this calculation to produce an energy profile. The stability of a droplet's equilibrium solution can then be determined by examining the eigenvalues of the Hessian matrix H_E, given by

$$H_E = \begin{pmatrix} E_{\ell\ell} & E_{\ell R} \\ E_{\ell R} & E_{RR} \end{pmatrix}, \tag{6.56}$$

where the derivatives are found using a central difference method.

6.5 Bifurcation analysis

The equilibrium solution of a droplet of size A under the influence of gravity on a solid surface with periodic wetting pattern can be obtained from Eqs. (6.45). The stability of these solutions can then be obtained form the energy of the system (6.51). With these, bifurcation diagrams can be constructed for different droplet sizes so that we can predict a droplet's behaviour as it evaporates on an inclined plane under the influence of gravity.

6.5.1 Periodic and symmetric chemical patterns

We start by considering a periodic and symmetric chemical pattern $\mathcal{F}(x) = \cos 2\pi x$ and droplet of fixed size A on an horizontal surface, where $\alpha = 0$ and examine how gravity affects the equilibrium solution of a droplet by varying the Bond number. Figure 6.7 shows the energy landscape of a droplet of size $A = 2$ on a flat surface with contact angle $\theta_0 = 60°$ and wetting strength $\epsilon = 0.2$. It is seen that as the Bond number increases, the behaviour of the the droplet's equilibrium solution changes. At droplet radius $R = 1.5$, when the Bond number $B = 0$, there is a stable point aligned with the minimum of the chemical pattern alongside two adjacent saddle nodes. As the Bond number increases to $B = 0.6$, the two saddle nodes collide with the stable node to become a saddle node. At $B = 0.7$, there are two saddle nodes at $R = 1.5$ and $R = 2$ respectively and an unstable point in between them. As the Bond number becomes $B = 0.8$, the saddle node at $R = 2$ becomes a stable point which multiplies to produce two extra adjacent saddle nodes as the Bond number becomes slightly higher, $B = 0.85$. Hence we see that gravity does not only changes the shape of a droplet, it also changes its stability.

Changing the Bond number changes the droplet equilibrium solutions and their stabilities the same way varying the size of a droplet does. As a result, the Bond number can be a bifurcation parameter that causes a change in the droplet behaviour when varied. Hence we construct a bifurcation diagram of the droplet radius with the Bond number

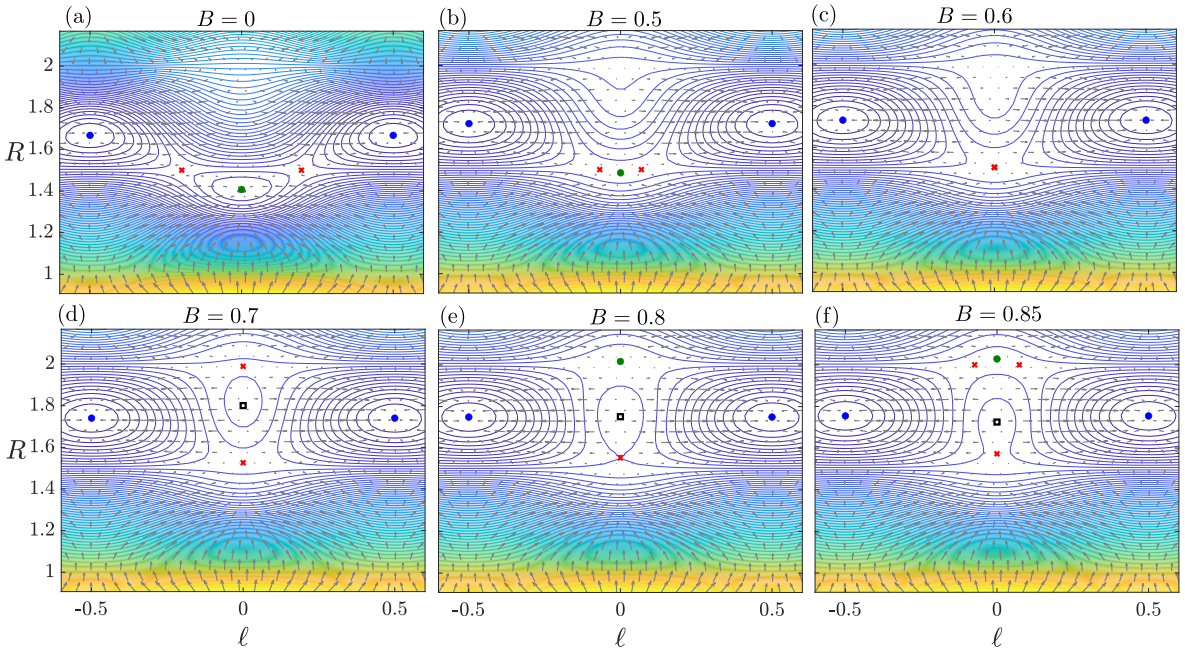

Fig. 6.7 Energy contour plots for $(A, \theta_0, \epsilon) = (2, 60°, 0.2)$, where energy levels increase from blue to yellow. Blue and green circles correspond to stable equilibrium solutions, crosses to saddle nodes that are stable to axisymmetric perturbations but unstable against lateral displacements, and empty squares correspond to unstable solutions. Panels (a-f) correspond to Bond numbers ranging from 0 to 0.85.

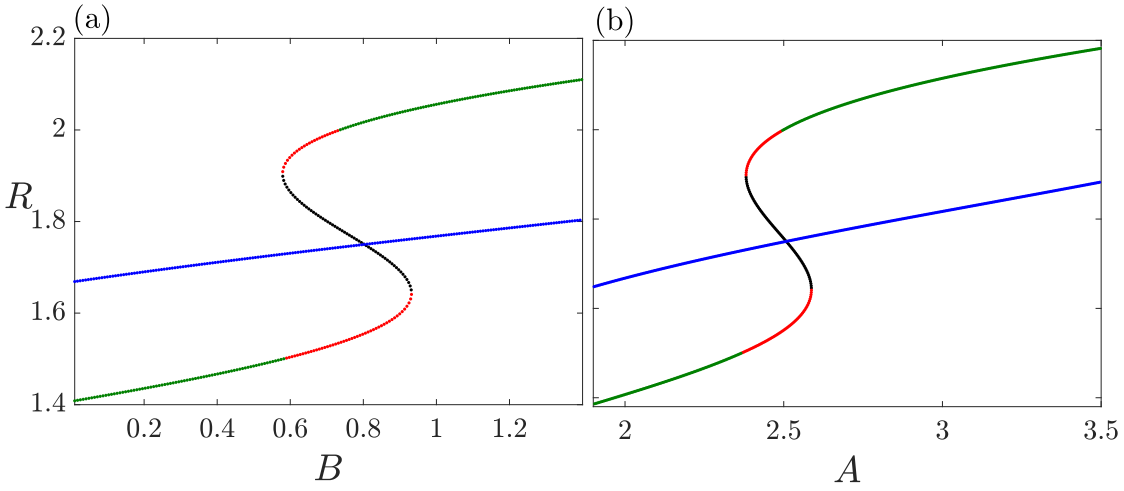

Fig. 6.8 Bifurcation diagram with the (a) Bond number B as the bifurcation parameter for $(A, \theta_0, \epsilon) = (2, 60°, 0.2)$, and (b) droplet size A as the bifurcation parameter for $(B, \theta_0, \epsilon) = (0, 60°, 0.2)$. Blue and green lines correspond to stable equilibrium solutions, red lines to saddle nodes that are stable to axisymmetric perturbations but unstable against lateral displacements, and black lines correspond to unstable solutions.

being the bifurcation parameter, (see Fig. 6.8(a)) similar to the bifurcation diagram where the droplet size is the bifurcation parameter and the Bond number is zero, (see Fig. 6.8(b)).

Figure 6.9 shows the relation between the droplet's radius and size for droplets aligned with the minimum and maximum of the chemical patterns. The blue, cyan and green lines correspond to stable equilibrium solutions for Bond numbers $B = 0$, $B = 0.5$, and $B = 1$ respectively, red lines to saddle nodes and black lines correspond to unstable solutions. We can see that as the Bond number increases, the qualitative relation between the radius R and droplet size A is unchanged, indeed, the pitchfork points, $R = n/2$, where $n \in \mathbb{Z}$ is the same in all cases. However, the critical droplet size A_p corresponding to the pitchfork radius becomes lower as the Bond number decreases because gravity becoming stronger causes the droplet radius to increase. Also, as the droplet size becomes small the effect of gravity is negligible so that the (R, A) curves becomes identical at lower droplet sizes.

A droplet evaporating on a smooth flat surface with a periodic wetting pattern under the influence of gravity would have similar behaviour as though gravity were absent. The only difference is that it will snap at a lower droplet size than it would in the absence of gravity. In essence gravity decreases the critical droplet size where a droplet snaps and hence delays the snap events. Due to symmetry, there is no bias for the change in position of the droplet, hence ruling out the possibility to induce droplet motion towards

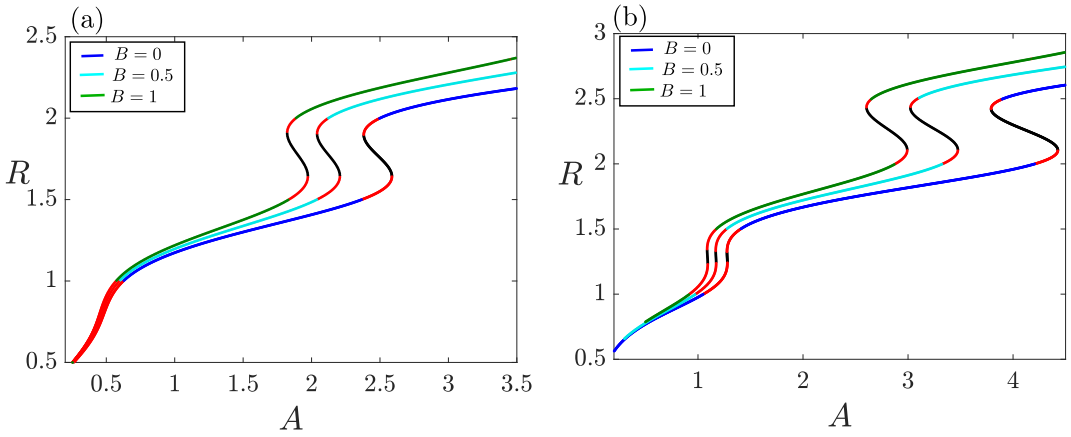

Fig. 6.9 Bifurcation diagrams for different Bond numbers with the droplet size being the bifurcation parameter for a droplet aligned with (a) the minimum and (b) maximum of the chemical pattern where $(\theta_0, \epsilon) = (60°, 0.2)$. Blue, cyan and green lines correspond to stable equilibrium solutions for Bond numbers $B = 0$, $B = 0.5$, and $B = 1$ respectively, red lines to saddle nodes that are stable to axisymmetric perturbations but unstable against lateral displacements, and black lines correspond to unstable solutions.

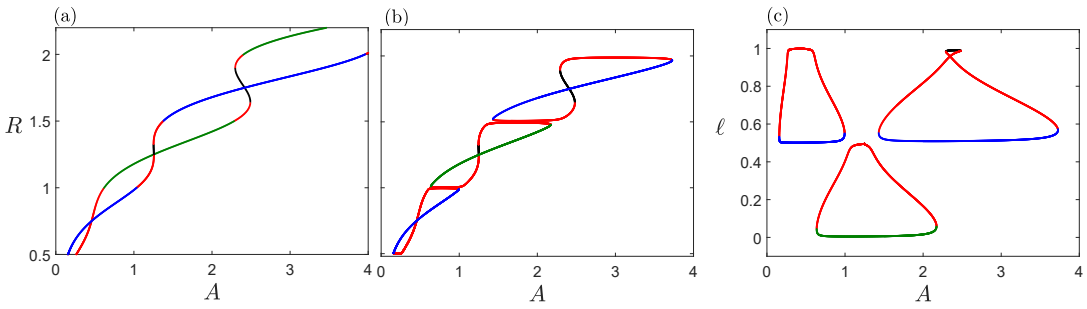

Fig. 6.10 Bifurcation diagrams for Bond number $B = 0.1$ and different inclination angles in the (a) (R, A) space for $\alpha = 0$ and (b) $\alpha = 5°$, (c) (ℓ, A) space for for $\alpha = 5°$, where $(\theta_0, \epsilon) = (60°, 0.2)$. Green, and blue lines correspond to stable equilibrium solutions aligned with or close to the minimum and maximum of the chemical pattern respectively, red lines to saddle nodes that are stable to axisymmetric perturbations but unstable against lateral displacements, and black lines correspond to unstable solutions.

a *preferred* direction. As a result the droplet could either move to the left of to the right. Hence the direction of motion of an evaporating droplet can not be controlled, however by tilting the surface via the inclination angle, the droplet can be made to move in a specific direction.

Figure 6.10 shows how the position and radius are related to the droplet size for Bond number $B = 0.1$, and different inclination angles $\alpha = 0$, and $\alpha = 5°$. It is seen that for non-zero inclination angle, there is a topological change in the bifurcation diagram with the solutions becoming disconnected at the pitchfork points. Hence the bifurcation diagram becomes a combination of different cycles of closed curves spanning form $R = n/2$ to $(n + 1)/2$, where, $n \in \mathbb{Z}$. Hence we see that the pitchfork bifurcations which occur when $B = 0$ become imperfect bifurcations under gravity. Importantly, however, the qualitative nature of the bifurcations appears unchanged.

Figure 6.11 shows the equilibrium solutions for droplets on a flat surface that has been tilted to the right and to the left with the inclination angles $\alpha = 5°$ and $\alpha = -5°$ respectively for Bond number $B = 0.1$. It is seen that for $\alpha > 0$, the stable branch of the closed curves near the minimum of the chemical pattern (blue line) has an upward cup shape. This makes the pitchfork point where the droplet's stability changes from stable to saddle node becomes slightly nearer to the stable branch to its right near $\ell = 1$ than the branch to its left located near $\ell = 0$. To predict which direction the droplet would move at the pitchfork point, we compute the quantity, $G(\ell) = |\Delta E/\Delta\ell|$ which defines the ratio of the energy difference to location difference between the pitchfork point (ℓ_p, A_p) and the point to its right (ℓ_r, A_p) or to its left (ℓ_l, A_p). For $\alpha > 0$, $G(\ell_r) > G(\ell_l)$, and as a result a droplet evaporating on the stable branch located near $\ell = 0.5$ starting at

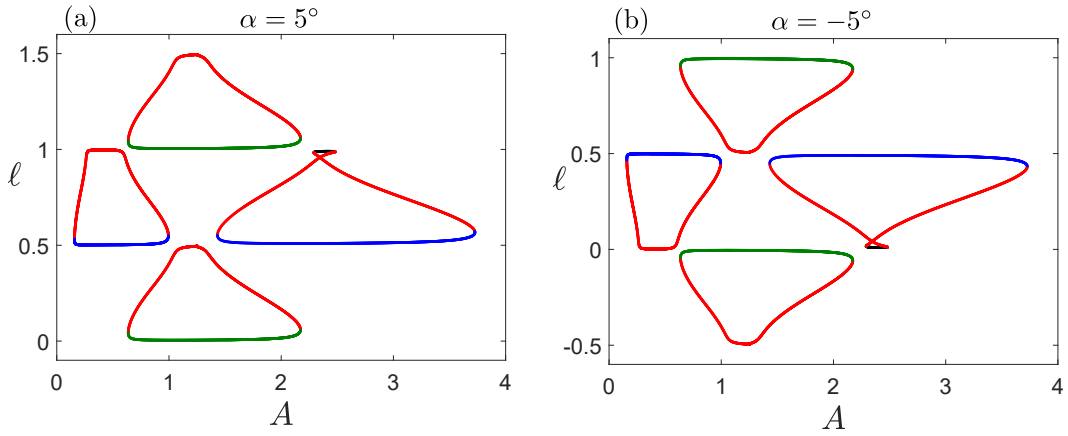

Fig. 6.11 Bifurcation diagrams for a droplet for $B = 0.1$ for (a) $\alpha = 5°$, and (b) $\alpha = -5°$. Green and blue represent stable equilibrium solutions close to the minimum and maximum of the chemical pattern respectively, red lines denote saddle nodes that are stable to axisymmetric perturbations but unstable against lateral displacements, and black lines correspond to unstable solutions.

say size $A = 3$ would snap to the right in the direction of gravity when its size reaches the critical pitchfork value A_p. When the surface is tilted to the left, that is, $\alpha < 0$, the bifurcation diagram is inverted and the stable branch is now curved downward and has a cap shape. As a result the pitchfork point is closer to the stable branch located near $\ell = 0$ than to the stable branch near $\ell = 1$. In this scenario $G(\ell_l) > G(\ell_r)$ so that the droplet would prefer to snap to the left in the direction of gravity. Hence the introduction of a non-zero inclination induces a bias that breaks the droplet plane of symmetry and causes the droplet to move in a *preferred* direction, moving to the right when $\alpha > 0$ and to the left when $\alpha < 0$. This implies that the direction of motion of an evaporating droplet can be controlled by the inclination of the solid.

6.5.2 Patterns with an amplitude gradient

The results shown in the previous section indicate that on an horizontal surface with $\alpha = 0$ and symmetric chemical patterns under the influence of gravity, a droplet will adopt equilibrium configurations which are aligned with either a maximum or a minimum of the pattern. As the droplet's size changes, the stability of such configurations alternates between stable and saddle nodes through a sequence of pitchfork bifurcations that can promote droplet lateral motion: any perturbation that breaks the plane symmetry will make the droplet change from a saddle node to a stable location. This means that the direction of motion of the droplet as it snap can't be controlled unless the surface is

inclined, in which case the droplet snaps to the right when $\alpha > 0$ and to the left when $\alpha < 0$.

To control the direction of motion of an evaporating droplet when $\alpha = 0$, we explore a non-symmetrical chemical pattern with the aim to determine whether it is possible to achieve directed displacement in the droplet's location as the droplet size is changed. For cases where $\alpha \neq 0$, we would also see if it is possible to move a droplet against gravity, for example we know that imposing $\alpha < 0$ moves the droplet to the left, the question now is that can a droplet be made to move to the right instead by prescribing a non-symmetrical contact angle pattern. To this end, we consider a pattern with an amplitude gradient described by the function:

$$\mathcal{F}(x) = \frac{2}{\pi} \arctan\left(\frac{x}{L}\right) \cos(2\pi x), \tag{6.57}$$

where L is the length over which the gradient varies, (we note that the change of sign of the gradient can be imposed by replacing x by $L - x$ in the argument of the arctan). We solve Eqs. (6.45) alongside Eq. (6.57) to find the equilibrium solutions for a given droplet size. Following the same procedure as in the previous section, we construct the bifurcation diagrams as the droplet size is changed.

Figure 6.12 shows the bifurcation diagrams for droplets on asymmetric pattern (6.57) with a strong bias $L = 6$ and wetting strength $\epsilon = 0.1$ for $\alpha = 0$ on the (ℓ, A) plane. Blue, black and green lines represent stable equilibrium solutions corresponding to Bond numbers $B = 0.1, 0.5$ and $B = 1$ respectively, red lines denote saddle nodes that are stable

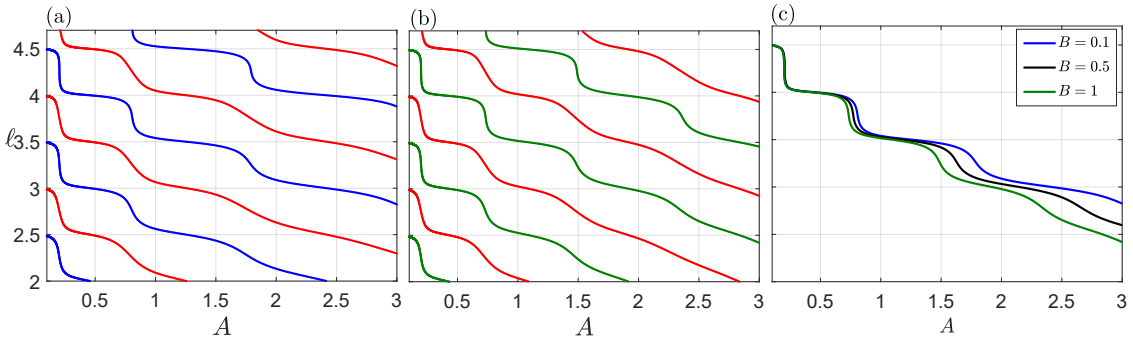

Fig. 6.12 Bifurcation diagrams for droplets on asymmetric pattern (6.57) with bias $L = 6$ and wetting strength $\epsilon = 0.1$ for $\alpha = 0$ on the (ℓ, A) plane for (a) $B = 0.1$, (b) $B = 1$, and (c) different Bond numbers. Blue, black and green lines represent stable equilibrium solutions corresponding to Bond numbers, $B = 0.1, 0.5$ and $B = 1$ respectively, red lines denote saddle nodes that are stable to axisymmetric perturbations but unstable against lateral displacements.

to axisymmetric perturbations but unstable against lateral displacements. Panels (a) and (b) show the bifurcation diagrams for Bond numbers $B = 0.1$ and $B = 1$ respectively. It is seen that, similar to the case with no gravity discussed in Section 3.1.4 of Chapter 3, disconnected branches of stable and saddle nodes emerges in both cases. Hence a droplet evaporating under the influence of gravity on a flat surface with an asymmetric pattern with gradient, will move in a preferred direction. In this case the droplet will move to the right, but if the direction of the gradient is reversed it will move to the left. Panel (c) shows a stable branch for different Bond numbers. It is observed that gravity shifts this branch to left. This shift however becomes insignificant as the size of the droplet decreases so that the curves are identical at small droplet sizes.

On an inclined plane, these bifurcation diagrams change. Figure 6.13 shows the bifurcation diagrams for droplets on asymmetric pattern (6.57) with bias $L = 6$ and wetting strength $\epsilon = 0.1$ for Bond numbers $B = 0.1, 0.2$ and $B = 0.3$ on the (ℓ, A) plane. Green lines represent stable equilibrium solutions, red lines denote saddle nodes that are stable to axisymmetric perturbations but unstable against lateral displacements. Panel (a) shows solutions for $B = 0.1$ and $\alpha = 5°$. It is seen that the stable and saddle node branches moves closer to each other but the direction of motion is still dictated by the

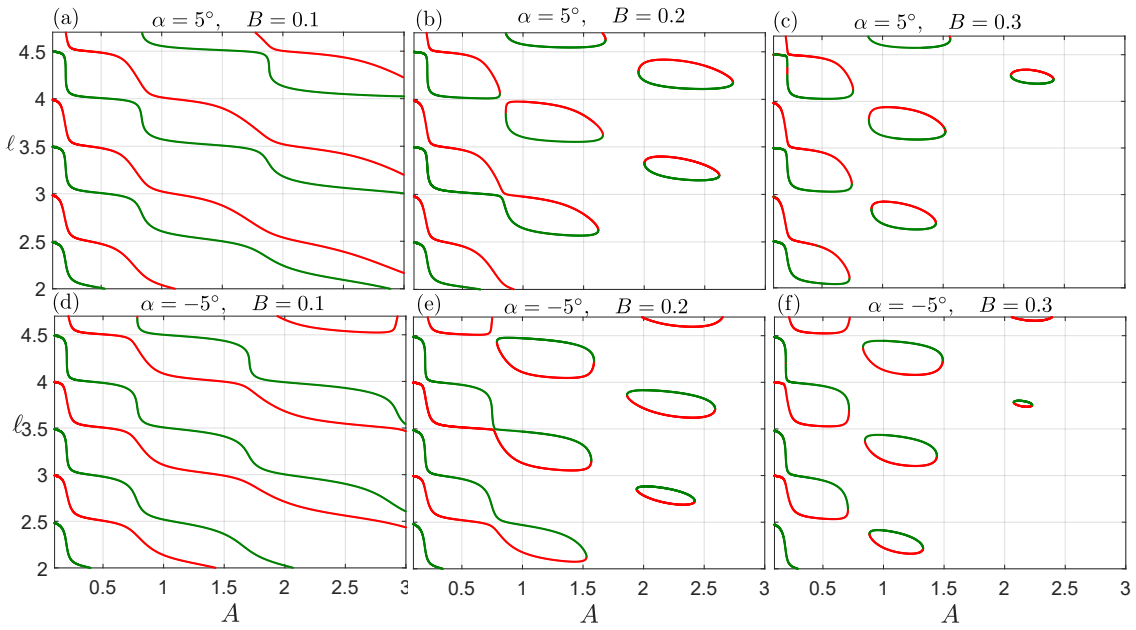

Fig. 6.13 Bifurcation diagrams for droplets on asymmetric pattern (6.57) with bias $L = 6$ and wetting strength $\epsilon = 0.1$ for Bond numbers $B = 0.1, 0.2$ and $B = 0.3$ on the (ℓ, A) plane for $\alpha = 5°$ (a-c) and $\alpha = -5°$ (d-f). Green lines correspond to stable equilibrium solutions, red lines to saddle nodes that are stable to axisymmetric perturbations but unstable against lateral displacements.

wetting pattern which dictates that an evaporating droplet on a stable branch would move to the right. As the Bond number increases slightly, (see panels (b) and (c)) there is a competition between the wetting pattern and gravity. For solutions at lower locations and droplet size where the effect of gravity is weak, the wetting pattern dictates the direction of motion of the droplet. At higher location where the pattern with gradient is weak, the gravitational forces dominates creating closed curves that makes the droplet snap to the right in the direction of gravity. Panel (d) shows the case where the surface inclination is reversed, $\alpha = -5°$. In this scenario, even though gravity dictates that the droplet would move to the left, it will actually move to the right due to the asymmetric pattern. However as gravity increases, there is a competition between the wetting pattern and gravity effects in determining the direction of motion of an evaporating droplet, (see panels (e) and (f)).

The bias on the asymmetric pattern (6.57) can be weakened by reducing L. Figure 6.14 shows the bifurcation diagrams for droplets on asymmetric pattern (6.57) with a weak bias $L = 0.6$ and wetting strength $\epsilon = 0.1$ for $\alpha = 0$ on the (ℓ, A) plane. Blue, black and green lines represent stable equilibrium solutions corresponding to Bond numbers $B = 0.1, 0.5$ and $B = 1$ respectively, red lines denote saddle nodes that are stable to axisymmetric perturbations but unstable against lateral displacements. Panels (a) and (b) show the bifurcation diagrams for Bond numbers $B = 0.1$ and $B = 1$ respectively. It is seen that, similar to the case with no gravity, disconnected branches of solutions emerges in both cases so that a droplet moves in a preferred direction as the stability of the equilibrium solution changes from stable to saddle node. Panel (c) shows a branch of

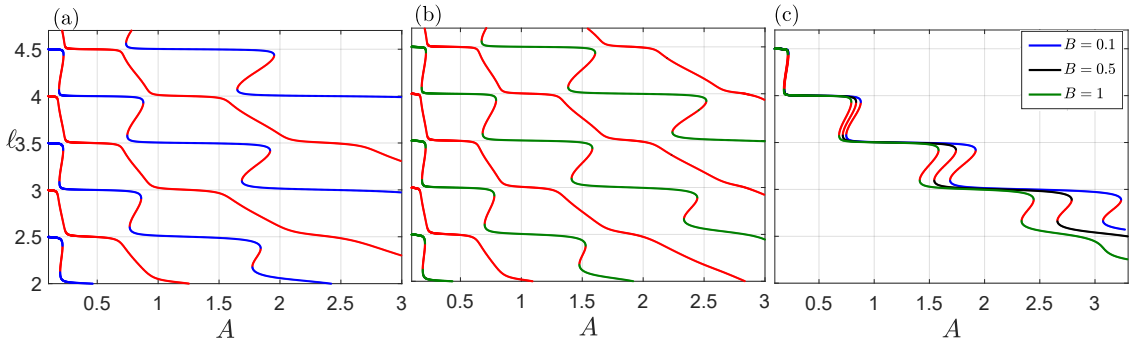

Fig. 6.14 Bifurcation diagrams for droplets on asymmetric pattern (6.57) with bias $L = 0.6$ and wetting strength $\epsilon = 0.1$ for $\alpha = 0$ on the (ℓ, A) plane for (a) $B = 0.1$ (b) $B = 1$, (c) different Bond numbers. Blue, black and green lines represent stable equilibrium solutions corresponding to Bond numbers $B = 0.1, 0.5$ and $B = 1$ respectively, red lines denote saddle nodes that are stable to axisymmetric perturbations but unstable against lateral displacements.

solutions for different Bond numbers. It is observed that gravity shifts this branch to left and as a result the critical droplet size where the stability of the droplet changes from stable to saddle node decrease. This means that a droplet will snap at a lower volume in the presence of gravity. This delay in the snap event however becomes insignificant as the size of the droplet decreases so that the curves are identical at small droplet sizes.

On an inclined plane interesting changes occur in the topology of the bifurcation diagram. Figure 6.15 shows the bifurcation diagrams for droplets on asymmetric pattern (6.57) with bias $L = 0.6$ and wetting strength $\epsilon = 0.1$ for Bond numbers $B = 0.1, 0.2$ and $B = 0.3$ on the (ℓ, A) plane. Panels (a) show solutions for $B = 0.1$ and $\alpha = 5°$ for different Bond numbers. Green lines represent stable equilibrium solutions, red lines denote saddle nodes that are stable to axisymmetric perturbations but unstable against lateral displacements. A combination of continuous and closed curves arises depending on the location. For solutions at lower locations and droplet size where the effect of gravity is weak, continuous solution curves emerges that makes an evaporating droplet on such branches move to the right following the direction of the wetting pattern. At higher location where the pattern's gradient is weak and at higher droplet sizes, the gravitational forces dominates creating closed curves that makes the droplet snap to the right in the

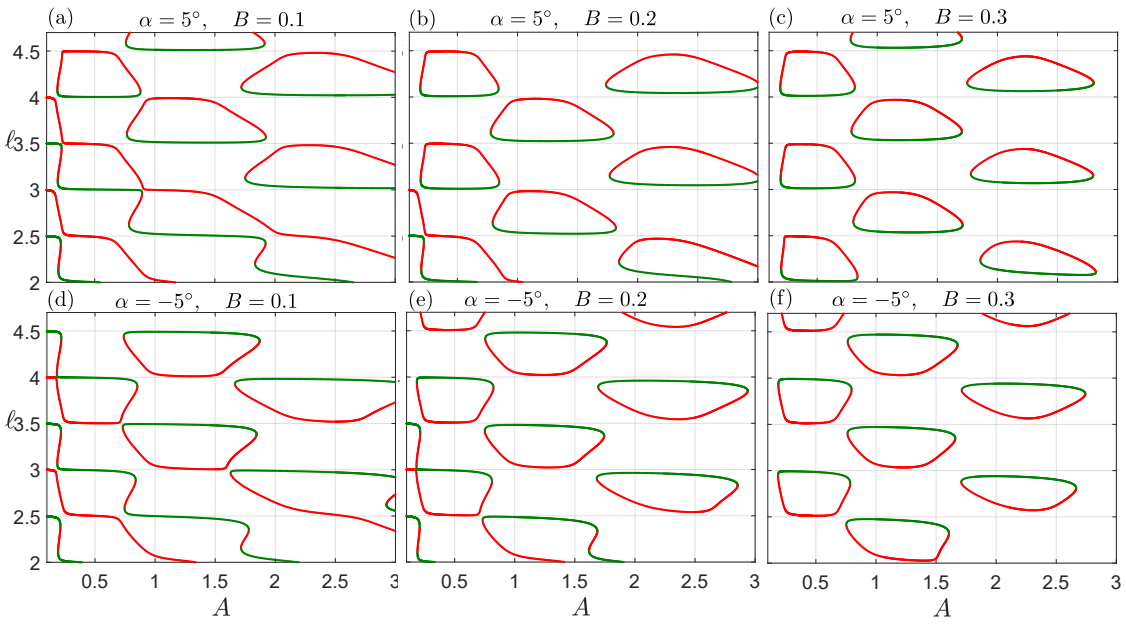

Fig. 6.15 Bifurcation diagrams for droplets on asymmetric pattern (6.57) with bias $L = 0.6$ and wetting strength $\epsilon = 0.1$ for Bond numbers $B = 0.1, 0.2$ and $B = 0.3$ on the (ℓ, A) plane for $\alpha = 5°$ (a-c) and $\alpha = -5°$ (d-f). Green lines correspond to stable equilibrium solutions, red lines to saddle nodes that are stable to axisymmetric perturbations but unstable against lateral displacements.

direction of gravity. As the Bond number becomes larger, gravity dominates more, (see panels (b) and (c)) and entirely dictates the direction of motion of an evaporating droplet. Panel (d) shows the solution for $B = 0.1$ and $\alpha = -5°$. In this scenario when the gravitational force is weak the wetting pattern drives the droplet to the right, but as gravity increases, the droplet direction is dictated by gravity which moves it to the left, (see panels (e) and (f)).

6.6 Summary

In this chapter, we have analysed the equilibrium properties of droplets under the influence of gravity on a flat surface with periodic wetting patterns. By performing asymptotic analysis in the limit of small Bond numbers, we see that gravity changes a droplet's shape by increasing its radius and decreasing its height while keeping its size constant. The asymptotic analysis however fails at some droplet sizes and as a result we derive exact equations which leads to elliptic integrals which we treat numerically.

Essentially on an horizontal surface where the inclination $\alpha = 0$, it is observed that gravity increases a droplet's radius relative to its height so that its radius matches the radius of a droplet of higher volume with gravity absent. By imposing a non-zero inclination it is seen that the droplet shape become asymmetric tilting to the right if $\alpha > 0$ and to the left if $\alpha < 0$, noting that droplet solution in this scenario only exist if the inclination is less that a critical value.

By considering the energy of the system, we determine that stability of the equilibrium solutions of a droplet and observe that on a symmetric pattern, gravity changes the stability of a droplet the same way a droplet size would in the absence of gravity. It is also discovered that gravity decreases the critical droplet size where a droplet snaps as its evaporates. Meaning that a droplet snap is delayed due to the presence of gravity. On an inclined plane the topology of the bifurcation diagram changes. Instead of curves aligned with either the minimum or maximum of the chemical pattern. Closed isolated solution curves emerges.

On an inclined plane, the ratio of the energy difference to location difference of the pitchfork point and the nearest stable point to its left or right suggests that a droplet would prefer to move to the right if $\alpha > 0$ as it approaches the pitchfork point where its stability changes from stable to saddle node. When $\alpha < 0$, the droplet would prefer the opposite direction. Implying that the direction of motion of an evaporating droplet can be dictated by the inclination of the surface on which it is evaporating.

We also observe that on an asymmetric pattern with amplitude gradient a droplet can be made to move in the opposite direction dictated by gravity when the effect of gravity is weak.

Chapter 7

Gravitational effects on droplet evaporation: Numerical simulations

In the previous chapter, we considered the theory behind droplets under the influence of gravity by solving the Young-Laplace equation which is a balance between the surface tension, capillary and gravity forces. We saw that gravity is able to change the equilibrium configurations of a droplet and can influence the direction of motion upon evaporation. In this chapter we explore this from a computational viewpoint to quantify the dynamics of droplets evaporating under the effects of gravity. We first consider a droplet on an horizontal surface with zero inclination to observe that gravity changes the shape of a droplet by decreasing its height and increasing its radius. For a non-zero inclination, the droplet slides down the surface. Evaporation is then switch on so that as the size of the droplet decreases quasi-statically, it follows the trajectory dictated by bifurcation analysis.

We consider small density contrast and make use of the Boussinesq approximation where the effect of the density difference in the liquid and gas phases is only important in the body force term of the Navier-Stokes equations and is neglected in the inertia terms [68, 69]. Hence the system of Navier-Stokes and Cahn-Hilliard (NS-CH) equations

that was introduced in Chapter 2 is modified as follows:

$$\frac{\partial \phi}{\partial t} + \mathbf{u} \cdot \boldsymbol{\nabla} \phi = M \nabla^2 \eta(\phi), \tag{7.1a}$$

$$\eta = \frac{\sigma}{\chi} \left(F'_m(\phi) - \chi^2 \nabla^2 \phi \right), \tag{7.1b}$$

$$\boldsymbol{\nabla} \cdot \mathbf{u} = 0, \tag{7.1c}$$

$$\rho_L \left(\frac{\partial \mathbf{u}}{\partial t} + (\mathbf{u} \cdot \boldsymbol{\nabla}) \mathbf{u} \right) = - \boldsymbol{\nabla} p + \mu \nabla^2 \mathbf{u} - \phi \boldsymbol{\nabla} \eta + \rho(\phi) \mathbf{g}, \tag{7.1d}$$

where ρ_L is the liquid density, $\mathbf{g} = g(\sin\alpha, -\cos\alpha)$ is the gravitational field, where g is the acceleration due to gravity and α is the surface inclination. We define the total density of the mixture ρ, as an harmonic average of the densities in the liquid and gas phases [70]:

$$\frac{1}{\rho} = \frac{1}{\rho_L} \left(\frac{\phi_e + \phi}{2} \right) + \frac{1}{\rho_G} \left(\frac{\phi_e - \phi}{2} \right), \tag{7.2}$$

here ρ_G, is the density of the gas. The dimensionless density for a liquid-gas mixture is thus defined as:

$$\rho^* = \frac{\rho}{\rho_L} = \frac{2}{(\phi_e + \phi) + (\phi_e - \phi)/\lambda_\rho}, \tag{7.3}$$

where λ_ρ is the density ratio defined as $\frac{\rho_G}{\rho_L}$, so that the dimensionless density ranges from λ_ρ to 1. This harmonic interpolation of the dimensionless density is preferred to

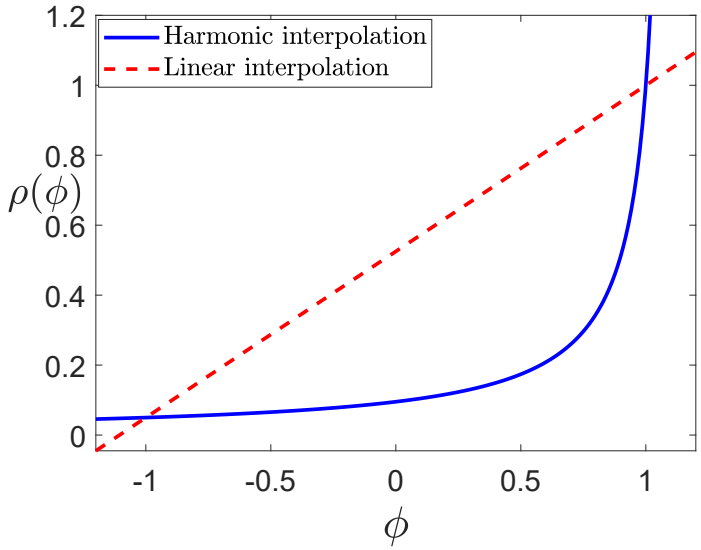

Fig. 7.1 Harmonic (solid blue line) and linear (red dashed line) interpolation of the dimensionless density for density ratio $\lambda_\rho = 0.05$.

a linear interpolation $\rho(\phi) = (\phi_e + \phi) + (\phi_e - \phi)\lambda_\rho$, which leads to unphysical negative density (when the density ratio is large) [71]. Figure 7.1 shows the harmonic and linear interpolation of the dimensionless density profile with density ratio $\lambda_\rho = 0.05$. The blue solid line and the red dashed line denote the harmonic and linear averages respectively. It is seen that for values of the phase-field $\phi < -\phi_e$, negative density emerges for the linear interpolation. As a result, we use the harmonic average to ensure positive values of the density.

By making use of the dimensionless density defined in Eq. 7.3, it is convenient to non-dimensionalise Eqs. (7.1) with the dimensionless variables:

$$\mathbf{r}^* = \frac{\mathbf{r}}{L}, \quad \mathbf{u}^* = \frac{\mathbf{u}}{U}, \quad t^* = \frac{Ut}{L}, \quad p^* = \frac{p}{\rho_L U^2}, \quad \eta^* = \frac{\eta}{\eta_0}, \quad \phi^* = \frac{\phi}{\phi_e}, \tag{7.4}$$

where $\eta_0 = \sigma/L$. With these new variables the system of governing equations become:

$$\frac{\partial \phi}{\partial t} + \mathbf{u} \cdot \boldsymbol{\nabla} \phi = \frac{1}{Pe} \nabla^2 \eta, \tag{7.5a}$$

$$\eta = \frac{1}{Cn} \left(-\phi + \phi^3 - Cn^2 \nabla^2 \phi \right), \tag{7.5b}$$

$$\boldsymbol{\nabla} \cdot \mathbf{u} = 0, \tag{7.5c}$$

$$\frac{\partial \mathbf{u}}{\partial t} + (\mathbf{u} \cdot \boldsymbol{\nabla}) \mathbf{u} = -\boldsymbol{\nabla} p + \frac{1}{Re} \nabla^2 \mathbf{u} - \frac{1}{We} \phi \boldsymbol{\nabla} \eta + \frac{B}{We} \rho(\phi) \mathbf{g}, \tag{7.5d}$$

where we have defined the dimensionless parameters:

$$Re = \frac{\rho_L U L}{\mu}, \qquad Pe = \frac{UL^2}{\sigma M}, \qquad We = \frac{\rho_L L U^2}{\sigma}, \qquad Cn = \frac{\chi}{L}, \qquad B = \frac{\rho_L g L^2}{\sigma},$$

corresponding to the Reynolds, Peclet, Weber, Cahn and Bond numbers respectively. The Reynolds, Peclet, Weber, Cahn and Bond numbers define the ratios between inertia and viscous forces, advective and diffusive transport, inertia and surface tension, diffuse interface width and the characteristic length scale, and gravity and surface tension respectively. The values of the dimensionless parameters used in this chapter are $Re = 1$, $We = 0.2$. As discussed in Chapter 2, the Cahn number is taken be $Cn = 0.01$ to ensure that the Cahn–Hilliard model approaches a sharp-interface limit [46]. For the same reason, the Peclet number is set to $Pe = 1/(3Cn^2)$ [72, 48]. We will consider different values of the Bond number to study the effect of gravity on droplet shape and evaporation.

As we have done in previous chapters, we consider a periodic variation of the surface chemical properties along the lateral coordinate x, which we model using a spatially-

dependent function $\Theta(x)$, given by:

$$\Theta(x) = \theta_0 + \epsilon \mathcal{F}(x, \lambda), \tag{7.6}$$

where θ_0 is the reference homogeneous contact angle, ϵ controls the strength of the chemical pattern and $\mathcal{F}(x, \lambda)$ is a generic periodic function with a wavelength λ. To facilitate direct comparison between theoretical and simulation results, we note that the cross-sectional area of a droplet A, and Bond number B are related to the wavelength as follows:

$$A = \frac{A'}{\lambda^2}, \qquad B = B'\lambda^2,$$

where A' and B' are the values of the droplet area and Bond number that would be imposed in our simulations. The value of the wavelength λ, will be taken to be $1/6$. The system of equations (7.5) is discretized in time using finite difference and in space using the finite element method described in Section 2.3 of Chapter 2. The domain of integration is taken to be 1×0.5.

We note that the formulation introduced in Eqs. (7.5) depends on the numerical parameter λ_ρ, which represents the density ratio. This parameter is not known a priori and needs to be determined. To this end we will perform a data analysis to estimate the optimal value of λ_ρ that gives the best agreement between the numerical computations and analytical solutions of the equilibrium shapes of droplets.

Consider $h_S(x_i)$ for $i = 1, \ldots, N$ to be a set of N data points obtained from solving numerically Eqs. (7.5). Here, h_S represents the profile of the droplet at different spatial points x_i. On the other hand, consider h_T to be the theoretical solution of the droplet's profile obtained from the Young-Laplace formulation. We then define the root mean square error as:

$$E = \sqrt{\frac{1}{N}\sum_{i=1}^{N}\Big(h_S(x_i) - h_T(x_i)\Big)^2}. \tag{7.7}$$

The value of the density ratio that gives the least error will be our optimum value. Figure 7.2 shows comparisons between numerical simulations of the CH-NS system of equations and theoretical solution of the Young-Laplace equation on a flat homogeneous surface with contact angle $\theta_0 = 90^\circ$ and Bond number $B = 1$. Panel (a) shows the errors E for different values of the density ratio denoted by the red circles fitted with a cubic curve in blue solid line. It is seen that the minimum error is attained when the density ratio $\lambda = 0.18$. With this value an agreement between simulation and theoretical results can be achieved. Panel (b) shows droplet equilibrium shape $h(x)$ for theoretical h_T and

simulation h_S results represented by the blue and red lines respectively. It is observed that there is an excellent agreement between the two results.

7.1 Numerical challenges

Once the optimal value for λ_ρ has been found we then use it to perform numerical computations of droplets evaporating under the influence of gravity. We note, however, that there are some numerical challenges that arise when solving the CH-NS equations under the Boussinesq approximation. In this section we summarise them and discuss ways

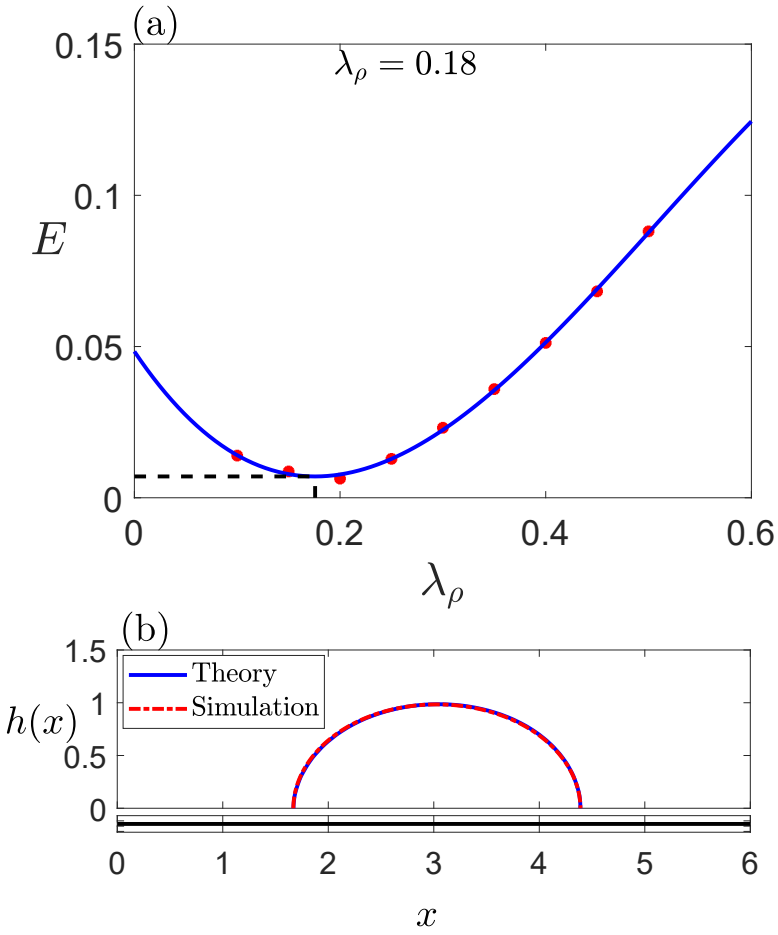

Fig. 7.2 Comparison between numerical simulations of the CH-NS system of equations and theoretical solution of the Young-Laplace equation on a flat homogeneous surface. Panel (a) shows errors E for different values of the density ratio denoted by the red circles fitted with a cubic curve in blue solid line. Panel (b) shows droplet equilibrium shape $h(x)$ for theoretical and simulation results represented by the blue and red lines respectively for $(\theta_0, \epsilon, B, \alpha) = (90°, 0, 1, 0)$.

of overcoming them. First, we find that the equilibrium shape in Fig. 7.2(b) is sensitive to changes in model parameter values such as the Reynolds and Weber number. This is non-physical and is a result of a numerical error that comes with simulating gravitational effects on droplets. Figure 7.3 shows the numerical simulations of the CH-NS system of equations on a flat homogeneous surface. Panel (a) shows the evolution of the maximum magnitude of the velocity in the domain of integration for Bond numbers $B = 0$ and $B = 1$. It is seen that for Bond number $B = 0$, the velocity of the droplet goes to zero at equilibrium. Under these conditions, the Navier-Stokes equation (7.5d) becomes:

$$\boldsymbol{\nabla} p = -\frac{1}{We}\phi\,\boldsymbol{\nabla}\,\eta,$$

which gives the balance between the capillary and surface tension forces equivalent to the Young-Laplace equation. However, in the presence of gravity, Fig. 7.3(a) shows that the droplet's velocity is constant with respect to time at equilibrium but not equal to zero which is non-physical since the droplet is stationary but has a non-zero velocity. This non-zero velocity $\bar{u}$ adds an additional term, say Q, in the steady-state Navier-Stokes equation:

$$We\,\boldsymbol{\nabla} p = -\phi\,\boldsymbol{\nabla}\,\eta + B\rho(\phi)\mathbf{g} + Q, \tag{7.8}$$

where $Q = \frac{We}{Re}\nabla^2\bar{\mathbf{u}} - We(\bar{\mathbf{u}}\cdot\boldsymbol{\nabla})\bar{\mathbf{u}}$. This term depends on the Weber and Reynolds numbers and as a result the equilibrium shape of a droplet would be sensitive to changes in the dimensionless parameters. This implies that our simulation only solves an approximation of the Young-Laplace equation.

This non-zero equilibrium velocity also induces mass loss to the droplet, (Fig. 7.3(b)). The rate of the mass loss is however of the order 10^{-4} and can be negligible. This mass loss can be corrected if the phase-field is advected by the bulk velocity. This can be achieved by replacing $\mathbf{u}\cdot\boldsymbol{\nabla}\,\phi$ with $\boldsymbol{\nabla}\cdot(\mathbf{u}\,\phi)$ in Eq. (7.1a) [73, 74] in which case the velocity is no longer solenoidal and the continuity equation (7.1c) must be taken in its full form:

$$\frac{\partial\rho}{\partial t} + \boldsymbol{\nabla}(\rho\cdot\mathbf{u}) = 0. \tag{7.9}$$

In this scenario, the Boussenesq approximation is not valid any more since density contrast is now important in terms not involving gravity. However, this only corrects the mass loss and the non-zero velocity which introduces an additional term Q to the Young-Laplace equation is still present.

The occurrence of non-zero velocity $\bar{\mathbf{u}}$ is common in numerical simulations and can be corrected by redefining the velocity $\mathbf{u}$ of the system as $\hat{\mathbf{u}} = \mathbf{u} - \bar{\mathbf{u}}$, so that $\hat{\mathbf{u}}$ becomes zero. However, since the non-zero velocity, which depends on the model parameters such

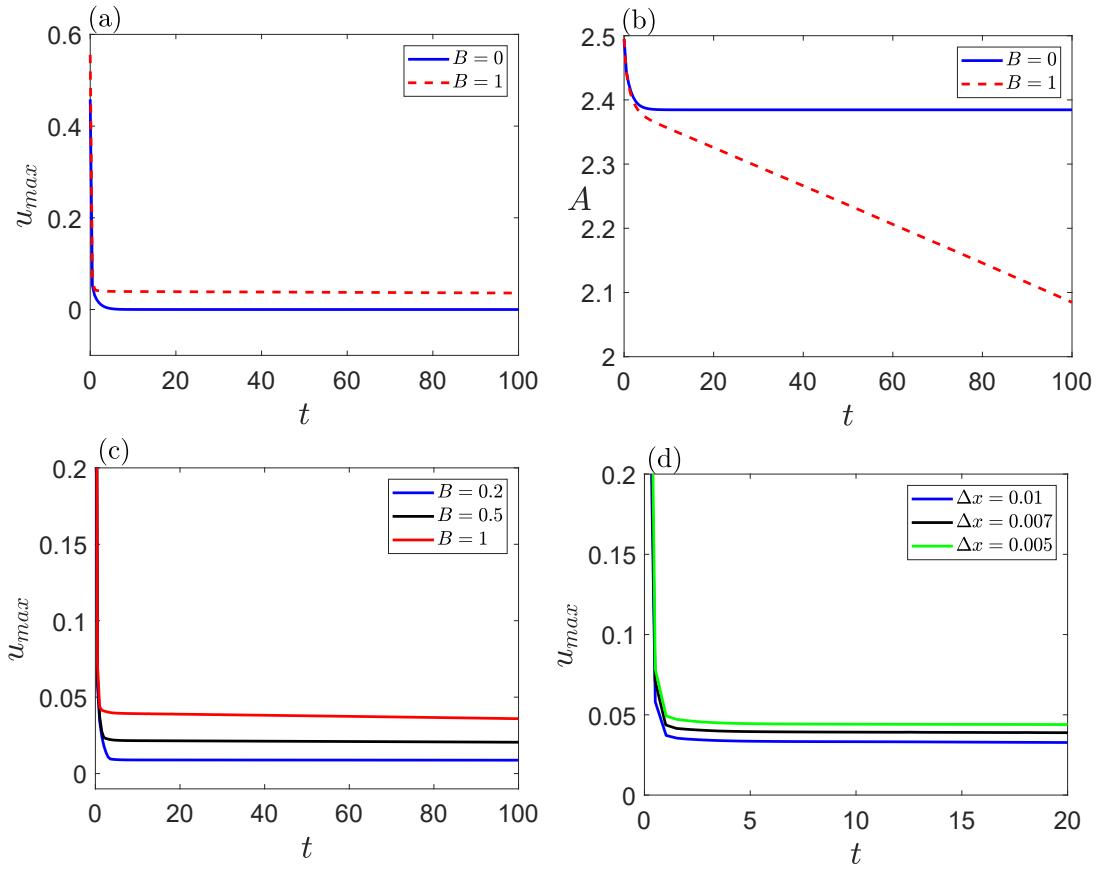

Fig. 7.3 Numerical simulations of the CH-NS system of equations on a flat homogeneous surface. Panel (a) shows the evolution of the maximum magnitude of the velocity in the domain of integration for Bond numbers $B = 0$ and $B = 1$. Panel (b) shows the evolution of droplet size or Bond numbers $B = 0$ and $B = 1$. Panel (c) shows the evolution of the maximum magnitude of the velocity in the domain of integration for different Bond numbers. Panel (d) shows the evolution of the maximum magnitude of the velocity in the domain of integration for different mesh cell sizes Δx, for $(\theta_0, \epsilon, \alpha) = (90°, 0, 0)$.

as the Weber and Reynolds numbers, will first have to be computed, the computational task increases, and the velocity will have to be redefined every time these parameters change. Also, the velocity becoming zero at the start of the simulation means that the Cahn-Hilliard equation will be decoupled from the Navier-Stokes equation. As a result, a better approach will be to eradicate this non-zero velocity or find ways to reduce it. Panel (c) of Fig. 7.3 shows that by decreasing the value of the Bond number, the velocity of the droplet can be reduced thereby decreasing the non-zero velocity in the model. The velocity also decreases by increasing the mesh cell size Δx in our simulation, (see Fig. 7.3(d)). This implies that it can be reduced or even eradicated by considering large mesh sizes. The disadvantage of doing this is that the liquid-gas interface in our

simulation will not be well captured with large mesh sizes. However by using mesh adaptivity [73, 75, 76], mesh sizes can be small close to the interface and large else where. This is beyond the scope of this thesis and as a result we proceed with our current model and consider small Bond numbers to reduce the term Q introduced by the non-zero velocity. In this regime, we can obtain good agreements between simulation and theoretical results since Q is small.

7.2 Model verification

In this section, we will verify our model by running a series of experiments for different inclinations on homogeneous and heterogeneous surfaces with Bond number $B = 0.1$. Figure 7.4 shows the numerical simulations of the CH-NS system of equations for a droplet of size $A = 2.4$ initially located at $\ell = 3$ on a flat surface. Panel (a) shows the evolution of the droplet location for different inclinations on an homogeneous surface with contact angle 60°. It is seen that the droplet always move to the right for $\alpha > 0$, with the droplet speed $v(t) = \Delta\ell/\Delta t$ increasing with inclination, (see Panel (b)). When the inclination is negative, $\alpha < 0$, the droplet moves in the opposite direction as expected, (see panel (c)).

Figure 7.5 shows the numerical simulations of the CH-NS system of equations for droplet size $A = 2.4$ on a flat surface with a symmetric wetting pattern given by Eq. (7.6) with $\mathcal{F}(x) = \cos 2\pi x$ and wetting strength $\epsilon = 0.1$ and homogeneous contact angle $\theta_0 = 60°$ for Bond number $B = 0.1$ and inclination α ranging from 47° to 60° for different

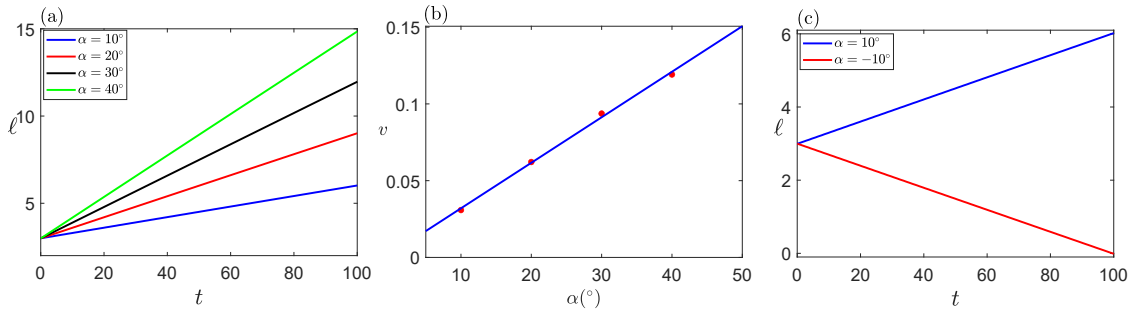

Fig. 7.4 Numerical simulations of the CH-NS system of equations for Bond number $B = 0.1$ and droplet size $A = 2.4$ on a flat homogeneous surface with different inclinations. Panel (a) shows the evolution of the location ℓ of the mid point of the droplet on an homogeneous surface with contact angle, $\theta_0 = 60°$ for inclinations α ranging from 10° to 40°. Panel (b) shows the dependence of the droplet speed v on the inclination angle. Panel (c) shows the evolution of the location of the mid point of the droplet for positive and negative inclinations.

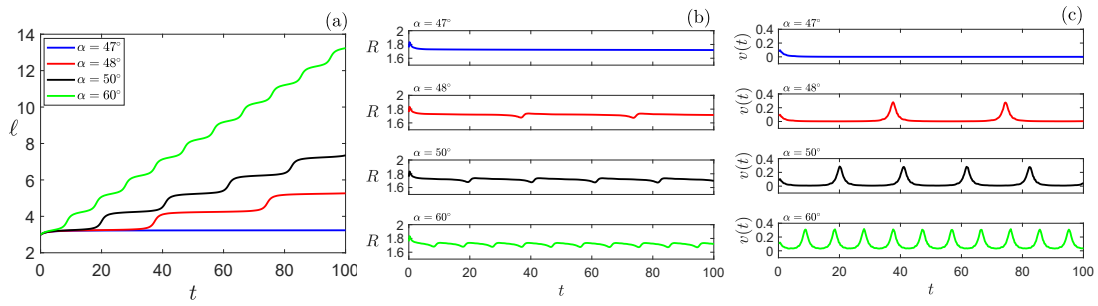

Fig. 7.5 Numerical simulations of the CH-NS system of equations for Bond number $B = 0.1$ and droplet size $A = 2.4$ on a flat surface with a symmetric wetting pattern $\mathcal{F}(x) = \cos 2\pi x$ with wetting strength $\epsilon = 0.1$ and homogeneous contact angle $\theta_0 = 60°$ for different inclinations α ranging from 47° to 60°. Panel (a) shows the evolution of the location ℓ of the mid point of the droplet. Panel (b) shows the evolution of the droplet radius R. Panel (c) shows the evolution of speed of the droplet $v(t)$.

inclinations. In agreement with Eq. (6.17) of Chapter 6, it is seen that the droplet moves downhill in the direction of gravity when the inclination exceeds a critical value $\alpha = 47°$, similar to what Savva et al. [77] observed, where a droplet attains its equilibrium shape when the surface inclination is below a critical value. Panel (a) shows the evolution of the droplet mid-point which initially is at $\ell = 3$. It is seen that the droplet attains an equilibrium configuration when the inclination is below a critical value $\alpha = 47°$ and moves to the right otherwise in the direction of gravity. In this scenario the droplet moves slowly and jumps rapidly covering a wavelength of the chemical pattern when it reaches the minimum of the chemical pattern. Also, it is observed that the distance the droplet covers increases as the inclination increases. The evolution of the droplet radius is also shown in panel (b) of Fig. 7.5. It is seen that there is a sudden change in the droplet radius as its location changes. The number of such rapid change in the droplet radius increases as the surface inclination increases. The evolution of the droplet speed is shown in panel (c). It is observed that the speed of the droplet is close to zero except when the droplet approaches the minimum of the chemical pattern where its speed rapidly increases and decreases in a snap event.

7.3 Droplet evaporation

The evaporation of a 2D droplet on a solid surface is examined in this section. We assume that the evaporation is quasi-static and driven by mass diffusion in the gaseous phase. We use a diffuse interface formulation to model such a system, which includes both a wetting boundary condition of the solid substrate $\mathbf{n} \cdot \boldsymbol{\nabla} \phi \approx \frac{\sqrt{2}}{3Cn} \cos\theta_e$, where θ_e is the

equilibrium contact angle given by Eq. (7.6) and an open top boundary $\boldsymbol{\nabla}\eta\cdot\mathbf{n}=-\eta_w$, where η_w controls the evaporation rate, (see Chapter 2).

We first consider a droplet evaporating on a symmetric chemical pattern given by Eq. (7.6) with $\mathcal{F}(x)=\cos(2\pi x)$ and $\epsilon=0.1$. The droplet is initially aligned with a maximum of the chemical pattern. We set the evaporation rate to $\eta_w=2$. Figure 7.6 shows the comparison between theoretical results and numerical simulations of the CH-NS system of for droplets on symmetric pattern $\mathcal{F}(x)=\cos 2\pi x$ with wetting strength $\epsilon=0.1$ and homogeneous contact angle $\theta_0=60^\circ$ for Bond number $B=0.1$ and different inclination angles. The green lines represent stable equilibrium solutions, red lines denote saddle nodes that are stable to axisymmetric perturbations but unstable against lateral displacements. Numerical simulations of the CH-NS system of equations are denoted by the blue lines.

Panel (a) shows the results for $\alpha=0$ and it is seen that there is an excellent agreement between theoretical and simulation results. Initially the droplet is on a stable branch at $(\ell,A)=(3,2.4)$ and as its size decreases via evaporation it remains in the same location until it reaches the pitchfork point where its stability changes from stable to saddle node that is stable to axisymmetric perturbations but unstable against lateral displacement. As a result the droplet moves rapidly in a snap event to the nearest stable branch. The droplet could either move to the left or to the right due to the symmetry of the chemical pattern. In this scenario, the droplet moves to the right and remains at the stable branch

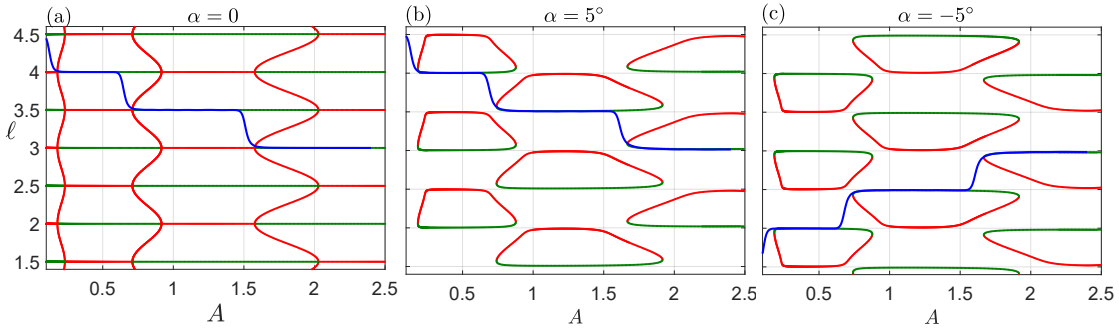

Fig. 7.6 Comparison between theoretical results and numerical simulations of the CH-NS system of for droplets on symmetric pattern $\mathcal{F}(x)=\cos 2\pi x$ with wetting strength $\epsilon=0.1$ and homogeneous contact angle $\theta_0=60^\circ$ for Bond number $B=0.1$ and different inclination angles (a) $\alpha=0$ (b) $\alpha=5^\circ$ (c) $\alpha=-5^\circ$ on the (ℓ,A) planes. Green lines correspond to stable equilibrium solutions, red lines to saddle nodes that are stable to axisymmetric perturbations but unstable against lateral displacements. Numerical simulations of the CH-NS system of equations are denoted by the blue lines.

until its size reaches the pitchfork value where it changes location rapidly again in a snap event. This cycle continues until the droplet vanishes.

Panel (b) of Fig. 7.6 shows the result for $\alpha = 5°$. In this case the bifurcation diagram has become disconnected by gravity forming a series of close cycles of solution branches with stable branches tilting in the direction of gravity. As a result a bias is introduced by gravity that breaks the droplet symmetry as it approaches the pitchfork point. In this scenario, the droplet moves to the right in the direction of gravity as it snaps. When the direction of gravity reversed by imposing $\alpha = -5°$ the droplet moves in the opposite direction snapping to the left as it reaches the pitchfork point where its stability changes, (see panel (c)). This shows that the direction of motion of an evaporating droplet can be controlled by surface inclination α.

A droplet on an horizontal surface with $\alpha = 0$ and symmetric chemical patterns under the influence of gravity can either move to the left or right as it approaches the pitchfork points. The direction of movement of the droplet as it snaps cannot be controlled without the inclination of the surface, in which case the droplet snaps to the right when $\alpha > 0$ and to the left when $\alpha < 0$. As a result, we explore non symmetrical chemical pattern in order to control the course of movement of an evaporating droplet when $\alpha = 0$ to determine whether a change in droplet size allows directed movement as its location is changed. Also we will investigate if it is possible to move a droplet against gravity. For instance, we know that imposing $\alpha < 0$ moves the droplet to the left. Now the question is, can a droplet be moved to the right by prescribing an unsymmetrical contact angle pattern. To this end, we consider the pattern with a gradient amplitude discussed in Section 6.5.2 of Chapter 6:

$$\mathcal{F}(x) = \frac{2}{\pi} \arctan\left(\frac{x}{L}\right) \cos(2\pi x), \tag{7.10}$$

where L is the length over which the gradient varies, (we note that the change of sign of the gradient can be imposed by replacing x by $L - x$ in the argument of the arctan).

Figure 7.7 shows the comparison between theoretical results and numerical simulations of the CH-NS system of for droplets on asymmetric pattern (7.10) with strong bias $L = 6$, wetting strength $\epsilon = 0.1$ and homogeneous contact angle $\theta_0 = 60°$ for Bond number $B = 0.1$ and different inclination angles. Green lines correspond to stable equilibrium solutions, red lines to saddle nodes that are stable to axisymmetric perturbations but unstable against lateral displacements. Numerical simulations of the CH-NS system of equations are denoted by the blue lines. It is seen that there is a topological change in the bifurcation diagram and the branches now becomes disconnected stable and saddle node

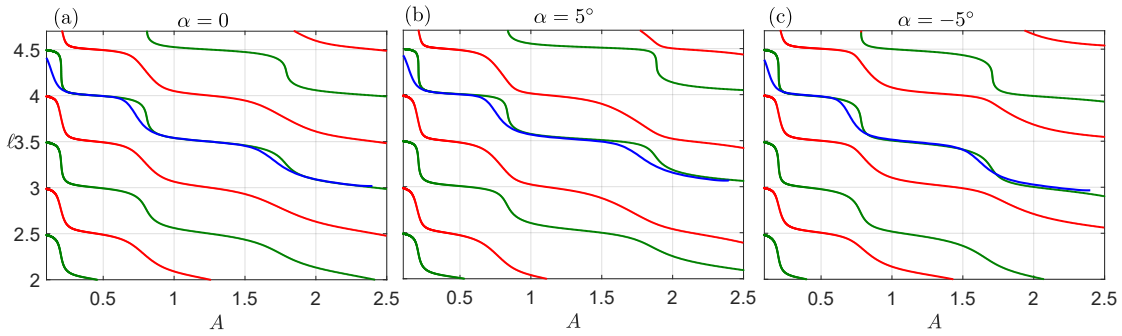

Fig. 7.7 Comparison between theoretical results and numerical simulations of the CH-NS system of for droplets on asymmetric pattern (7.10) with strong bias $L = 6$, wetting strength $\epsilon = 0.1$ and homogeneous contact angle $\theta_0 = 60°$ for Bond number $B = 0.1$ and different inclination angles (a) $\alpha = 0$ (b) $\alpha = 5°$ (c) $\alpha = -5°$ on the (ℓ, A) planes. Green lines correspond to stable equilibrium solutions, red lines to saddle nodes that are stable to axisymmetric perturbations but unstable against lateral displacements. Numerical simulations of the CH-NS system of equations are denoted by the blue lines.

branches. As a result a droplet on a stable branch continues to move to the right when $\alpha = 0$, (see panel (a)), when $\alpha = 5°$, (see panel (b)) and when (c) $\alpha = -5°$, (see panel (c)). The case where $\alpha = -5°$ is particularly interesting because gravity suggests that the droplet should move to the left but it moves to the right following the stable branch of the bifurcation diagram induced by the asymmetric pattern (7.10). Hence we see that an asymmetric pattern controls the direction of an evaporating droplet regardless of the direction of gravity.

Increasing the Bond number to $B = 0.2$ further changes the bifurcation diagram and creates a strong competition between the wetting pattern and gravity in determining the direction of motion of an evaporating droplet. Figure 7.8 shows the comparison between theoretical results and numerical simulations of the CH-NS system of for droplets on asymmetric pattern (7.10) with strong bias $L = 6$, wetting strength $\epsilon = 0.1$ and homogeneous contact angle $\theta_0 = 60°$ for Bond number $B = 0.2$ and different inclination angles. Green lines correspond to stable equilibrium solutions, red lines to saddle nodes that are stable to axisymmetric perturbations but unstable against lateral displacements. Numerical simulations of the CH-NS system of equations are denoted by the blue lines. Panel (a) shows the result for $\alpha = 5°$. It is seen that the bifurcation diagram changes into closed curves with stable branches tilting upwards. As a result gravity dictates that the droplet will move to the right. The asymmetric chemical pattern also shows that the droplet will move to the right. Hence the droplet moves to the right to a stable branch at a lower droplet size as it evaporates. Panel (b) shows the result for $\alpha = -5°$. In this scenario, gravity suggests that the droplet will move to the left and the wetting pattern

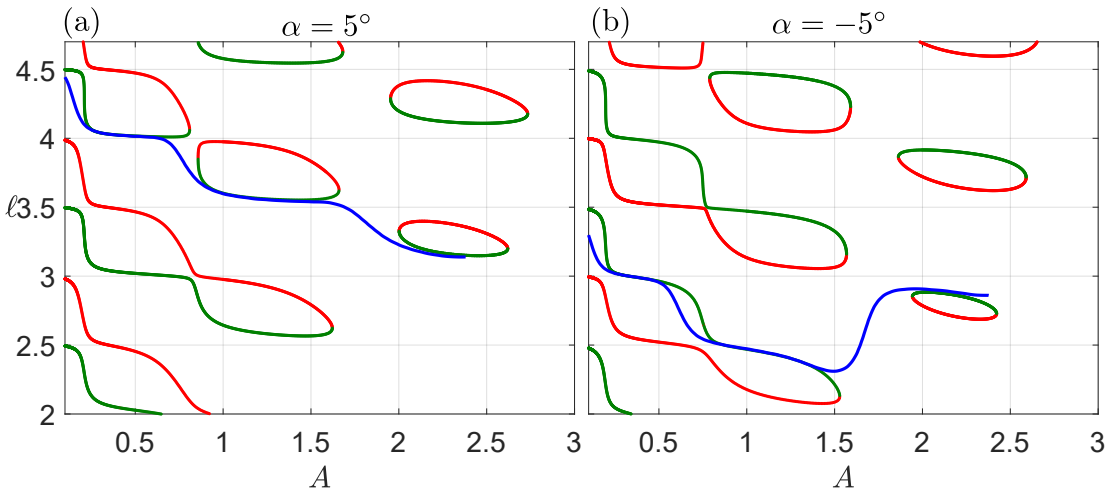

Fig. 7.8 Comparison between theoretical results and numerical simulations of the CH-NS system of for droplets on asymmetric pattern (7.10) with strong bias $L = 6$, wetting strength $\epsilon = 0.1$ and homogeneous contact angle $\theta_0 = 60°$ for Bond number $B = 0.2$ and different inclination angles (a) $\alpha = 5°$ (b) $\alpha = -5°$ on the (ℓ, A) planes. Green lines correspond to stable equilibrium solutions, red lines to saddle nodes that are stable to axisymmetric perturbations but unstable against lateral displacements. Numerical simulations of the CH-NS system of equations are denoted by the blue lines.

dictates that it will move to the right. Since gravity dominates at location $\ell = 2.8$, the droplet moves to the left to the point $\ell = 2.4$ as it snaps. At this location the wetting pattern is strong and the droplet moves to the right. Hence we see that the competition between the asymmetric wetting pattern and gravity determines the direction of motion of an evaporating droplet.

By considering a weak bias in the asymmetric pattern (7.10), there is also a strong competition between gravity and the asymmetric wetting pattern to determine the direction of motion of evaporating droplets. Figure 7.9 shows the comparison between theoretical results and numerical simulations of the CH-NS system of for droplets on asymmetric pattern (7.10) with weak bias $L = 0.6$, wetting strength $\epsilon = 0.1$ and homogeneous contact angle $\theta_0 = 60°$ for Bond number $B = 0.1$ and different inclination angles. Green lines correspond to stable equilibrium solutions, red lines to saddle nodes that are stable to axisymmetric perturbations but unstable against lateral displacements. Numerical simulations of the CH-NS system of equations are denoted by black, magenta and blue lines. Panel (a) shows results for $\alpha = 0$. It is seen that there are disconnected branches and that there is an excellent agreement between theoretical and simulation results with the droplet snapping to the right at the pitchfork point where its stability changes as dictated by the asymmetric pattern. Panel (b) of Fig. 7.9 shows results for

$\alpha = 5°$. The bifurcation diagram shows that there are disconnected branches at lower locations where the wetting pattern is strong and closed curves at higher locations where the effect of gravity is strong. As a result, starting evaporation at different locations results in the droplet moving to the right in all cases since both gravity and wetting pattern dictates a rightward movement. Panel (c) shows results for $\alpha = -5°$, where the asymmetric pattern dictates a rightward movement and gravity dictates a leftward movement. Hence the direction of motion of an evaporating droplet depends on the initial location of the droplet. With an initial location of $\ell = 2.1$ where the wetting pattern is strong, the droplet, (black line) moves to the right at the pitchfork points as dictated by the chemical pattern. Also, at location $\ell = 3$, although the solution branches have been closed by gravity, the effect of the wetting pattern is still present. This makes the droplet, (magenta line) move to the right as it snaps. At initial location $\ell = 4$, the effect of gravity is now very strong and the droplet, (blue line) moves to the left $\ell = 3$ as dictated by gravity at the pitchfork point. Since the effect of the wetting pattern is present at this location, the droplet snaps back to the right at it reaches the pitchfork point.

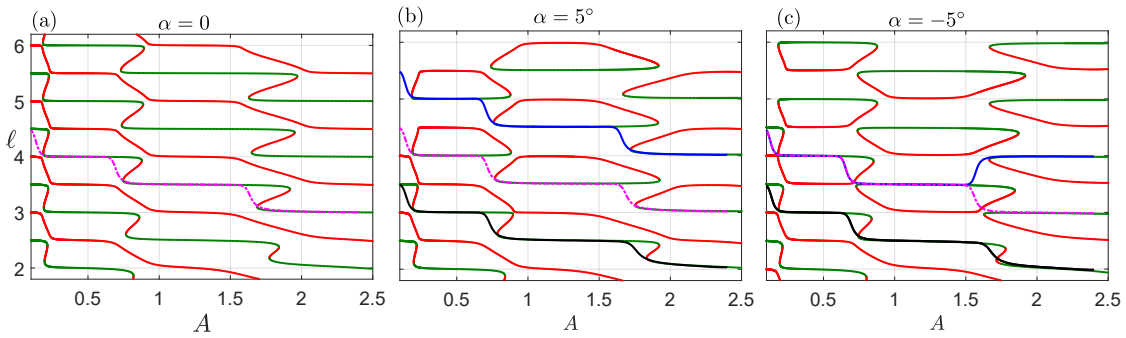

Fig. 7.9 Comparison between theoretical results and numerical simulations of the CH-NS system of for droplets on asymmetric pattern (7.10) with weak bias $L = 0.6$, wetting strength $\epsilon = 0.1$ and homogeneous contact angle $\theta_0 = 60°$ for Bond number $B = 0.1$ and different inclination angles (a) $\alpha = 0$ (b) $\alpha = 5°$ (c) $\alpha = -5°$ on the (ℓ, A) planes. Green lines correspond to stable equilibrium solutions, red lines to saddle nodes that are stable to axisymmetric perturbations but unstable against lateral displacements. Numerical simulations of the CH-NS system of equations are denoted by black, magenta and blue lines.

7.4 Summary

In this chapter, we compared the theoretical results derived in Chapter 6 with simulations of the Cahn-Hilliard and Navier-Stokes system of equations that models droplets under the influence of gravity. We observed that on an horizontal surface with symmetric pattern. The direction of motion of an evaporating droplet cannot be controlled except the surface in inclined, in which case the droplet moves to the right when the inclination $\alpha > 0$ and to the left when $\alpha < 0$.

With asymmetric pattern, the direction of motion of an evaporating droplet can be effectively controlled. In the scenario where gravity is weak the asymmetric pattern moves an evaporating droplet against gravity. As gravity increases slightly there is a competition between gravity and the wetting pattern in determining a droplet's direction of motion upon evaporation.

The non-zero velocity that emerges when gravity is introduced into the CH-NS system of equations means that numerically we have only solved an approximation of the Young-Laplace equation. However, it is interesting to see that these preliminary numerical results are in good agreement with the theoretical findings obtained in Chapter 6.

Chapter 8

Concluding remarks and future research

8.1 General conclusions

The control of droplet evaporation on smooth surfaces have been achieved in this thesis using chemical patterns. First we considered regimes where the droplet sizes are less than the capillary length scale so that the effect of gravity is negligible. In this limit, symmetric patterns were examined using bifurcation analysis. The equilibrium solutions of droplets on such surfaces were obtained by solving the Young-Laplace equation, which is a balance between capillary and surface tension forces. The stability of the equilibrium solutions were then studied. As the stability of a droplet changes from stable to saddle node, the droplet moves suddenly to a stable branch in a snap event. This is promoted by an hierarchy of bifurcations triggered by the underlying patterns. In this scenario, the droplet can move to the left or to the right since the pattern is symmetric. However, by imposing an asymmetric pattern, the droplet can be made to move in a specific direction. In the regime where the droplet size becomes larger than the capillary length scale where gravity effects becomes important, this asymmetric pattern can also move a droplet against gravity. Also, on topographic surfaces, imposing a chemical pattern can either amplify or annihilate the snap process and also control the direction of motion of evaporating droplets. Dynamic simulations of Cahn-Hilliard and Navier-Stokes (CH-NS) system of equations were performed to verify these results with excellent agreements.

8.1.1 Diffuse interface formulation

We introduced the Cahn-Hilliard and Navier-Stokes system of equations in Chapter 2, which were used throughout this thesis to study droplet dynamics on solid surfaces. We described a numerical algorithm for solving the CH-NS system using the finite element method. The method's validity was tested through a series of numerical experiments that included droplet equilibrium shapes as well as the dynamics of a droplet spreading and relaxing to equilibrium. We discovered that droplets spread faster as they become less viscous and have a higher surface tension. A gradient in the chemical potential was used to simulate droplet evaporation on solid surfaces. It was observed that footprint $R(t)$ of a droplet evaporating on an homogeneous surface follows the $R(t) \sim (t_e - t)^{1/2}$ law, where t is time and t_e is the evaporation time.

8.1.2 Droplet evaporation on smooth chemical patterns

In Chapter 3, we discussed analytical and computational findings for quasi-static evaporation of a 2D droplet on a smooth, chemically patterned surface. Pinning-free patterns with a smooth and periodic variation of the local equilibrium contact angle were considered. Pitchfork bifurcations occur at well described locations of the chemical pattern, regardless of the homogeneous contact angle and magnitude of the chemical variation, according to a detailed bifurcation analysis. We also discovered that the amplitude critical value ϵ_c scales with the size of the droplet A_c as $\epsilon_c \sim A_c^{-1/2}$, implying that cusp bifurcations are preferred in the microscopic limit. When a bias is introduced into the chemical pattern, the bifurcation diagrams undergo a topological transition, with equilibrium solutions being represented by disconnected branches in the parameter space. The droplet's midpoint, i.e. $\ell(A)$, continuously parametrizes those branches, which can be either stable or saddle points, meaning that increasing the droplet's size can result in a continuous lateral displacement.

Using the Cahn-Hilliard and Navier-Stokes systems of equations, we also investigated droplet dynamics during evaporation. On a symmetric pattern, an evaporating droplet can either snap to the left or to the right when it reaches the pitchfork point where its stability changes. Our results show that the *snap evaporation* reported on non-planar symmetric substrates [34] is also observed on planar surfaces with symmetric chemical patterns, and in both cases, this is a consequence of a hierarchy of pitchfork and saddle-node bifurcations. However, with asymmetrical chemical patterns, the presence of disconnected branches leads to a smooth droplet's motion where its location continuously changes towards one direction, hence showing that droplet's motion can be controlled

upon evaporation. The ideas presented here can be used in applications of droplet control and mass transport.

8.1.3 Snap dynamics

The snap dynamics of evaporating droplets on a smooth asymmetric pattern were investigated in Chapter 4. As the footprint reaches the pitchfork points where the droplet's stability varies from stable to saddle node, a droplet evaporating on smooth periodic asymmetric patterns exhibits rapid changes in its location and footprint. We calculated these critical pitchfork points numerically and demonstrated that the critical droplet size at which snaps occur is related to wetting strength and decreases as wetting strength increases. This was confirmed by performing a series of simulations with various wetting strengths, indicating that the critical droplet size can be regulated by adjusting the wetting strength. It was also observed that the snap time τ decreases as the wetting strength ϵ increases, while the quantity q related to the snap speed increases with the wetting strength. By considering different values of the Ohnesorge number Oh, we saw that the snap time increase with the Ohnesorge number, and the quantity q related to the snap speed decreases as the Ohnesorge number increases. Meaning that the viscosity, inertia and surface tension of a droplet affects its snap time and speed.

We concluded that the maximum snap speed is linked to the droplet size according to $v_{max} \sim A^{-1/2}$ by considering energy conversion during snap events under certain assumptions. The quantity q that quantifies droplet snap speeds obeys the following scaling law $q \sim Oh^{-1}$, which we deduced from the dissipation energy law. As a result, by specifying variables in terms of wetting strength ϵ and Ohnesorge number Oh, the speed $v(t)$ can be rescaled to obtain a single universal curve for all wetting strengths and Ohnesorge numbers.

These results indicates that the snap time and speed can be effectively controlled by varying the wetting strength ϵ, droplet size A, its viscosity, surface tension and inertia.

8.1.4 Droplet evaporation on smooth topographies

In Chapter 5, the effect of imposing chemical patterns on a topography was discussed. We saw that on such surfaces, the combination of periodic chemical and topographical patterns can either amplify or annihilate snap effects. When both patterns are in phase the snap event is amplified with the droplet snapping at an increased speed. However, when the chemical and topographic patterns are out of phase, the snap process is annihilated and the droplet size decreases continuously without a sudden change in its

radius or location. In this scenario, the direction of evaporating droplets can be effectively controlled through the sign of the wetting strength of the chemical pattern.

8.1.5 Influence of gravity on droplets

We looked at droplets evaporating under the influence of gravity on a flat surface with periodic wetting patterns in Chapter 6. We discovered that gravity changes the shape of a droplet by increasing its radius and decreasing its height while holding its size constant by conducting asymptotic analysis in the limit of small Bond numbers. However, the asymptotic analysis fails at certain droplet sizes, so we devised exact equations that lead to elliptic integrals, which we solve numerically. For non-zero inclination, it was observed that the droplet shape become asymmetric tilting to the right if $\alpha > 0$ and to the left if $\alpha < 0$

We determined the stability of the equilibrium solutions of a droplet by considering the energy of the system and observed that on a symmetric pattern, gravity changes the stability of a droplet in the same way that droplet size would in the absence of gravity. Gravity also reduces the critical droplet size at which a droplet snaps as it evaporates. That is, the presence of gravity causes a droplet snap to be delayed. The topology of the bifurcation diagram changes on an inclined plane. Instead of curves aligned with the chemical pattern's minimum or maximum. Isolated closed solution curves emerge.

A droplet would tend to travel downhill to the right if $\alpha > 0$ as it reaches the pitchfork point where its stability changes from stable to saddle node. When $\alpha < 0$, the droplet will prefer to move in the opposite direction. Indicating that the inclination of the surface can determine the direction of motion of an evaporating droplet. However, when the influence of gravity is weaker than the intensity of the wetting pattern, a droplet can be made to move in the opposite direction determined by gravity on an asymmetric pattern with amplitude gradient. These results were confirmed by simulations of the Cahn-Hilliard and Navier-Stokes system of equation in Chapter 7 with excellent agreements. These results show that with asymmetric pattern, the direction of motion of an evaporating droplet can be effectively controlled.

8.2 Future research

Several interesting extensions can be made to the work considered in this thesis. This include studying droplets evaporation on asymmetric topographies, investigating the influence of gravity on droplets evaporation on smooth topographies. Other droplet

dynamics can also be considered, for example mass transfer problems, where liquid can be pumped in/out of the droplet through a pore. Also, since we have studied two-dimensional droplets in this thesis, extensions can be made to three-dimensional droplets.

8.2.1 Droplets evaporation on asymmetric topographies

Having quantified a physical mechanism by which is possible to control the motion of an evaporating droplet on a planar surface with asymmetric wetting patterns. The direction of motion of a droplet evaporating on a non-planar surface can also be controlled by exploiting asymmetric topographies, such as those shown in Fig. 8.1. One of the key advantage of considering these surfaces (as opposed to flat surfaces with wetting patterns) is that they are much easier to implement experimentally.

The bifurcation analysis discussed in Chapters 3 and 5 can be used to study how the the direction of motion of evaporating droplets can be controlled. Computationally this problem can be investigated by solving the Cahn-Hilliard and Navier-Stokes system of equations discussed in Chapter 2. The analytical treatment for this problem will be based on finding equilibrium solutions of the droplet, denoted by $h(x)$, for a given surface topography design, which is described in terms of a generic function $\mathcal{F}(x)$. In the absence of gravity such solutions satisfy the Young-Laplace equation:

$$\frac{\Delta p}{\gamma} = \frac{y_{xx}}{(1+y_x^2)^{3/2}}, \tag{8.1}$$

where $y(x) = h(x) + \mathcal{F}(x)$, Δp is the pressure across the liquid/gas interface and γ is the surface tension. For a fixed droplet area A, the solutions of the above equation can be described in terms of the droplet's midpoint and contact radius, (ℓ, R), and the apparent contact angle θ_a, which is given by

$$\tan(\theta_0 - \theta_a) = \pm \mathcal{F}_x(\ell \pm R), \tag{8.2}$$

where θ_0 is the constant local contact angle of the surface. The stability of these solutions can then be determined by analysing the interfacial energy of the system:

$$E(\ell, R) = \frac{2\gamma R\theta_a}{\sin\theta_a} - \gamma\cos\theta_0 \int_{\ell-R}^{\ell+R} \sqrt{1+(\mathcal{F}_x(x))^2}\, dx. \tag{8.3}$$

This formulation can be used to construct bifurcation diagrams as the volume A of the droplet is varied, hence establishing the path of stable equilibrium solutions that the droplet may follow as its volume slowly changes in time due to evaporation.

8.2.2 Influence of gravity on droplets evaporation on smooth topographies

The influence of gravity on droplet shape and evaporation on a planar surfaces with well defined chemical patterns was considered theoretically in Chapter 6 and confirmed by simulations of the Cahn-Hilliard and Navier-Stokes equations in Chapter 7. This can be extended to include gravity effects on droplets on a non-planar surface $\mathcal{F}(x)$ by considering the Young-Laplace equation:

$$\Delta p + B(x\sin\alpha + y\cos\alpha) = -\frac{y_{xx}}{(1+y_x^2)^{\frac{3}{2}}}, \tag{8.4}$$

with $y(x) = h(x)+\mathcal{F}(x)$, where h, Δp, B, and α are the droplet shape, the pressure across the liquid/gas interface, Bond number and surface inclination respectively. Equation 8.4 can then be solved to obtain the droplet shape h, radius R and location ℓ subject to the boundary conditions:

$$\theta_a^+ = \theta_0 - \tan^{-1}\mathcal{F}_x(\ell + R), \tag{8.5a}$$
$$\theta_a^- = \theta_0 - \tan^{-1}\mathcal{F}_x(\ell - R), \tag{8.5b}$$

where θ_0, θ_a^-, and θ_a^+ are the homogeneous, left and right contact angles respectively. The dynamics of the problem can be investigated through simulations of the Cahn-Hilliard and Navier-Stokes system of equations used in this thesis.

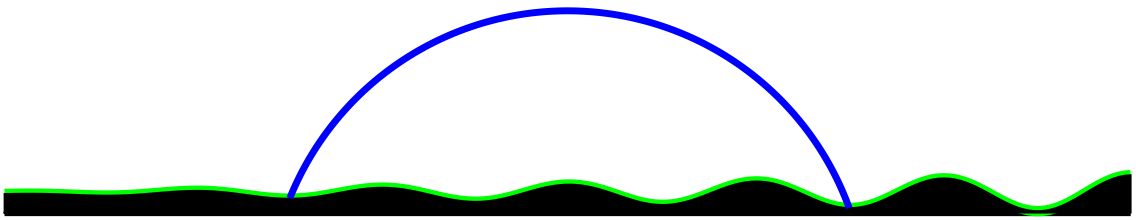

Fig. 8.1 Droplet on an asymmetric topography with positive gradient.

8.2.3 Other droplet dynamics

This analysis can also be extended to a wider class of physical problems that are characterised by volume variations of the droplet. For example, droplet condensation, where the volume would be increasing in time, and mass transfer problems, where liquid can be pumped in/out of the droplet through a pore [52] on a non-planar surface with or without gravity. The equilibrium solutions and their stability can be studied via bifurcation analysis discussed in Chapter 3 and the dynamics studied through simulations of the Cahn-Hilliard and Navier-Stokes system of equations used in this thesis.

8.2.4 Three dimensional droplets

This thesis only discusses two-dimensional droplets. However, extensions can be made to three dimensions. Computationally, this will involve extending the variational formulation of the Cahn-Hilliard and Navier-Stokes system of equations given in the Appendix B to three dimensions.

Appendix A

Wetting boundary condition: contact angle

In this Appendix we derive Eq. (2.13) of the main text, which is a relationship between the contact angle of the droplet θ_e, and the parameter a imposed in the wetting boundary condition of the diffuse interface formulation. To find the relation between a and the equilibrium contact angle θ_e, we first compute the surface tensions as follows. By considering a flat interface y in a one-dimensional system where the solid is located at $y = 0$, and noting that the chemical potential η (2.2) vanishes at equilibrium, we have that

$$F'_m(\phi) = \chi^2 \frac{d^2\phi}{dy^2}.$$

Integrating the above relation from ϕ_e to ϕ and noting that $F_m(\phi_\mathrm{e}) = 0$ gives:

$$F_m(\phi) = \frac{\chi^2}{2}\left(\frac{d\phi}{dy}\right)^2, \tag{A.1}$$

which can be used in the bulk free energy equation (2.1) so that it becomes:

$$\begin{aligned}
\mathcal{F}[\phi] &= \int_0^\infty \frac{\sigma}{\chi}\left[F_m(\phi) + \frac{\chi^2}{2}\left(\frac{d\phi}{dy}\right)^2\right] dy + F_w(\phi), \\
&= \int_0^\infty \sigma\chi\left(\frac{d\phi}{dy}\right)^2 dy + F_w(\phi), \\
&= \sigma\int_\phi^{\phi_\mathrm{e}} \sqrt{2F_m(\phi)}\, d\phi + F_w(\phi), \\
&= \frac{\sigma}{\sqrt{2}}\int_\phi^{\phi_\mathrm{e}} \pm(1-\phi^2)\, d\phi + F_w(\phi),
\end{aligned} \tag{A.2}$$

where we have used $F_m(\phi) = \frac{1}{4}(1-\phi^2)^2$. The surface tension on the solid-gas interface is then given as:

$$\begin{aligned}\gamma_{sg} &= \frac{\sigma}{\sqrt{2}}\int_{\phi_{sg}}^{-1}(1-\phi^2)\,d\phi + F_w(\phi_{sg}),\\ &= \frac{\sigma}{\sqrt{2}}\left[-\frac{2}{3} - (1+\omega)\phi_{sg} + \frac{\phi_{sg}^3}{3}\right],\end{aligned} \tag{A.3}$$

where $F_w(\phi_{sg}) = -a\phi_{sg}$, ϕ_{sg} is the value of the phasefield at the solid-gas interface and the parameter ω called the wetting potential is defined as $\omega = \frac{\sqrt{2}}{\sigma}a$. Similarly, the surface tension on the solid-liquid interface is given as:

$$\begin{aligned}\gamma_{sl} &= \frac{\sigma}{\sqrt{2}}\int_{\phi_{sl}}^{+1}(\phi^2-1)\,d\phi + F_w(\phi_{sl}),\\ &= \frac{\sigma}{\sqrt{2}}\left[-\frac{2}{3} + (1-\omega)\phi_{sl} - \frac{\phi_{sl}^3}{3}\right].\end{aligned} \tag{A.4}$$

Since the phasefield at the liquid-gas interface is zero, the wetting function at the liquid-gas interface $F_m(\phi_{lg})$ vanishes. As a result, the surface tension on the liquid-gas interface is obtained as:

$$\gamma = \frac{\sigma}{\sqrt{2}}\int_{-1}^{+1}(1-\phi^2)\,d\phi = \frac{2\sqrt{2}}{3}\sigma. \tag{A.5}$$

To simplify Eqs. (A.3) and (A.4), we need to find expressions for ϕ_{sg} and ϕ_{sl} in terms of the wetting potential ω. Equation (2.3) in one-dimension gives $\frac{d\phi}{dy} = -\frac{a}{\sigma\chi}$. Combining this with Eq. (A.1) we have that

$$1-\phi^2 = \pm\omega,$$

where ϕ_{sg} can now be obtained by noting that $\phi_{sg} < 0$, so that :

$$\phi_{sg} = -(1+\omega)^{\frac{1}{2}}. \tag{A.6}$$

Similarly, ϕ_{sl} is obtained by taking $\phi_{sl} > 0$:

$$\phi_{sl} = (1-\omega)^{\frac{1}{2}}. \tag{A.7}$$

Inserting equations (A.3), (A.4), (A.6), (A.7) in Young's equation (2.12), we obtain:

$$\cos\theta_e = \frac{1}{2}\left[(1+\omega)^{3/2} - (1-\omega)^{3/2}\right].$$

Appendix B

FEniCS Python code

FEniCS [61], is an open-source computing platform for solving partial differential equations. Variational forms expressed in the unified form language [62] allows the translation of finite element equations into a format which FEniCS recognises. In this thesis, the variational forms of the Cahn-Hilliard and Navier-Stokes (CH-NS) system of equations (2.5) are written in Python programming language as follows:

```
# ======================================================================
# Diffuse-interface hydrodynamic model for droplet evaporation
# ======================================================================
#
# Begin program
from __future__ import print_function
import random
import numpy as np
import math
from mshr import *
from dolfin import *
from array import *
import scipy as sp
import scipy.optimize

# Print log messages only from the root process in parallel
parameters["std_out_all_processes"] = False;

# Load Initial condition (read from file if True)
load = False
#load = True
init_file = 'initial_condition.xml'  #initial file

########################################
```

```
# Initial Droplet parameters
########################################
Th00 = 70*pi/180  # Initial angle
epsc = 0.1        # Chemical amplitude of variation
                  # (set this to zero if there is no chemical pattern)
epsT = 0.05       # Topographic of variation
                  # (set this to zero if surface is flat)
lamd = 1/6        # Wave length of variation
 # Rescaled Initial Volume (add 0.1 to account for initial relaxation)
 V    = (2.4 + 0.1)*lamd**2

# Find droplet radius given its volume
def Radius(Th00, epsc, lamd, V):
  arr= np.linspace(0,10,1000)
  FF = np.zeros((arr.size))
  c=0
  def F(x):
    Th= Th00 + epsc*cos(2*pi*x)
    return V-(x**2/2)*(2*Th - sin(2*Th))/(sin(Th))**2
  for y in arr:
    FF[c]=F(y)
    c=c+1
  #Locate the points wwhere the function F equals zero
  F1=FF[0:-1]*FF[1:]
  filter=F1<0
  F2=F1[filter]
  N=F2.size
  rd = np.zeros(N)
  R00 = arr[1:][filter] #droplet radius inital conditions
    #Find droplet radius
  for i in range(N):
    rd[i] = sp.optimize.newton(F,  R00[i])
  return rd[0]

d = Radius(Th00, epsc, lamd, V)

# Droplet shape and location
x0 = 3.0*lamd             # Droplet midpoint
Th = Th00 + epsc*cos(2*pi*d)
R0 = d/sin(Th)          # Droplet radius
Y0 = d/tan(Th)


########################################
```

```
#  Model parameters
########################################
Ch     = 1.0e-02      # Cahn number
dt     = 1.0e-02      # time step
mob    = 3*Ch**2      # mobility parameter
# time stepping family, e.g. theta=1 -> backward Euler,
#theta=0.5 -> Crank-Nicolson
theta = 0.5
Rey   = 1    # Reynolds number
Web   = 0.2 # Weber number

Cn = Constant(1/Ch)  # 1/Cahn number
k  = Constant(dt)    # time step
We = Constant(1/Web) # 1/Weber number
Re = Constant(1/Rey) # 1/Reynolds number
Pe = Constant(mob) # 1/Peclet number

print("Re =", Rey)
print("We =", Web)
print("Pe =", 1/mob)

#############################################################
# Form compiler options, mesh, and test/trial functions
#############################################################
parameters["form_compiler"]["optimize"]     = True
parameters["form_compiler"]["cpp_optimize"] = True

# Create mesh and build function space
TT = 0.5     # Top mesh bound
RR = 1       # Left mesh bound

domain_n_points = 80
domain_points = list()
for n in range(domain_n_points + 1):
    x = n*1./domain_n_points
    domain_points.append( Point(x,   epsT*lamd*cos(2*pi/lamd*(x-RR/2)))
   )
domain_points.append( Point(RR, abs(epsT*lamd)))
domain_points.append( Point(RR, TT))
domain_points.append( Point(0., TT))
domain_points.append( Point(0., abs(epsT*lamd)))
domain1 = Polygon(domain_points)
mesh = generate_mesh(domain1, 80)

```

```
112 #Save mesh
113 mesh_file = File("mesh.xml")
114 mesh_file << mesh
115
116 # Sub domain for Periodic boundary condition
117 class PeriodicBoundary(SubDomain):
118     # Left boundary is "target domain" G
119     def inside(self, x, on_boundary):
120         return bool(x[0] < DOLFIN_EPS and x[0] > -DOLFIN_EPS and
    on_boundary)
121     # Map right boundary (H) to left boundary (G)
122     def map(self, x, y):
123         y[0] = x[0] - RR
124         y[1] = x[1]
125
126 # Create periodic boundary condition
127 pbc = PeriodicBoundary()
128 P1  = FiniteElement("Lagrange", mesh.ufl_cell(), 1)
129 # Velocity space
130 W   = VectorFunctionSpace(mesh, "Lagrange", 2, constrained_domain=pbc)
131 # Pressure space
132 P   = FunctionSpace(mesh, "Lagrange", 1, constrained_domain=pbc)
133  # Phasefield and chemical potential space
134 ME  = FunctionSpace(mesh,P1*P1,constrained_domain=pbc)
135
136 # Trial and test functions of the space ``ME`` are now defined::
137 # Define trial and test functions
138 du    = TrialFunction(ME)
139 q, v  = TestFunctions(ME)
140 y = TrialFunction(W)
141 p = TrialFunction(P)
142 w = TestFunction(W)
143 r = TestFunction(P)
144
145 # Define functions
146 u  = Function(ME)    # current solution
147 u1 = Function(W)
148 p1 = Function(P)
149
150 u0 = Function(ME)   # solution from previous converged step
151 y0 = Function(W)
152
153 # Split mixed functions
154 dc, dmu = split(du)
```

```
155 c,  mu  = split(u)
156 c0, mu0 = split(u0)
157
158 ###########################################################
159 # Initial and boundary conditions
160 ###########################################################
161 # A class which will be used to represent the initial conditions is
    created::
162 class InitialConditions(UserExpression):
163     def __init__(self, **kwargs):
164         random.seed(2 + MPI.rank(MPI.comm_world))
165         super().__init__(**kwargs)
166     def eval(self, values, x):
167       if sqrt((x[0]-x0)**2+(x[1]+Y0)**2)<=R0:
168         values[0] = 1
169       else:
170         values[0] = -1
171       values[1] = 0.0
172     def value_shape(self):
173         return (2,)
174
175 # Load or create intial conditions and interpolate
176 if (load==False):
177   # Create intial conditions
178   u_init = InitialConditions(degree=1)
179 else:
180   # Load intial conditions
181   u_init = Function(ME, init_file)
182
183 u.interpolate(u_init)
184 u0.interpolate(u_init)
185
186 # Create boundaries
187 class LowerBoundary(SubDomain):
188     def inside(self, x, on_boundary):
189         tol = 1E-14   # tolerance for coordinate comparisons
190         return on_boundary and x[1] >= -abs(epsT*lamd) and x[1]<=abs(
    epsT*lamd)
191
192 class TopBoundary(SubDomain):
193     def inside(self, x, on_boundary):
194         tol = 1E-14   # tolerance for coordinate comparisons
195         return on_boundary and near(x[1],  TT, tol)
196
```

```
197 class LeftBoundary(SubDomain):
198     def inside(self, x, on_boundary):
199         tol = 1E-14   # tolerance for coordinate comparisons
200         return on_boundary and near(x[0], 0.0, tol)
201 
202 class RightBoundary(SubDomain):
203     def inside(self, x, on_boundary):
204         tol = 1E-14   # tolerance for coordinate comparisons
205         return on_boundary and near(x[0], RR, tol)
206 
207 #Mark boundaries
208 mesh_function = MeshFunction("size_t", mesh, mesh.topology().dim()-1)
209 
210 Gamma_1 = LowerBoundary()
211 Gamma_1.mark(mesh_function, 1)
212 
213 Gamma_2 = TopBoundary()
214 Gamma_2.mark(mesh_function, 2)
215 
216 Gamma_3 = LeftBoundary()
217 Gamma_3.mark(mesh_function, 3)
218 
219 Gamma_4 = RightBoundary()
220 Gamma_4.mark(mesh_function, 4)
221 
222 # Define no-slip conditions at the lower and top boundaries
223 noslip1  = DirichletBC(W, (0, 0), mesh_function, 1)
224 noslip2  = DirichletBC(W, (0, 0), mesh_function, 2)
225 bcu = [noslip1, noslip2]
226 
227 #  define ds
228 ds = Measure('ds', domain=mesh, subdomain_data=mesh_function)
229 n  = FacetNormal(mesh)
230 
231 ############################################################
232 # Governing equations formulation
233 ############################################################
234 # Wetting condition
235 zeta = sqrt(2)/3 # wetting Constant
236 Wetting    = Expression('zeta*cos(Th00 + epsc*cos(2*pi/lamd*(x[0]-0.5))
    )',zeta = zeta, Th00=Th00, epsc=epsc, lamd=lamd, degree=1)
237 
238 # Compute the chemical potential df/dc
239 c    = variable(c)
```

```
f1   = 1/4*(1-c**2)**2
dfdc = diff(f1, c)

f    = -c*grad(mu)  # Capillary force

# Define strain-rate tensor
def epsilon(u):
  return 0.5*(nabla_grad(u) + nabla_grad(u).T)


# (n+theta)
mu_mid = (1.0-theta)*mu0 + theta*mu
c_mid  = (1.0-theta)*c0 + theta*c

# Weak statement of the equations
# Cahn-Hilliard equation
def L(vm):
  L0 = inner(c - c0,q)*dx + dt*inner(dot(y0,grad(c_mid)),q)*dx + \
  Pe*dt*inner(grad(mu_mid),grad(q))*dx - Pe*dt*vm*q*ds(2)
  LL1 = mu*v*dx - dfdc*Cn*v*dx - Ch*dot(grad(v),grad(c))*dx + Wetting*v
   *ds(1)
  out = L0 + LL1
  return out

# Navier Stokes equation
# Tentative velocity step
F1=(1/k)*inner(y - y0,w)*dx + inner(grad(y0)*y0,w)*dx + \
  Re*inner(2*epsilon(y),epsilon(w))*dx - We*inner(f,w)*dx

a1 = lhs(F1)
L1 = rhs(F1)

# Pressure update
a2 = inner(grad(p), grad(r))*dx
L2  =   -(1/k)*div(u1)*r*dx

# Velocity update
a3   = inner(y, w)*dx
L3   = inner(u1, w)*dx - k*inner(grad(p1), w)*dx

# Class for interfacing with the Newton solver
class CahnHilliardEquation1(NonlinearProblem):
    def __init__(self, a, L):
        NonlinearProblem.__init__(self)
```

```
283         self.L = L
284         self.a = a
285     def F(self, b, x):
286         assemble(self.L, tensor=b)
287     def J(self, A, x):
288         assemble(self.a, tensor=A)
289
290 # Compute directional derivative about u in the direction of du (
    Jacobian)
291 a = lambda vm:  return derivative(L(vm), u, du)
292
293 # Create nonlinear problem and Newton solver
294 # sd is the evaporation rate
295 def Evaporate(sdI):
296     vm = Constant(sdI)
297     return CahnHilliardEquation1(a(vm), L(vm))
298
299 #Define Newton Solver
300 solver = NewtonSolver()
301 solver.parameters["linear_solver"] = "lu"
302 solver.parameters["convergence_criterion"] = "incremental"
303 solver.parameters["relative_tolerance"] = 1e-6
304
305 # Use amg preconditioner if available
306 prec = "amg" if has_krylov_solver_preconditioner("amg") else "default"
307 ###########################################################
308 ###########################################################
309
310 def droplet_solution(sd, Tfinal, Nt,file_name):
311   #Create files for saving results
312   mfile = File(file_name.strip()+"/Potential/result.pvd","compressed")
313   cfile = File(file_name.strip()+"/Phasefield/result.pvd","compressed")
314   yfile = File(file_name.strip()+"/Velocity/result.pvd","compressed")
315   pfile = File(file_name.strip()+"/Pressure/result.pvd","compressed")
316   file =  File(file_name.strip()+"/final_u_".strip()+".xml")
317
318   # Assemble matrices
319   A1 = assemble(a1)
320   A2 = assemble(a2)
321   A3 = assemble(a3)
322
323   # Step in time
324   it   = 0.0     # iteration counter
325   t    = 0.0     # time
```

```
326
327 ts  = np.linspace(0,Tfinal,Nt)
328 itc = 0
329
330 while (t < Tfinal):
331   u0.vector()[:] = u.vector()
332   #Allow droplet to relax before starting evaporation
333   if (t < 4):
334     sdI = 0
335     print('evaporation OFF')
336   else:
337     sdI = sd
338     print('evaporation ON')
339   (no_of_iterations,converged) = solver.solve(Evaporate(sdI), u.
    vector())
340
341   #begin("Computing tentative velocity")
342   b1 = assemble(L1)
343   [bc.apply(A1, b1) for bc in bcu]
344   solve(A1, u1.vector(), b1, "gmres", prec)
345   #end()
346
347   # Pressure correction
348   #begin("Computing pressure correction")
349   b2 = assemble(L2)
350   solve(A2, p1.vector(), b2, "gmres", prec)
351   #end()
352
353   # Velocity correction
354   #begin("Computing velocity correction")
355   b3 = assemble(L3)
356   [bc.apply(A3, b3) for bc in bcu]
357   solve(A3, u1.vector(), b3, "gmres", prec)
358   #end()
359
360   # Move to next time step
361   y0.assign(u1)
362   it += 1
363   t  += dt
364   #Save files
365   if (t>=ts[itc]):
366     cfile << (u.split()[0], t)
367     mfile << (u.split()[1], t)
368     yfile <<  u1
```

```
369       pfile <<  p1
370       print("**********************************")
371       print("****// SAVED //***", it, t, ts[itc])
372       print("**********************************")
373       itc += 1
374
375     print("iteration, dt =", it, dt)
376     print("Time (% total)=", t, (100*t/Tfinal))
377   #Save final configuration
378   file << u
379
380 def main():
381   sd  = -2 #Dirichlet condition on chemical potential that drives
       evaporation
382   Tfinal = 100      # Total time
383   Nsaved = 200       #Number of saved files
384   file_name = "Output" # Output file names
385   droplet_solution(sd, Tfinal, Nsaved,file_name)
386
387 if __name__ == "__main__":
388   main()
389
390 ############################
391 ######END PROGRAM##########
392 ############################
```

Listing B.1 Python code that solves the CH-NS stokes system of equations for droplet evaporating on smooth surfaces.

Appendix C

Bifurcation theory

The theory of bifurcation deals with mathematically analysing changes in the qualitative or topological structure of a particular family, such as the integral curves in a family of vectors and the solutions to a differential equation or a dynamical system. A bifurcation occurs if a smooth change in system parameter (bifurcation parameter) leads to sudden changes of quality or topology.

For a droplet that evaporates, the bifurcation parameter is the size of a droplet that changes the stability of the equilibrium solutions of the droplet. To understand the concept of dynamical systems, we consider a one-dimensional differential equation:

$$\frac{dx}{dt} = f(x), \quad x \in \mathbf{R}, \tag{C.1}$$

where we take t as time, x as the position of an imaginary particle moving along the real line, and $\frac{dx}{dt}$ as the velocity of that particle. The equilibrium solution of this dynamical system (C.1) is obtained when the imaginary particle is stationary, $f(x) = 0$. For a droplet on a solid surface, the relation between the size A of a droplet, its contact radius R and contact angle θ is given as:

$$A = \frac{R^2}{2}\frac{2\theta - \sin(2\theta)}{\sin^2\theta}. \tag{C.2}$$

For a given area A, this can be viewed as a nonlinear function for the droplet radius

$$f(R) = A - \frac{R^2}{2}\frac{2\theta - \sin(2\theta)}{\sin^2\theta} = 0. \tag{C.3}$$

The equilibrium solutions can be obtained by solving for R. The stability of the equilibrium solutions of a dynamical system can be understood by examining the flow

described by Eq. (C.1). As shown in Fig. C.1, the flow is to the right when $f(x) > 0$ and to the left when $f(x) < 0$. At the points when $f(x) = 0$, there is no flow; such points are called fixed points or equilibrium points. As Fig. C.1 depicts, there are two types of fixed points; the black circle denote the stable fixed points where the flow is approaching in both directions, and the white circle represent unstable fixed points, where the flow moves away in both directions. In terms of the differential equation (C.1), fixed points represent equilibrium solutions, x^* (since if $x = x^*$ initially, then $x(t) = x^*$ for all time). Hence, an equilibrium is defined to be stable if all sufficiently small disturbances away from it damp out in time.

The equilibrium solution R_e of a droplet of size A can be obtained from Eq. (C.3). The stability of the equilibrium solution can then be examined by considering the energy equation of the system defined in Section 1.2.2 of Chapter 1 as:

$$E(R) = \frac{2\theta R}{\sin\theta} - 2R\cos\theta_e, \tag{C.4}$$

where R and θ are related through Eq. (C.2) and θ_e is the droplet's equilibrium contact angle. The equilibrium solution R_e of the system corresponds to the extrema of the energy function E. The stability of R_e can be determined by computing the second derivative of E with respect to R at R_e, $E''(R_e)$. If $E''(R_e) > 0$, the solution R_e is a minimum and hence stable. If $E''(R_e) < 0$, then R_e is a maximum and unstable consequently.

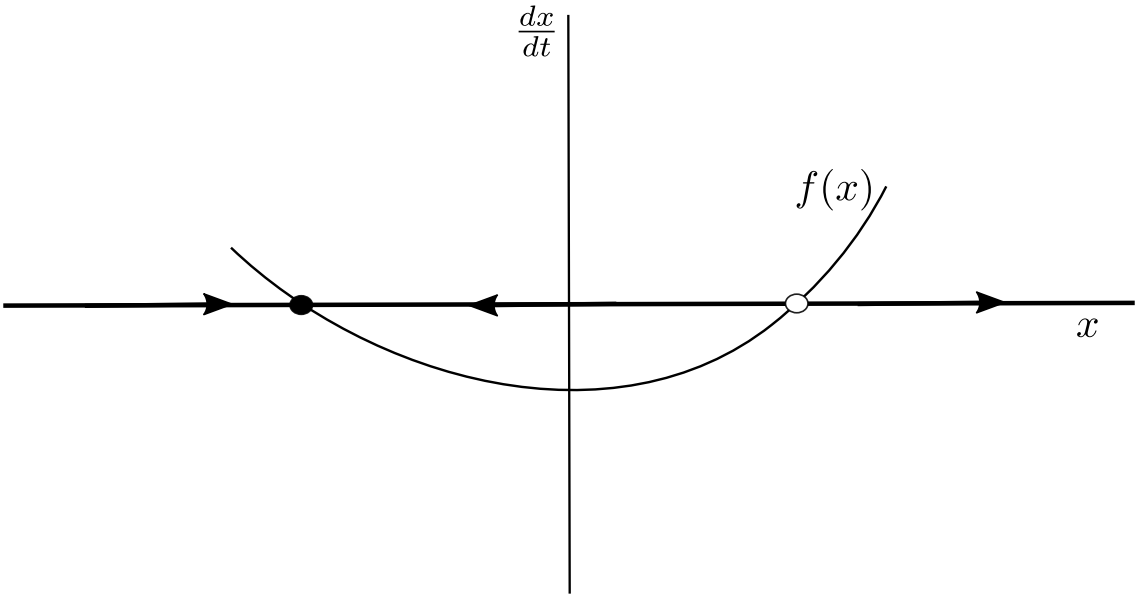

Fig. C.1 Equilibrium points of a one-dimensional dynamical system. Black circle denote stable point while white circle denote unstable point.

For a scenario where the equilibrium contact angle becomes dependent on the droplets location ℓ, the energy of the system is a function of both the droplet's location ℓ and radius R, $E(\ell, R)$. In this case the stability of the equilibrium solutions can be obtained by examining the eigenvalues of the following Hessian matrix H_E given by:

$$H_E(\ell, R) = \begin{pmatrix} E_{\ell\ell} & E_{\ell R} \\ E_{\ell R} & E_{RR} \end{pmatrix}. \tag{C.5}$$

Let λ_1 and λ_2 be the eigenvalues of the Hessian matrix $H_E(\ell_e, R_e)$ at the equilibrium point (ℓ_e, R_e). If $\lambda_1 > 0$ and $\lambda_2 > 0$, then (ℓ_e, R_e) is a minimum and hence stable. If $\lambda_1 < 0$ and $\lambda_2 < 0$, then (ℓ_e, R_e) is a maximum and unstable as a result. If $\lambda_1 \lambda_2 < 0$, then (ℓ_e, R_e) is a saddle point or saddle node.

The qualitative structure of a flow will vary with different parameters. Fixed points, in particular, may be produced or destroyed or have their stability altered. These qualitative changes are referred to as bifurcations, and the parameter values at which they occur are called bifurcation points. There are different types of bifurcations that can be observed. We will only restrict ourselves to the types that emerge in our results. The most common is the saddle-node bifurcation which is a local bifurcation in which two fixed points (or equilibria) of a dynamical system collide and annihilate each other, (see Fig. C.2(a)), its normal form is $\dot{x} = r + x^2$. It is the basic mechanism by which fixed points are created and destroyed. This bifurcation is seen in Section 3.1.3 of Chapter 3 where the stability of an evaporating droplet changes from saddle-node to unstable node as the droplet evaporates.

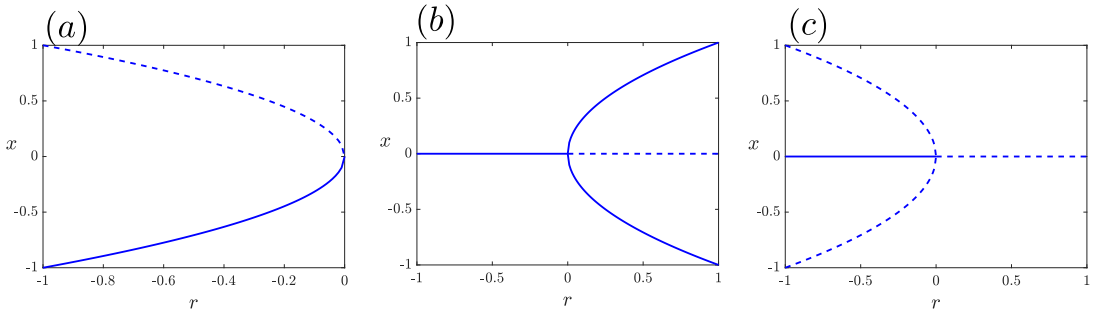

Fig. C.2 (*a*) Saddle node bifurcation. Two fixed points collide and annihilate each other (*b*) Supercritical pitchfork bifurcation. One stable fixed point becomes two stable and one unstable point. (*c*) Subcritical pitchfork bifurcation. One stable fixed collide with two unstable points to become unstable. Solid lines denote stable points while dashed lines denote unstable points.

The pitchfork bifurcation is another important type of bifurcation common in physical problem with symmetry. In such cases, fixed points tend to appear and disappear in symmetrical pairs. In pitchfork bifurcation, the system transitions from one fixed point to three fixed points, (see Fig. C.2(b, c)). It is of two types, supercritical with the normal form $\dot{x} = rx - x^3$, where a three stable points collide to become unstable and subcritical with normal form $\dot{x} = rx + x^3$ where a stable point collide with two unstable points into an unstable point. For an evaporating droplet, Section 3.1.2 of Chapter 3 discusses the stability transitions corresponding to pitchfork bifurcations where a stable point collides with two saddle nodes to become a saddle node (subcritical pitchfork bifurcation), and a saddle node collides with two saddle nodes to become a stable solution (inverted subcritical pitchfork bifurcation). It is this point where the stability of a droplet changes that it moves abruptly in a snap event.

Both saddle-node and pitchfork bifurcations have just one bifurcation parameter r. If we have two parameters, other types of bifurcation can emerge, e.g., a cusp bifurcation. The cusp bifurcation is a bifurcation of equilibria in a two-parameter dynamical system at which the critical equilibrium has one zero eigenvalue and the quadratic coefficient for the saddle-node bifurcation vanishes. Its normal form is a hybrid of both saddle node and pitchfork bifurcations:

$$\dot{x} = r_1 + r_2 x - x^3 \tag{C.6}$$

If $r_1 = 0$, we have the normal form for a supercritical pitchfork bifurcation, and there's a perfect symmetry between x and $-x$. But this symmetry is broken when $r_1 \neq 0$; as a result, r_1 is an imperfection parameter, (see Fig. C.3(a, b)). This property of imperfect bifurcation is exploited in Section 3.1.4 of Chapter 3 to control the direction of motion of evaporating droplets. By varying r_1 two branches of saddle-node bifurcation curve $B_{1,2}$, emerge which meet tangentially at the cusp point and are given by [78], (see Fig. C.3(d)):

$$B_{1,2} = \{(r_1, r_2) : r_1 = \mp \frac{2}{3\sqrt{3}} r_2^{3/2}, r_2 > 0\}. \tag{C.7}$$

These branches are derived by considering the critical case when the horizontal line $-r_1$ is just tangent to either the local minimum or maximum of the curve $r_2 x - x^3$, (see Fig. C.3(c)). To find the values of r_1 at which this bifurcation occurs, we note that the cubic has a local maximum when $\frac{d}{dx}(r_2 x - x^3) = r_2 - 3x^2 = 0$. Hence $x_{max,min} = \pm\sqrt{\frac{r}{3}}$, and the value of the cubic at the local maximum and minimum give the bifurcation curves (C.7).

$$r_2 x_{max} - x_{max}^3 = \frac{2r_2}{3}\sqrt{\frac{r_2}{3}}$$

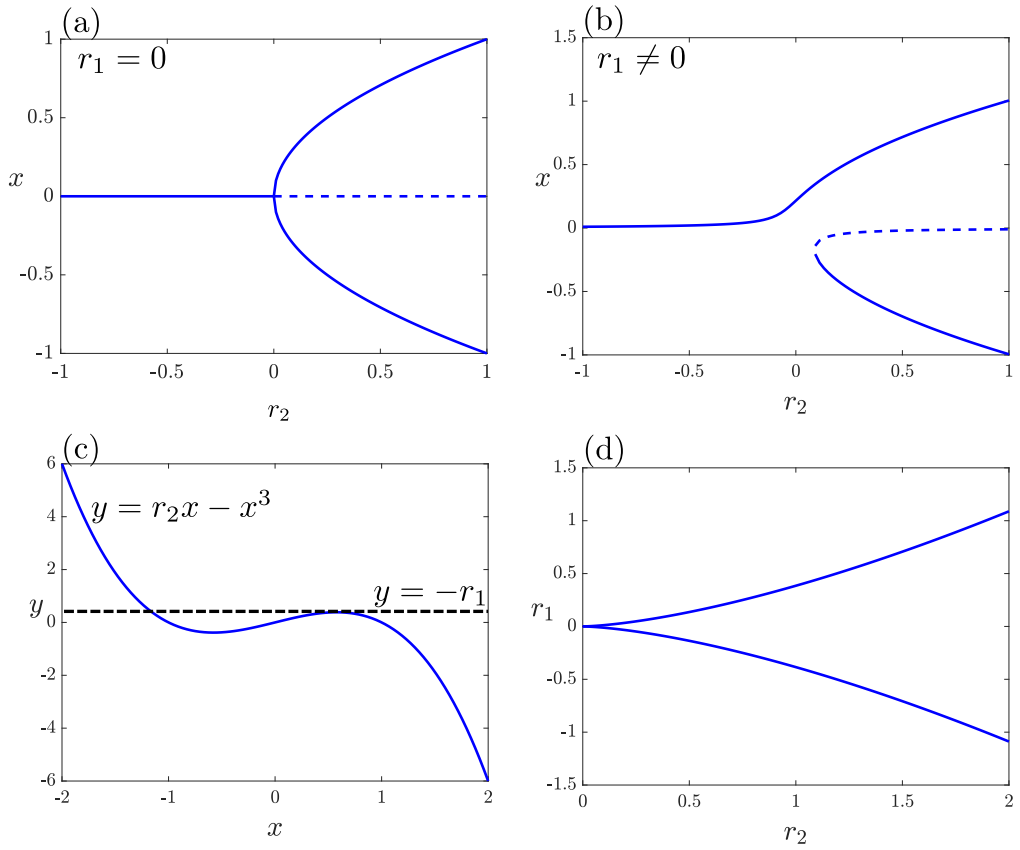

Fig. C.3 (a) Pitchfork bifurcation when $r_1 = 0$. (b) Pitchfork branches become disconnected when $r_1 \neq 0$. (c) Plot of the cubic $r_2 x - x^3$ curve and line $-r_2$. The line intersects the curve at the turning point of the cubic curve at the cusp point. (d) Two branches of the saddle-node bifurcation that meets tangentially at the cusp point. Solid lines denote stable points while dashed lines denote unstable points.

For an evaporating droplet, the emergence of the cusp bifurcation is presented in Section 3.1.3 of Chapter 3 where the size of the droplet A and the amplitude of the contact angle variation serves as two bifurcation parameters.

Appendix D

Cusp bifurcation on a topography

On a non-planar surface $\zeta(x)$, a droplet exhibits cusp bifurcation as its size and the amplitude of the surface is varied and reach a critical value (A_c, ϵ_{Tc}) similar to what is observed on a flat surface with chemical pattern discussed in Section 3.1.3 of Chapter 3. Considering a surface ζ given as:

$$\zeta(x) = \epsilon_T \cos(2\pi x), \tag{D.1}$$

where ϵ_T is the amplitude of the variation. We will show that cusp bifurcation emerges as the droplet size and surface amplitude reach critical values A_c and ϵ_{Tc} respectively. To this end, we first start by noting that on such surfaces, the apparent contact angle of a droplet is obtained as:

$$\theta_a = \theta_e + \tan^{-1}[\epsilon_T 2\pi \cos(2\pi\ell)\sin(2\pi R)], \tag{D.2}$$

where θ_e is the equilibrium contact angle. The cross sectional area of a droplet on the surface $\zeta(x)$ is also obtained as:

$$A = \frac{R^2}{2}\frac{2\theta_a - \sin 2\theta_a}{\sin^2\theta_a} - 2\epsilon_T R\cos(2\pi\ell)\left(\frac{\sin(2\pi R)}{2\pi R} - \cos(2\pi R)\right). \tag{D.3}$$

To understand the scaling relation between ϵ_{Tc} and A_c, we consider the regime where ϵ_T is small. In this limit, $\epsilon_T \ll 1$ and at a fixed location $\ell = 0$, the contact angle Eq. (D.2) can be written as:

$$\theta_a = \theta_e + \theta_1(R)\epsilon_T + \mathcal{O}(\epsilon_T^2), \tag{D.4}$$

where $\theta_1(R) = 2\pi\sin(2\pi R)$. With this expansion of the contact angle, we can now also find an expansion for the droplet area. We begin by noting that the droplet area A, (D.3)

can be rewritten as:

$$A = A_0(\theta_a) + \epsilon_T A_1(R), \tag{D.5}$$

where

$$A_0(\theta_a) = \frac{1}{2}\frac{2\theta_a - \sin 2\theta_a}{\sin^2 \theta_a}, \tag{D.6a}$$

$$A_1(R) = -2R\left(\frac{\sin 2\pi R}{2\pi R} - \cos 2\pi R\right). \tag{D.6b}$$

Using Taylor's series expansion Eq. (D.6a) becomes:

$$A_0 = \frac{1}{2}\frac{2(\theta_e - \epsilon_T\theta_1) - \sin 2\theta_e + 2\theta_1\epsilon_T \cos 2\theta_e}{\sin^2 \theta_e - 2\epsilon_T\theta_1 \sin\theta_e \cos\theta_e} + \mathcal{O}(\epsilon_T^2).$$

This can be simplified as:

$$A_0 = A_0(\theta_e) - 2\theta_1\epsilon_T(1 - \cot\theta_e A_0(\theta_e)),$$

where $A(\theta_e)$ is as defined in equations (D.6a). Inserting A_0 into equation (D.5) so that in the limit of $\epsilon \to 0$, it becomes:

$$A = R^2 A_0(\theta_e) + \epsilon_T A_2,$$

where

$$A_2 = -2\theta_1 R^2(1 - \cot\theta_e A_0(\theta_e)) + A_1. \tag{D.7}$$

To find the radii R_s at which the saddle-node bifurcations occur, we find the stationary points for A, these are the points where: $dA/dR = 0$.

$$\frac{dA}{dR} = A_0 - \epsilon_T(\alpha_1 \sin 2\pi R + \alpha_2 2\pi R \cos 2\pi R) = 0, \tag{D.8}$$

where

$$\alpha_1 = 2\pi(2A_0 \cot\theta_e - 1)$$
$$\alpha_2 = 2\pi(1 - A_0 \cot\theta_e).$$

Equation (D.8) then becomes:

$$\sin X + \alpha X \cos X = \frac{\beta}{\epsilon_T}, \tag{D.9}$$

where $X = 2\pi R$, $\alpha = \frac{\alpha_2}{\alpha_1}$, and $\beta = \frac{A_0}{\alpha_1}$. Hence,

$$\alpha = \frac{4(\theta_e \cos\theta_e - \sin\theta_e)}{\sin 3\theta_e + 5\sin\theta_e - 8\theta_e \cos\theta_e}, \tag{D.10a}$$

$$\beta = \frac{\sin\theta_e(\theta_e - \cos\theta_e \sin\theta_e)}{2\pi(\sin^3\theta_e - 2\sin\theta_e + 2\theta_e \cos\theta_e)}. \tag{D.10b}$$

Let $g(X) = \sin X + \alpha X \cos X$, this corresponds to the onset of cusp bifurcation. We are interested in the stationary points X_s of g. These are points where $dg/dX = 0$:

$$(1+\alpha)\cos X_s - \alpha X_s \sin X_s = 0 \tag{D.11}$$

Expanding the function $g(X)$ around the cusp point X_c gives:

$$g(X) = g(X_c) + g'(X_c)(X - X_c) + \frac{1}{2}g''(X_c)(X - X_c)^2 + \mathcal{O}(X^3).$$

Since $g'(X_c) = 0$, we have that:

$$X = X_c \pm \sqrt{\frac{2}{g''(X_c)}(g(X) - g(X_c))}. \tag{D.12}$$

The cusp point is the point where $X = X_c$, this occurs when $g(X) = g(X_c)$ at a critical amplitude, ϵ_{Tc}:

$$\epsilon_{Tc} = \frac{\beta(\theta_e)}{g(X_s)}, \tag{D.13}$$

we then find that the solutions near the cusp bifurcation are given by:

$$X \simeq X_c \pm \delta \left(\frac{1}{\epsilon_T} - \frac{1}{\epsilon_{Tc}}\right)^{1/2}, \tag{D.14}$$

where $\delta = \sqrt{2\beta(\theta_e)/g''(X_c)}$ is a constant that depends on θ_e only. The critical value where the cusp bifurcation emerges, where $X = X_c$ occurs when $g(X) = g(X_c)$, and is given by:

$$\epsilon_c = \frac{\beta(\theta_0)}{g(X_c)} \sim \beta(\theta_0) A_c^{-1/2}, \tag{D.15}$$

where we have approximated $g(X_c) \sim X_c$, transformed back to the radius variable R, and made use of the fact that at the onset of the cusp bifurcation $A \sim R^2$. For values of the equilibrium contact angle θ_e for which the constants given in Eq. (D.10) are defined, β is finite. Hence, an important conclusion is that cusp, and, consequently saddle node bifurcations are observed for any surface, as long as $\epsilon_T \neq 0$ and $\alpha_1 \neq 0$. The emergence

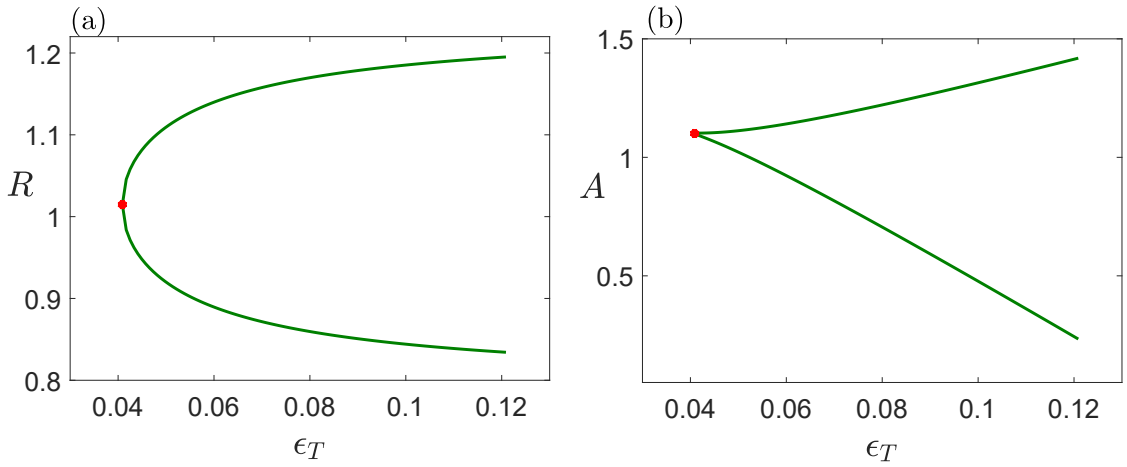

Fig. D.1 Emergence of a cusp bifurcation as the strength of the surface pattern, ϵ_T, is increased for the case with $\theta_0 = 70°$. Plots on the (a) (ϵ, R), and (b) (ϵ, A) planes. Red asterisk mark the critical values at which a cusp bifurcation occurs.

of a cusp bifurcation as the strength of the surface pattern ϵ_T, is increased for the case with $\theta_0 = 70°$ is shown in Fig. D.1. Panel (a) shows the evolution of the droplet radius as the wetting strength changes given by Eq. (D.14). Panel (b) shows the evolution of the droplet size and the wetting strength. It is seen that the two solution branches meet tangentially at the cusp point denoted by the red asterisk which mark the critical values at which a cusp bifurcation occurs.

References

[1] A. Romanova. Water droplets on green leaves. https://unsplash.com/photos/qne-JIASprE, 2019.

[2] G. Ibba. Water droplet on air-plane window. https://unsplash.com/photos/JyK2NreQosU, 2017.

[3] R. D. Deegan, O. Bakajin, T. F. Dupont, G. Huber, S. R. Nagel, and A.T. Witten. Capillary flow as the cause of ring stains from dried liquid drops. *Nature*, 389:827–829, 1997.

[4] J. Park and J. Moon. Control of colloidal particle deposit patterns within picoliter droplets ejected by ink-jet printing. *Langmuir*, 22:3506–3513, 2006.

[5] A. D. Eales, N. Dartnell, S. Goddard, and A. F. Routh. The impact of trough geometry on film shape. a theoretical study of droplets containing polymer, for p-oled display applications. *J. Colloid Interface Sci.*, 458:53–61, 2015.

[6] V. Dugas, J. Broutin, and E. Souteyrand. Droplet evaporation study applied to dna chip manufacturing. *Langmuir*, 21:9130–9136, 2005.

[7] T. Pravinraj and R. Patrikar. A droplet actuation technique for a lab-on-chip device using partial wetting surface without external force. *Sens. Actuators, A*, 285:482–490, 2019.

[8] P. G. de Gennes. Wetting: statics and dynamics. *Rev. Mod. Phys*, 57:827–863, 1985.

[9] J. Eggers and H. A. Stone. Characteristics lengths at moving contact lines for a perfectly wetting fluid: the influence of speed on the dynamic contact angle. *J. Fluid Mech*, 505:309–321, 2004.

[10] T. Young. An essay on the cohesion of fluids. *Philos. Trans. Soc. London*, 95:65–87, 1805.

[11] C. Huh and L. E. Scriven. Hydrodynamic model of steady movement of a solid/liquid/fluid contact line. *J. Colloid Interface Sci*, 35:85–101, 1971.

[12] R. G. Cox. The dynamics of the spreading of liquids on a solid surfaxe. part 1. viscous flow. *J. Fluid Mech*, 168:169–194, 1986.

[13] M. N. Propescu, G. Oshanin, S. Dietrich, and A. M. Cazabat. Precursor films in wetting phenomena. *J. Phys: Condens. Matter*, 24:243102–243132, 2012.

[14] D. M. Anderson, G. B. McFadden, and A. A. Wheeler. Diffuse-interface methods in fluid mechanics. *Annu. Rev. Fluid Mech*, 30:139–165, 1998.

[15] L. H. Tanner. The spreading of silicon oil drops on horizontal surfaces. *J. Phys. D: appl. Phys*, 12:1473 – 1484, 1979.

[16] D. Bonn, J. Eggers, J. Indekeu, J. Meunier, and E. Rolley. Wetting and spreading. *Rev. Mod. Phys*, 81:739–805, 2009.

[17] M. Queralt-Martin, M. Pradas, R. Rodriguez-Trujilo, M. Arundell, E. Corvera Poire, and A. Hernandez-Machado. Pinning and avalanches in hydrophobic microchannels. *Phys. Rev. Lett*, 106, 2011.

[18] H. Kusumaatmaja, C. M. Pooley, S. Girardo, D. Pisignano, and J. M. Yeomans. Capillary filling in patterned channels. *Phys. Rev. E*, 77:067301, 2008.

[19] M. E. R. Shanahan. Simple theory of stick-slip wetting hysteresis. *Langmuir*, 11:1041–1043, 1995.

[20] T. Wong, S. H. Kang, S. K. Y. Tang, E. J. Smythe, B. D. Hatton, A. Grinthal, and J. Aizenberg. Bioinspired self-repairing slippery surfaces with pressure-stable omniphobicity. *Nature*, 477:443–447, 2011.

[21] J. D. Smith, R. Dhiman, S. Anand, E. Reza-Garduno, R. E. Cohen, G. H. McKinley, and K. K. Varanasi. Droplet mobility on lubricant-impregnated surfaces. *Soft Matter*, 9(6):1772–1780, 2013.

[22] J. H. Guan, É. Ruiz-Gutiérrez, B. B. Xu, D. Wood, G. McHale, R. Ledesma-Aguilar, and G. G. Wells. Drop transport and positioning on lubricant-impregnated surfaces. *Soft Matter*, 13(18):3404–3410, 2017.

[23] P. De Gennes, F. Brochard-Wyart, and D. Quere. *Capillarity and Wetting Phenomena*. Springer, 2002.

[24] R. Bhardwaj, X. Fang, and Attinger D. Pattern formation during the evaporation of a colloidal nanoliter drop: a numerical and experimental study. *New J. Phys.*, 11, 2009.

[25] N. Murisic and L. Kondic. On evaporation of sessile drops with moving contact lines. *J. Fluid Mech*, 679:219–246, 2011.

[26] A. M. Cazabat and G. Guena. Evaporation of macroscopic sessile droplets. *Soft Matter*, 6, 2010.

[27] J. M. Stauber, S. K. Wilson, B. R. Duffy, and K. Sefiane. On the lifetimes of evaporating droplets. *J. Fluid Mech*, 744:R2, 2014.

[28] D. Erik, K. E. Stefan, Z. Xuehua, Z. Harold JW, and L. Detlef. Stick-jump mode in surface droplet dissolution. *Langmuir*, 31:4696–4703, 2016.

[29] G. J. Dunn, S. K. Wilson, B. R. Duffy, S. David, and K. Sefiane. A mathematical model of the evaporation of a thin sessile liquid droplet: Comparison between experiment and theory. *Colloids Surf, A Physicochem Eng Asp*, 323:50–55, 2008.

[30] J. P. Burelbach, S. G. Bankoff, and S. H. Davis. Nonlinear stability of evaporating/-condensing liquid films. *J. Fluid Mech*, 195:463–494, 1988.

[31] A. Amini and G. M. Homsy. Evaporation of liquid droplets on solid substrates. i. flat substrate with pinned or moving contact line. *Physical Review Fluids*, 2:043603, 2017.

[32] G. Guena, C. Poulard, and A. M. Cazabat. The dynamics of evaporating sessile droplets. *J. Colloid Sci.*, 69:1–8, 2007.

[33] C. Poulard, G. Guena, and A. M. Cazabat. Diffusion-driven evaporation of sessile drops. *J. Phys.: Condens. Matter*, 17:4213–4227, 2005.

[34] G. G. Wells, E. Ruiz-Gutierrez, Y. Le Lirzin, A. Nourry, B. V. Orme, M. Pradas, and R. Ledesma-Aguilar. Snap evaporation of droplets on smooth topographies. *Nat. Commun*, 9:1380–1387, 2018.

[35] R. G. Picknett and R. Bexon. The evaporation of sessile or pendant drops in still air. *J. Colloid Interface Sci.*, 61(2):336–350, 1977.

[36] Q. Li, P. Zhou, and H. J. Yan. Pinning-depinning mechanism of the contact line during evaporation on chemically patterned surfaces: A lattice Boltzmann. *Langmuir*, 32:939–9396, 2016.

[37] F. G. H. Schofield, A. W. Wray, D. Pritchard, and S. K. Wilson. The shielding effect extends the lifetime of two-dimensional sessile droplets. *J. EngMath*, 120:89–110, 2020.

[38] L. Wang and T. J. McCarthy. Covalently attached liquids: instant omniphobic surfaces with unprecedented repellency. *Angewandte Chemie International Edition*, 55(1):244–248, 2016.

[39] J. H. Guan, G. G. Wells, B. Xu, G. McHale, D. Wood, J. Martin, and S. Stuart-Cole. Evaporation of sessile droplets on slippery liquid-infused porous surfaces (slips). *Langmuir*, 31(43):11781–11789, 2015.

[40] S. Armstrong, G. McHale, R. Ledesma-Aguilar, and G. G. Wells. Pinning-free evaporation of sessile droplets of water from solid surfaces. *Langmuir*, 35(8):2989–2996, 2019.

[41] C. Huh and S. G. Mason. Effects of surface roughness on wetting. *J. Colloid Interface Sci*, 60:11–38, 1977.

[42] L. M. Pismen and Y. Pomeau. Disjoining potential and spreading of thin liquid layers in the diffuse-interface model coupled to hydrodynamics. *Phys. Rev. E*, 62:2480–2492, 2000.

[43] D. N. Sibley, A. Nold, N. Savva, and S. Kalliadasis. On the moving contact line singularity: Asymptotics of a diffuse-interface model. *Eur. Phys. J. E*, 36:26, 2013.

[44] D. N. Sibley, A. Nold, N. Savva, and S. Kalliadasis. A comparison of slip, disjoining pressure, and interface formation models for contact line motion through asymptotic analysis of thin two-dimensional droplet spreading. *J Eng Math*, 94:19–41, 2015.

[45] P. Seppecher. Moving contact lines in the Cahn-Hilliard theory. *Int. J. Eng. Sci*, 34:977–992, 1996.

[46] P. Yue, C. Zhou, and J. J. Feng. Sharp-interface limit of the Cahn-Hilliard model for moving contact lines. *J. Fluid Mech*, 645:279–294, 2010.

[47] D. N. Sibley, A. Nold, and S. Kalliadasis. Unifying binary fluid diffuse-interface models in the sharp-interface limit. *J. Fluid Mech*, 736:5–43, 2013.

[48] F. Magaletti, F. Picano, M. Chinappi, L. Marino, and C. M. Casciola. The sharp-interface limit of the Cahn-Hilliard/ Navier-Stokes model for binary fluids. *J. Fluid Mech*, 714:95–126, 2013.

[49] X. Feng. Fully discrete finite element approximations of the Navier-Stokes-Cahn-Hilliard diffuse interface model for two-phase fluid flows. *SIAM J. Numer. Anal*, 44:1049–1072, 2006.

[50] J. W. Cahn. Critical point wetting. *J. Chem. Phys*, 66:3667–3672, 1977.

[51] B. Aymard, U. Vaes, M. Pradas, and S. Kalliadasis. A linear, second-order, energy stable, fully adaptive finite element method for phase-field modelling of wetting phenomena. *J. Comput. Phys. X*, 2:100010, 2019.

[52] M. Pradas, N. Savva, J.B. Benziger, I. G. Kevrekidis, and S. Kalliadasis. Dynamics of fattening and thinning 2d sessile droplets. *Langmuir*, 32:4736–4745, 2016.

[53] J. Huang, H. Huang, and X. Wang. Wetting boundary conditions in numerical simulation of binary fluids by using phase-field method: some comparative studies and new development. *Int. J. Numer. Meth. Fluids*, 77:123–158, 2015.

[54] J. W. Cahn. Critical point wetting. *J. Chem. Phys*, 66:3667, 1977.

[55] P. Papatzacos. Macroscopic two-phase flow in porous media assuming the diffuse-interface model at pore level. *Transp. Porous Media*, 66:139, 2002.

[56] K. Park, M. Fernandino, and C. A. Dorao. Numerical solution of incompressible Cahn-Hilliard and Navier-Stokes system with large density and viscosity ratio using the least-squares spectral element method. *JFFHMT*, 3:73–85, 2016.

[57] R. Ledesma-Aguilar, D. Vella, and J. Yeomans. Lattice-Boltzmann simulations of droplet evaporation. *Soft Matter*, 10:8267–8275, 2014.

[58] H. Ding, P. D. M. Spelt, and C. Shu. Diffuse interface model for incompressible two-phase flows with large density ratios. *J. Comput. Phys*, 226:2078–2095, 2007.

[59] B. E. Rapp. *Microfluidics: Modelling, Mechanics, and Mathematics*. Elsevier, 2017.

[60] A. J. Chorin. Numerical solution of the Navier-Stokes equations. *Math. Comp*, 22:745–762, 1968.

[61] M. S. Alnæs, J. Blechta, J. Hake, A. Johansson, B. Kehlet, A. Logg, C. Richardson, J. Ring, M. E. Rognes, and G. N. Wells. The fenics project version 1.5. *ANS*, 3(100), 2015.

[62] M. S. Alnæs, A. Logg, K. B. Ølgaard, M. E. Rognes, and G. N. Wells. Unified form language: A domain-specific language for weak formulations of partial differential equations. *TOMS*, 40(2), 2014.

[63] M. Ewetola, R. Ledesma-Aguilar, and M. Pradas. Control of droplet evaporation on smooth chemical patterns. *Phys. Rev. Fluids*, 6:033904, 2021.

[64] M. Pradas, N. Savva, J.B. Benziger, I.G. Kevrekidis, and S. Kalliadasis. Dynamics of fattening and thinning 2d sessile droplets. *Langmuir*, 32:4736–4745, 2016.

[65] S. Strogatz. *Non linear Dynamics and Chaos.* Addison-Wesley, 1985.

[66] N. Lettalleur, F. Plouraboué, and M. Prat. Average flow model of rough surface lubrication: flow factors for sinusoidal surfaces. *J. Tribol*, 2002.

[67] N. Savva, G. A. Pavliotis, and S. Kalliadasis. Contact lines over random topographical substrates. part 1. statics. *JFM*, page 358–383, 2011.

[68] H. Geun Lee and J. Kim. A comparison study of the Boussinesq and the variable density models on buoyancy-driven flows. *J Eng Math*, 75:15–27, 2012.

[69] X. Feng, J. Kou, and S. Sun. A novel energy stable numerical scheme for Navier-Stokes-Cahn-Hilliard two-phase flow model with variable densities and viscosities. *ICCS*, 10862:113–128, 2018.

[70] C. Liu and J. Shen. A phase field model for the mixture of two incompressible fluids and its approximation by a fourier-spectral method. *Physica D*, 179:211–228, 2003.

[71] J. Kim. Phase-field models for multi-component fluid flows. *Commun. Comput. Phys*, 12:613–661, 2012.

[72] H. Ding, P. D. M. Spelt, and C. Shu. Diffuse interface model for incompressible two-phase flows with large density ratios. *J. Comput. Phys*, 226:2078–2095, 2007.

[73] Y. Chen and J. Shen. Efficient adaptive energy stable schemes for the incompressible Cahn-Hilliard Navier-Stokes phase-field models. *J. Comput. Phys.*, 308:40–56, 2016.

[74] J. Kim, S. Lee, Y. Choi, S. M. Lee, and D. Jeong. Basic principle and practical applications of the Cahn-Hilliard equation. *Math. Probl. Eng*, 2016.

[75] M. Hintermuller amd M. Hinze and C. Kahle. An adaptive finite element Moreau-Yosida-based solver for a coupled Cahn-Hilliard/Navier-Stokes system. *J. Comput. Phys.*, 235:810–827, 2013.

[76] M. Hintermuller, M. Hinze, C. Kahle, and T. Keil. A goal-oriented dual-weighted adaptive finite element approach for the optimal control of a nonsmooth Cahn-Hilliard-Navier-Stokes system. *Optim Eng*, 19:629–662, 2018.

[77] N. Savva and S. Kalliadasis. Droplet motion on inlined heterogeneous substrates. *J. Fluid Mech*, 725:462–491, 2013.

[78] Y. A. Kuznetsov. *Elements of Applied Bifurcation Theory.* Springer, 2004.